ADAPTIVE GRIDS IN WEATHER AND CLIMATE MODELING

by

Christiane Jablonowski

A dissertation submitted in partial fulfillment
of the requirements for the degree of
Doctor of Philosophy
(Atmospheric and Space Sciences and Scientific Computing)
in The University of Michigan
2004

Doctoral Committee:

Professor Joyce E. Penner, Chairperson
Professor John P. Boyd
Professor Quentin F. Stout
Professor Bram van Leer

ACKNOWLEDGEMENTS

This dissertation is the result of a joint interdisciplinary effort and would not have been possible without the support of many people. First of all, I would like to say thank you to my committee, my advisor Joyce E. Penner, Quentin F. Stout, Bram van Leer and John P. Boyd. I very much appreciated the support and advice you provided. In addition, many thanks to Michael Herzog for our project discussions and often spontaneous brain-storming sessions.

Many thanks go to Quentin Stout who always had time for discussions about all the numerical and computational difficulties I encountered during this endeavor. This often led to very long lunch meetings or coffee breaks. Special thanks also go to Bram van Leer who gave me very good advice with respect to the numerical interpolation methods. Furthermore, I wish to thank Ken Powell for his insights. And of course, this work would have never been possible without Robert Oehmke. He is the developer of the spherical adaptive grid library that he wrote for his Ph.D. thesis in the Electrical Engineering and Computer Science Department at the University of Michigan. The library is a major building block of the project. A thousand thanks, Bob. I very much appreciated your friendship, work, our meetings and e-mails that answered all upcoming questions.

Many more people were involved who made this interdisciplinary collaboration work. I owe a great deal of thanks to the NASA/GSFC team S.-J. Lin, Kevin Yeh and Ricky Rood who provided me with the atmospheric model and their expertise.

Furthermore, special thanks to the NCAR team, especially to David Williamson, for the collaboration, invaluable advice and generous computing resources. I thank Steve Thomas, Rich Loft and Aimé Fournier (NCAR) and Frank Giraldo (NRL, Monterey) for testing the newly developed test case with their models. I am now very much looking forward to joining NCAR as a postdoctoral researcher. In addition, thanks to Detlev Majewski from the German Weather Service DWD for providing me with the weather code GME.

In addition, thank you, Margaret Reid, Jan Beltran, Sandy Pytlinski, Kathy Norris and Sue Griffin for the excellent administrative support in the department. You made things a lot easier.

Last but not least I wish to say thank you to my family and friends who accompanied me during this long journey. In particular, thanks to my Mom, Jabi and Tanja who I at least saw twice a year. In addition, thank you, Anne and Michael, for your friendship, feisty squash and 'Doppelkopf' matches and countless dinner meetings. Thank you, Dave, Laurie, A.J. and Heather for your friendship, companionship and fun evenings. Dave, I hope I was a good housemate. And of course special thanks to you, Rainer, for our long-lasting relationship that kept me grounded during all those years. You kept up with our friend 'Mr. Pole' and all his neighbors. I deeply appreciate your patience and support.

This work was supported by NASA Headquarters under the Earth System Science Fellowship Grant NGT5-30359. In addition, partial funding was provided by the Department of Energy under the SciDAC grant DE-FG02-01ER63248. I am grateful for the support.

TABLE OF CONTENTS

ACKNOWLEDGEMENTS . . . . **iii**

LIST OF FIGURES . . . . **ix**

LIST OF TABLES . . . . **xv**

LIST OF APPENDICES . . . . **xvii**

CHAPTER

I. Introduction: Adaptive grids in weather and climate modeling **1**

- 1.1 Motivation and research questions 1
- 1.2 Adaptive and nonuniform grids 7
  - 1.2.1 Nested grids 7
  - 1.2.2 Stretched grids 9
  - 1.2.3 Dynamically adaptive mesh refinements 11
  - 1.2.4 Summary: Dynamic grid adaptation 14
- 1.3 Adaptive grid libraries 15
- 1.4 Overview of the thesis 20

II. The hydrostatic finite-volume dynamical core **23**

- 2.1 Model design and numerics 24
  - 2.1.1 Governing equations 24
  - 2.1.2 Horizontal discretization 28
  - 2.1.3 Vertical representation 37
  - 2.1.4 Summary 39
- 2.2 Pole problem in latitude-longitude grids 40
  - 2.2.1 Polar cap 41
  - 2.2.2 Polar filters 46
- 2.3 Divergence damping 60

III. Adaptive mesh refinements in spherical geometry **67**

- 3.1 The adaptive finite-volume dynamical core 68

3.1.1 Block data structure 68
3.1.2 Model resolution 72
3.1.3 Grid point positions 76
3.2 Software engineering aspects 79
3.2.1 Adaptive spherical grid library 79
3.2.2 Program flow 86
3.2.3 Performance 87
3.3 Fine-coarse grid interfaces 91
3.3.1 Interpolation and averaging techniques 91
3.3.2 Model interfaces 108
3.3.3 Flux corrections 110

IV. Reduced grid and static adaptations 113

4.1 Error measures and global diagnostics 114
4.1.1 Normalized error norms 114
4.1.2 Global invariants 117
4.1.3 Reference solutions 117
4.2 Reduced grid 119
4.2.1 Design of the reduced grid 120
4.2.2 Advection tests 122
4.2.3 Non-linear shallow water tests 125
4.3 Static adaptations 136

V. Adaptation criteria and 2D dynamic adaptations 147

5.1 Adaptation criteria 148
5.1.1 Flow-based criteria 150
5.1.2 Adaptation criteria for the finite-volume dynamical core 152
5.2 Dynamic adaptations: Shallow water tests 157
5.2.1 Advection tests with the full grid 157
5.2.2 Advection tests with the reduced grid 170
5.2.3 Flow over a mountain 173

VI. Test of the adaptive 3D dynamical core 189

6.1 New idealized test cases for dynamical cores: The Jablonowski-Williamson test 190
6.1.1 Design of the test case 192
6.1.2 Formal test definition and test strategy 196
6.2 Static adaptations 201
6.3 Dynamic adaptations 208

VII. Summary and future research directions **213**

APPENDICES **221**

BIBLIOGRAPHY **257**

LIST OF FIGURES

1.1 Components of a General Circulation Model. 6
1.2 Stretched grid. 10

2.1 Grid staggering techniques after Arakawa. 34
2.2 Latitude-longitude regular grid. 34
2.3 Terrain-following Lagrangian control-volume coordinate system of the Lin-Rood dynamical core. 38
2.4 Orientation of the local unit vectors in spherical coordinates near the North Pole. 42
2.5 Relationship between the multi-valued wind components in spherical coordinates and the unique wind vector in a North Polar stereographic projection. 44
2.6 Response function of different Shapiro filters. 53
2.7 Meridional velocity at day 4 (*McDonalds and Bates* [1989] test case) with and without additional Shapiro filtering in meridional direction at the poles. 55
2.8 Geopotential height (test case 6) with Shapiro filtering. 57
2.9 Differences of the Shapiro-filtered run (test case 6). 58
2.10 Geopotential height (test case 3) with and without Shapiro filtering. 59
2.11 Coefficients for the divergence damping mechanism. 63
2.12 Differences of the zonal wind with the analytic solution at day 10 with and without divergence damping (test case 2, $\alpha = 90$). 65

3.1 Distribution of grid points over the sphere with and without block structure. 68
3.2 Refinement and coarsening principles with 2 refinement levels. . . . 69
3.3 Adapted blocks. 70
3.4 Ghost cell updates for blocks at the same refinement level. 70
3.5 Ghost cell updates for blocks at different refinement levels. 71
3.6 Splitting of one coarse cell into 4 fine-grid cells. 76
3.7 Flux calculations at a fine-coarse grid interface 77
3.8 Cascading refinements. 83

3.9 Information exchange among nearest neighbors. 83
3.10 Load-balancing strategy. 85
3.11 High level view of the program flow with adaptive mesh functionality. 87
3.12 CPU timing data for different block sizes. 88
3.13 Differences of the geopotential height with the analytic solution after refining the whole domain with refinement level 1. Comparison of two normalized coordinates. 100
3.14 Cascade interpolations of the wind components. 102
3.15 Differences of the zonal wind with the analytic solution. Comparison of different interpolation techniques. 104
3.16 Differences of the geopotential height with the analytic solution (test case 6). 105
3.17 Fine-coarse grid interface. 108
3.18 Reduced grid interface without adaptations. 109
3.19 Reduced grid interface with adaptations. 109
3.20 Flux and kinetic energy updates at fine-coarse grid interfaces. . . . 110

4.1 Distribution of blocks and grid points over the sphere with a reduced grid. 121
4.2 Physical grid distance (km) in longitudinal direction for the full grid and reduced grid setups. 121
4.3 Reduced grid: Polar stereographic projections of the cosine bell transported over the North Pole. 124
4.4 Reduced grid: North polar stereographic projections of the geopotential height, the zonal and meridional wind (McDonald test case). 126
4.5 Zonal wind at day 14 (test case 2, $\alpha = 45°$) with different reduced grid setups. 127
4.6 Zonal wind differences with reference solution at day 14 (test case 2, $\alpha = 45°$). 128
4.7 Normalized l_2 height and wind error norms for reduced grid runs (test case 2, $\alpha = 45°$). 129
4.8 Reduced grid simulations with 1 reduction (test case 6). Comparison of interpolation techniques. 131
4.9 Normalized l_2 and l_∞ height errors for the full and different reduced grid. 132
4.10 Normalized global integrals of total energy and potential enstrophy for the full grid and reduced grids (test case 6). 133
4.11 Normalized global integrals of the mass for reduced grid simulations with 1 reduction (test case 6). 134
4.12 Geopotential height at day 14 (test case 2, $\alpha = 45°$) with static refinements. 136

4.13 Zonal and meridional wind at day 14 (test case 2, $\alpha = 45°$) with static refinements. 137
4.14 Normalized l_2 height errors (test case 2, $\alpha = 45°$) for statically adapted runs. 138
4.15 Geopotential height fields at day 7 with statically refined blocks (test case 6). 140
4.16 Normalized l_2 height errors for statically adapted runs (test case 6). 141
4.17 Initial geopotential height and static adaptations (test case 4). . . . 142
4.18 Geopotential height and height errors at day 5 (test case 4). 145
4.19 Normalized l_2 and l_∞ height error norms for adapted and non-adapted model runs (test case 4). 146

5.1 Choices for refinement criteria illustrated with the initial state of test case 4. 154
5.2 Snapshots of the cosine bell with adapted grid at different time steps (test case 1, $\alpha = 90°$). 159
5.3 Cosine bell after one revolution with refinement and different rotation angles. 161
5.4 Cosine bell after one revolution with different refinement levels ($\alpha = 45°$). 162
5.5 North polar stereographic projections of the cosine bell with different refinement levels. 163
5.6 Normalized l_2 and l_∞ height errors (test case 1). 169
5.7 North polar stereographic projections of the cosine bell (test case 1, $\alpha = 90°$) with reduced grid and refinements. 171
5.8 Normalized l_2 and l_∞ height errors for the full grid and different reduced grids (test case 1, $\alpha = 90°$). 173
5.9 Initial geopotential height and orography with statically adapted grid (test case 5). 174
5.10 Initial absolute values of the relative vorticity and the geopotential gradient (test case 5). 175
5.11 Relative vorticity and the geopotential height field & orography (statically adapted) with relative vorticity-based refinement (test case 5). 179
5.12 Geopotential gradient and the geopotential height field & orography with gradient-based refinement criterion (test case 5). 180
5.13 Meridional wind at day 15 with two adaptation criteria (test case 5). 182
5.14 Normalized l_2 and l_∞ height errors for adapted and non-adapted runs (test case 5). 183
5.15 Normalized global total energy and potential enstrophy for adapted and non-adapted runs (test case 5). 185

5.16 Relative vorticity and the geopotential height field & orography with relative vorticity refinement criterion and dynamically adapted mountain (test case 5). 187

6.1 Jablonowski-Williamson test: Initial zonal wind and temperature. . 193
6.2 Jablonowski-Williamson test: Surface geopotential and initial temperature profiles. 194
6.3 Jablonowski-Williamson test: Absolute and potential vorticity of the initial state. 194
6.4 Jablonowski-Williamson test: Potential temperature and Brunt-Vaisala frequency. 195
6.5 Zonal wind perturbation. 196
6.6 Jablonowski-Williamson test: Surface pressure at day 8 for dynamical core runs with static adaptations. 203
6.7 Jablonowski-Williamson test: Surface pressure at day 10 for dynamical core runs with static adaptations. 204
6.8 Global minimum and maximum surface pressure. 206
6.9 Refinement of one block versus a latitudinal band: Surface pressure after eight hours. 207
6.10 Polvani test: Surface pressure in the Northern Hemisphere at day 3, 4, 8 and 10 with dynamic refinements. 210

A.1 Test case 1: Initial geopotential height of the cosine bell. 224
A.2 Test case 1 & 2: Zonal wind for $\alpha = 0°$. 225
A.3 Test case 1 & 2: Zonal and meridional wind for the rotation angles $\alpha = 45°$ and $\alpha = 90°$. 226
A.4 Test case 2: Initial geopotential height for $\alpha = 45°$. 227
A.5 Test case 2: Initial geopotential height for $\alpha = 90°$. 227
A.6 Test case 3: Initial latitude-height profiles of the geopotential height and zonal wind. 228
A.7 Test case 4: Initial geopotential height and analytic solution at day 5.229
A.8 Test case 5: Initial latitude-height profile of the zonal wind. 230
A.9 Test case 5: NCAR reference solution of $h = h^* + h_s$ at day 10 and 15.231
A.10 Test case 5: NCAR reference solution of the zonal wind at day 15. . 232
A.11 Test case 5: NCAR reference solution of the meridional wind at day 15. 232
A.12 Test case 6: Initial geopotential height, zonal and meridional wind. . 234
A.13 Test case 6: NCAR reference solution of the geopotential height at day 7 & 14, the zonal wind and meridional wind at day 14. 235
A.14 McDonald shallow water test: Initial geopotential height. 236

A.15 McDonald shallow water test: Initial zonal and meridional wind. . . 237
A.16 Jablonowski-Williamson test: Surface pressure at day 8. 243
A.17 Jablonowski-Williamson test: Surface pressure and surface temperature in the Northern Hemisphere at day 10 for the horizontal resolutions $1.25^\circ \times 1^\circ$ and $0.625^\circ \times 0.5^\circ$. 244
A.18 Polvani test: Initial zonal wind, temperature, potential temperature and temperature perturbation. 246
A.19 Polvani test: Surface pressure fields in the Northern Hemisphere at day 8 and 10, resolutions are $2.5^\circ \times 2^\circ$ and $1.25^\circ \times 1^\circ$. 247

LIST OF TABLES

3.1 Refinement levels and corresponding global grid resolutions on the sphere. 74
3.2 Characteristics of the reduced grid configurations in comparison to the regular longitude-latitude grid (full grid). 76
3.3 Impact of the equidistant and non-equidistant y-coordinate on the accuracy of the PPM interpolation scheme 101
3.4 Height and wind error norms for different interpolation schemes. . . 106

4.1 Error statistics for the cosine bell advection test over the poles (test case 1, $\alpha = 90°$) with two reduced grid configurations. 122
4.2 Error statistics for the Rossby Haurwitz test (test case 6). 132
4.3 Error measures and statistics for test case 4 after five model days. . 146

5.1 Dynamic adaptation strategies. 153
5.2 Minimum amplitude of the cosine bell after one revolution for adapted and non-adapted runs (test case 1). 164
5.3 Error measures and statistics for the solid body rotation of the cosine bell for different refinement levels and rotation angles. 166
5.4 Error measures and statistics for the solid body rotation of the cosine bell at day 12 with different CLF numbers (test case 1, $\alpha = 0°$). . . 168
5.5 Error measures and statistics for the solid body rotation of the cosine bell with reduced grids and one refinement level (test case 1, $\alpha = 90°$).172
5.6 Characteristics of the dynamically adapted runs with vorticity and geopotential gradient criteria (test case 5). 176
5.7 Maximum refinement levels in different geographical regions (test case 5). 177

B.1 Vertical coefficients for the 26 model levels. 251

LIST OF APPENDICES

A. Overview of the 2D shallow water and 3D dynamical core test set . . . 223

- A.1 The standard test suite for the 2D shallow water equations . 223
  - A.1.1 Test case 1: Advection of a cosine bell 223
  - A.1.2 Test case 2: Steady state geostrophic flow 225
  - A.1.3 Test case 3: Steady state geostrophic flow with compact support 228
  - A.1.4 Test case 4: Forced nonlinear system with a translating low 228
  - A.1.5 Test case 5: Flow over a mountain 229
  - A.1.6 Test case 6: Rossby-Haurwitz wave 233
- A.2 McDonald-Bates shallow water test 236
- A.3 Idealized tests for 3D dynamical cores 238
  - A.3.1 Jablonowski-Williamson baroclinic wave test 238
  - A.3.2 Polvani baroclinic wave test 245

B. Vertical coordinate 249

C. Symbols and Acronyms 253

CHAPTER I

Introduction: Adaptive grids in weather and climate modeling

1.1 Motivation and research questions

Adaptive Mesh Refinement (AMR) techniques provide an attractive framework for atmospheric flows since they allow an improved resolution in limited regions without requiring a fine grid resolution throughout the entire model domain. The model regions at high resolution are kept at a minimum and can be individually tailored towards the research problem associated with atmospheric model simulations.

A solution-adaptive grid is a virtual necessity for resolving a problem with different length scales. In order to avoid under-resolving high-gradient regions in the problem, or conversely, over-resolving low-gradient regions at the expense of more critical regions, solution adaptation is a powerful tool saving several orders of magnitude in computing resources for many problems. Climate and weather models, or generally speaking computational fluid dynamics (CFD) codes, are among the many applications that are characterized by multiscale phenomena and their resulting interactions. For instance, large-scale weather systems such as midlatitude cyclones drive small-scale frontal zones, thunderstorms or rain events. These small-scale features may then influence the larger scale if, as an example, evaporation processes and turbulence at the surface trigger sensible and latent heat fluxes. But although today's atmospheric general circulation models (GCMs), and in particular weather prediction codes, are already capable of uniformly resolving horizontal scales of order $20 km$ (e.g. the model IFS of the European Centre for Medium-Range Weather Forecasts), the atmospheric motions of interest span many more scales than those captured in a fixed resolution model run. The widely varying spatial and temporal scales, in addition to the nonlinearity of the dynamical system, raise an interesting and challenging modeling problem. Solving such a problem more efficiently and accurately requires variable resolution.

Grid refinement techniques in atmospheric modeling are a relatively new and powerful tool, which will enable the atmospheric science community to address future scientific questions. For example, one of today's most important atmospheric research problems deals with the role of clouds within the climate system. Cloud convective processes change the vertical distribution of heat and water substances. Although small in scale on a cloud-by-cloud basis, the cumulative effect alters the large-scale flow in general circulation models and is considered one of the key feedback mechanisms in climate change scenarios. Today's climate models with typical horizontal resolutions of order $200 - 300 km$, and even smaller scale weather predictions codes, do not capture the cloud activities on their computational grids. They rather treat these processes as sub-grid scale phenomena. Cloud processes, as well as many other small-scale components like radiation or friction, become part of the so-called physics parameterization package of a GCM. The parameterizations approximate the cumulative effect of small-scale transactions in order to take their average effect on the climate system into consideration. It is this, often empirically tuned but state-of-the-art, forcing mechanism that drives the resolved dynamics scale.

In the future AMR climate and weather codes might offer an interesting alternative to today's standard uniform grid approaches. If adaptive grids are capable of actually resolving selected features of interest as they appear, such as convection in tropical regions, then the corresponding parameterizations can locally be dropped and replaced by the underlying physics principles. This poses new and interesting questions concerning the small-scale large-scale flow interactions as well as possible hydrostatic and non-hydrostatic model interplays. The goal of the adaptive mesh model run is not only to capture the onset and evolution of small-scale phenomena but also to simulate their consequent interaction with the surrounding large-scale flow pattern. Every scale of atmospheric motion affects every other scale due to the nonlinearity in the equations. Thus the trend of increased spatial resolution for short-term weather predictions and even long-term climate predictions (*Duffy et al.* [2003]) is on-going and today mostly determined by the availability of sufficient computing resources. As a result, resolving the so-called mesoscale phenomena with typical length scales of tens or hundreds of kilometers has been one of the key aspects to improving forecasts in past decades. As pointed out by *Boville* [1991], improvements can be found in nearly all aspects of the climatic state at finer resolutions. However, *Boyle* [1993] and *Williamson et al.* [1995] also noted that improving the horizontal resolution alone does not necessarily lead to a more accurate climate prediction. The nonlinear dynamics-physics interactions demand a careful tuning of the physics parameterizations with respect to the underlying computational mesh.

The discussion about suitable horizontal resolutions raises an important research problem for atmospheric AMR applications. What are the features of interest for an adaptive weather or climate simulation and will the adaptive model be capable of detecting them early on the coarse initial grid? In contrast to today's typical AMR implementations, such as shock-tracking codes in CFD, the features of interest are less well-defined for atmospheric flows. Shocks or discontinuities that are common in aerodynamic or astrophysical applications are rarely found in meteorological flows that are, from a global climate or weather perspective, dominated by large-scale wave perturbations. In such a rather smoothly varying flow field, detectable features of interest on a coarse grid may therefore be characterized by the atmospheric wave activity with corresponding vorticity patterns, pressure gradients, temperature fronts or tracer distributions.

Adaptive models, even if statically adaptive with only few refinement levels, can play another key role with respect to today's orography treatment in GCMs, especially for climate studies. Static adaptations in mountainous terrain with reinitialized orography profile can improve the rather crude representation of topographic features on the computational grid. This will lead to a more realistic topographic forcing of waves on all atmospheric scales. As an alternative, static refinement options for climate studies could also include broad bands in the midlatitudes in order to capture the baroclinic wave activities at higher resolutions (see also the statically adaptive approach by *Prusa and Smolarkiewicz* [2003]). The waves are a key mechanism for the energy transfer from tropical to polar regions and therefore determine the resulting energy budgets. Today, it is an open question whether AMR techniques will be an efficient alternative to the classical nested grid or even stretched-grid approaches that are currently used to improve local weather or regional climate predictions.

To summarize, dynamically adaptive grids offer an attractive framework for future high resolution climate and weather studies that can focus on certain geographical regions or atmospheric events. So far, dynamically adaptive general circulation models on the sphere are not standard in the atmospheric science community. They are a current research trend that is pursued by research groups at the National Center for Atmospheric Research (NCAR, Boulder, Colorado, USA), the University of Cambridge (Great Britain), the Center for Atmospheric Science (Science Applications International Corporation, Virginia, USA) and the University of Michigan (Ann Arbor, MI, USA). This thesis is a step towards developing adaptive grid techniques for future weather and climate predictions.

Whether adaptive atmospheric models for climate and weather predictions will prevail in the future crucially depends on two major aspects. First, it must be shown that adaptive atmospheric modeling is not just feasible, but also accurate with respect to the resulting flow patterns and furthermore, capable of detecting the features of interest reliably. Second, adaptive model simulations must also be computationally less expensive than comparable uniform high resolution runs. As a consequence (and with respect to the fact that climate modeling is a grand-challenge application) any adaptive climate model and its numerics need to perform and scale well on today's distributed-memory parallel computer architectures. Adaptive modeling is a truly interdisciplinary scientific computing effort. Not only does it raise atmospheric science questions, but also computer science and applied mathematics aspects.

This thesis will address many of these research questions. It is concentrated on the design, implementation and analysis of one component of an adaptive climate or weather model, the so-called dynamical core. Besides the physics parameterization package, the dynamical core is the second building block of a GCM and describes the adiabatic equations of motion. The two components *dynamics* and *physics*, together with their processes and closely interconnected nonlinear interactions, are illustrated in figure 1.1. The encircled areas differentiate the two building blocks. Despite the large number of interconnections, a dynamical core can quickly be isolated from the

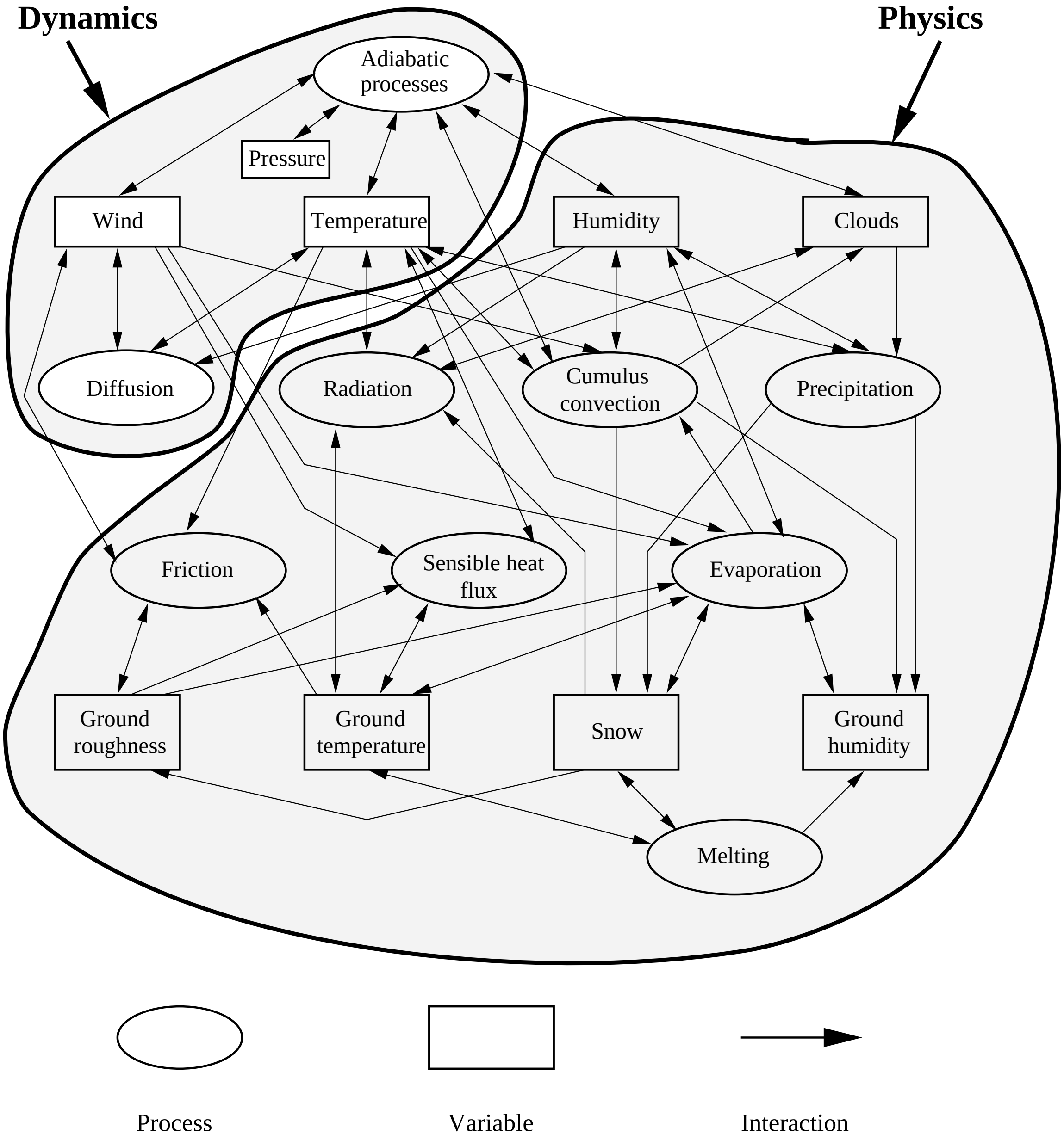

Figure 1.1: Processes and interactions modeled in a typical General Circulation Model. The model components *dynamics* and *physics* are indicated by the encircled areas.

physics package and is considered an independent program unit in modern software engineering designs. In particular, this is true for the NASA/NCAR finite-volume dynamical core used in this thesis which is the foundation for the adaptive grid design. This hydrostatic dynamical core, based on the so-called 3D primitive equations (PE), can furthermore easily be transformed into a 2D shallow water system. Therefore, the adaptive approach can not only be assessed with newly developed 3D idealized test cases for dynamical cores, but also with the well-established standard test suite for the shallow water equations on the sphere. This is a distinct advantage of the model formulation.

1.2 Overview of adaptive and nonuniform grids in climate, weather and ocean modeling

The advantages of using nonuniform grids with increased resolution over areas of interest have been discussed in the context of atmospheric regional modeling for decades (see also *Fox-Rabinovitz et al.* [1997] for an overview). In particular, nested grids, stretched grids and dynamically adaptive mesh refinement methods have been discussed in the literature. The following section gives an overview of past and current research trends with respect to non-uniform and adaptive grid modeling ideas. Special attention is paid to atmospheric science applications.

1.2.1 Nested grids

Nested-grid approaches are widely used at National Weather Centers for detailed local forecasts. Here, a finer grid is permanently embedded in a coarse resolution model, which periodically updates the initial and lateral boundary conditions of the refined region. Even multiple nested models are feasible as demonstrated by *Ginis et al.* [1998] with a primitive-equation ocean model. This nested-grid configuration makes it possible to combine realistic large-scale simulations with mesoscale forecasts for selected regions. Such approaches can be either implemented in a one-way interaction, as in *Davies* [1976] and *Miyakoda and Rosati* [1977], or as a two-way interactive system (*Zhang et al.* [1986]). The former is the simplest nested-grid approach since the fine grid information does not affect the solution on the coarse grid. The latter includes a feedback mechanism that updates the coarse grid fields with the fine grid solution at any location where the two grids coincide. Nested grid models are powerful tools for short-term forecasts. Even non-hydrostatic components can be included in regional models. But the success of a nested forecast mostly relies on the accuracy of the forcing along the static boundaries. Most often the boundary update for a fine grid mesoscale domain is driven by independently developed codes for large-scale systems (as an example see *Spall and Holland* [1991]). Difficulties arise when mass, heat and momentum fluxes are inconsistent across the interfaces. This incompatibility can cause numerical instabilities that seriously degrade the solution in the entire domain. As a result, nested-grid applications have mostly been used for short-term integrations that do not crucially rely on exact conservation principles. From a high-level viewpoint, nested grids with two-way interactions can be viewed as a variant of a static AMR approach, though typical AMR applications do not employ multiple model components.

Furthermore, movable nested grids have been developed that are most commonly used in atmospheric and oceanic feature tracking applications. Examples include the tropical cyclone prediction system by *Ley and Elsberry* [1976] and the cyclone air-sea interaction studies by *Falkovich et al.* [1995] and *Rowley and Ginis* [1999]. Here, a fine grid region or even a cascade of fine grid domains are initially placed over a region of interest. As demonstrated by *Kurihara and Bender* [1980] and *Wang* [2001], the grids are then shifted during the model run according to appropriate criteria like the location of the minimum surface pressure or the gravitational center of the cyclone (see also *Kurihara et al.* [1979]). In some cases, nested-grid models require prior knowledge about future refinement regions, e.g. the main trajectory path (*Jones* [1977]). Consequently, they can not be considered truly adaptive since the nesting remains subjective and inflexible. Despite those different aspects, nested grids and movable nested grids have one important principle in common. The total number of grid points stays constant during a model simulation and is determined by the subjective choice of the initial setup.

1.2.2 Stretched grids

Another kind of variable-resolution model is based on the static, stretched grid approach. With such an approach, grid intervals outside a uniform fine-resolution area of interest are stretched uniformly over the rest of the globe (e.g. *Staniforth and Mitchell* [1978]). As a result, a single global variable-resolution grid is obtained that is held fixed during the model integrations. In a later study, *Gravel and Staniforth* [1992] concluded that the forecast accuracy and reliability on such a smoothly varying grid is superior in comparison to abruptly varying meshes. This conclusion was formulated although, in contrast to the earlier paper, no noise or grid shocks were found in the abruptly varying systems.

Figure 1.2[1] shows a stretched grid that is characterized by two high-resolution bands surrounding the globe (see also the stretched grids by *Fox-Rabinovitz et al.* [1997], *Fox-Rabinovitz et al.* [2001]). Here, the two intersections indicate the regions of

---

[1] The figure shows the stretched grid of the model GEM developed by the Canadian Meteorological Centre, courtesy of Jean Côté.

interest which can be shifted according to user-defined criteria. For example, the Canadian Meteorological Center focuses its operational weather forecast model with stretched grid bands over portions of North America in order to gain resolution and forecast accuracy for this region (*Coté et al.* [1998]). Other stretched grids, like the variable-resolution conformal-cubic grid developed by *McGregor* [1996] and *McGregor and Katzfey* [1998], are focused only on a single region of interest. They therefore avoid the computational overhead invoked by the global band structure. As an alternative, non-uniform resolutions can also be achieved when applying a stretching coordinate transformation with relocated pole points. This approach has been investigated by *Hardiker* [1997] with respect to hurricane forecast studies. Additionally, the technique proposed by *Courtier and Geleyn* [1988] with conformal grid transformations has been applied to the operational French numerical weather prediction system ARPEGE.

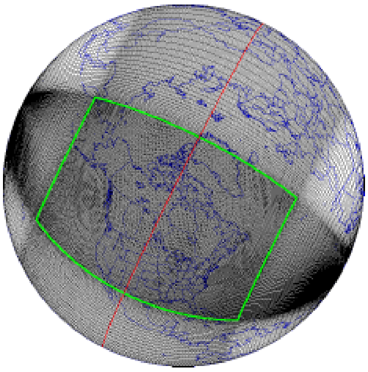

Figure 1.2: Stretched grid.

In contrast to statically stretched grids, dynamically stretched grids offer additional flexibility concerning the feature of interest during a model simulation. They do not require prior knowledge about refinement regions and can therefore be viewed as a globally adaptive variant of the adaptive mesh approach. Dynamic grid deformations are based on time-dependent global coordinate transformations. As in the statically stretched case, the total number of grid points stays constant during the model run, but grid points can now be dynamically focused according to user criteria. In atmospheric modeling, this continuous dynamic grid adaptation technique was first applied by *Dietachmayer and Droegemeier* [1992a] and *Dietachmayer and Droegemeier* [1992b]. They used the adaptive zoning method by *Brackbill and Saltzmann* [1982] with weighting functions for idealized studies of Burger's equation and frontogenesis experiments. More recent examples include the adaptive advection tests by *Iselin et al.* [2002] and the 3D anelastic, non-hydrostatic dynamics package with grid deformations by *Prusa and Smolarkiewicz* [2003].

1.2.3 Dynamically adaptive mesh refinements

The goal of dynamic grid adaptations pursued in this thesis is not to move the grid, but rather to refine the grid in advance of any important physical process that needs additional grid resolution, and to coarsen the grid behind the region. Dynamically adaptive grid approaches have long been used in astrophysical, aeronautical and other computational fluid dynamics problems (*Berger and Oliger* [1984], *Berger and Colella* [1989]). However, in atmospheric science they were first applied approximately a decade ago when *Skamarock et al.* [1989] and *Skamarock and Klemp* [1993] published their adaptive grid techniques for limited-area models in Cartesian coordinates. For example, *Skamarock et al.* [1989] described the model problem of a 2D barotropic cyclone that is embedded in a rectangular refinement block. This block tracked the cyclone controlled by a local truncation error estimate. The refinements were limited to one block and the applied nesting of the refinement block within the coarse model domain developed some discontinuities at the interface boundaries. These oscillations were then avoided with an extended overlap region at fine-coarse grid interfaces as also discussed by *Skamarock* [1988] with a multi-level primitive-equation model. Both Skamarock and Klemp's research efforts were based on an adaptive grid library developed by *Berger and Oliger* [1984].

Recently, *Bacon et al.* [2000] and *Boybeyi et al.* [2001] introduced an adaptive non-hydrostatic regional weather and dispersion model OMEGA which addresses atmospheric transport and diffusion questions. This operational multiscale environment model is based on unstructured, triangulated grids with rotated Cartesian coordinates that can dynamically and statically be adapted to features of interest. The sophisticated modeling system has mainly been designed to assess real-time, regional hazards as well as plume-modeling scenarios, but it also has adaptive weather forecasting capabilities. Meanwhile, OMEGA has been used as a hurricane forecasting system in limited-area regions on the sphere (*Gopalakrishnan et al.* [2002], *Bacon et al.* [2002]). The hurricanes were well-tracked with triangulated adaptation regions. Current research activities by the OMEGA team also include the adaptive simulation of the atmospheric general circulation with physics modules.

Dynamically adaptive advection codes

Atmospheric dynamics on all scales is dominated by the advection process. The numerical solution of the advection problem is therefore fundamentally important for the overall accuracy of the flow solvers and tracer transport mechanisms. Various dynamically adaptive advection codes have been designed so far. Most recently, *Hubbard and Nikiforakis* [2003] described the development of an adaptive 3D passive advection code for tracer transport problems on the sphere (see also brief discussion in section 1.3). Other dynamically adaptive transport approaches for atmospheric science applications include the passive 2D advection algorithms by *Behrens* [1996] and *Behrens et al.* [2000] who formulated an adaptive grid triangulation method in the x-y plane. *Kessler* [1999] implemented a finite element advection technique and evaluated different refinement criteria for the adaptive transport process. Other studies by *Stevens and Bretherton* [1996] and *Stevens et al.* [1999] concentrate on numerical aspects of adaptive multi-level solvers and *Tomlin et al.* [1997] investigated adaptive gridding options for modeling chemical transports with multiscale sources. In particular, *Tomlin et al.* [1997] focused on interactions among emission plumes and the ambient air. This is also discussed by *Odman et al.* [1997], *Sarma et al.* [1999] and *Srivastava et al.* [2000] in their adaptive air quality studies.

Adaptive and non-uniform shallow water models

The shallow water equations describe the 2D non-linear flow of an incompressible fluid. They represent the 2D atmospheric flow conditions in a shallow, hydrostatic atmospheric layer and are therefore considered an idealized testbed for 3D model developments. Most often, the horizontal discretization for primitive-equation based dynamics packages is designed and tested within this 2D shallow water framework.

Due to their close resemblance to the full 3D dynamical core equations, adaptive shallow water models are of particular interest for future adaptive 3D dynamics packages. Several statically and dynamically adaptive shallow water models have been proposed in the literature. So far, all dynamically adaptive approaches deal with the shallow water equations in the x-y Cartesian plane, whereas the statically adaptive models are predominantly in spherical coordinates. Statically adaptive models on the sphere have been developed by *Ruge et al.* [1995], *Fournier et al.* [2000], *Fournier et al.* [2004] and *Barros and Garcia* [2004]. The first two studies discuss a refined representation of the orography data, whereas *Fournier et al.* [2004] resolved a pre-determined cyclone track in midlatitudes at higher resolutions. *Barros and Garcia* [2004], on the other hand, nested a fine-resolution region of interest within the coarse global mesh and provided intermediate refinement levels in order to ensure a smooth transition zone. Here the resolution between neighboring grid points can only differ by a factor of 2. Alternatively, *Coté et al.* [1993] designed a shallow water model on a statically stretched grid that focuses on a selected forecast region.

Dynamically adaptive shallow water models have been designed by *Behrens* [1995] and *Behrens* [1998] who implemented adaptive grid triangulations in the x-y plane. *Hess* [1999] investigated the local adaptive approach on block-structured data with multigrid solvers and *Giraldo* [2000a] assessed an adaptive triangulation method with global remeshing capabilities. Here the grid points in the refined areas are not added locally, but rather the mesh is globally redistributed. Such an approach is based on a remapping or stretching technique.

So far, a dynamically adaptive shallow water model on the sphere had never been built. This thesis presents the first dynamically adaptive approach to the solution of the shallow water equations on the sphere.

1.2.4 Summary: Dynamic grid adaptation

In summary, two fundamental dynamic grid adaptation strategies can be distinguished. Grid points can either be globally redistributed (remapping technique) or locally added and removed (AMR technique). The former approach keeps the total number of grid points constant while the latter varies the number of grid points as demanded by time-dependent flow features. Both strategies have different underlying concepts. The goal of global grid redistribution techniques is to find the most accurate solution for a fixed computational cost, whereas the local adaptive approach aims at a fixed accuracy for a minimum cost. In particular, this is true if local refinements are placed in regions with the highest truncation errors based on truncation error estimates. If flow-dependent refinement criteria are applied that try reducing errors with respect to a specific flow feature, the overall error of the simulation might not be significantly reduced. Instead, the errors associated with the feature of interest are diminished.

Although all approaches to refining the grid domain are different in nature, they all have one aspect in common. The varying resolution may cause artificial reflections and refractions of waves due to compatibility problems at the interface between two resolutions. For instance, a disturbance that propagates from the fine to a coarser mesh may undergo false reflection back to the fine grid or aliasing when entering the coarser domain. These interface-generated problem may further lead to numerical oscillations that can seriously affect the results over the entire computational domain. In addition, local interactions in non-uniform grids are no longer isotropic since the derivatives in horizontal directions might not involve the same scales (*Courtier and Geleyn* [1988]). Therefore, an optimal interface should not only allow all resolvable waves to propagate smoothly with minimal changes in amplitude and phase, but also needs to conserve the exchanged energy, mass and momentum between the grid systems (*Zhang et al.* [1986]). This poses additional questions concerning the optimal interpolation schemes between refinement levels (*Alapaty et al.* [1998]).

1.3 Adaptive grid libraries

Public-domain adaptive-mesh libraries have increasingly become available over the last two decades. The rapid development in recent years shows the importance of current AMR research activities which are greatly facilitated by enhanced computing resources. This section provides a brief, concise overview of possible starting points for AMR model developments. From a historic viewpoint, an important milestone was the adaptive mesh package pioneered by *Berger and Oliger* [1984] which successfully showed the feasibility and efficiency of adaptive methods for hyperbolic equations. It can be considered the first viable approach to adaptive modeling for

CFD applications.

A collection of today's publicly available adaptive mesh refinement libraries is listed below. The majority of these software packages support dynamic grid adaptations in Cartesian coordinates on structured grids. The range of applications that utilize the libraries covers a broad field of disciplines. Among them are the classical CFD areas like models for hydrodynamic and magnetohydrodynamic simulations with shocks. In addition, particle problems, laser-plasma interactions and electromagnetic wave distributions have been successfully tracked with AMR approaches.

Overview of adaptive grid libraries

AMR library by Berger-Oliger The Berger-Oliger AMR library is a collection of FORTRAN routines for the numerical solution of hyperbolic conservation laws in 2 and 3 space dimensions. The underlying data structure is based on rectangular boxes in Cartesian coordinates. The library has been developed by *Berger and Oliger* [1984] and *Berger and Colella* [1989] for serial computer architectures (see also *Berger* [2003]).

AMRCLAW AMRCLAW is a joint project between Randall LeVeque (University of Washington, Seattle) and Marsha Berger (Courant Institute, New York University). The package contains the Berger AMR library (see above, also *Berger and LeVeque* [1998]) and LeVeque's numerics toolbox CLAWPACK, the Conservation LAW PACKage (*LeVeque and Berger* [2003]).

AMR library in BATS-R-US BATS-R-US is a parallel AMR space-weather first-principles magnetohydrodynamic (MHD) model developed at the University of Michigan (Ann Arbor, Michigan, see also *Hansen et al.* [2002]). The data structure is based on Cartesian self-similar blocks which can be adaptively refined in 3 dimensions. The AMR package in BATS-R-US has been the predecessor of the newly developed spherical adaptive grid library with block data used in this thesis. The BATS-R-US software has been successful developed and used in space weather modeling for over 10 years. It is most commonly run to model the solar-wind interaction with solar-system bodies.

CHOMBO The CHOMBO infrastructure provides a set of tools for implementing finite difference methods for the solution of partial differential equations on Cartesian, block-structured adaptively refined rectangular grids. Chombo has been designed at the Lawrence Berkeley National Laboratory (LBNL, Berkeley, California). Both elliptic and time-dependent modules are included, as well as support for parallel platforms and standardized self-describing file formats (HDF5). In addition, a visualization package ChomboVis is publicly available.

DAGH The Distributed Adaptive Grid Hierarchy (DAGH) is a software framework that supports adaptive finite difference techniques for the solution of partial differential equations in Cartesian coordinates. It has been designed for sequential or parallel computing environments and provides a programming interface for traditional Fortran 77/90, C or C++ kernels (see also *Parashar and Browne* [1999]). The DAGH library is no longer under further development.

AMR++ library in Overture AMR++ is an adaptive mesh refinement class library that is a part of the *Overture* framework developed at the Lawrence Livermore National Laboratory (LLNL, Livermore, California). Overture (see also *Brown et al.* [2003]) is an object-oriented library which manages overlapping grids for partial differential equations in serial or parallel computing environments. The AMR toolkit provides additional adaptive mesh refinement capabilities on these structured, even curvilinear, overlapping grids. The framework is designed for finite difference or finite-volume methods.

PARAMESH PARAMESH is a collection of Fortran 90 subroutines that allows the conversion of serial codes with logically Cartesian structured meshes to parallel codes with adaptive mesh refinements. The data structure is based on a block-structured approach. The parallel implementation utilizes either SHMEM calls (communication library originally developed by CRAY) or the Message Passing Interface MPI. The PARAMESH toolkit has been designed by the NASA Goddard Space Fight Center, Greenbelt, Maryland (*MacNeice et al.* [2003]).

PYRAMID Pyramid is a software library for performing parallel adaptive mesh refinement (PAMR) on unstructured meshes. This software library can be used in a variety of unstructured parallel computational applications, including parallel finite element, parallel finite-volume, and parallel visualization applications using triangular or tetrahedral meshes. PYRAMID is distributed by the NASA Jet Propulsion Laboratory, Pasadena, California (*Lou and Norton* [1999]).

SAMRAI The SAMRAI (Structured Adaptive Mesh Refinement Application Infrastructure) library is an object-oriented C++ software framework for computational physics applications. It provides tools for structured AMR and facilitates the development of physics models with modern numerical methods and parallel, high-performance computing requirements. Like Overture, SAMRAI has also been developed at LLNL (*Hornung et al.* [2003]).

With respect to the atmospheric sciences, only the Berger-Oliger approach (*Berger and Oliger* [1984]) has been applied to atmospheric science questions so far. The underlying concept of this software package supports a Cartesian grid hierarchy of fine grids that overlay the coarse grid domain. All grids at all refinement levels are not only maintained, but are actively used for boundary data updates during the course of the integration. Grid boxes are dynamically created and removed based on a Richardson-type estimate of the local truncation error. Here, the overall goal is to maintain a fixed accuracy of the simulation at minimum cost.

The Berger-Oliger library has been applied multiple times in the context of limited area or regional atmospheric modeling. Examples include *Skamarock et al.* [1989] and *Skamarock and Klemp* [1993] (see also section 1.2.3 on page 11) who investigated adaptive meshes for regional weather prediction applications in Cartesian coordinates. They implemented an adaptive 3D hydrostatic (*Skamarock et al.* [1989]) as well as an adaptive non-hydrostatic (*Skamarock and Klemp* [1993]) model and simulated flow fields in limited-area regions. *Fulton* [1997] focused on movable nested meshes for hurricane track predictions and later used the truncation error estimates for an adaptive multigrid cyclone track application (*Fulton* [2001]). *Blayo and Debreu* [1999] applied the Berger-Oliger approach to an adaptive ocean model and most recently, *Hubbard and Nikiforakis* [2003] developed a fully 3D adaptive, passive advection code on the sphere. This model in spherical coordinates transports a tracer component with prescribed wind speeds. The grid resolution adapts in 3 dimensions according to a local gradient indicator of the tracer compound. This model is the first dynamically adaptive 3D advection code on the sphere. Its numerics is based on a monotonic, conservative finite-volume approach.

1.4 Overview of the thesis

The goal of this thesis is to design, build and test a block-structured hydrostatic dynamical core for GCMs that can adapt its horizontal resolution statically and dynamically based on user-defined adaptation criteria.

In this thesis, adaptive grid techniques are applied to a revised version of NASA/ NCAR's next-generation dynamical core for climate and weather research. This hydrostatic so-called Lin-Rood dynamics package (*Lin and Rood* [1997]) is based on a conservative 2D finite-volume discretization in flux form and utilizes a floating Lagrangian coordinate in the vertical direction. The algorithmic design and the numerics are reviewed in chapter II. Furthermore, questions concerning the so-called pole problem, the convergence of the meridians in spherical coordinates, are addressed. This includes a discussion about the polar cap treatment and various polar filters that help stabilize the gravity waves in high latitudes. In addition, the divergence damping mechanism is explained.

Chapter III introduces the fundamental ideas behind the adaptive mesh refinement strategy used in this thesis. One of the main building blocks of the adaptive model is an AMR grid library that manages a block-structured data layout in spherical coordinates. This communication library for parallel processors has been newly developed by *Oehmke and Stout* [2001] and *Oehmke* [2004] in the Computer Science Department at the University of Michigan, Ann Arbor. The block-wise data structure allows cache-efficient high-performance computations with minimal changes to the existing finite-volume flow solvers. Besides discussing these computing and performance aspects, chapter III also gives an overview of interpolation techniques for ghost cell updates and split-join operations in case of adaptations. Additionally, flux updates across interfaces are addressed which ensure global mass conservation.

The adaptive dynamical core is run in two model configurations: the full 3D hydrostatic dynamical core on the sphere and the corresponding 2D shallow water configuration that has been extracted out of the 3D version. This shallow water setup serves as an ideal testbed for the horizontal discretization and the 2D adaptive mesh strategy. 2D test cases are chosen from the standard test suite for the shallow water equations (*Williamson et al.* [1992]). An idealized 3D test case is newly derived as part of this research effort.

Chapter IV concentrates on the assessment of solely static adaptations in the 2D shallow water framework. The shallow water tests evaluate the design and accuracy of a so-called reduced grid setup that can be viewed as a static coarsening in longitudinal direction at the poles. Furthermore, static refinements in pre-defined regions of interest are assessed which reveal the stability of the scheme in presence of the varying resolution at grid interfaces. Appropriate error measures are introduced which are also used in the following chapters.

Chapter V is focused on dynamic adaptations in the 2D shallow water setup. Dynamic adaptations are based on flow characteristics and guided by refinement criteria that detect user-defined features of interest at run time. Possible choices for refinement criteria are reviewed with emphasis on flow-based refinement indicators, like vorticity or gradient assessments. The shallow water tests reveal the feasibility of the dynamically adaptive approach and furthermore are used to compare different choices for the adaptation criterion.

In chapter VI, 3D idealized dynamical core tests of the static and dynamic adaptations are presented. This chapter includes the derivation of the newly developed Jablonowski-Williamson baroclinic wave test case (*Jablonowski and Williamson*

[2004]). This test case, together with the new *Polvani et al.* [2004] test case, shows that adaptive mesh refinements are a viable choice for future adaptive weather and climate models. Furthermore, new questions concerning the orography representation in adaptive model runs are revealed.

Chapter VII provides a summary of the scientific merit and major accomplishments of this thesis. It opens the discussion about future research directions and points out the challenging steps towards an adaptive, complete General Circulation Model with physics modules.

CHAPTER II

The hydrostatic finite-volume dynamical core

In this thesis the development of the adaptive dynamical core for weather and climate research is based on the so-called Lin-Rood finite-volume dynamical core that has been designed at the NASA Goddard Space Flight Center (NASA/GSFC) in the late 1990's. This hydrostatic global dynamics package in flux form is built upon the *Lin and Rood* [1996] advection algorithm, which utilizes advanced oscillation-free numerical approaches to solving the transport equation. In particular, *Lin and Rood* [1996] extended a Godunov-type methodology to multiple dimensions and made use of 2nd order van Leer-type (*van Leer* [1974], *van Leer* [1977]) and 3rd order piecewise parabolic (PPM) methods (*Colella and Woodward* [1984], *Carpenter et al.* [1990]). In 1997, the advection scheme became the fundamental building block of a shallow water code (*Lin and Rood* [1997], *Lin* [1998a]) which then led to the development of the current 3D, primitive-equation (PE) based, finite-volume dynamics package (*Lin et al.* [2001]).

Today, the 3D dynamical core is used operationally for data assimilation applications at NASA/GSFC and, in 2001, it was included in NCAR's climate-prediction system CCSM, the Community Climate System Model. This climate prediction system contains the Community Atmosphere Model, CAM, with physics and dynamics components. In particular, the finite-volume dynamical core is now one of the three standard dynamics modules in CAM and can be chosen at compile time for the individual model setup. The Lin-Rood finite-volume core performs well in NCAR/NASA's internal comparative studies (S.-J. Lin, personal communication). It has the potential to become NCAR's dynamics package of choice for future long-term climate change scenario calculations (*CCSM* [2003]).

Chapter II is organized in three sections. The overall model design and its underlying numerical scheme are reviewed in Section 2.1. This includes a discussion about the governing equations in 2 and 3 dimensions and addresses horizontal as well as vertical discretization issues. Section 2.2 examines the special treatment of the polar regions in the regular latitude-longitude spherical grid. Besides the polar cap concept, filtering techniques are introduced that help stabilize high-frequency gravity waves in polar regions. Gravity waves are also the main focus of Section 2.3. Here the divergence damping mechanism and its impact on the resulting flow field are explained.

2.1 Model design and numerics

2.1.1 Governing equations

The dynamical core is built upon a 2D shallow water approach in the horizontal plane with floating Lagrangian coordinates in the vertical direction (see also Section 2.1.3). The underlying hyperbolic shallow water system is comprised of the mass continuity equation and momentum equation as shown in equations 2.1 and 2.2. Here the flux-form of the mass conservation law and the vector-invariant form of the momentum equation are selected (see also *Lin and Rood* [1997])

$$
\begin{aligned}
\frac{\partial}{\partial t} h + \nabla \cdot (h\,\vec{v}) &= 0 && (2.1)\\
\frac{\partial}{\partial t} \vec{v} + \Omega_a \vec{k} \times \vec{v} + \nabla\bigl(\Phi + \mathcal{K}\bigr) &= 0 && (2.2)
\end{aligned}
$$

where $\vec{v} = u\vec{i} + v\vec{j}$ is the horizontal velocity vector and $\Omega_a = \zeta + f$ denotes the absolute vorticity. The absolute vorticity is composed of the relative vorticity $\zeta = \vec{k} \cdot (\nabla \times \vec{v})$ and the Coriolis force $f = 2\Omega \sin\varphi$ with the latitude φ and the physical constant Ω = angular velocity of the earth (see also Appendix C for an overview of physical constants). Furthermore, $\vec{k}$ is the unit vector in the vertical direction, ∇ represents the horizontal gradient operator, $\Phi = \Phi_s + gh$ symbolizes the free surface geopotential with Φ_s = surface geopotential, h = depth or mass of the fluid and g = gravitational acceleration. In addition, $\mathcal{K} = \frac{\vec{v} \cdot \vec{v}}{2}$ stands for the kinetic energy. A distinct advantage of this vector-invariant formulation is that the metric terms, which are singular at the poles in the curvilinear spherical coordinate system, are hidden by the definition of the relative vorticity.

In three dimensions, the set of equations is very closely related to the shallow water system when replacing the height of the shallow water system with the pressure thickness δp of a Lagrangian layer. Furthermore, the thermodynamic equation 2.4 in conservation form is added to the set

$$
\begin{aligned}
\frac{\partial}{\partial t} \delta p + \nabla \cdot (\delta p\,\vec{v}) &= 0 && (2.3)\\
\frac{\partial}{\partial t} (\Theta\,\delta p) + \nabla \cdot (\Theta\,\delta p\,\vec{v}) &= 0 && (2.4)\\
\frac{\partial}{\partial t} \vec{v} + \Omega_a \vec{k} \times \vec{v} + \nabla_p \Phi + \nabla \mathcal{K} &= 0 && (2.5)
\end{aligned}
$$

where $\delta p = -\rho g \delta z$ is the pressure thickness of a layer bounded by two Lagrangian surfaces in the hydrostatic system with density ρ and height z. The thermodynamic variable Θ is the potential temperature and ∇_p symbolizes a newly derived pressure gradient operator for the finite-volume representation of the pressure gradient force. This operator constitutes the main difference between the shallow water system and the 3D model setup. The underlying method has been developed by *Lin* [1997] and was furthermore discussed by *Janjić* [1998] and *Lin* [1998b]. In this primitive-equation formulation, the prognostic variables of the dynamical core are the wind components u and v, the potential temperature Θ and the pressure thickness δp. The geopotential Φ, on the other hand, is computed diagnostically via the vertical integration of the hydrostatic relation in pressure coordinates

$$\frac{\partial \Phi}{\partial p} = \frac{-1}{\rho} \tag{2.6}$$

with cell-averaged density ρ. In the presence of orography as a lower boundary condition this integration then starts at the geopotential level Φ_s of the surface field. It is important to note that the hydrostatic relationship is the vertical coupling mechanism for the dynamical system. In addition, the pressure level p_n of each Lagrangian surface can be directly derived when adding the pressure thicknesses within the vertical column

$$p_n = p_{top} + \sum_{k=1}^{n} \delta p_k \qquad \text{for n} = 1,2,3, \cdots, N_{lev} \tag{2.7}$$

Here n denotes the vertical index starting from 1 at the lower bounding surface of the uppermost Lagrangian layer. The pressure at the model top p_{top} is prescribed and set to 2.19hPa in the current formulation. There are a total of $N_{lev} + 1$ Lagrangian surfaces that enclose N_{lev} Lagrangian layers. The lowermost Lagrangian surface coincides with the Earth's surface field and, as a consequence, the surface pressure is then automatically determined by the pressure $p_{N_{lev}}$ at the lowest level. In all 3D simulations presented in chapter VI, $N_{lev} = 26$ vertical levels have been selected (see also Appendix B for more detailed information on the vertical coordinate system). They are identical to the vertical levels operationally used for climate studies with NCAR's modeling system CCSM.

The rather unusual form of the primitive equations and in particular the mass continuity equation 2.3 can be derived when integrating the standard form of the 3D continuity equation (see *Durran* [1999]) in the vertical direction. This is demonstrated starting from the continuity equation with a generalized vertical coordinate ξ. Starting from the mass conservation law

$$\frac{\partial}{\partial t}\left(\frac{\partial p}{\partial \xi}\right) + \nabla_\xi \cdot \left(\vec{v}\,\frac{\partial p}{\partial \xi}\right) + \frac{\partial}{\partial \xi}\left(\dot{\xi}\,\frac{\partial p}{\partial \xi}\right) = 0 \tag{2.8}$$

with pressure p and ∇_ξ as the horizontal gradient operator on constant ξ-surfaces, the continuity equation for the pressure thickness δp of a Lagrangian layer with bounding upper and lower surfaces at ξ_u and ξ_l can be determined via the vertical integration

$$\int_{\xi_l}^{\xi_u} \left[\frac{\partial}{\partial t}\left(\frac{\partial p}{\partial \xi}\right) + \nabla_\xi \cdot \left(\vec{v}\,\frac{\partial p}{\partial \xi}\right) + \frac{\partial}{\partial \xi}\left(\dot{\xi}\,\frac{\partial p}{\partial \xi}\right)\right] d\xi = 0. \tag{2.9}$$

In practice, ξ is often replaced by an orography following coordinate system like the hybrid η coordinate used in the finite-volume dynamical core (see also description in Appendix B). After rearranging terms, expression 2.9 becomes

$$\frac{\partial}{\partial t}\int_{\xi_l}^{\xi_u} \frac{\partial p}{\partial \xi}\, d\xi + \nabla_\xi \cdot \left(\vec{\overline{v}} \int_{\xi_l}^{\xi_u} \frac{\partial p}{\partial \xi}\, d\xi\right) + \frac{\partial}{\partial \xi}\int_{\xi_l}^{\xi_u} \left(\dot{\xi}\,\frac{\partial p}{\partial \xi}\right) d\xi = 0. \tag{2.10}$$

The integrated form is then given by

$$\frac{\partial}{\partial t}\big[p(\xi_u) - p(\xi_l)\big] + \nabla_\xi \cdot \Big(\vec{\overline{v}}\big[p(\xi_u) - p(\xi_l)\big]\Big) + \frac{\partial\big[\dot{\xi}_u p(\xi_u) - \dot{\xi}_l p(\xi_l)\big]}{\partial \xi} = 0 \tag{2.11}$$

where the overbar denotes the volume-mean wind speeds. Since there are no vertical transport processes across the bounding surfaces of a Lagrangian layer, the last term on the left hand side vanishes and the general form of the continuity equation for δp follows

$$\frac{\partial}{\partial t}\delta p + \nabla_{\xi} \cdot \left(\vec{v}\,\delta p\right) = 0 \quad . \tag{2.12}$$

The integrated form of the momentum equation and thermodynamic equation can be derived accordingly.

Because of their equivalent designs, the 2D shallow water version can be easily extracted out of the full 3D dynamical core. The main idea is to eliminate the influence of the thermodynamic equation in the momentum equation for the shallow water setup. The thermodynamic equation is linked to the momentum equation only via the computation of the geopotential gradient. Overall, three steps need to be performed. First, the number of vertical layers needs to be set to 1. Second, the potential temperature field Θ must be initialized with the constant $1\,K$ and must not change during the shallow water run (e.g. the transport and updates of $\delta p\,\Theta$ can be omitted). Furthermore, the δp field now stands for the geopotential height h instead of a pressure thickness. Third, the physical constants c_p, R_d and κ need to be overwritten and set to unity. This guarantees that the operator ∇_p in the 3D momentum equations (explained in *Lin* [1997]) becomes equivalent to the operator ∇ in the 2D momentum equation (eqn. 2.2).

2.1.2 Horizontal discretization

The finite-volume dynamical core utilizes a flux form algorithm for the horizontal discretization, which, from the physical point of view, can be considered a discrete representation of the basic physical laws in the finite-volume space. However, from the mathematical standpoint, it can be viewed as a numerical method for solving the governing equations in integral form. This leads to a more natural and often more precise representation of the advection processes, especially in comparison to finite difference techniques. The transport processes are modeled by two-dimensional fluxes into and out of the finite control-volume where volume-mean quantities are predicted. This underlying finite-volume principle of the Lin-Rood advection algorithm is reviewed below using the mass continuity equation of the shallow water equations as an example.

Finite-volume discretization

Finite-volume methods are closely related to finite difference schemes. They are often viewed as a finite flux-differencing approximation to the differential equation and derived on the basis of the integral form of the conservation law (see discussion in *LeVeque* [2002]). The mass conservation law (equation 2.1) in integral form is given by

$$\int_{t_n}^{t_{n+1}} \int_{\Omega} \Big(\frac{\partial}{\partial t} h\Big) \, d\Omega \, dt + \int_{\Omega} \int_{t_n}^{t_{n+1}} \nabla \cdot (h\,\vec{v}) \, dt \, d\Omega = 0 \tag{2.13}$$

where Ω represents a control volume. In the following derivation only two-dimensional control volumes with surface areas A_Ω are considered. Using the relationships

$$\int_{\Omega} h \, d\Omega \;=\; \bar{h} \int_{\Omega} d\Omega \;=\; \bar{h}\, A_\Omega \tag{2.14}$$

$$\int_{t_n}^{t_{n+1}} (h\,\vec{v}) \, dt \;=\; <h\,\vec{v}> \int_{t_n}^{t_{n+1}} dt \;=\; <h\,\vec{v}> \;\Delta t \;=\; \vec{F}\,\Delta t \tag{2.15}$$

where $\Delta t = t_{n+1} - t_n$ is the duration of a time step, the overbar denotes a spatially-averaged quantity, the angled brackets indicate the averaging over a time step ($\vec{F}$ is defined as the time-averaged flux vector), equation 2.13 can be rewritten as

$$\int_{t_n}^{t_{n+1}} \Big(\frac{\partial}{\partial t} \bar{h}\Big) \, dt + \frac{\Delta t}{A_\Omega} \int_{\Omega} \nabla \cdot \vec{F} \, d\Omega = 0 \quad . \tag{2.16}$$

Applying the Gauss divergence theorem yields

$$\int_{t_n}^{t_{n+1}} \Big(\frac{\partial}{\partial t} \bar{h}\Big) \, dt + \frac{\Delta t}{A_\Omega} \oint_{\partial\Omega} \vec{F} \, \cdot \, d\vec{n} = 0 \tag{2.17}$$

in which $\vec{n}$ is an outward-pointing normal to the boundary $\partial\Omega$ of the control volume. With

$$\int_{t_n}^{t_{n+1}} \left(\frac{\partial}{\partial t}\bar{h}\right) dt = \bar{h}\,\Big|_{t_n}^{t_{n+1}} = \bar{h}^{n+1} - \bar{h}^{n} \tag{2.18}$$

the discrete representation of the conservation law becomes

$$\bar{h}^{n+1} = \bar{h}^{n} - \frac{\Delta t}{A_\Omega} \sum_{i=1}^{4} l_i\, \vec{F_i} \cdot \vec{n_i} \tag{2.19}$$

where the sum comprises the 4 line segments with lengths l_i that surround a rectangular 2D control volume. F_i symbolizes the time-averaged fluxes at the cell interfaces and n_i indicates the normal surface vectors to the ith line segment. Assuming an orthogonal x-y control volume with surface area $A_\Omega = \Delta x\, \Delta y$ and corresponding fluxes F and G in x and y direction, equation 2.19 is equivalent to

$$\begin{aligned} \bar{h}_{i,j}^{n+1} &= \bar{h}_{i,j}^{n} - \frac{\Delta t}{\Delta x_i\, \Delta y_j} \Big[\big(\Delta y_j \, (F_{i+\frac{1}{2},j} - F_{i-\frac{1}{2},j})\big) + \\ &\qquad \big(\Delta x_i \, (G_{i,j+\frac{1}{2}} - G_{i,j-\frac{1}{2}})\big)\Big] \qquad (2.20) \\ &= \bar{h}_{i,j}^{n} - \frac{\Delta t}{\Delta x_i} \left(F_{i+\frac{1}{2},j} - F_{i-\frac{1}{2},j}\right) - \frac{\Delta t}{\Delta y_j} \left(G_{i,j+\frac{1}{2}} - G_{i,j-\frac{1}{2}}\right) \qquad (2.21) \end{aligned}$$

in which the indices i, j define the grid point position of the cell center and the half index represents the boundaries of the grid box.

For a spherical grid, the lengths of the line segments $\Delta x, \Delta y$ and the surface area $A_\Omega = \Delta x_i\, \Delta y_j$ in equation 2.20 need to be substituted with the corresponding representation in spherical space

$$\begin{aligned} \Delta x_i &= a\, \cos\varphi\, \Delta\lambda_i \qquad (2.22) \\ \Delta y_j &= a\, \Delta\varphi_j \qquad (2.23) \\ A_\Omega &= a^2 \left(\sin\varphi_{j+\frac{1}{2}} - \sin\varphi_{j-\frac{1}{2}}\right) \Delta\lambda_i \qquad (2.24) \end{aligned}$$

with a = Earth's radius, $\Delta\lambda_i = (\lambda_{i+\frac{1}{2}} - \lambda_{i-\frac{1}{2}})$ and $\Delta\varphi_i = (\varphi_{j+\frac{1}{2}} - \varphi_{j-\frac{1}{2}})$ measured in radians.

In the NASA/NCAR Lin-Rood finite-volume dynamical core though, a slightly different flux-differencing approach has been implemented (see *Lin and Rood* [1997]) that corresponds to equation 2.20 when replacing A_Ω with the approximation $A_\Omega = a^2 \cos\varphi \, \Delta\lambda \, \Delta\varphi$. As a result, the discrete finite-volume conservation law for the cell-averaged height field in spherical coordinates becomes

$$\begin{aligned} \bar{h}^{n+1}_{i,j} &= \bar{h}^{n}_{i,j} - \frac{\Delta t}{a \, \cos\varphi_j \, \Delta\lambda_i} \left(F_{i+\frac{1}{2},j} - F_{i-\frac{1}{2},j}\right) \\ & \quad - \frac{\Delta t}{a \, \cos\varphi_j \, \Delta\varphi_j} \left(\cos\varphi_{j+\frac{1}{2}} \, G_{i,j+\frac{1}{2}} - \cos\varphi_{j-\frac{1}{2}} \, G_{i,j-\frac{1}{2}}\right). \end{aligned} \tag{2.25}$$

Here F and G denote the time-averaged 1D numerical fluxes in longitudinal and meridional direction. In a more compact notation, equation 2.25 can also be written as

$$\bar{h}^{n+1}_{i,j} = \bar{h}^{n}_{i,j} + F_{net} + G_{net} \tag{2.26}$$

where the net fluxes for the grid box i, j are defined as

$$\begin{aligned} F_{net} &= -\frac{\Delta t}{a \, \cos\varphi_j \, \Delta\lambda_i} \left(F_{i+\frac{1}{2},j} - F_{i-\frac{1}{2},j}\right) \\ &= -\frac{\Delta t}{a \, \cos\varphi_j \, \Delta\lambda_i} \, \delta_\lambda \, F \end{aligned} \tag{2.27}$$

$$\begin{aligned} G_{net} &= -\frac{\Delta t}{a \, \cos\varphi_j \, \Delta\varphi_j} \left(\cos\varphi_{j+\frac{1}{2}} \, G_{i,j+\frac{1}{2}} - \cos\varphi_{j-\frac{1}{2}} \, G_{i,j-\frac{1}{2}}\right) \\ &= -\frac{\Delta t}{a \, \cos\varphi_j \, \Delta\varphi_j} \, \delta_\varphi \left(\cos\varphi \, G\right) \end{aligned} \tag{2.28}$$

with the standard discrete difference operator δ. This notation closely resembles the form of the equations in *Lin and Rood* [1997] and *Lin* [1998a] when defining the time-averaged fluxes as $\mathcal{X}$ and $\mathcal{Y}$ and omitting the subscript 'net' in equations 2.27 and 2.28.

Equation 2.26 states that the rate of change of the scalar field h is only due to the net fluxes, which are solely determined by the fluxes through the interfaces of the control volume. Such an approach automatically leads to a conservative discretization. There are many ways of computing the numerical fluxes F and G which so far have not been discussed. Here the choices are focused on higher-order Godunov-type schemes. In particular, the second-order van Leer algorithm (*van Leer* [1977]) and the third-order piecewise parabolic method (PPM, *Colella and Woodward* [1984]) have been selected. These methods are outlined later in this chapter.

The Lin-Rood advection algorithm

The advection algorithm developed by *Lin and Rood* [1996] is based on the finite-volume representation shown in equation 2.26. The following section briefly describes the transport process and flux computations as applied in the NASA/NCAR finite-volume dynamical core. In order to match the *Lin and Rood* [1996] notation the shallow water height h is replaced by a density-like field Q

$$\frac{\partial}{\partial t} Q + \nabla \cdot (Q\,\vec{v}) = 0\,. \tag{2.29}$$

When advancing the Q field for one time step from Q^n to Q^{n+1}, a sequential operator-splitting approach

$$\begin{aligned} Q^x &= Q^n + F_{net}(Q^n) && (2.30)\\ Q^{yx} &= Q^x + G_{net}(Q^x) && (2.31)\\ \Rightarrow Q^{yx} &= Q^n + F_{net}(Q^n) + G_{net}(Q^x) + G_{net}F_{net}(Q^n) && (2.32) \end{aligned}$$

is applied which introduces a directionally anti-symmetric splitting error. A directional-bias free algorithm can then be obtained when averaging two asymmetric operations $\frac{1}{2}(Q^{yx} + Q^{xy})$ to arrive at

$$Q^{n+1} = Q^n + F_{net}\big[Q^n + \frac{1}{2}G_{net}(Q^n)\big] + G_{net}\big[Q^n + \frac{1}{2}F_{net}(Q^n)\big]. \tag{2.33}$$

Equation 2.33 still suffers from a so-called deformational error (*Smolarkiewicz* [1982]) which is removed by replacing the inner flux form operators with their advective counterparts f and g. The resulting symmetric scheme, which is implemented in the finite-volume dynamical core, is given by

$$Q^{n+1} = Q^n + F_{net}\big[Q^n + \frac{1}{2}g_{net}(Q^n)\big] + G_{net}\big[Q^n + \frac{1}{2}f_{net}(Q^n)\big]. \tag{2.34}$$

For the inner, advective 1D operators f and g, a first-order upwind method is employed. The outer 1D fluxes are either modeled by the *van Leer* [1977] algorithm (scheme I with or without monotonicity constraints) or by the monotonicity-preserving PPM method (piecewise parabolic method, see *Colella and Woodward* [1984] and *Carpenter et al.* [1990]). The choice of the flux scheme is guided by Lin-Rood's two-step algorithmic approach to advancing the prognostic variables from t^n to t^{n+1} on a so-called D-grid (see also figure 2.1). During the first step, time-centered velocity components at $t^{n+\frac{1}{2}}$ are calculated on a C-grid with the unconstrained 2nd order van Leer algorithm. In step 2, these auxiliary time-centered winds are then used in order to approximate the time-averaged fluxes for the update of the prognostic variables on the D-grid. This is done with the more accurate 3rd order monotonic PPM method. The use of the time-centered wind speeds at the staggered C-grid positions avoids tackling a so-called Riemann-problem for the approximation of the time-averaged fluxes at cell interfaces.

The grid staggering techniques are illustrated in figure 2.1. In the dynamical core, all staggering options displayed in figure 2.1 are employed at different stages of the algorithm (see details in *Lin and Rood* [1997]). Wind data other than the prognostic wind fields on the D-grid are interpolated via linear interpolations.

In practice, it has been observed (*Lin and Rood* [1997]) that the PPM method

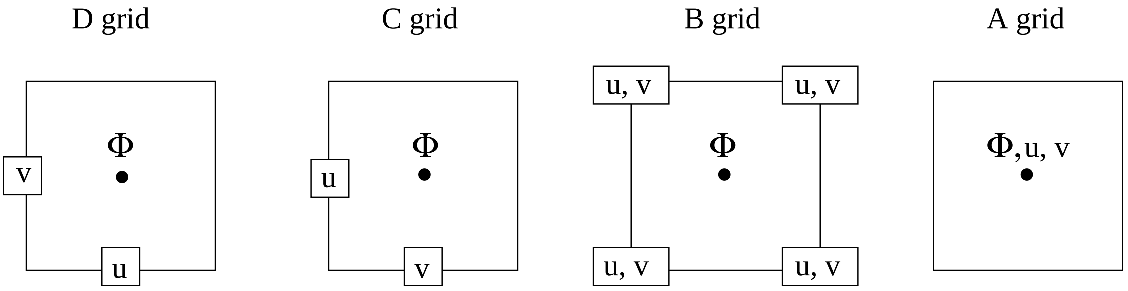

Figure 2.1: Grid staggering techniques (named after Arakawa, see *Arakawa and Lamb* [1977]). u and v indicate the positions of the zonal and meridional wind, Φ symbolizes a scalar quantity, e.g. the geopotential, which is defined at the cell center.

does not lead to superior results in polar regions in comparison to the more economical 2nd order van Leer approach. Since the chosen computational latitude-longitude grid converges at the pole points (figure 2.2) an increased resolution in longitudinal direction is provided in physical space. With respect to accuracy, this allows switching from the PPM method to the van Leer scheme poleward of 75° N/S. On the other hand, the flux calculations in the meridional direction remain unchanged (PPM).

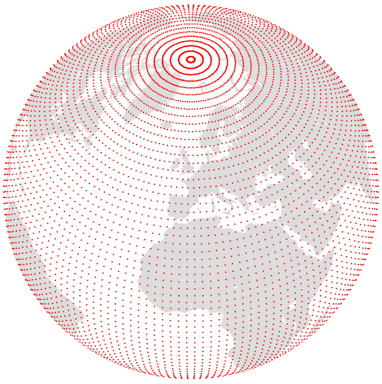

Figure 2.2: Regular grid.

Test results with and without the switch of the algorithm are almost indistinguishable from each other while the former reduces the computational costs on the order of 10-15%. Furthermore, the switch to the van Leer approach in polar regions is beneficial as it adds slightly more implicit diffusion. This helps stabilize high-speed gravity waves in high latitudes as discussed in Section 2.2.2.

Numerical schemes: van Leer and PPM method

The advection method implemented in the Lin-Rood dynamical core can be viewed as a multi-dimensional extension of higher-order Godunov-type schemes like the van Leer or PPM method. These are based on the reconstruct-evolve-average approach (REA as explained by *LeVeque* [2002]) and use piecewise linear (van Leer) or piecewise parabolic (PPM) subgrid distributions for the piecewise continuous reconstruction of the flow field. The transport problem is then solved exactly and new initial data at time t^{n+1} are obtained by averaging the transported quantity over each control volume.

The advection step is upstream-biased and monotonic if limiters are applied to the subgrid distributions. These are used in case of PPM (see details in *Lin and Rood* [1996]) which leads to a total variation diminishing (TVD) method. The selected slope limiter is the monotonized central-difference limiter (MC limiter) proposed by *van Leer* [1977] which is applied as a pure 1D operator during the reconstruction step. Limiting can enforce a strictly monotonic advection algorithm in the 1D case. However, very minor violations of the monotonicity constraint in the two-dimensional flow are possible and have indeed been observed by *Lin and Rood* [1996] and in the adaptive grid runs in Chapter V.

In general, the selected order of the subgrid distribution determines the overall accuracy of the transport scheme. In the van Leer case with piecewise linear reconstructions, the resulting fluxes (for example the fluxes F at an interface in the longitudinal direction) are first-order accurate. On an equidistant 1D grid this leads to a locally second-order advection algorithm since the leading error term cancels when calculating the flux difference. The numerical fluxes are given by (see also

Allen et al. [1991] or *Lin et al.* [1994])

$$F_{i+\frac{1}{2}} = \begin{cases} u_{i+\frac{1}{2}} \left[Q_i + \frac{\Delta Q_i}{2} \left(1 - \frac{u_{i+\frac{1}{2}} \Delta t}{\Delta x_i} \right) \right] & for \; u_{i+\frac{1}{2}} \geq 0 \\ u_{i+\frac{1}{2}} \left[Q_{i+1} - \frac{\Delta Q_{i+1}}{2} \left(1 + \frac{u_{i+\frac{1}{2}} \Delta t}{\Delta x_{i+1}} \right) \right] & for \; u_{i+\frac{1}{2}} < 0 \end{cases} \tag{2.35}$$

where Q stands for the transported quantity and ΔQ symbolizes the slope of the linear subgrid distribution in the longitudinal direction. Here the slope is evaluated with a central differencing approximation $\Delta Q_i = \frac{1}{2}(Q_{i+1} - Q_{i-1})$ and can further be limited as indicated above (see also *Lin et al.* [1994] for a comparison of suitable slope limiters or alternative positive definite constraints). The same basic algorithm applies to the fluxes G in meridional direction.

In order to gain accuracy in the PPM case, the piecewise polynomials in a control volume are approximated by parabolic functions with two degrees of freedom, denoted with δa^x and b^x (*Nair and Machenhauer* [2002], compare also to notation δa, a_6 in *Carpenter et al.* [1990]). They represent the slope and the curvature of the parabola

$$h(x) = \bar{h} + \delta a^x \, x + b^x \left(\frac{1}{12} - x^2 \right) \tag{2.36}$$

with $\bar{h}$ = cell average (see also *van Leer* [1977]). This quadratic subgrid distribution is further analyzed in Section 3.3.1 on page 91 with respect to the interpolation mechanisms in an adaptive grid run. The resulting fluxes of the PPM algorithm are derived in *Colella and Woodward* [1984]. The PPM advection scheme is 3rd order accurate for linear advection problems on uniform 1D grids.

The advection algorithm is the fundamental building block of the horizontal discretization. It is not only used to predict the time evolution of the mass (eqn. 2.3) and potential temperature field (eqn. 2.4), but also determines the absolute vorticity fluxes and kinetic energy in the momentum equation (eqn. 2.5). Further details are presented in *Lin and Rood* [1997].

If the PPM scheme is selected as the primary transport algorithm for an adaptive mesh refinement (AMR) design, *Berger and Colella* [1989] ask

> Why is an adaptive grid needed provided that the solution technique, a third-order Godunov scheme, has quite high resolution? Provided AMR is used is it still necessary to use a high order scheme or could we reduce the order of the accuracy and therefore the computational cost ?

As shown in *Woodward and Colella* [1984] a higher order method still gives more resolution per computational cost than a simpler, lower order scheme on a finer grid. Therefore it is not recommended to decrease the order of accuracy even in the AMR application. *Lin and Rood* [1997] also confirmed that the PPM simulations are far more accurate and less diffusive, especially in a long-term 60-day shallow water test run with uniform resolution. Minor deviations after day 14 grew into clearly visible differences of the height field by day 30 when comparing the van Leer scheme to the PPM advection algorithm. This is an important observation for long-term climate studies. Consequently, since the PPM method is more expensive than simple schemes the computational savings of an AMR run versus a uniform grid run can be substantial as demonstrated later in Chapter V.

2.1.3 Vertical representation

The vertical discretization utilizes a “Lagrangian control-volume” approach, which is based on a terrain-following “floating” Lagrangian coordinate system and a fixed “Eulerian” reference frame. The underlying idea is to start the time integration from the terrain-following Eulerian reference system. The finite-volumes are then allowed to float vertically as dictated by the hydrostatic flow and, as a consequence, the two Lagrangian surfaces bounding the finite-volumes will deform as illustrated in figure 2.3. This deformation can be strong, especially in the presence of persistent

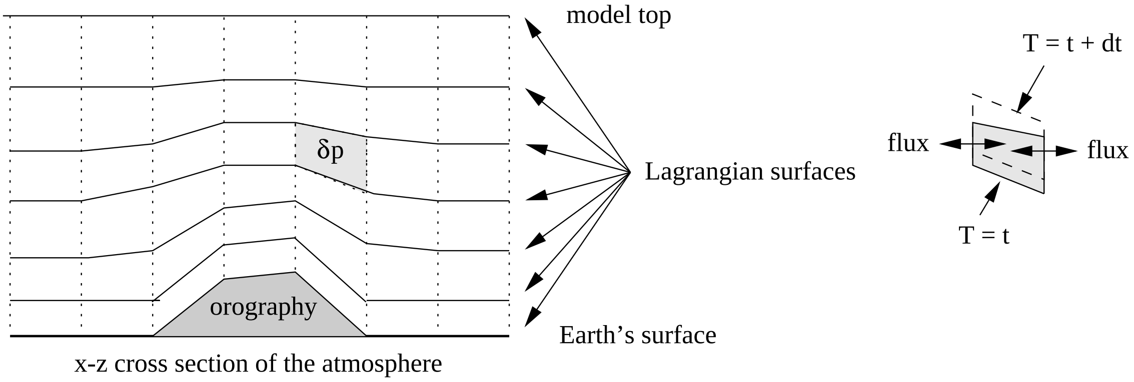

Figure 2.3: Terrain-following Lagrangian control-volume coordinate system of the Lin-Rood dynamical core. The *pressure thickness* δp of a cell is proportional to the total mass. The cell boundaries deform during the forecast (right) and after specific time intervals they are mapped back onto a fixed Eulerian reference system (not shown).

diabatic heating and cooling which ultimately will degrade the accuracy of the 2D flow simulation within a Lagrangian layer. Therefore, the surfaces are mapped back monotonically and conservatively to the fixed Eulerian reference system. Here, a hybrid $\sigma - p$ coordinate system has been chosen for the reference framework, which is most commonly called an η system (see also *Simmons and Burridge* [1981]). The η coordinate is a combination of the orography-following σ coordinate and fixed pressure levels. Further explanations are given in Appendix B on page 249.

It is essential to note that Lagrangian surfaces are non-penetrable material surfaces that do not allow transport processes across the boundaries. This approach effectively reduces the dimensionality of the transport problem from 3 to 2. The 3D model can therefore also be viewed as a vertically staggered shallow water system with 2D transport algorithms within each layer. The periodic vertical remapping step essentially performs the function of a conservative vertical advection process as viewed from the fixed Eulerian reference frame (*van Leer* [1979],?]). It vertically redistributes mass, momentum and total energy from the floating Lagrangian volumes back to the fixed coordinate system. In the adaptive dynamical core formulation, a one-hour remapping interval has been chosen.

The conservative and monotonic mapping is described in detail in the theoretical basis document by *Lin et al.* [2001]. Here a brief overview of the fundamental 3-step principle is given. In general, the one-dimensional mapping is based on a vertical reconstruction of the pressure thickness (mass) δp, the wind components u, v and the volume mean total energy Γ which is composed of the mean internal, potential and kinetic energy. In step 1 of the algorithm, monotonic piecewise parabolic subgrid distributions of the aforementioned quantities are computed (compare also to PPM algorithm by *Colella and Woodward* [1984]). These are then used to calculate the redistributed δp, u, v and Γ values in the Eulerian reference frame (step 2). In order to ensure conservation, the hydrostatic pressure is selected as the mapping coordinate. Finally the layer-mean internal energy, and consequently the temperature, are recovered using the redistributed total, kinetic and potential energy. This step guarantees the conservation of the total energy. Any dissipated kinetic energy that is lost during the remapping process gets automatically transformed into local frictional heating.

2.1.4 Summary

In summary, the novel attributes of the Lin-Rood finite-volume dynamical core are:

- its built-in physical conservation laws.
- the terrain-following, “floating” Lagrangian vertical coordinate which elimi-

nates vertical advection and therefore reduces the dimension of the problem from 3 to 2.

- a monotonicity-preserving and mass-, momentum- and total energy-conserving algorithm that maps the vertical coordinate back to a “fixed” Eulerian reference coordinate.

- the two-dimensional conservative transport between two bounding “horizontal” Lagrangian surfaces that define the control volume (*Lin and Rood* [1996]). The transport algorithm is free of Gibb’s oscillations.

- the precise representation of the terrain. An accurate and physically consistent finite-volume integration of the pressure gradient force for the Lagrangian control-volume is used (*Lin* [1997], *Lin* [1998b]).

- the highly efficient computational design of the algorithm which has been developed for vector- or RISC based parallel computers. The algorithm is highly local in nature, which not only has an advantage for modeling flows with sharp gradients, but also makes the code more suitable for domain decomposition techniques in distributed computing environments (resulting in low communication overhead on parallel processors).

2.2 Pole problem in latitude-longitude grids

NASA/NCAR’s finite-volume dynamical core is implemented in spherical coordinates on a regular latitude-longitude grid. As a result, the meridians converge at the pole points as illustrated in figure 2.2 on page 34. Most commonly, this is called the pole problem on the spherical grid. It leads to extremely small grid boxes or, more appropriately finite-volumes, in the immediate vicinity of the poles. This is further quantified in table 3.1 in Chapter III.

Although the longitudinal resolution in radians stays nominally constant, the physical distance between neighboring nodes in the longitudinal direction contracts. As a consequence, the Courant-Friedrichs-Lewy (CFL) stability condition near the pole is rather restrictive in comparison to the midlatitudes or the tropical region. In order to maintain numerical stability in the explicit finite-volume scheme, the CFL < 1 condition poses a severe time step limitation. In an explicit method, the time step is then determined by the CFL condition for the fastest traveling wave in the system. In a hydrostatic fluid, these are the gravity waves at speeds of order $200 - 300 m/s$.

In addition, pole points in the spherical grid raise a different problem. They are singularities in the curvilinear coordinate system that do not allow the evaluation of metric terms directly at the poles. Therefore, special polar treatment is needed with respect to wind speed and vorticity considerations. These aspects are covered in Section 2.2.1. In Section 2.2.2, filtering strategies are presented that help relax the severe polar time step restriction.

2.2.1 Polar cap

Polar stereographic projections

The wind speeds at the poles in the spherical coordinate system are multi-valued vector components, although in physical (e.g. Cartesian) space the vector is uniquely defined. This is a consequence of the rapidly varying spherical unit vectors at high latitudes as illustrated by the orientation of the coordinate directions for u and v in figure 2.4. In particular, the spherical wind components undergo a complete reversal

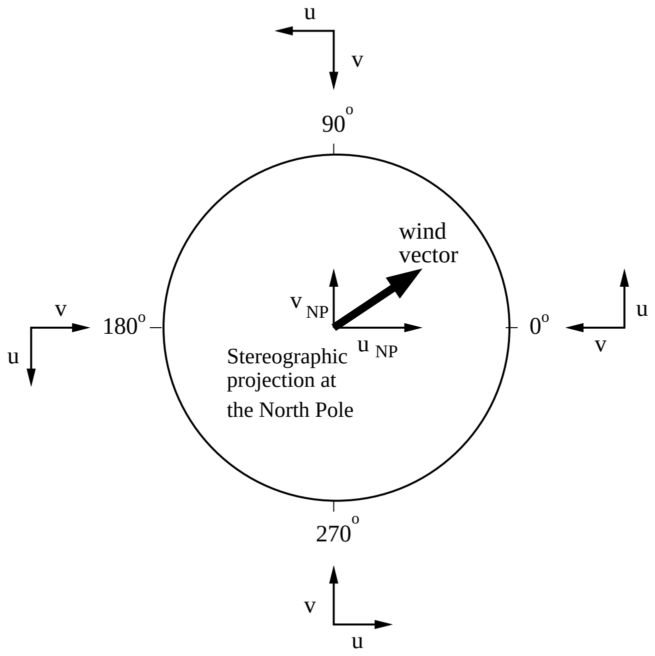

Figure 2.4: Orientation of the local unit vectors in spherical coordinates near the North Pole. The wind vector at the pole is indicated by the thick arrow, the wind components u and v in a stereographic projection are labeled with 'NP'.

of sign when viewed from the local coordinate system of a cross polar position. Therefore, even a very smoothly varying wind field in polar regions, as observed from space, appears to change quickly in the spherical representation.

Due to the singularities of the pole points in the spherical grid, the wind speeds at the poles can not be directly computed. A standard solution to this problem has long been proposed in the literature (e.g. see *Williamson and Browning* [1973] or *Phillips* [1959]). The basic idea is to apply a coordinate transformation or map projection to the polar region in order to compute a unique solution to the transport problem in the transformed system. The solution can then be mapped back onto the spherical mesh.

Alternatively, this idea can also be used to approximate the wind components at the pole points. Instead of solving the transport problem in the map-projected system, the wind vector is then estimated based on the averaged wind information at the adjacent neighbors in the closest latitudinal ring around the pole. This is the so-called polar cap. Typically, a polar stereographic projection is used for the transformation. The wind vector in the polar tangent plane is then uniquely defined and can be projected back in order to recover the multi-valued spherical representation. The corresponding formalism for the North Polar stereographic projection is given by (see also *Phillips* [1959])

$$u_{NP} = \frac{1}{N}\sum_{i=1}^{N}\big[-u_i \sin\lambda_i - v_i \cos\lambda_i\big] \tag{2.37}$$

$$v_{NP} = \frac{1}{N}\sum_{i=1}^{N}\big[u_i \cos\lambda_i - v_i \sin\lambda_i\big] \tag{2.38}$$

where N stands for the number of grid points along the subpolar latitude circle and (u_i, v_i) symbolize the wind components in spherical coordinates. This averaging procedure incorporates all subpolar neighbors and, as an aside, requires extra communication on parallel computer architectures. The resulting unique wind representations u_{NP} and v_{NP} in the north polar tangent plane are then used for the consequent remapping step

$$u_i = -u_{NP} \sin\lambda_i + v_{NP} \cos\lambda_i \tag{2.39}$$

$$v_i = -u_{NP} \cos\lambda_i - v_{NP} \sin\lambda_i \tag{2.40}$$

that retrieves the multi-valued components. This relationship is illustrated in figure 2.5 where the North Pole is symbolically stretched out in the longitudinal direction.

The equivalent expressions for the Southern Hemisphere are specified below (eqn. 2.41-2.44). Here it needs to be taken into account that the sense of the meridional

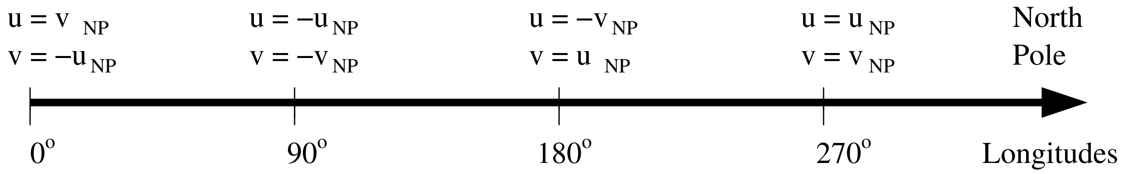

Figure 2.5: Relationship between the multivalued wind components in spherical coordinates and the unique wind vector in a North Polar stereographic projection labeled with 'NP' (see also figure 2.4).

wind at the South Pole (SP) is reversed in comparison to the North Polar representation

$$u_{SP} = \frac{1}{N}\sum_{i=1}^{N}\big[-u_i\,\sin\lambda_i + v_i\,\cos\lambda_i\big] \tag{2.41}$$

$$v_{SP} = \frac{1}{N}\sum_{i=1}^{N}\big[u_i\,\cos\lambda_i + v_i\,\sin\lambda_i\big]\ . \tag{2.42}$$

As before, the remapping step

$$u_i = -u_{SP}\,\sin\lambda_i + v_{SP}\,\cos\lambda_i \tag{2.43}$$

$$v_i = u_{SP}\,\cos\lambda_i + v_{SP}\,\sin\lambda_i \tag{2.44}$$

recovers the spherical wind components at the South Pole.

Vorticity calculation

In the chosen set of equations (see Section 2.1.1), the absolute vorticity $\Omega_a = \zeta + f$ is treated as a transported variable. As a consequence, the relative vorticity ζ as well as the Coriolis term f need to be computed in the whole model domain including both pole points. This can easily be done for the Coriolis parameter, but poses a problem for the standard relative vorticity formulation in spherical coordinates.

In spherical coordinates, the relative vorticity is defined by

$$\zeta = \vec{k}\cdot(\nabla\times\vec{v}) = \frac{1}{a\,\cos\varphi}\Big[\frac{\partial v}{\partial\lambda} - \frac{\partial u\,\cos\varphi}{\partial\varphi}\Big] \tag{2.45}$$

which requires the evaluation of the metric term $\frac{1}{\cos\varphi}$ at any given location. Such a term is undefined at both poles, although from a physical standpoint the vorticity is well-defined throughout the model domain. Therefore, a different approach has been applied at the pole points. The underlying idea is based on an alternative circulation measure and the Stokes' theorem which allow the non-singular computation of the vorticity at arbitrary points in the mesh.

Besides the definition shown in equation 2.45, the vertical component of the relative vorticity ζ is also defined as the circulation C about a closed contour in the horizontal plane divided by the area A of the enclosed region.

$$\zeta = \frac{C}{A} = \lim_{A\to 0}\left(\oint \vec{v}\cdot d\vec{l}\right)A^{-1} \tag{2.46}$$

This relationship is exact in the limit where the area A approaches 0 (see also *Holton* [1992] for further details). In a discrete spherical system, the circulation about a closed latitude ring, in particular near the poles, can be approximated by

$$\begin{aligned}
\oint \vec{v}\cdot d\vec{l} &= \oint |\vec{v}|\ \cos\varphi\ dl \\
&= \int_0^{2\pi} u\ \cos\varphi\ a\, d\lambda \\
&\approx \sum_{i=1}^{N} u_i\ \cos\varphi\, a\,\Delta\lambda_i \qquad (2.47)\\
&= \frac{2\,\pi}{N}\, a\ \cos\varphi \sum_{i=1}^{N} u_i \qquad \text{for constant } \Delta\lambda \text{ only.} \qquad (2.48)
\end{aligned}$$

where dl represents a line element of the contour, u stands for the locally tangential (here longitudinal) component of the velocity vector $\vec{v}$, N symbolizes the number of grid points along the latitude circle, $\Delta\lambda$ stands for the longitudinal grid resolution in radians, a is the Earth's radius and φ is the chosen latitute for the line integral. Typically, this latitude is determined by the position of the closest neighbors surrounding the poles (polar cap). The vorticity is then given by $\zeta = C/A$ where the area of the (north) polar cap A is equal to

$$\begin{aligned} A &= \int_0^{2\pi} \int_{\frac{\pi}{2}-\frac{\Delta\varphi}{2}}^{\frac{\pi}{2}} a^2 \, \cos\varphi \, d\varphi \, d\lambda \\ &= 2\,\pi\,a^2 \left(\sin\left(\frac{\pi}{2}\right) - \sin\left(\frac{\pi}{2} - \frac{\Delta\varphi}{2}\right)\right) \\ &= 2\,\pi\,a^2 \left(1 - \sin\left(\frac{\pi}{2} - \frac{\Delta\varphi}{2}\right)\right). \end{aligned} \tag{2.49}$$

Here the area of the north polar cap is computed at the latitude $\varphi = (\frac{\pi}{2} - \frac{\Delta\varphi}{2})$ where $\Delta\varphi$ represents the constant latitudinal grid spacing at the pole in the adaptive model. The south polar cap calculation can be derived accordingly. Based on equations 2.48 and 2.49 it follows that the resulting relative vorticity value at the North Pole is equal to

$$\zeta = \frac{C}{A} = \frac{\cos\varphi \, \sum_{i=1}^{N} u_i}{N\,a\left(1 - \sin\left(\frac{\pi}{2} - \frac{\Delta\varphi}{2}\right)\right)}$$

which substitutes for the standard relative vorticity calculation (eqn. 2.45). The formulation derived above requires an identical grid resolution along the chosen subpolar latitude circle. As a consequence, the adaptive grid strategy discussed in Chapter III must take this requirement into account.

2.2.2 Polar filters

As discussed earlier in this chapter, the maximum stable time step in an explicit time stepping scheme is constrained by the CFL condition for the fastest propagating modes, which are the gravity modes in a hydrostatically approximated atmosphere or ocean model. A non-hydrostatic model contains additional sound waves that travel at comparable speeds of order $300 ms^{-1}$. These high-frequency but low-energy waves are often of minor geophysical importance for accurate climate or weather forecasts. They are most commonly considered noise for the large scale slow-moving waves of interest, the Rossby-wave modes, with typical wind speeds that are an order of magnitude slower than gravity wave motions. The accuracy of the forecast solely depends on the ability of the model to capture these relevant atmospheric processes.

Gravity waves, if incorrectly treated in the explicit forecasting system, can significantly add noise to the solution or may even cause numerical instabilities. Other sources for numerically unstable integrations include nonlinear instabilities, e.g. the aliasing effect (see also *Haltiner and Williams* [1980] or *Durran* [1999]), that can lead to a spurious growth of short unresolvable waves, which if left unchecked create unstable simulations.

The following example illustrates the severity of the time step problem on a spherical grid. In a shallow water model, the gravity wave speed is given by $c = \sqrt{gh}$ with the gravitational constant g and the height h of the shallow water system. A representative height of $h = 10km$ leads to a gravity wave speed of $313m/s$. Considering that typical horizontal resolutions for climate studies are of order $2.5^\circ \times 2.5^\circ$ with 144x72 grid points, the shortest grid distance closest to the poles (here e.g. at $\varphi = 88.75^\circ$) is determined by the circumference of this latitude ring divided by the number of longitudinal grid points. Here the shortest physical spacing between neighbors is given by $\Delta x = 2\pi\, a \cos(88.75^\circ)/144 = 6064.48m$. As a consequence, the $CFL = u\frac{\Delta t}{\Delta x} < 1$ condition requires a time step of about $19.37s$ for stable calculations. This small time step at such a coarse resolution is very impractical, especially with respect to future adaptive mesh refinements in polar regions. In particular, the time step needs to be divided by a factor of 4 at the next refinement level 1.25° in order to obey the $CFL < 1$ condition. Here a factor of 2 comes from the doubling of the number of grid points that reduces the grid distance by a factor of 2. The second factor of 2 emerges due to the metric term $\cos\varphi$ in the distance calculation. The refined grid points lie even closer to the poles which effectively halves the circumference of the shortest polar latitude ring (see also table 3.1 on page 74).

In order to obtain a reasonably efficient numerical scheme, several strategies can be pursued that circumvent the rather severe time step limitations imposed by high-speed but physically insignificant waves. As pointed out above, these techniques are especially important for models with regular latitude-longitude grids, since the convergence of the meridians provide an unnecessarily high longitudinal resolution for gravity waves in polar regions. Gravity waves contain comparatively small amounts of energy which justifies a slightly inaccurate treatment of these wave motions[1]. In particular, gravity waves are not important for short-term synoptic or planetary-scale circulations. For long-term climate studies though, the zonal drag force owing to gravity waves must be included in the momentum balance, most commonly in form of a parameterization.

The standard numerical approaches to stable simulations with increased global time steps are listed below.

1. Use of massive dissipation (e.g. explicit diffusion), which acts mainly on the shortest waves.

2. Implicit or semi-implicit numerical scheme for gravity waves.

3. Filtering of the high frequency modes in the longitudinal direction without changing the well-resolved low frequency waves. Examples include Fourier or digital filtering techniques.

---

[1] This conclusion does not apply to atmospheric science questions that are particularly targeted at gravity-wave induced mesoscale phenomena.

4. Fractional step methods: Time-splitting approach in polar regions with iterative sub-cycling of terms in the equation that are responsible for gravity waves.

5. Use of a reduced grid which effectively increases the grid spacing in polar regions.

6. Use of alternative computational meshes (icosahedral grid or a cubed sphere) that avoid converging grid lines at the poles.

Other techniques include the use of a modified set of equations, so-called filtered equations, that do not contain the high-speed modes. It is important to note that the CFL condition can be violated in options 1-3, whereas it needs to be fulfilled in options 4-6, provided no additional filtering is applied. Options 1-3 are most commonly used in today's GCMs, but an increasing trend towards alternative gridding schemes has been observed in recent years (*Majewski et al.* [2002], *Giraldo and Rosmond* [2004], *Fournier et al.* [2004]). Using an alternative grid with appropriate time step might not entirely prevent a model from becoming unstable. Aliasing errors, or the misrepresentation of unresolved waves at longer wavelengths, tend to accumulate energy at the finest grid point scales in a nonlinear model. This effect is due to nonlinear wave interactions and also called nonlinear computational instability (*Haltiner and Williams* [1980]). The energy may need to be removed by a filter on a periodic basis depending on the particular numerical method. Alternatively, a strong diffusion mechanism, whether explicit or implicit as part of the numerical scheme, could provide the necessary dissipation.

Polar filtering strategy in the finite-volume dynamical core

In the adaptive finite-volume dynamical core, the polar filtering technique (option 3) has been selected that slightly deviates from the polar filtering mechanism used in NASA/NCAR's finite-volume model (*Lin et al.* [2001]). The filtering is exclusively applied at latitudes poleward of 60° N/S and selectively dampens the fast-traveling modes in the longitudinal direction. A combination of a Fast-Fourier-Transformation (FFT) filter developed at ECMWF and a digital 2nd order Shapiro filter is used. This is a similar approach as applied by *Kalnay-Rivas et al.* [1977]. The FFT algorithm is confined to few latitude circles closest to the poles whereas the more economical digital filter covers the remaining model domains down to 60° N/S. As a result, the maximum stable time step is now mostly determined by the CFL condition for gravity waves at 60° N/S which is far less restrictive than the previous example. In particular, when assuming the same 2.5° resolution with a grid spacing of $134.678km$ at 60° N/S, this leads to a maximum stable time step of $\Delta t = 134678m/313ms^{-1} = 430s$. Though, in the presence of high advective wind speeds in polar regions this time step might need to be reduced. The gravity wave time step limitation at 60° N/S is then overwritten by the now even more restrictive advective flow speed. Further more aggressive filtering at lower latitudes could allow an even longer maximum time step with respect to gravity wave motions but possibly with some adverse side effects on the flow fields. This can be observed if filter effects are cumulative in time. This is true for the digital Shapiro filters (*Shapiro* [1970]) especially when selecting a low-order filtering mechanism.

Filtering techniques have long been used for global atmospheric modeling. Examples include *Williamson and Browning* [1973], *Williamson* [1976], *Takacs and Balgovind* [1983] and *Purser* [1988a] who examined different FFT filtering strategies and their advantageous or detrimental effects. For instance, *Takacs and Balgovind* [1983] compared the filtering of tendencies versus the filtering of the prognostic variables which led to a discussion of conservation properties. In general, filtering prevents nonlinear instabilities, but conservation properties are lost unless a-posteriori restoration mechanisms are applied (*Takacs* [1988]). For example the conservation of mass principle is violated if the mass variable needs to be filtered for numerical stability reasons. Similar difficulties emerge with respect to the conservation of total energy. In the adaptive finite-volume dynamical core, filtering of the prognostic mass variable h or δp is not applied, whereas the filtering of the horizontal wind speed components u and v has been found to be imperative for stable calculations. Otherwise, a false energy cascade to small scales develops in polar regions with significant energy build-ups and instabilities after short time intervals (see discussion below).

Digital filter

The digital filtering technique selected for the adaptive dynamical core simulations is a one-dimensional 2nd order Shapiro filter (*Shapiro* [1975]). It replaces the original 3-point digital filter with variable coefficients developed by S.-J. Lin (unpublished) that is applied in the subtropics and midlatitude regions up to 66° N/S (NASA/NCAR version). Its filter coefficients depend not only on the given latitude φ but also on the underlying grid resolutions $\Delta\lambda, \Delta\varphi$ so that the filter is strongest at 66° N/S and becomes weaker towards the equator. Although this strategy works well for uniform grids, it poses a problem for an adaptive grid simulation with varying resolutions along latitude circles. In order to provide a consistent, quasi-resolution-independent filtering technique, the digital filters proposed by *Shapiro* [1970], *Ray-*

mond and Garder [1988], *Raymond* [1988] and *Purser* [1987] have therefore been assessed. These filters are based on constant coefficient, one-dimensional grid point operators where the order n of the filtering technique depends on the width of the numerical stencil. In general, the wider the stencil ($= 2n+1$), the more scale-selective the filter which leads to less dampening of the flow-relevant longer waves.

The smoothing operation of the so-called optimal 2nd order Shapiro filter (*Shapiro* [1975]) is defined by

$$\bar{f}_i = \frac{1}{16}\big(- f_{i-2} + 4f_{i-1} + 10f_i + 4f_{i+1} - f_{i+2}\big) \tag{2.50}$$

where the overbar denotes the smoothed variable f at grid point index i. This filter completely eliminates the unwanted $2\Delta x$ waves and significantly reduces the amplitudes of other poorly-resolved short waves, especially the $4\Delta x$ wave that also tends to accumulate energy during the model integration. Its response or damping function $\rho_n(k)$ is given by (*Shapiro* [1971])

$$\begin{aligned} \rho_n(k) &= 1 - sin^{2n}\Big(k\frac{\Delta x}{2}\Big) \\ &= 1 - sin^{2n}\Big(\pi\frac{\Delta x}{L}\Big) \end{aligned} \tag{2.51}$$

where k, the wavenumber, is $2\pi/L$ and L is the wavelength of the components in terms of the grid resolution Δx. n stands for the order of the filter. The response of different Shapiro filters with respect to the wave spectrum is illustrated in figure 2.6 on the next page. The figure shows the filter responses after 1 and 1000 applications and clearly depicts the cumulative character of the smoothing operation, especially for low order filters. This is not a concern for waves close to the pole points (compare also figure 2.8 on page 57), but must be taken into consideration in case filtering techniques are to be applied at lower latitudes. For example, if filtering in midlatitudes or even in the tropics becomes necessary due to stability reasons, a

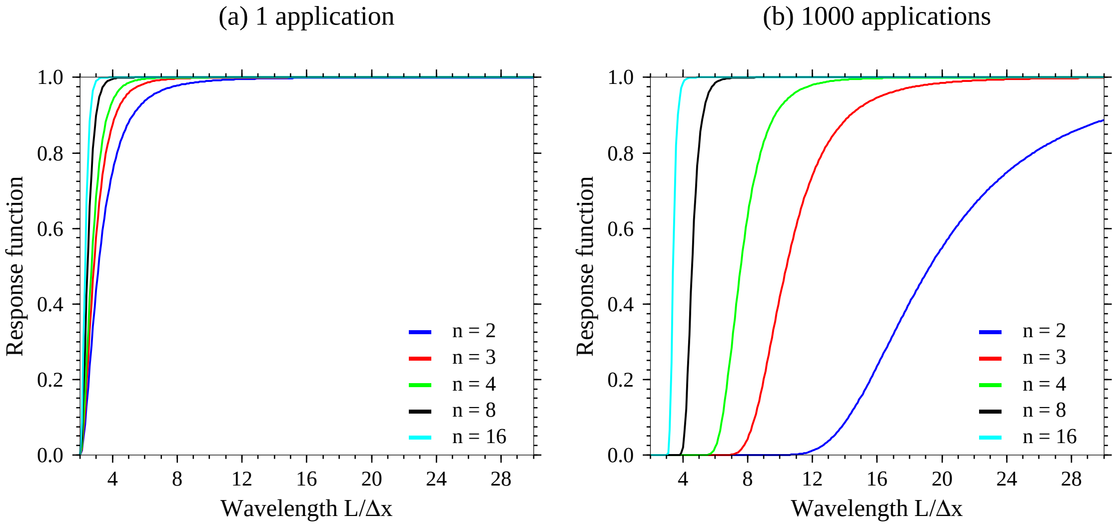

Figure 2.6: Response function of different Shapiro filters after (a) 1 application and (b) 1000 applications. n indicates the order of the Shapiro filter.

low order filter like the 2nd order Shapiro filter must be avoided and replaced by either a highly scale-selective FFT or higher order digital filters like the commonly used 8th or 16th order Shapiro filter. An 8th order Shapiro operator effectively eliminates all components with wavelengths less than four grid intervals but does not damp the waves with wavelengths greater than six grid intervals (*Shapiro* [1975]). This filter has been successfully applied by *Ruge et al.* [1995].

In practice, a high order digital filter is desirable but can not be easily implemented in the block-structured adaptive grid model discussed in this thesis (the block structure is explained in Chapter III). The wide numerical stencils of the higher order methods pose a problem for the data structure that is based on independent, comparatively small, block units with e.g. 9x6 cells plus surrounding ghost regions with 3 cells in each direction. In particular, the 2nd order Shapiro filter applied here has a 5-point stencil which already requires the use of 2 ghost cells at a block boundary. A 3rd order Shapiro filter is still feasible in the 3-ghost-cell setup without sacrificing the order of the filtering mechanism close to the block boundaries. Any higher order filter would suffer from this boundary effect or would require a wider ghost cell region.

Applications of the Shapiro filter

The following section provides a brief overview of the advantages and disadvantages of the Shapiro filtering approach. In general, filtering is solely applied in the longitudinal direction poleward of 60° N/S, whereas filtering in the meridional direction does not need to be considered with one exception. Despite the longitudinal filtering, shallow water test runs with uniform grids have shown that numerical noise can still develop in close proximity to both pole points. This effect is displayed in figure 2.7 using the *McDonalds and Bates* [1989] test case. Here the meridional wind v at day 4 is presented with and without one additional smoothing operation in meridional direction across the pole points. The effect can clearly be observed in subfigure (b). The noisy but stable perturbations (subfigure a), which originate solely at the poles, are successfully dampened by this strategy. The same conclusion can be drawn for similar perturbations in shallow water test case 5 (not shown, see also Appendix A for explanations of the test cases).

Filtering techniques must be carefully handled. As discussed earlier, strong low order filters, like the 2nd, 3rd or 4th order Shapiro filters, applied at low- or midlatitudes can significantly diffuse and degenerate the flow pattern and should therefore only be rarely used, if not completely avoided. An example that illustrates the detrimental effects of rather aggressive and unnecessary filtering is presented in figure 2.8. The example depicts test case 6 of the standard shallow water test suite. This flow field comprises a wave number 4 pattern that should move to the east without

(a) No Shapiro filtering in meridional direction

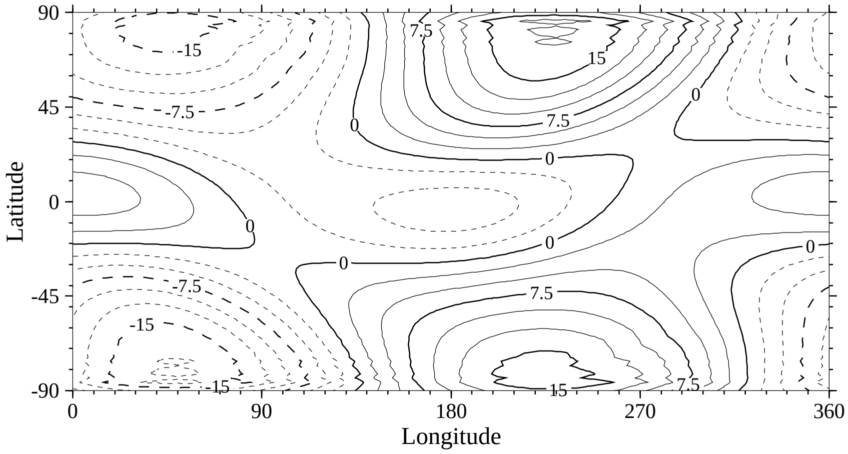

(b) Shapiro filtering in meridional direction

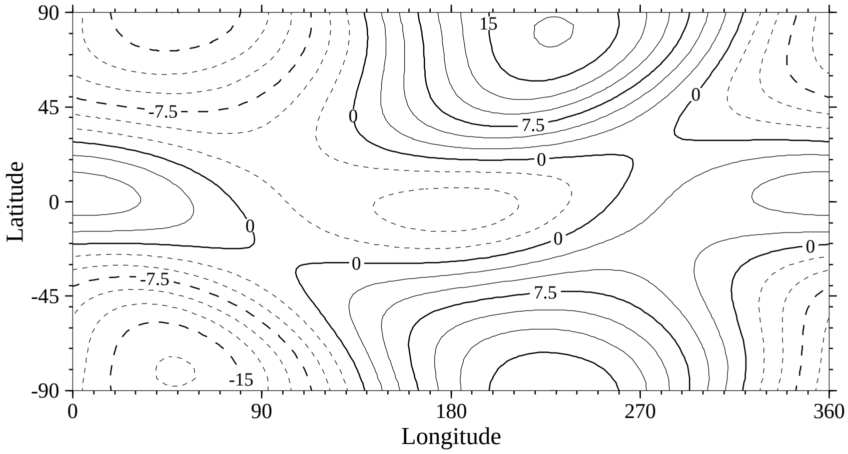

Figure 2.7: Meridional velocity v at day 4 (*McDonalds and Bates* [1989] test case). (a) No additional Shapiro filtering of v in meridional direction at the poles, (b) additional Shapiro filtering of v (confined to the circle closest to the poles). Contour interval is 2.5 m/s. Resolution is $2.5° \times 2.5°$ with $\Delta t = 240s$.

changing its shape (compare also to figure A.13 on page 235 for the high resolution reference field). In both model runs, an identical FFT filter is applied to the horizontal wind components poleward of 75° N/S. Additionally, the strong 2nd order Shapiro filter is used at every time step in (a) the regular model domain $60^\circ - 75^\circ$ N/S and (b) the whole remaining 75° S - 75° N model area. Figure 2.8 shows the geopotential height field at model day 14. It can clearly be seen that the additional digital filtering in midlatitudes and the tropics leads to a very diffusive and inaccurate solution in comparison to the reference run. The filter effects significantly accumulate during the course of the 3360 time step simulation (see also cumulative effect in figure 2.6 on page 53).

The difference of the strongly filtered flow pattern with the NCAR reference solution (A.13d) is further quantified in figure 2.9 on page 58. Here, the difference field of the meridional velocity v at day 14 is displayed which shows a $\pm 21\, m/s$ or almost 25% decrease in the top wind speeds. The errors are pure amplitude errors without changes in the phase speed of the wave.

As an alternative to 2nd order filtering, a 3rd order or 7-point stencil Shapiro filter can also be applied poleward of 60° N/S. This leads to almost indistinguishable flow patterns in most cases. Though one difficulty has been encountered when applying the 3rd order Shapiro filter to shallow water test 3 which consists of a steady state flow with compact support (see Appendix A). The slightly more lenient filter response function of the 3rd order filter (compare figure 2.6) allowed the growth of a $4\Delta x$ numerical instability (not shown) when long time steps were used ($\Delta t = 600s$, 2.5° grid). These waves, as well as the even shorter $3\Delta x$ or $2\Delta x$ waves, are only marginally resolved on the computational grid. In practice, the slightly stronger 2nd order Shapiro filter is therefore recommended. It is the default option for all following

(a) Filtering polewards of 60^o N/S

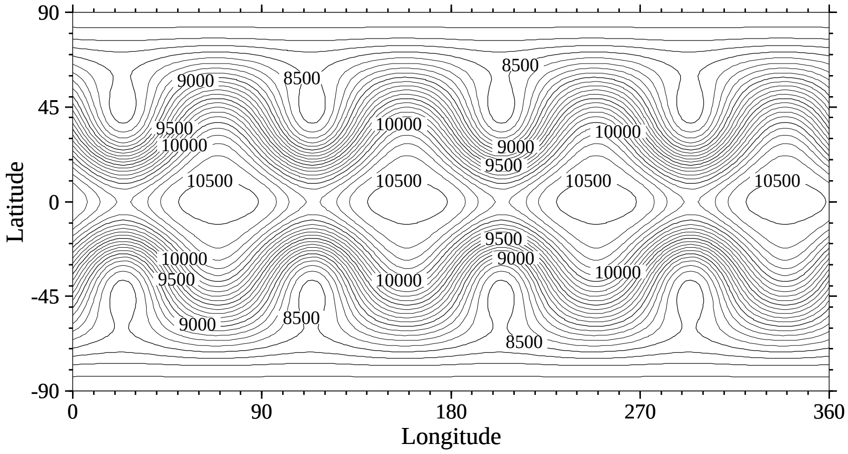

(b) Filtering of the whole domain

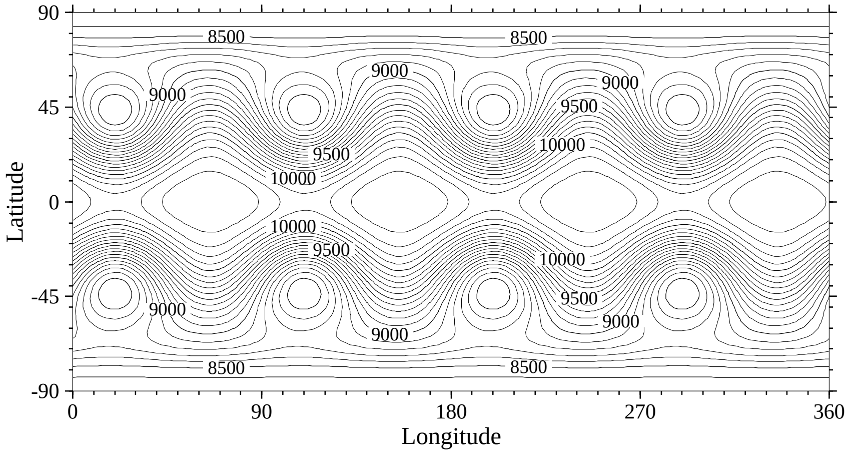

Figure 2.8: Geopotential height at day 14 (test case 6). (a) 2nd order Shapiro filter is applied to the wind fields u and v poleward of 60^oN/S. (b) Same filter is applied in the whole 75° S - 75° N domain. Contour interval is 100 m. Resolution is $2.5° \times 2.5°$ with $\Delta t = 360s$.

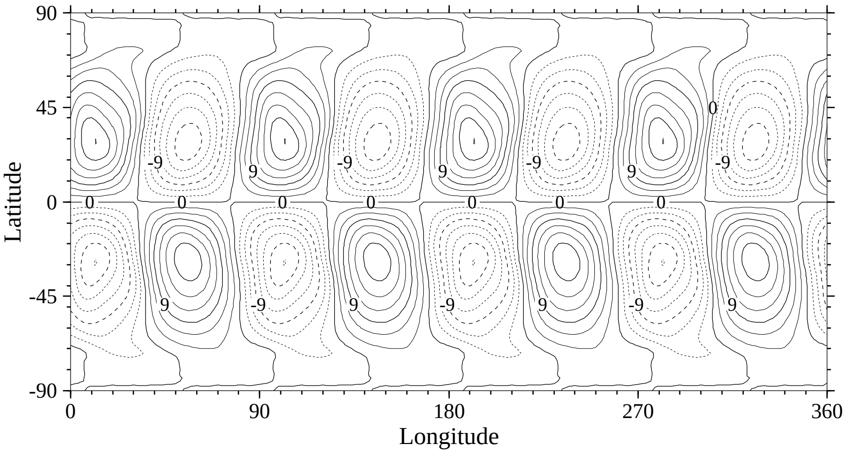

Figure 2.9: Differences of the Shapiro-filtered run (filtered in the whole domain) with the analytic solution. Here, the meridional wind v at day 14 (test case 6) is shown. Contour interval is 3 m/s.

model runs.

The crucial need for a filtering mechanism in the polar $60° - 75°$ N/S range is further depicted in figure 2.10 which displays the flow field of test case 3 in the Northern Hemisphere. Test results for the geopotential height field after a 23-hour simulation are shown with and without the digital 2nd order Shapiro filtering technique. An FFT filter is applied poleward of 75° N/S. Here, the chosen time step $\Delta t = 600s$ purposely violates the CFL condition for gravity waves in the polar region and as a consequence, a numerical instability at 75° N develops in subfigure (a). This position clearly marks the edge of the FFT filtering mechanism.

Besides filtering, two alternative approaches to stable solutions have also been examined for this scenario. First, the time step has been reduced in order to resolve the gravity wave activity in polar regions south and north of 75° N/S. Second, a so-called reduced grid setup with 2 reductions has been tested that effectively increases the longitudinal grid spacing poleward of 60° N/S. This concept is explained in detail in Chapter IV. As before, the FFT filter is still applied in regions poleward of 75° N/S. All alternative strategies suppressed the unstable waves successfully and led to

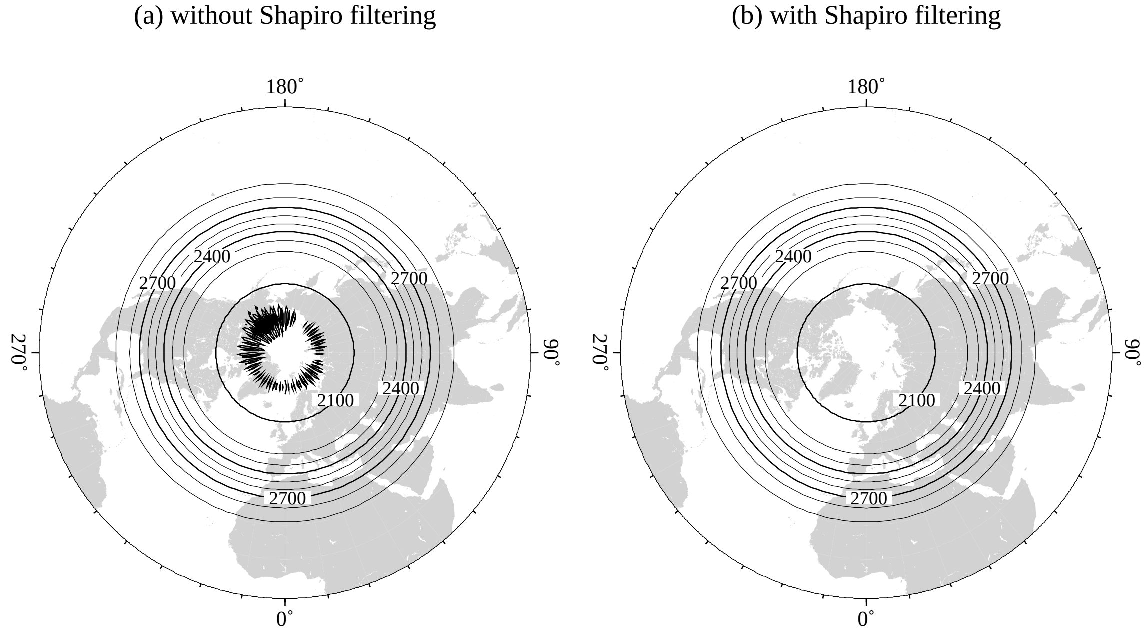

Figure 2.10: Geopotential height field after 23 model hours (test case 3) plotted on a North polar stereographic projection (outer circle is the equator). (a) No Shapiro filtering poleward of 60^o, (b) 2nd order Shapiro filter is applied poleward of 60^o. Contour interval is 100 m. Resolution is $2.5^\circ \times 2.5^\circ$ with $\Delta t = 600s$.

almost indistinguishable test simulations.

In conclusion, digital filtering promotes computational stability by eliminating or severely dampening the highly noisy short waves at high latitudes. The filtering must be selectively applied in order to avoid a detrimental damping effect in the midlatitudes or tropical regions. In the finite-volume dynamical core, digital filtering techniques complement, but do not substitute for the even more effective FFT filtering technique used near the pole points. Attempts to replace the FFT filter with a digital *Shapiro* [1975] or *Purser* [1987] algorithm did not prevent the numerical instabilities at the latitude circle closest to the poles. Therefore, all adaptive model runs presented in this thesis employ the FFT filtering technique in blocks adjacent to the pole points (see also Chapter III concerning the block data structure). As an important consequence, all blocks at the poles are kept at the same refinement level in order to fulfill the global longitudinal data dependencies of the FFT algorithm. This constraint has also been formulated for the vorticity calculation at the poles in Section 2.2.1.

2.3 Divergence damping

In a model simulation, gravitational noise can severely contaminate the atmospheric flow patterns and needs to be removed during the calculation (as discussed in the preceding section 2.2.2). One alternative approach to reducing gravitational noise is the use of a divergence damping mechanism that selectively dampens the amplitude of the velocity divergence fluctuations. This effectively reduces the gravity wave activity since gravity waves are associated with high-frequency variations of the divergence field. Here, a weak divergence damping mechanism is applied in the whole model domain which is based on S.-J. Lin's divergence damping implementation (unpublished). Such a damping mechanism is typically included in the horizontal momentum equation as shown in equation 2.52 (for an explanation of the symbols see also equation 2.2 in section 2.1.1).

$$\frac{\partial \vec{v}}{\partial t} = -\Omega_a \vec{k} \times \vec{v} - \nabla\Big(\Phi + \mathcal{K} - c\,D\Big) \tag{2.52}$$

Here c is the coefficient of the divergence damping and D denotes the divergence. In spherical coordinates D is given by

$$\begin{aligned} D &= \frac{1}{a\ \cos\varphi}\Big[\frac{\partial u}{\partial \lambda} + \frac{\partial}{\partial \varphi}(v\cos\varphi)\Big] && (2.53)\\ &\approx \frac{1}{a\ \cos\varphi}\Big[\frac{\Delta u}{\Delta \lambda} + \frac{\Delta(v\cos\varphi)}{\Delta \varphi}\Big] && (2.54)\end{aligned}$$

where a is the radius of the Earth (see also appendix C) and (λ, φ) denote the longitude and latitude. The second expression 2.54 shows the discretized form with the finite-difference operator Δ that involves the two surrounding neighbors at staggered grid locations. $\Delta\lambda$ and $\Delta\varphi$ are the longitudinal and latitudinal grid distances in radians, respectively. It must be noted that the inclusion of the divergence damping does not modify the character of the hyperbolic equation. It can be considered an additional right hand side term that adds some diffusion to the momentum equation.

In the current shallow water formulation, the empirical divergence damping coefficient c is computed as a time step, resolution and latitude dependent parameter. It is defined by

$$c = \begin{cases} \frac{a^2\ \cos\varphi\ \Delta\varphi\ \Delta\lambda}{32\,\Delta t} & for\ \ \cos\varphi \le 0.5 \\ \\ \frac{a^2\ \Delta\varphi\ \Delta\lambda}{64\,\Delta t} & for\ \ \cos\varphi > 0.5 \end{cases} . \tag{2.55}$$

with the units $\frac{areaA}{time} = \frac{m^2}{s}$. Δt denotes the time step. In polar regions (poleward of 60°N/S) the corresponding area A is chosen to be the approximated area of the actual grid cell at the latitude φ

$$A = \int_{\lambda}^{\lambda+\Delta\lambda} \int_{\varphi}^{\varphi+\Delta\varphi} a^2 \cos\varphi \, d\varphi \, d\lambda \tag{2.56}$$

$$\approx a^2 \cos\varphi \, \Delta\varphi \, \Delta\lambda \quad . \tag{2.57}$$

In the midlatitudes and the tropics though, the area is set to the approximated area of a grid cell at the equator (with $\cos\varphi = 1$). After inserting equations 2.55 and 2.54 into equation 2.52 it follows

$$\frac{\partial \vec{v}}{\partial t} = -\Omega_a \vec{k} \times \vec{v} - \nabla\Big(\Phi + \mathcal{K} - \big[c_u \, \Delta u \, + c_v \, \Delta(v \cos\varphi)\big]\Big) \tag{2.58}$$

where c_u and c_v symbolize the damping coefficients that are already divided by the metric terms of the discretized divergence operator (eqn. 2.54). In the tropics and midlatitudes with $\cos\varphi > 0.5$, c_u and c_v are given by

$$c_u = \frac{a \, \Delta\varphi}{64 \, \Delta t \, \cos\varphi} \tag{2.59}$$

$$c_v = \frac{a \, \Delta\lambda}{64 \, \Delta t \, \cos\varphi} \quad . \tag{2.60}$$

In the polar regions with $\cos\varphi \leq 0.5$ the coefficients are

$$c_u = \frac{a \, \Delta\varphi}{32 \, \Delta t} \tag{2.61}$$

$$c_v = \frac{a \, \Delta\lambda}{32 \, \Delta t} \tag{2.62}$$

accordingly. Here the c_u and c_v coefficients no longer depend on the given latitude. In contrast to S.-J. Lin's derivation of the divergence damping mechanism (unpublished), the coefficients c_u and c_v have been multiplied by an empirical factor of 2 in order to moderately increase the damping effect. This eliminates very mild oscillations at lower and mid-latitudes which have been observed with the original coefficients (in the absence of S.-J. Lin's digital filtering technique in midlatitudes, unpublished).

In case of an identical grid resolution $\Delta\lambda = \Delta\varphi$ in both dimensions this formulation leads to the profiles illustrated in figure 2.11. The figure shows the coefficients $c_u = c_v$ for selected grid resolutions $\Delta\lambda$ and some corresponding time steps.

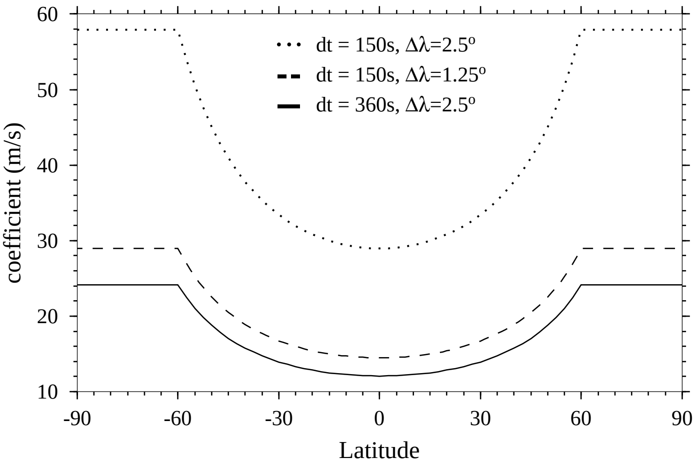

Figure 2.11: Coefficients $c_u = c_v$ for the divergence damping mechanism at different resolutions $\Delta\lambda$ with varying time steps.

It is important to note that the divergence damping coefficient c in equation 2.55 is rather small in comparison to typical values suggested in the literature. Depending on the grid resolution, the latitude and the time step the coefficient is most often close to $10^6 m^2 s^{-1}$. This is the lower limit for divergence damping coefficients published in the literature. For example, *McDonalds and Bates* [1989] and *Bates et al.* [1990] used constant coefficients of order $10^6 - 10^7 m^2 s^{-1}$. In addition, *Haltiner and Williams* [1980] reported on typical coefficients of order $10^7 - 10^8 m^2 s^{-1}$. In their model simulations the gravitational noise was greatly reduced. But it was also concluded that negative side effects can be observed as coefficients exceed $10^7 m^2 s^{-1}$. In a full GCM, it led to abnormal high pressure buildups in the vicinity of orography and eliminated precipitation in an 8-layer primitive-equation model.

In the 2D finite-volume dynamical core the damping is rather mild and does not degrade the overall solution. In the 3D version, the coefficients additionally depend on the vertical level (S.-J. Lin, unpublished). The effective diffusion of the velocity divergence helps stabilize the flow patterns and complements the Shapiro and Fourier filtering techniques, already applied in polar regions. In order to assess the damping effect more closely, non-adapted shallow water experiments with and without divergence damping have been performed. The tests are based on the steady-state shallow water test 2 with an $\alpha = 90^\circ$ rotation angle at a uniform $2.5^\circ \times 2.5^\circ$ resolution (see also appendix A). The time step is $\Delta t = 360s$. Figure 2.12 on the next page illustrates the difference of the zonal velocity field with the analytic solution at day 10 for both model runs. It can clearly be seen that the divergence damping smoothes the spurious oscillations in the error field. The abrupt decrease in noise poleward of 60° N/S is a consequence of the additional digital Shapiro and FFT filtering at those latitudes. In order to assess the effect of the time step on the smoothness of the flow pattern, test case 2 has been repeated using a reduced time step ($\Delta t = 150s$) and no damping mechanism. The tests showed that the spurious oscillations were not prevented and resulted in an even noisier field (not shown).

In all test cases shown in the thesis, divergence damping has always been applied although most of these idealized tests do not need the damping mechanism with respect to computational stability. In general, the divergence damping effect will become more important in full GCM model simulations with real orography.

(a) without divergence damping

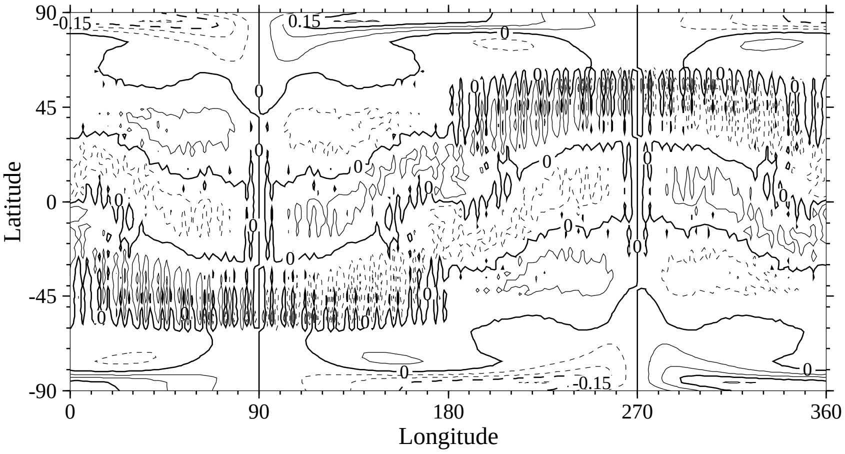

(b) with divergence damping

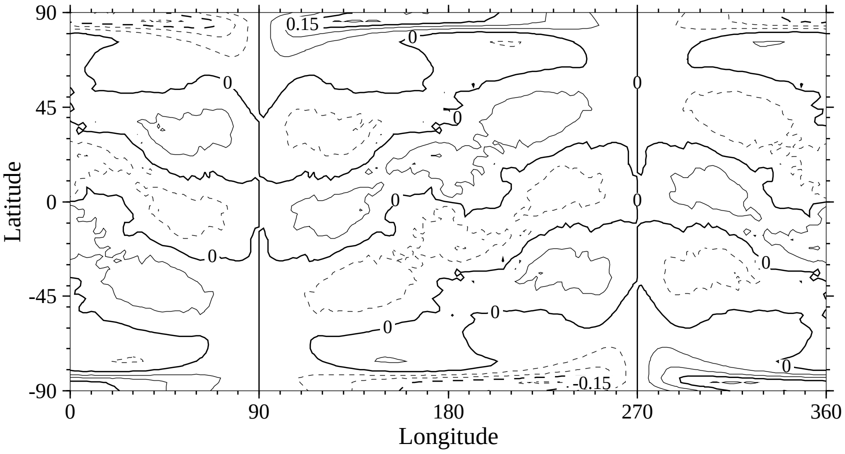

Figure 2.12: Differences of the zonal wind u with the analytic solution at day 10 (test case 2, $\alpha = 90$), (a) without divergence damping, (b) with divergence damping. Contour interval is 0.05 m/s.

CHAPTER III

Adaptive mesh refinements in spherical geometry

In the past, dynamically adaptive mesh refinements for atmospheric science applications have been mostly concerned with refinement regions in limited-area models on a Cartesian grid. Cartesian grids are well-suited for AMR techniques due to their regular structure and clear relationships among neighboring grid points. For example, the location of a neighbor in the Cartesian system is unambiguously defined by its coordinate position.

In a spherical coordinate system this is not necessarily true. The main differences occur due to the singular nature of the spherical grid at the pole points. The identification of neighbors across the poles, together with their special treatments, adds extra complexity to the AMR problem in spherical geometry. As a consequence, an adaptive grid library for AMR applications on the sphere must be able to address these additional pole point issues.

This chapter gives an overview of an adaptive mesh refinement strategy in spherical geometry that has been applied to the NASA/NCAR finite-volume dynamical core. The two main building blocks of the adaptations are the underlying block data structure and a newly-developed spherical adaptive grid library for parallel computer architectures (*Oehmke and Stout* [2001]). This data structure, the refinement principles, a reduced grid setup and the corresponding model resolutions are introduced in Section 3.1. Section 3.2 is primarily focused on the software engineering aspects of the adaptive mesh approach. First, the design of the spherical adaptive mesh library is reviewed which leads to a brief discussion about the AMR software concept of the dynamical core. In addition, performance issues are addressed. In Section 3.3 the fine-coarse grid interfaces in an adaptive grid simulation are closely examined. This includes an assessment of suitable interpolation strategies and surveys the grid arrangements and flux interactions at the grid interfaces.

3.1 The adaptive finite-volume dynamical core

3.1.1 Block data structure

The foundation of the AMR design is based on a block-structured data layout that allows cache-efficient, high performance computations with minimal changes to the transport algorithms of the finite-volume dynamical core. The concept of the block data structure is displayed in figure 3.1 that shows an orthographic projection of the Earth with a regular and block-structured grid point distribution. Each self-similar block comprises a constant number of $N_x \times N_y$ grid cells in longitudinal

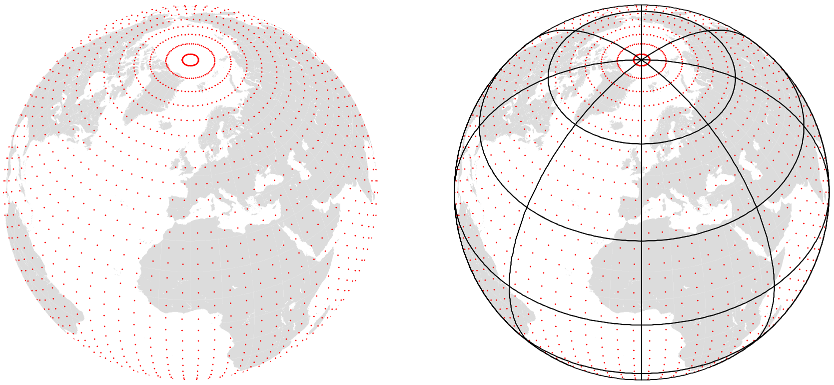

Figure 3.1: Distribution of grid points over the sphere (orthographic projection centered at 0E,45N), without a block-structure (left) and with the block-structure (right). The resolution is 5° in both figures.

and latitudinal direction. The computational grid covering the Earth can then be viewed as a collection of individual blocks that are independent data units. Here the block data principle is solely applied to the horizontal directions so that the whole vertical column is contained in a block in case of 3D model setups. Other block data approaches, as described in *Stout et al.* [1997] or *MacNeice et al.* [2003], employ a 3D strategy that includes a block distribution in the third dimension.

The block data structure is well-suited for adaptive mesh applications. The basic AMR principle is explained in figure 3.2. Starting from an initial mesh at constant resolution with for example 3 × 3 cells per block, a 'parent' block is divided into 4 'children' in the event of refinement requests. Each child becomes an independent new block with the same number of grid cells in each dimension, thereby doubling the resolution in the region of interest. Coarsening, on the other hand, reverses the refinement principle. Then 4 children are coalesced into a single self-similar parent block which reduces the grid resolution in each direction by a factor of 2. In the present AMR design, neighboring blocks can only differ by one refinement level. This guarantees accurate inflow and outflow conditions at the interface boundaries and leads to continuously cascading refinement regions.

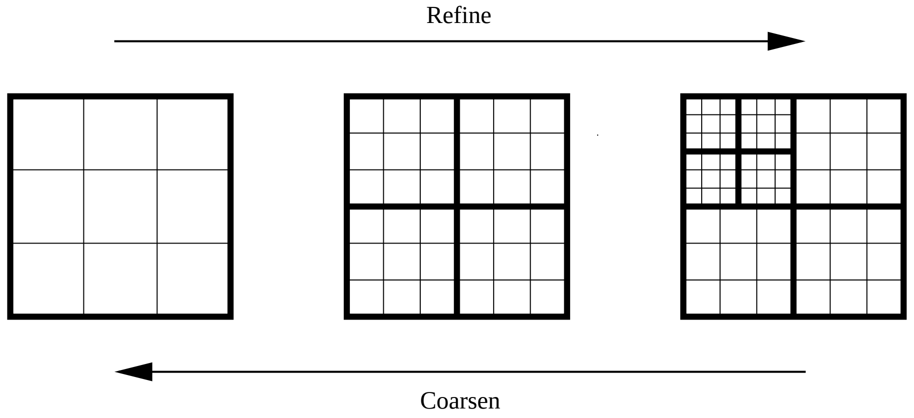

Figure 3.2: Refinement and coarsening principles with 2 refinement levels. Each block contains 3x3 cells.

An example of such a cascading grid projected onto the sphere is given in figure 3.3. Here a single region of interest, an idealized mountain as indicated by the contour lines, is refined at a maximum refinement level of 3. The figure clearly depicts the consequent refinement requests in order to ensure the adaptation constraint. In addition, the blocks adjacent to the pole are held at a constant refinement level. This fulfills the requirements of the polar cap and gravity wave treatment in the polar region as discussed in Section 2.2.

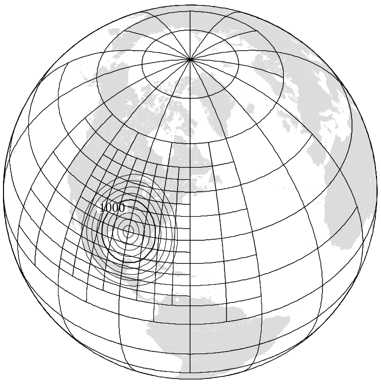

Figure 3.3: Adapted blocks.

Each block is a logically rectangular unit with additional ghost cell regions around its boundaries. As a result, the information along adjacent block interfaces is shared which allows the use of an iterative solution procedure. The flow solver is then individually applied to all blocks within the grid before ghost cell updates along the boundaries become necessary. Here, 3 ghost cells in each direction are added in order to satisfy the requirements of the solution technique.

There are two types of interfaces in the adaptive grid setup as illustrated in figures 3.4 and 3.5. If the adjacent blocks are at the same refinement level (figure 3.4) the neighboring information can easily be exchanged since the data locations

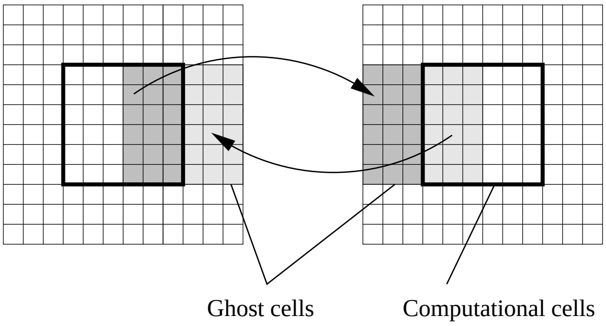

Figure 3.4: Ghost cell updates for blocks at the same refinement level.

overlap. The ghost cell data are then assigned the appropriate solution values of the neighboring block which is indicated by the gray-shaded areas. If on the other hand the resolution changes between adjacent blocks (figure 3.5), interpolation and averaging routines become necessary in order to fill in the missing ghost cell information at different grid point positions. These techniques are further explained in Section 3.3.1. Special attention is paid to ensure conservation principles along the varying grid interfaces.

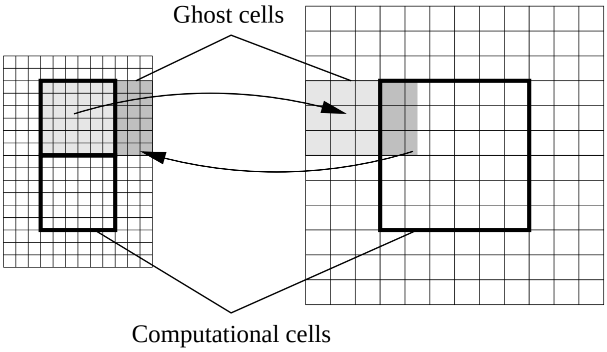

Figure 3.5: Ghost cell updates for blocks at different refinement levels.

It is important to note that blocks do not overlay each other in the current setup. Instead, each block is assigned a unique surface patch on the sphere. This is in contrast to alternative approaches presented in the literature (*Berger and Colella* [1989], *Brown et al.* [2003]). For example, *Berger and Colella* [1989] reported on a block data AMR principle with variable block sizes that maintains all the blocks at all refinement levels during the course of an integration. The flow is solved concurrently on the coarse and overlaying fine meshes. The fine resolution regions then overwrite the coarse resolution data wherever the properly nested grids overlap.

Adaptive blocks are also well-suited for parallel computing concepts with a distributed memory architecture. Since blocks are treated as independent units they can easily be distributed among many processors. During the simulation each processor loops over its assigned blocks in order to solve the PDEs on a block-by-block basis. At the end of the time step procedure the processors are synchronized which allows the update of the ghost cell regions across the communication network.

Self-similar blocks are flexible and from a computational viewpoint efficient units that can be used for static and dynamic adaptations. Static refinements are placed in user-determined regions of interest, like mountain ranges or coastlines, at the beginning of a forecast. This approach even allows an accurate reinitialization of the initial data after refinements occurred, for example with an improved representation of the orography profile. Another static adaptation option is the reduced grid that statically coarsens the longitudinal resolution in polar regions (see also Chapter IV). Dynamic adaptations, on the other hand, are a powerful method when features of interest are to be tracked according to user-defined refinement criteria. These can include flow-dependent indicators or measures of the numerical error (discussed in Chapter V).

3.1.2 Model resolution

The horizontal resolutions as well as the total number of blocks in an adaptive grid run can vary considerably during the course of an integration. Although there are from a computational standpoint no limits other than memory size and processor speed, the physical problem to be solved might well pose restrictions on the adaptive grid simulation. This is in particular true for hydrostatic dynamical cores in atmospheric science. The range of sensible resolutions varies from hundreds of kilometers to tens of kilometers which sets an upper limit on the number of suitable refinement levels. This limit is on the order of 3-5 depending on the initial coarse resolution. In contrast, other adaptive mesh applications like BATS-R-US, the interplanetary magnetohydrodynamics model at the University of Michigan (*Hansen et al.* [2002]), typically work with 10-15 refinement levels (*Stout et al.* [1998]).

The initial uniform grid setup not only determines the coarsest horizontal resolution for the adaptive model run, but also the geometrical flexibility of the adaptations. Here a trade-off must be considered since an increased number of cells per block leads to more efficient but less flexible adaptive model simulations. From a computational viewpoint, these larger blocks are more efficient since, as an example, the ghost-cell to computational-cell ratio is improved. But on the other hand, large block sizes can not be optimally adapted and are therefore less flexible with respect to refining local atmospheric phenomena. These aspects are further discussed in Section 3.2.3. The initial resolution solely depends on user-defined input parameters. These are the number of blocks in longitudinal and meridional direction ($B_x \times B_y$) as well as the number of cells per block ($N_x \times N_y$) in each dimension. The only constraints are $B_x, B_y \geq 2$ (with $B_x = even$) and $N_x, N_y \geq 6$. The latter guarantees that the 3-ghost-cell region of a neighboring coarse block is completely contained in the fine block. The former is necessary in order to find unique neighboring blocks across the pole points.

Typical resolutions considered here are mainly driven by the flexibility argument. Therefore, the number of cells per block is rather marginal with respect to computational efficiency. Unless noted otherwise, most model runs presented in the following chapters start with the initial parameter set $[B_x = 8, B_y = 6, N_x = 9, N_y = 6]$ which describes a global $5^\circ \times 5^\circ$ resolution. The maximum refinement level is set to 4. Table 3.1 gives an overview of the corresponding resolutions in spherical coordinates and physical space. The effect of the converging meridians in polar regions can clearly be seen which significantly reduces the physical grid spacing. This has far-reaching

Refin. level	Resolution $\Delta\lambda$, $\Delta\varphi$	Max. # grid points lon x lat (full grid)	Resolution Δx (km) at different φ			
			equator	60° N/S	75° N/S	near pole
0	5°	72 x 36	556.0	278.0	143.9	24.26
1	2.5°	144 x 72	278.0	139.0	72.0	6.06
2	1.25°	288 x 144	139.0	69.5	36.0	1.52
3	0.625°	576 x 288	69.5	34.8	18.0	0.38
4	0.3125°	1152 x 576	34.8	17.4	9.0	0.09

Table 3.1: Refinement levels and corresponding global grid resolutions on the sphere.

consequences with respect to numerical stability and time stepping issues as already discussed in Section 2.2.2. Furthermore, it can be observed that the grid spacing at refinement level 4 approaches the limits of the hydrostatic approximation. The hydrostatic approximation, or the neglect of the vertical acceleration in the vertical momentum equation, is well-represented in the atmosphere down to horizontal scales around 10 km. At smaller scales, additional dynamical effects, like internal wave breaking events, start to become important. Therefore, the adaptive model is restricted to 4 refinement levels when starting with a coarse initial 5° × 5° setup. In case of a more typical 2.5° × 2.5° climate resolution, which corresponds to the spectral T42 setup, 3 refinement levels are feasible before non-hydrostatic motions should be taken into consideration. In addition, questions arise whether an even higher horizontal resolution would be still consistent with the fixed non-adapted vertical resolution (*Lindzen and Fox-Rabinovitz* [1989], *Fox-Rabinovitz and Lindzen* [1993]).

In a realistic model setup, for example for weather prediction applications, an even finer initial grid must be considered. Otherwise the calculation might suffer from a severe underrepresentation of the initial field at the 5° × 5° resolution (*Simmons* *and Hollingsworth* [2002]) and no significant improvements of the simulation can be expected by an adapted model run. This is due to the fact that the initial data on adapted blocks are interpolated from the coarse parent grid. However, in idealized test cases an initial resolution of $5^\circ \times 5^\circ$ is often sufficient since the initial data are considerably smooth. This is particularly true for the shallow water test cases 2,3,5 in Chapters IV-V and the 3D baroclinic wave simulations in Chapter VI.

Reduced grid resolution

Adaptive blocks can also be used to define a static coarsening step in longitudinal direction at the beginning of the forecast. These coarsenings are confined to the polar regions and are most commonly called a reduced grid arrangement (see also figure 4.1 on page 121). Numerous reduced grid setups have been proposed in the literature and a detailed overview is given in Chapter IV. The reduced grid proposed here is a new variant since it is based on the self-similar adaptive block design which offers less flexibility with respect to the positions of the reduction levels. Therefore, a finer initial grid based on the parameter set $[B_x = 16, B_y = 12, N_x = 9, N_y = 6]$ has been chosen. This $2.5^\circ \times 2.5^\circ$ grid resolution allows two reduction levels poleward of 60° N/S which marks the southern/northernmost limit for the selected design. The corresponding grid resolutions for a uniform grid with 1 and 2 reduction levels at 75° N/S and 60° N/S, respectively, are listed in table 3.2. The table clearly depicts the increase in the grid spacing in polar latitudes. As a consequence, the time step is less restricted by the CFL numbers near the poles (see also discussion in Section 2.2.2).

Reduced grid	Resolution $\Delta\lambda$ x $\Delta\varphi$ at different φ			Resolution Δx (km) at different φ			
	equator	60° N/S	75° N/S	equator	60° N/S	75° N/S	near pole
0 (fg)	2.5° x 2.5°			278.0	139.0	72.0	6.06
1 (rg1)	2.5° x 2.5°		5° x 2.5°	278.0	139.0	143.9	12.13
2 (rg2)	2.5° x 2.5°	5° x 2.5°	10° x 2.5°	278.0	278.0	287.8	24.26

Table 3.2: Characteristics of the reduced grid configurations in comparison to the regular longitude-latitude grid (full grid).

3.1.3 Grid point positions

As pointed out in Section 2.1.2 the prognostic data in the finite-volume dynamical core are arranged on an Arakawa D-grid (figure 2.1 on page 34). In case of adaptations this leads to a slightly more complicated grid staggering pattern in comparison to the most commonly used Arakawa A-grids in adaptive CFD applications. The assignment of the variables u, v and Φ to their grid locations is shown in figure 3.6. Here the coarse cell, as indicated by the blue color, is split into 4 children whose positions are marked in black.

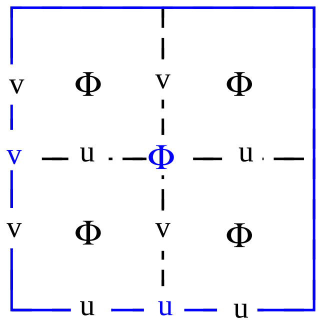

Figure 3.6: Splitting of one coarse cell into 4 fine-grid cells. The location of the coarse data is indicated in blue, the fine grid data are in black.

This grid has a built-in asymmetric property. Since the velocity components are defined at staggered positions, the scalar quantities Φ in a block with $N_x \times N_y$ grid cells are not completely surrounded by the velocity field. The northernmost and easternmost boundaries of the block do not contain prognostic wind data and the missing information is provided by the ghost regions. This is not a problem in a uniform grid simulations since neighboring blocks are at the same resolution and replace the missing ghost cell information with accurate data. But it has important implications with respect to transport processes at the interfaces of an adapted grid where ghost cell information needs to be interpolated. When examining the flux calculations at a fine-coarse grid boundary, it can be observed that the precision of the flux computation relies on the direction of the wind speed. This is illustrated in figure 3.7 which depicts a simple monotone approximation to the advective flux, the upstream or donor cell method. Here the meridional flux G at the cell edge is

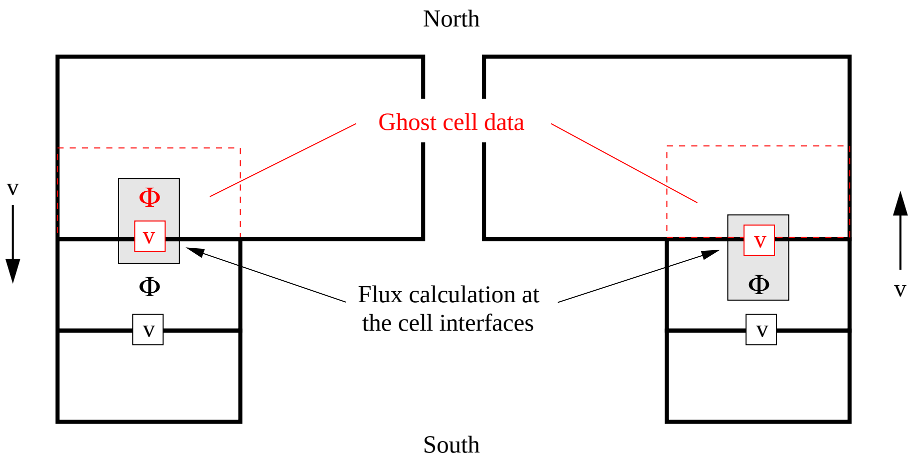

Figure 3.7: Flux calculations at a fine-coarse grid interface with asymmetric coordinate positions.

calculated by $G = v\Phi$ with respect to the upstream direction. The figure shows two fine-coarse grid interfaces with opposite v wind directions. The goal is to compute G at the northernmost interface of the refined block. The available information for the flux computation is either given as a true model variable (black) or as a ghost-cell value (red). In the left part of the figure with a northerly wind component a flux calculation at the cell interface involves the 2 ghost-cell data indicated in red. Both values enclosed in the gray-shaded box are interpolated from the neighboring coarse cell. This might be slightly less accurate than the comparable flux computation shown on the right hand side. With the southerly wind direction, the flux can now be computed with the true variable Φ and 1 interpolated wind component (ghost cell in red in the gray-shaded box).

The differences in the precision of the fluxes at the boundaries are marginal but certainly have an impact over time, especially if low order interpolation schemes are used for the ghost cell updates at the boundaries. For example, it has been observed in shallow water test case 6 with first-order interpolations that a reduced grid simulation developed an asymmetric solution in the two Hemispheres over time. This effect was then diminished when applying a second-order interpolation scheme at the interfaces which enhanced the accuracy of the ghost cell information (figure 4.8 on page 131).

If asymmetric solutions are to be reduced further, true overlap regions can be introduced (e.g. with the width of 1 for the velocity field at the northernmost or easternmost boundary). Then the wind components can be computed concurrently at the interface on the two meshes, though at staggered locations (see figure 3.6). Special care must be taken to avoid spurious noise. This can include a synchronization step that assigns the averaged fine-grid wind data to the coarse neighboring cell. Whether the asymmetric property can be completely avoided by this procedure remains open. As indicated on the left hand side in figure 3.7, even the simple flux calculation still involves a second ghost value Φ. Furthermore, many more ghost cell data are involved in higher order flux calculations like the van Leer or PPM method outlined in Chapter II. The same ideas apply to the zonal fluxes in the W-E direction at the easternmost boundary.

3.2 Software engineering aspects

3.2.1 Adaptive spherical grid library

Besides the block-structured data layout, the second building block of the adaptive finite-volume dynamical core is a newly-developed spherical adaptive grid library for parallel computer architectures. This library has been designed by *Oehmke* [2004] and *Oehmke and Stout* [2001] who give detailed information on the underlying principles and software engineering aspects. The following section presents a brief overview.

The AMR library manages the block data structure on the sphere and adds the adaptive grid functionality. All details of the AMR technique are hidden inside the library. The user then utilizes the library functions by subroutine calls and provides additional user-specific routines that, for example, compute the interpolations within ghost cell regions. The characteristics and functions of the library are:

Sphere The library provides functions for the creation of a sphere or a reduced sphere with a block-structured data layout. It maintains the geometric information for the initialization of the spherical coordinates and later allows the reinitialization of the blocks after adaptations occur. Each block covers a unique surface patch on the sphere.

Book-keeping The library maintains the adjacency information for all blocks at arbitrary refinement levels including the blocks at the pole points.

Iterators Iterators allow users to loop over all the blocks on a processor. They can be viewed as pointers that pick out the next independent block index for user-specific computations. Consecutive blocks may lie at arbitrary positions on the sphere.

Communication The library provides transfer functions that enable the ghost cell updates especially on distributed memory machines. The communication is based on the message passing interface MPI (for distributed neighboring blocks) or on memory copies for adjacent blocks on the same processor. The transfer module maintains send and receive buffers and utilizes the adjacency information during the user-initiated ghost cell exchange.

Load-balancing The load-balancing module is responsible for distributing the blocks among the processors during the adaptive run. Blocks are transfered among processors in order to assign an equal amount of work to the each processor.

Adaptations The library manages the coarsenings and refinements of the blocks based on adaptation flags. These flags are set by the user via library functions. The adaptation module redefines the block connections after adaptations occurred and enforces the adaptation constraint that adjacent blocks can differ by no more than one refinement level.

User interface The user can easily access the library functions by Fortran90 subroutine calls. In addition, user-defined subroutines need to be provided that specify the algorithms for the split & join operations as well as the ghost cell updates. These routines then include the interpolation and averaging procedures for the initialization of new blocks and the data exchange among neighboring blocks at different resolution. The interface routines need to cover three categories: (1) the exchange of data among blocks at the same refinement level, (2) the fine-to-coarse and the (3) coarse-to-fine interfaces.

In order to utilize the adaptive grid library in the finite-volume dynamical core the basic data structure of the former 3D arrays like $\Phi(N_{lon}, N_{lat}, N_{lev})$ has been changed to accommodate the block design. Here N_{lon}, N_{lat} and N_{lev} stand for the total number of longitudes, latitudes (in a latitude stripe due to a 1D data decomposition) and vertical levels on the sphere. The new data structure $\Phi(N_x, N_y, N_{lev}, N_{Block})$ then contains the block index as a fourth dimension where N_x, N_y indicate the number of cells per block and N_{Block} is the total number of blocks on a processor. This input parameter stays constant and needs to provide enough buffer space for newly created blocks during the adaptive model run. The vertical dimension remains unchanged. Typical values for N_x and N_y are reported in Section 3.1.2.

There is one more imperative revision to be noted. The original Lin-Rood design contained a grid point distribution that placed cell centers with scalar variables directly at the poles. Such a fixed position of variables at the poles contradicts the flexible AMR paradigm and would prevent adaptations near the pole points. Therefore, the grid point distribution has been shifted by half a grid length in the meridional direction in order to avoid this difficulty.

Adaptations

During the course of a model run adaptations are triggered according to adaptation flags. In the current implementation, the refinement or coarsening flag is set if one or more grid points within a block fulfill the user-defined adaptation criterion. Then the whole block is flagged so that, in case of refinements, the block is split into four children during the next adaptation cycle. Coarsenings are slightly harder to trigger than refinements. They require that all four children set the coarsening flag simultaneously. Additionally, coarsenings are only allowed if they do not violate the constraint that neighboring blocks can only differ by one refinement level. This is checked by the AMR library functions. Typically, a time interval of n time steps is required before new adaptations are allowed. This is called an adaptation cycle that needs to be determined by the user. For pure advection tests an adaptation interval of $n = 1$ time step has been successfully selected (Chapter V) but such a short cycle is not recommended for non-linear flow simulations. This is due not only to computational overhead considerations (e.g. calling the AMR library functions produces overhead) but also to the observation that refinements and coarsenings might toggle if the refinement criterion is only marginally met. A longer time interval allows the flow to evolve smoothly before new adaptations are triggered. Here, a time interval of 2 hours has been selected for the adaptive runs in Chapters V and VI. This time interval ensured that the selected features of interest did not leave the regions of interest during the adaptation cycle. Otherwise a shorter time interval needs to be selected.

As a first glimpse, it is interesting to see how the adaptations are able to track a selected feature. This is qualitatively displayed in figure 3.8 on the next page where 3 refinement levels are used to follow a Gaussian hill around the globe. In this passive advection test the Gaussian hill is transported by prescribed wind speeds. No coarsenings have been applied in order to illustrate the trace of the feature with its cascading refinement regions. The figure shows the adapted blocks during this 12-day simulation and clearly depicts the neighboring constraint that also applies to adjacent blocks in the diagonal direction.

Neighbors

These neighboring relationships are more closely examined in figure 3.9, which shows a schematic view of the block setup in the spherical system. In general, all blocks in a non-adapted grid have eight neighbors as denoted by the North/South

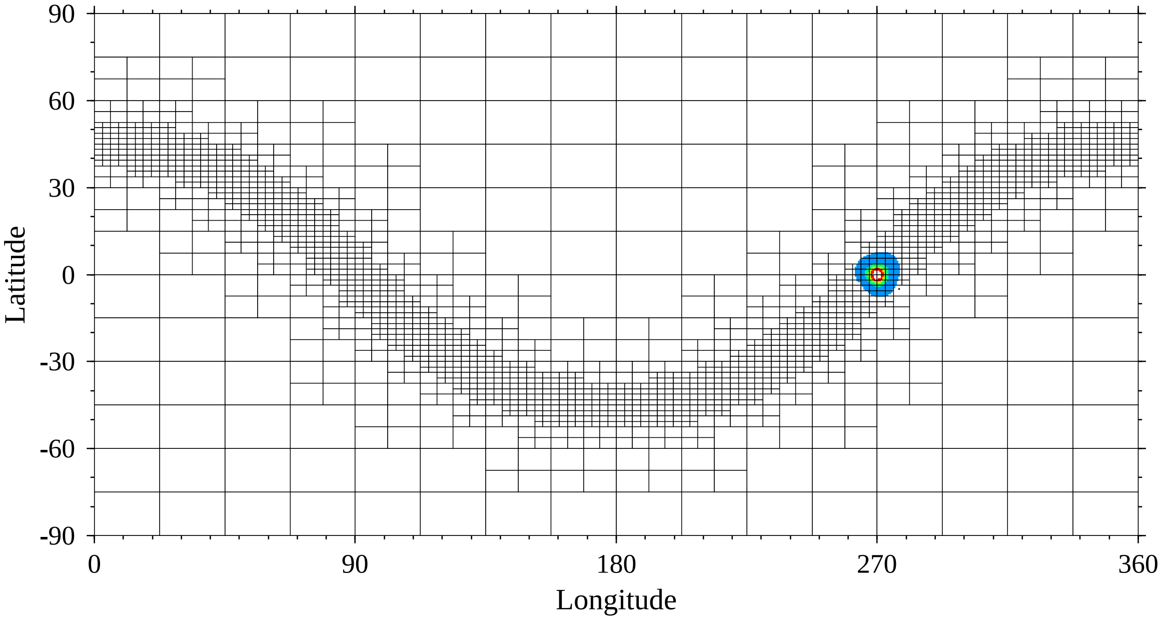

Figure 3.8: Cascading refinements: Advection of a tracer (Gaussian hill, colored contours) around the globe tracked with 3 refinement levels (in the figure without coarsening). The adapted blocks are shown. Base resolution is 2.5° × 2.5°, each block contains 9x6 cells.

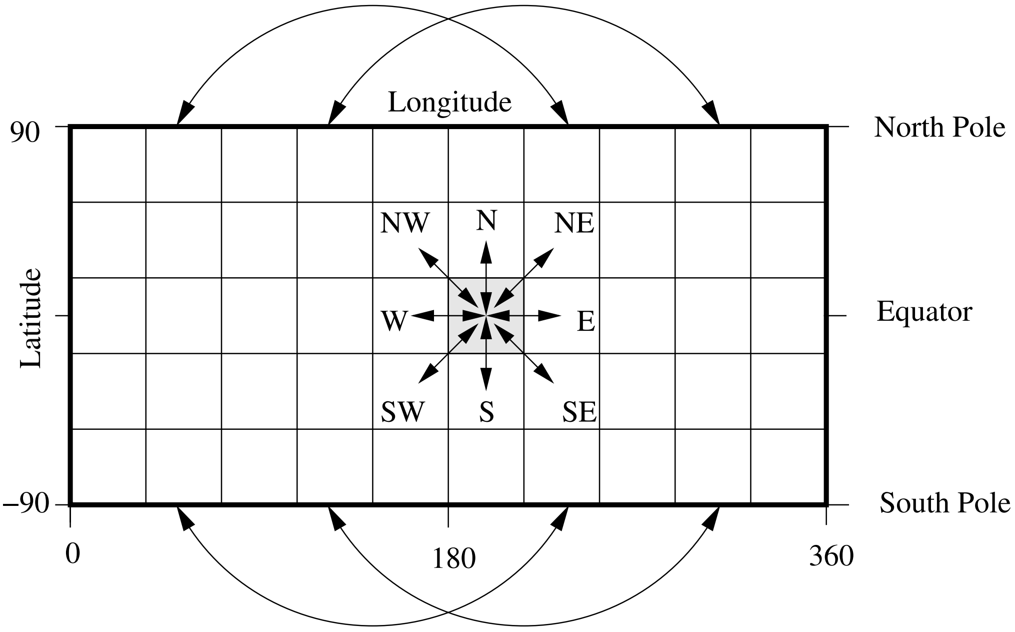

Figure 3.9: Information exchange among nearest neighbors. Neighbors at the poles are located across the poles.

and East/West direction. These neighbors can easily be determined by their λ, φ coordinate position. At the poles though, 3 of the 8 neighbors lie at cross-pole positions as indicated schematically by the long arrows. The spherical adaptive grid library takes this requirement into account and correctly locates the neighbors of the pole blocks. Therefore, an even number of blocks in longitudinal direction must be selected. If all neighbors of the coarse block in the gray-shaded box (figure 3.9) were refined once then the total number of neighbors would increase to 12.

Load-balancing

The load-balancing strategy currently implemented in the spherical adaptive grid library strives to maintain an approximately equal number of blocks on all processors. Assuming that the workload per block is equal, this ensures a well-balanced work load per processor. No attention is paid to the actual location of the blocks which consequently leads to a scattered 2D domain decomposition on the parallel machine. This is displayed in figure 3.10 on the facing page which shows two snapshots of an adapted passive advection test with 4 processors. Here, a cosine bell (contours not shown) is transported around the globe and crosses the pole at day 3 in subfigure (a). Subfigure (b) depicts the final stage after 12 days. The adapted blocks are colored according to the assigned processors. It can clearly be seen that the domains of the processors are discontinuous which increases the amount of data that needs to be communicated across the network. In continuous regions, such a communication is replaced by memory copies. The slightly enhanced overhead of the scattered approach might still have negligible effects as far as the overall parallel performance is concerned. For example, such a load-balancing strategy has not been found to present a problem in the magnetohydrodynamics code BATS-R-US. In this code the blocks

(a) 72 hours

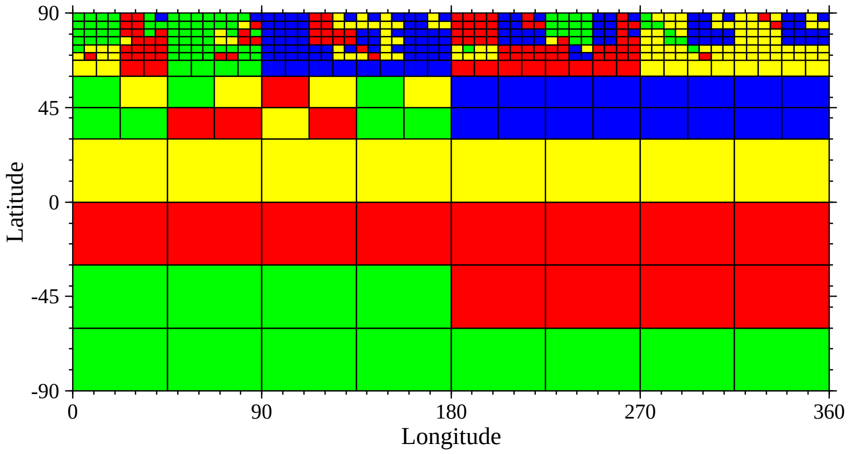

(b) 288 hours

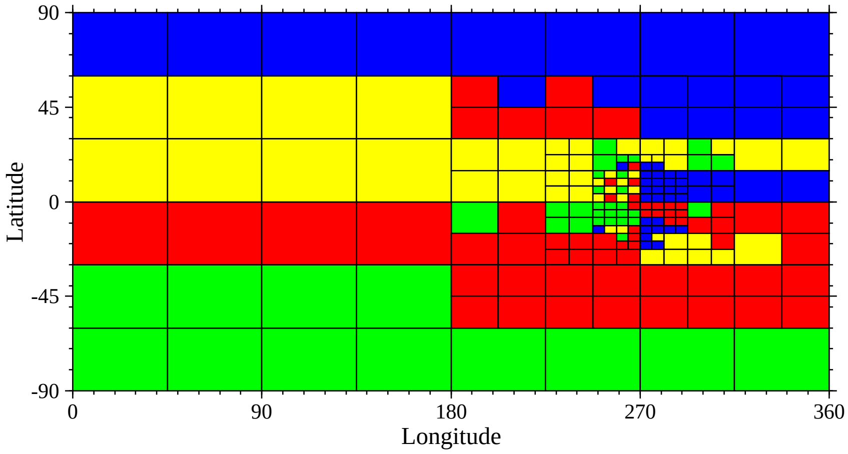

Figure 3.10: Load-balancing strategy illustrated with the cosine bell advection test (test case 1, $\alpha = 90°$) after (a) 72 hours and (b) 288 hours (1 evolution). The contours of the cosine bells are omitted (see figure 5.2). Each color represents a processor, the blocks are colored accordingly.

have a high ratio of calculation to communication so that the actual mapping of the blocks to processors does not play a key role with respect to the parallel performance (*Stout et al.* [1998]). As indicated by *Dennis* [2003], this conclusion might not apply to an atmospheric dynamical core and needs to be evaluated further in the future. As an alternative, a load-balancing strategy could be employed that is based on the space-filling curve approach. Such an approach has already been successfully applied to parallel oceanic and atmospheric science applications as documented by *Blayo et al.* [1999], *Behrens and Zimmermann* [2000] and *Dennis* [2003] (see also *Griebel and Zumbusch* [1999]). The space-filling curve principle ensures that blocks from the same geometric regions are mapped onto the same processors which minimizes the communication across the network. This offers an interesting perspective for future high-performance computing assessments.

3.2.2 Program flow

The adaptive finite-volume dynamical core is built upon the spherical adaptive grid library whose function calls are predominantly visible in the main driver routines for the dynamics calculations. From a high level viewpoint, the program flow can be described as in figure 3.11. Besides initial initialization procedures, the program mainly consists of an outermost time loop in which the adaptive dynamics are embedded. Here, the pure dynamics calculation can be viewed as a black-box solver that iteratively computes the transport processes on a block-by-block basis until all blocks are updated. Such a loop over the blocks is hidden in the “Calculate the Dynamics” box that is succeeded by a ghost cell exchange. If an adaptation cycle is reached after n time steps, the adaptation criterion is evaluated which determines the resulting program flow. In case of adaptation requests the corresponding AMR

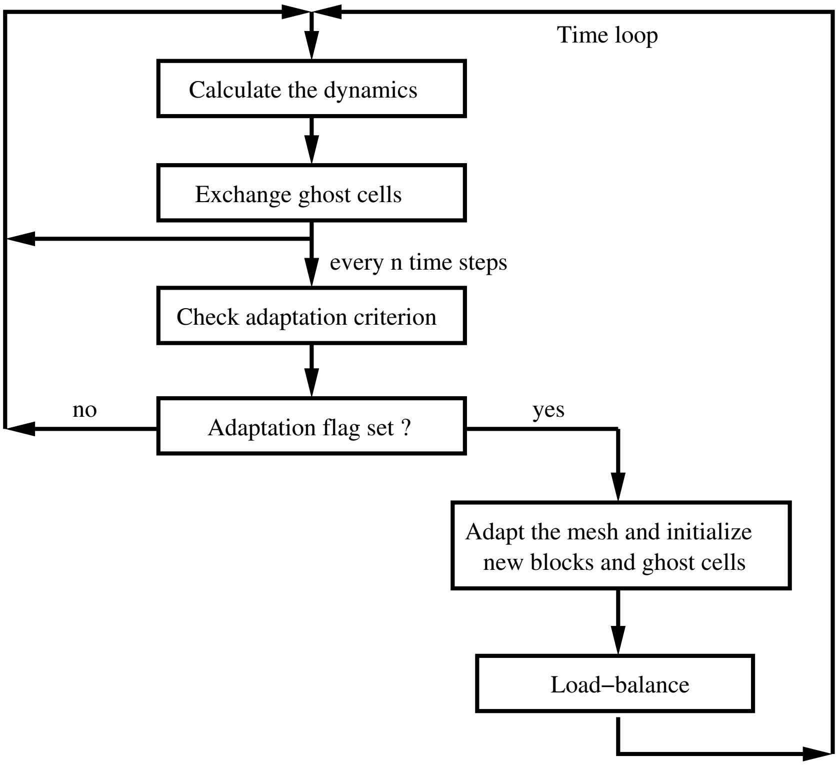

Figure 3.11: High level view of the program flow with adaptive mesh functionality.

library functions are called that create or destroy the flagged blocks. This is followed by a load-balancing step before returning to the main time loop. On the other hand, if no adaptation flags are set the program continues directly with the next time step.

3.2.3 Performance

The computational performance of the adaptive blocks strongly relies on the number of cells per block. In general, it can be observed that bigger block sizes lead to a sharp increase in efficiency until a saturation level is reached (*Stout et al.* [1997]). This saturation level is associated with the cache size of the individual computer architecture and no improvements could be measured with further increases in block sizes. On the contrary, *Stout et al.* [1997] reported a slight decrease in efficiency after exceeding the optimal block size. The same characteristic has also been found in the adaptive Lin-Rood simulations. Here, the 2D shallow water version at a constant

2.5° × 2.5° resolution has been used in order to assess the performance with respect to varying block sizes. For these runs, shallow water test case 2 ($\alpha = 0°$) has been chosen. All runs employ the same $\Delta t = 400s$ time step and are integrated over a 14-day period or 3024 time steps.

Various combinations of the input parameters B_x, B_y, N_x, N_y (see Section 3.1.2 for an explanation of the symbols) have been selected that arrive at the identical initial 2.5° × 2.5° setup. The smallest block size considered in this study is the standard block size for the adaptive model runs. Here the 16x12 blocks are comprised of only 9x6=54 cells per block which offers maximum flexibility with respect to adaptation regions. On the other hand, the biggest block size with 72x36=2592 cells per block and 2x2 blocks in each direction does not allow finely tuned adaptive feature tracking simulations. These are the trade-offs that need to be considered. The comparison is displayed in figure 3.12. The figure shows the total CPU time, as measured on a SUN Ultrix workstation, for the 14-day integration with different block sizes. It is apparent that the ideal block size lies between 1500-2000 cells per block. Here, the saturation point is reached with a 72x24=1728 cell setup that leads to an increase in speed by a factor of approximately 2.5 in comparison to the standard 54 cells per block. However, in case of adaptive grid refinements the larger block size will lessen

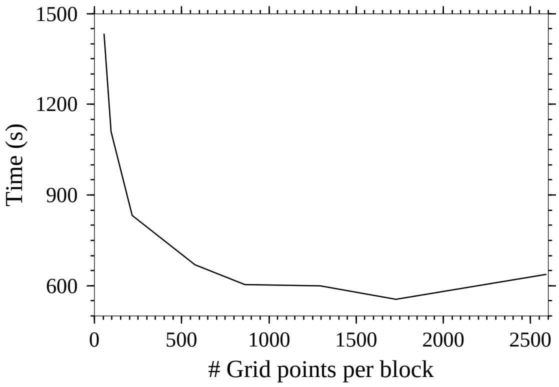

Figure 3.12: CPU timing data for different block sizes (test case 2, $\alpha = 90°$).

the speed advantage since many more blocks need to be refined in order to resolve a feature of interest at a fine resolution. In addition, the speed advantage of the large blocks is diminished when switching from the 2D regime to the full 3D simulation. Then a block contains the whole vertical column with e.g. 26 layers which increases the new standard block size with 9x6x26=1404 cells considerably. This block size is very close to the optimal block size found in *Stout et al.* [1997]. In practice, the ideal block size for the finite-volume dynamical core is a compromise between speed, memory requirements and flexibility. It needs to be determined empirically and probably is close to 10x10 cells per block.

The memory requirement is another aspect that is closely related to the initial block setup. Each block is surrounded by an additional 3-ghost-cell zone in the horizontal directions. This noticeably increases the memory requirements in case small blocks are used. For example, the ghost cell to computational cell ratio for the 9x6 grid setup is 2.33 whereas the ratio is 1.56 if 10x10 cells are chosen. Other applications, like BATS-R-US, typically work with ratios between 1.37 and 7 (*Hansen et al.* [2002]). In practice, the enhanced memory requirements are less of a concern in comparison to the speed of the computations.

Overhead

Adding the adaptive grid functionality to the finite-volume dynamical core significantly enhances the flexibility of the model simulations but also adds computational overhead. A thorough assessment of the overhead can be found in *Oehmke* [2004]. Here, a rough estimate is given that is based on a comparison of an adaptive advection test and a constant resolution model run. The tests have been performed with shallow water test case 1 ($\alpha = 0^\circ$) which describes the transport of a cosine bell along the equator. An adapted run with a $5^\circ \times 5^\circ$ base resolution and 2 refinement levels is compared to a uniform run on a $1.25^\circ \times 1.25^\circ$ grid. Identical time steps with $|CFL| = 0.95$ are used and both runs resolve the feature of interest at the same 1.25° resolution. The overhead is assessed by measuring the total CPU time of the 12-day model simulation and counting the number of blocks (with 9x6 cells) involved in the computation. Then the CPU time per block can be estimated for both model runs which gives an indication of the additional workload in the adapted case. In the concrete example, the uniform grid run with 32x24=768 blocks finished the transport of the cosine bell after 13800 CPU seconds. On the other hand, the number of blocks in the adapted run varied between 72-84 during the simulation and needed 1920 CPU seconds. These two run times differ by a factor of ≈ 7.2. As a result, the CPU time spent per block is $\frac{13800}{768} = 17.97$ CPU s/block in the uniform case and approximately $\frac{1920}{0.5(72+84)} = 24.61$ CPUs / block in the adapted run.

Based on this preliminary assessment, the overhead in the adapted run is on the order of 27% which compares well to the 20% overhead reported by *Berger and Colella* [1989]. Other hints in the literature are given by *Skamarock and Klemp* [1993]. They discussed that the break-even point where the cost of an adaptive run will be approximately equivalent to a fixed-grid simulation occurs when nearly 50-60% of the coarse domain needs refinement at the finest refinement level.

In order to gain more insight into the performance of the adaptive run two aspects need to be considered. First, it must be kept in mind that the pure advection test does not represent the full complexity of the nonlinear equations. The workload per block is low so that the communication and interpolation routines represent a higher percentage of the total workload. When switching to the nonlinear set the workload per block is increased by approximately a factor of 3 in the 2D shallow water setup. Furthermore in a full 3D simulation, this workload then gets multiplied by the number of vertical levels. This could lead to a relative decrease in overhead although additional communication steps need to be introduced in the two latter cases as well.

Second, the advection test used here depicts an idealized scenario where one adapted region tracks the cosine bell in a narrow ring around the equator. In a more realistic simulation, the blocks at different refinement levels are distributed among the model domain and many more refinement regions are present. Consequently, such a flow field requires more communication and interpolations at the mesh interfaces which increases the overhead.

Therefore the overhead assessment performed here should be considered a rough estimate to which future studies can be compared.

3.3 Fine-coarse grid interfaces

3.3.1 Interpolation and averaging techniques

In an adaptive model run grids at different resolutions require the use of interpolation and averaging routines in order to fill the ghost cell regions. In addition, interpolation and averaging procedures become necessary for split-join operations if block adaptations are requested. These routines are user-defined modules for the AMR library. They need to be carefully designed in order to guarantee not only the accuracy of the algorithm but also its conservative nature.

Numerous interpolation techniques can be found in the literature. For example, *Williamson and Rasch* [1989] (also *Rasch and Williamson* [1990]) investigated shape-preserving interpolation techniques and *Alapaty et al.* [1998] assessed various spatial interpolation schemes for nested grid models. In general, interpolation schemes are widely used in atmospheric semi-Lagrangian (SL) models that need to map the transported data onto a fixed spherical reference mesh. But a general difficulty needs to be considered. Most of the interpolation techniques and especially the high-order conservative interpolation techniques are well-designed and efficient for 1D problems on the Cartesian plane. But in the multi-dimensional case in curvilinear coordinates the multi-dimensional extensions of the 1D algorithms may not be straightforward or they may be computationally very expensive. The former is also due to the polar singularities in the global domain. The latter was shown by *Rancic* [1992] who extended the conservative PPM advection and remapping algorithm to 2 dimensions in Cartesian coordinates. The resulting mass-conserving semi-Lagrangian scheme performed well but increased the compute time by a factor of 2.5. Therefore, more efficient solutions to the multi-dimensional interpolation problem were proposed by *Purser and Leslie* [1991], *Leslie and Purser* [1995] and *Sun and Yeh* [1997] who introduced the new concept of "cascade interpolations" or "split interpolations" for SL models. Then the true multi-dimensional interpolation problem is broken up into a series of consecutive 1D interpolations that approximate the solution with high accuracy. For instance, *Rancic* [1995] showed the viable combination of the cascade interpolation principle with 1D PPM-like interpolations and *Nair et al.* [1999] applied the cascade interpolations to SL transport problems in spherical coordinates. Furthermore, *Nair and Machenhauer* [2002] presented a mass-conserving advection scheme on the basis of the PPM approach. This publication serves as one of the key references in the following section.

There are two design principles concerning the interpolation scheme for the adaptive finite-volume dynamical core. First, the interpolation method must conserve mass, but is allowed to be non-conservative for the wind components (no conservation of the momentum). Second, the order of the scheme to be selected should be a method that is consistent with the design of the transport algorithm as also postulated by *Clark and Farley* [1984]. These two principles lead to a natural 2D extension of the underlying 1D finite-volume approaches, the van Leer principle with linear subgrid distribution and a PPM-like interpolation scheme with quasi-biparabolic subgrid distribution. The latter PPM-type remapping algorithm is second-order accurate.

2D extensions of the van Leer approach

The first-order van Leer interpolation mechanism (*van Leer* [1977]) is based on the construction of linear subgrid distributions in each cell. In the 1D case in x-direction this requires the specification of a slope Δa^x in order to arrive at the polynomial $h(x)$

$$h(x) = \bar{h} + \Delta a^x \, x \tag{3.1}$$

where $\bar{h} = \int_{-1/2}^{1/2} h(x)\, dx$ is the cell-averaged (finite-volume) value and $x \in [\frac{-1}{2}, \frac{1}{2}]$ a normalized local coordinate defined in equation 3.6. For the straightforward 2D extension, a second slope Δa^y in y-direction is added to equation 3.1 which yields

$$h(x, y) = \bar{h} + \Delta a^x \, x + \Delta a^y \, y \tag{3.2}$$

with $y \in [\frac{-1}{2}, \frac{1}{2}]$ and $\bar{h} = \int_{-1/2}^{1/2} \int_{-1/2}^{1/2} h(x, y)\, dx\, dy$. The slopes at a point (i, j) are then defined as in van Leer's scheme I using centered finite differences

$$\begin{aligned} \Delta a^x &= \frac{1}{2} \left(h_{i+1,j} - h_{i-1,j}\right) && (3.3) \\ \Delta a^y &= \frac{1}{2} \left(h_{i,j+1} - h_{i,j-1}\right) \quad . && (3.4) \end{aligned}$$

The (i, j) indices for Δa^x and Δa^y are dropped for convenience. These slopes can be further manipulated if monotonicity constraints are required. Then the monotonized central-difference (MC) slope limiter (*van Leer* [1977])

$$\begin{aligned}\Delta a^x &= min\big(|\Delta a^x|, 2|h_{i+1,j} - h_{i,j}|, 2|h_{i,j} - h_{i-1,j}|\big)\ sgn(\Delta a^x) \qquad (3.5)\\ &\qquad \text{if } (h_{i+1,j} - h_{i,j})(h_{i,j} - h_{i-1,j}) > 0\\ &= 0 \quad \text{otherwise}\end{aligned}$$

picks out the smallest magnitude of three slopes: the centered difference and the two one-sided differences. However, if the value of $h_{i,j}$ represents an extreme value, the slope is set to zero. The same principle applies to the MC slope limiter in y direction (not shown).

When transforming the Cartesian coordinates to the spherical coordinate system (λ, φ) the local normalized (x,y) coordinates for each cell are defined by (see also *Nair and Machenhauer* [2002])

$$x = \frac{\lambda - \lambda_i}{\Delta\lambda_i} - \frac{1}{2} \qquad (3.6)$$

$$y = \frac{\mu - \mu_j}{\Delta\mu_j} - \frac{1}{2} \qquad (3.7)$$

with $\Delta\lambda_i = \lambda_{i+1} - \lambda_i$, $\Delta\mu_j = \mu_{j+1} - \mu_j$ and $\mu_j = \sin\varphi_j$. For each left and right position $\lambda = \lambda_i$ and $\lambda = \lambda_{i+1}$ follows $x = \frac{-1}{2}$ and $x = \frac{1}{2}$, respectively. The same idea applies to μ.

It is important to note that the slope Δa^y in the meridional direction is calculated with h values that are equidistant in the spherical φ coordinate. On the other hand, the local normalized y coordinate is computed in the non-equidistant μ system. In particular, the μ- coordinate lines become increasingly compressed toward the poles. This causes a slight inconsistency, namely the polynomial $h(x, y) \cong h(\lambda, \mu)$ does not fully represent the subgrid distribution in the transformed (λ, μ) system. It can be considered a mix of the (λ, μ) and (λ, φ) coordinates due to the equidistant slope Δa^y. There are three options that have been evaluated. First, the equidistant slope calculation (eqn. 3.4) could be replaced by a consistent non-equidistant slope calculation based on the μ-coordinate (as shown in *Colella and Woodward* [1984]). Second, the inconsistency can be ignored when assuming that the equidistant slope is still a good approximation even in polar latitudes when μ-values become compressed. This option is motivated by the findings in *Veldman and Verstappen* [1998] who argued in case of a convection-diffusion problem that the derivatives should still be estimated in an equidistant fashion on a nonuniform grid. Third, the equidistant slope calculation can be kept throughout the model domain but the local variable y is switched from the μ-system to the φ-system in polar regions. Then the y calculation poleward of 60° N/S is replaced by the equidistant expression

$$y = \frac{\varphi - \varphi_j}{\Delta\varphi_j} - \frac{1}{2} \tag{3.8}$$

with $\Delta\varphi_j = \varphi_{i+1} - \varphi_j$. In practice, options (2) and (3) have been assessed and the results are presented in figure 3.13 on page 100.

In order to use the van Leer approach for the interpolation of a conservative scalar (for example during a split operation for Φ as indicated in blue and black in figure 3.6 on page 76), two steps become necessary. First, a monotonic subgrid distribution $h(x, y)$ is computed that is based on the coarse grid data. Then the subgrid distribution needs to be integrated over the fine grid regions which guarantees the conservative mapping of the coarse cell. If assuming that the fine grid region of interest lies within the boundaries $x \in [x_l, x_u]$, $y \in [y_l, y_u]$ inside a coarse grid cell, the new $\bar{h}^r$ value for the refined grid cell is determined by

$$\begin{aligned} \bar{h}^r &= \frac{1}{\Delta x \Delta y} \int_{y_l}^{y_u} \int_{x_l}^{x_u} \left(\bar{h} + \Delta a^x\, x + \Delta a^y\, y\right) dx\, dy \qquad (3.9) \\ &= \bar{h} + \frac{\Delta a^x}{2\,\Delta x}\left(x_u^2 - x_l^2\right) + \frac{\Delta a^y}{2\,\Delta y}\left(y_u^2 - y_l^2\right) \end{aligned}$$

with $\Delta x = (x_u - x_l)$ and $\Delta y = (y_u - y_l)$.

In case of a non-monotonic non-conservative interpolation request, the unconstrained subgrid distribution does not need to be integrated. Instead, $h(x, y)$ can be immediately evaluated at the new refined grid position (x^r, y^r).

Both approaches, the monotonic-conservative and the non-monotonic non-conservative interpolations, have been tested in the finite-volume dynamical core and the results are documented in table 3.4 on page 106. In general, the van Leer interpolation approach is first-order accurate.

2D extensions of the PPM approach

The extension of the *Colella and Woodward* [1984] PPM interpolation scheme to two dimensions is closely related to the van Leer principles outlined above. Therefore, most of the symbols are reused. The starting point is the underlying quadratic subgrid distribution in x direction (see also *Nair and Machenhauer* [2002] and *Carpenter et al.* [1990])

$$h(x) = \bar{h} + \delta a^x \, x + b^x \left(\frac{1}{12} - x^2 \right) \tag{3.10}$$

where δa^x denotes the slope and b^x symbolizes the curvature of the parabola. These are defined by

$$\begin{aligned} \delta a^x &= h_R - h_L && (3.11) \\ b^x &= 6\,\bar{h} \; - \; 3\,(h_L + h_R) \quad . && (3.12) \end{aligned}$$

Here the subscripts L and R indicate the left and right cell edge value of h. For example, the left cell edge value in the ith cell is approximated by

$$h_{L,i} = \frac{1}{2} \left(\bar{h}_{i-1} + \bar{h}_i \right) \; - \; \frac{1}{6} \left(\Delta a^x_i - \Delta a^x_{i-1} \right) \tag{3.13}$$

where Δa^x stands for the van Leer slope (eqn. 3.3) with or without monotonicity constraint 3.5. The right edge value is given by $h_{R,i} = h_{L,i+1}$. The coefficients of the parabola δa^x and b^x can then be further modified in order to enforce monotonicity. The details are given in *Colella and Woodward* [1984] and *Lin and Rood* [1996].

For the 2D extension of the algorithm, a biparabolic function needs to be found. As shown by *Rancic* [1992], a true 2D extension of the PPM scheme requires the calculation of nine coefficients which leads to a rather expensive method. Therefore, a quasi-biquadratic approach with six coefficients is derived that closely resembles the scheme proposed by *Nair and Machenhauer* [2002] with four coefficients (excluding the readily available cell average). Here, a directionally bias-free cross-term is added to the *Nair and Machenhauer* [2002] algorithm that helps smooth the subgrid distribution near sharp edges. A similar mixed derivative term was also introduced by *van Leer* [1985] in an alternative definition of a biparabolic subgrid distribution function. Here the 2D subgrid distribution is given by

$$h(x,y) = \bar{h} + \delta a^x\, x + b^x \left(\frac{1}{12} - x^2\right) + \delta a^y\, y + b^y \left(\frac{1}{12} - y^2\right) + \frac{1}{2}\left(c^{xy} + c^{yx}\right) x\, y \quad (3.14)$$

where δa^y and b^y are defined as in equations 3.11-3.12 with respect to the meridional direction. The cross term consists of the two components c^{xy} and c^{yx} that are averaged in order to avoid a directional bias. In particular, c^{xy} and c^{yx} at a point (i,j) are determined by

$$c^{xy} = \frac{1}{2}\left(\Delta a^x_{i,j+1} - \Delta a^x_{i,j-1}\right) \quad (3.15)$$

$$c^{yx} = \frac{1}{2}\left(\Delta a^y_{i+1,j} - \Delta a^y_{i-1,j}\right) \quad (3.16)$$

where Δa^x and Δa^y are the slope limited centered difference slopes (eqns. 3.3, 3.4 and 3.5 as in the van Leer case). In addition, it is imperative that the cross terms be further limited via a second application of the MC slope limiter before the interpolation step is applied.

As mentioned in the linear case, such a subgrid distribution can either be used for conservative or non-conservative interpolation strategies. Here the same principles apply. In case of a conservative variable, $h(x,y)$ needs to be integrated in the fine grid domain as principally shown in equation 3.9. In case of non-conservative interpolations the biparabolic subgrid distribution can be evaluated immediately at any position within the $x \in [\frac{-1}{2}, \frac{1}{2}], y \in [\frac{-1}{2}, \frac{1}{2}]$ cell boundaries. The PPM algorithm can be used with or without the monotonicity constraints for the slopes Δa^x and Δa^y whereas the limiting of the b^x, b^y and cross parameters is essential with respect to accuracy. Otherwise, severe under- or overshoots at the cell corners might be generated. The PPM interpolation algorithm is a second-order interpolation scheme in each direction, although the order of accuracy is formally slightly reduced in the 2D quasi-biparabolic approach. Nevertheless, the PPM method is referred to as a second-order scheme in the following chapters in order to clearly distinguish the different methods in subsequent comparisons.

Averaging

Besides interpolations, data also need to be averaged for fine to coarse grid transfers and during join-operations in case of coarsenings. In particular, this is true for scalar components that are defined at cell centers. The staggered wind data on the other hand need 1D interpolations in order to update the coarse grid ghost regions with fine grid information. For scalar variables, the averaging step involves the four fine grid cells that are completely contained in the corresponding coarse grid box (compare figure 3.6 on page 76). Then a coarse grid value h^c can be directly determined by the weighted average

$$h^c = \frac{1}{A^c} \sum_{i=1}^{4} h_i^r \, A_i^r \tag{3.17}$$

where A^c, A^r stand for the area of the coarse and refined surface patches and h_i^r symbolizes the fine grid value in the ith grid box. This averaging strategy is mass-conservative. In case of a reduced grid setup, averaging processes at the reduced interfaces only involve two neighboring grid boxes (see also figure 3.18 on page 109).

Normalized local y coordinate

Both the van Leer and PPM interpolation algorithms are based on coordinate positions in a normalized local (x,y)-coordinate system. As discussed in Section 3.3.1 for the van Leer approach such a coordinate system might lead to slight inconsistencies in polar regions if spherical geometry is used. This has been assessed in figure 3.13 which shows a comparison of two spherical domains after refinements occurred. Both domains are completely refined and reinitialized via monotonic conservative PPM interpolations. In subfigure (a) the non-equidistant μ-coordinate is used for the computation of the local y position (eqn. 3.7) whereas this calculation is replaced by the equidistant y position poleward of 60° N/S (eqn. 3.8) in subfigure (b). The plots depict the difference of the geopotential height field with the analytic reference solution for shallow water test case 2 with the rotation angle $\alpha = 45°$ (see also Appendix A.1 for the description of the test case). It can clearly be seen that the non-equidistant approach leads to large errors near the poles which are eliminated when switching to the equidistant y-coordinate. This indicates that the non-equidistant μ-system, together with an equidistant slope assessment, no longer represents a good approximation in polar latitudes. Similar conclusions have also been drawn by *Nair and Machenhauer* [2002] who consequently applied special algorithms in the polar

(a) Non-equidistant μ-coordinate polewards of 60° N/S

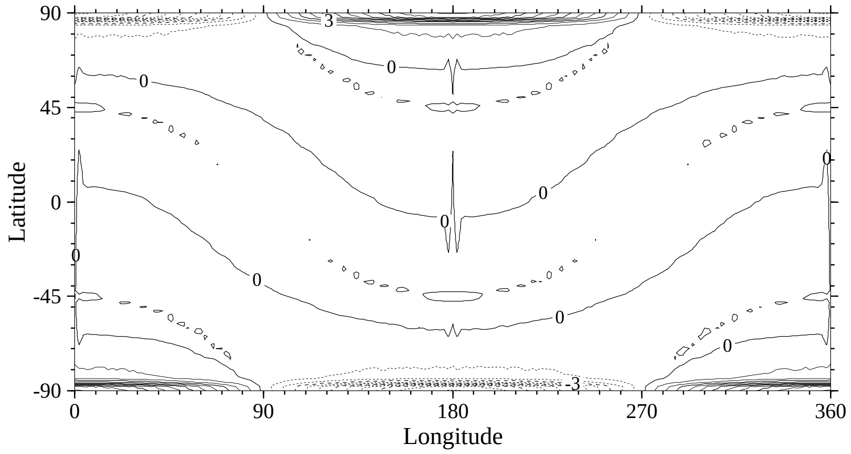

(b) Equidistant y-coordinate polewards of 60° N/S

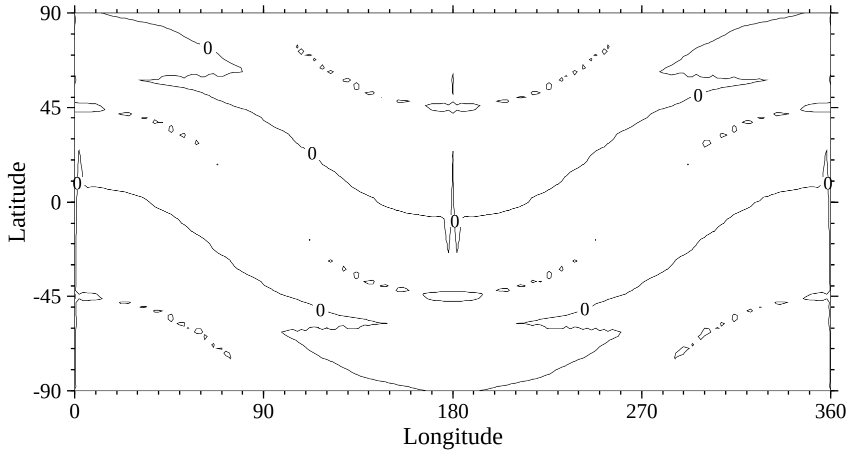

Figure 3.13: Differences of the geopotential height with the analytic solution after refining the whole domain with refinement level 1 (from a 2.5° × 2.5° to a 1.25° × 1.25° resolution). The data are initialized with second-order conservative interpolations (PPM method). (a) Interpolations with the non-equidistant μ-coordinate, (b) interpolations with the equidistant y-coordinate poleward of 60°N/S (test case 2, $\alpha = 45°$). Contour interval is 1 m.

Latitudinal domain of the interpolation coordinate y		Height error norms		
non-equidistant μ	equidistant φ	l_1	l_2	l_∞
	whole globe	6.988E-5	8.616E-5	5.703E-4
60°S - 60°N	poleward of 60° N/S	7.344E-5	9.027E-5	5.704E-4
75°S - 75°N	poleward of 75° N/S	7.618E-5	9.330E-5	5.704E-4
whole globe		8.958E-5	1.546E-4	3.463E-3

Table 3.3: Impact of the equidistant and non-equidistant y-coordinate on the accuracy of the monotonic, conservative PPM-type interpolation scheme. The whole domain is refined and reinitialized (test case 2, $\alpha = 45°$)

regions.

The errors are further quantified in table 3.3 which lists the normalized height error norms (see also Chapter IV for the definitions) for four refinement scenarios. In each scenario, the y-coordinate is based on a different combination of the equidistant and non-equidistant approaches and the errors assess the overall, horizontally integrated, error of the interpolation procedure. The table shows that the smallest errors are measured when the equidistant y coordinate occupies large portions of the domain. In practice, the second option has been selected for all adaptive runs presented in the following chapters. Then the μ-based y-coordinate is used in the region 60°S - 60°N, which is replaced by the equidistant φ-based y coordinate poleward of 60° N/S.

Interpolation strategies

In the adaptive Lin-Rood dynamical core a variety of interpolation strategies needs to be distinguished. This is due to the staggered positions of the prognostic variables (see figure 3.6 on page 76 and further details in Section 3.3.2) which do not allow a unified approach to the interpolation problem. In general, all scalar variables that are defined at the cell centers are interpolated with a monotonic conservative interpolation scheme. The scheme of choice is the 2D PPM method with monotonicity constraints as outlined in the previous section.

For the wind components though, the 2D PPM approach can not be applied because of the relative positions of coarse and fine grid wind data. This is documented in figure 3.14 that illustrates the interpolation problem for the zonal wind u (left figure) and the meridional wind v (right figure). Here, the coarse data are indicated in blue, the fine grid data are marked in black. The key interpolation strategy for this setup is based on the cascade-interpolation principle which makes use of consecutive one-dimensional operations. For example the fine grid u data are first interpolated in the zonal direction before the sweep in the meridional direction completes the interpolation cycle. This interpolation order is reversed for v. As in the scalar

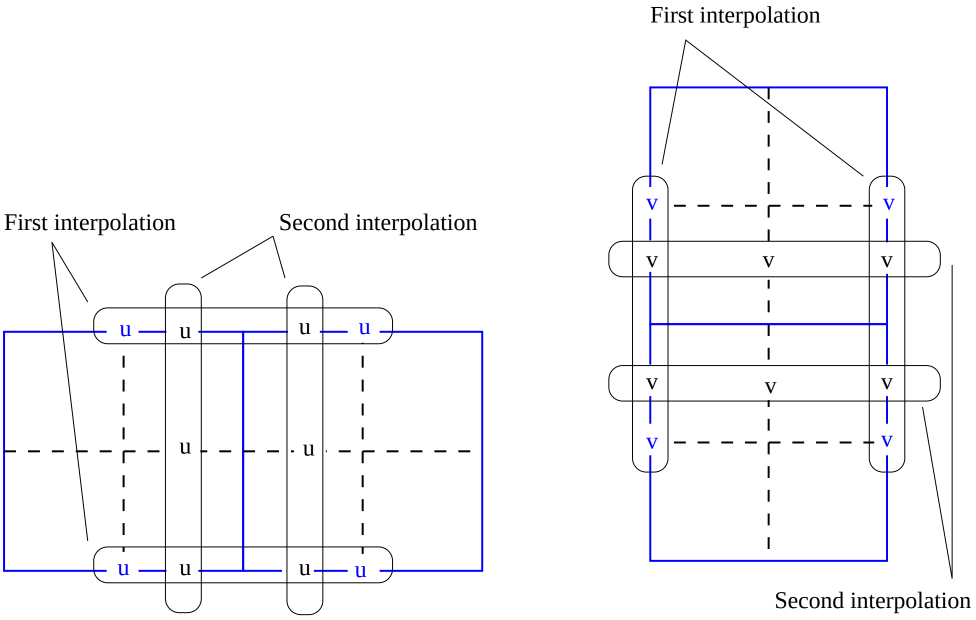

Figure 3.14: Cascade interpolations of the wind components u (left) and v (right). The zonal wind u is first interpolated in longitudinal direction (W-E) and then in meridional direction (N-S). The meridional wind v is interpolated in reverse order. The blue color indicates the coarse grid, the fine grid is in black.

case, the second-order PPM interpolation approach is chosen, but now as a 1D unconstrained non-conservative method. This approach has been observed to be more accurate than the monotonicity-constrained variant (see next paragraph).

In order to justify the selection of the more expensive PPM-type interpolation method as the default scheme, a comparison of three different interpolation techniques has been performed. This includes not only the van Leer and PPM-type methods but also takes a simple bilinear interpolation scheme into account. Bilinear interpolations are purely based on an assessment of the four nearest neighbors of a particular grid point. Then area weights are used to find a weighted average of the four neighbors at the new location. As in the van Leer case, such an approach is a first-order method.

The three interpolation schemes are compared in figure 3.15 using the initial zonal wind field of the shallow water test case 6 (see also Appendix A.1). Here the whole model domain at base resolution $2.5^\circ \times 2.5^\circ$ is refined once and new blocks are initialized via the three, non-conservative interpolation approaches (in (c) and (d) with and without monotonicity constraint). The figure depicts the difference of the interpolated wind field with the analytic reference solution on the refined grid. As expected, it can be seen that the interpolation error clearly diminishes when applying the finite-volume-type methods (b-d), especially in case of the second-order PPM-type interpolation scheme. In addition, it is apparent that the error significantly increases in the PPM case when monotonicity constraints are applied (d). Then the extrema in the wind field (compare also to the initial wind data in figure A.12 on page 234) are clipped which is a characteristic feature of both the van Leer and PPM monotonic algorithm. This leads to the typical error streaks displayed in subfigure (d).

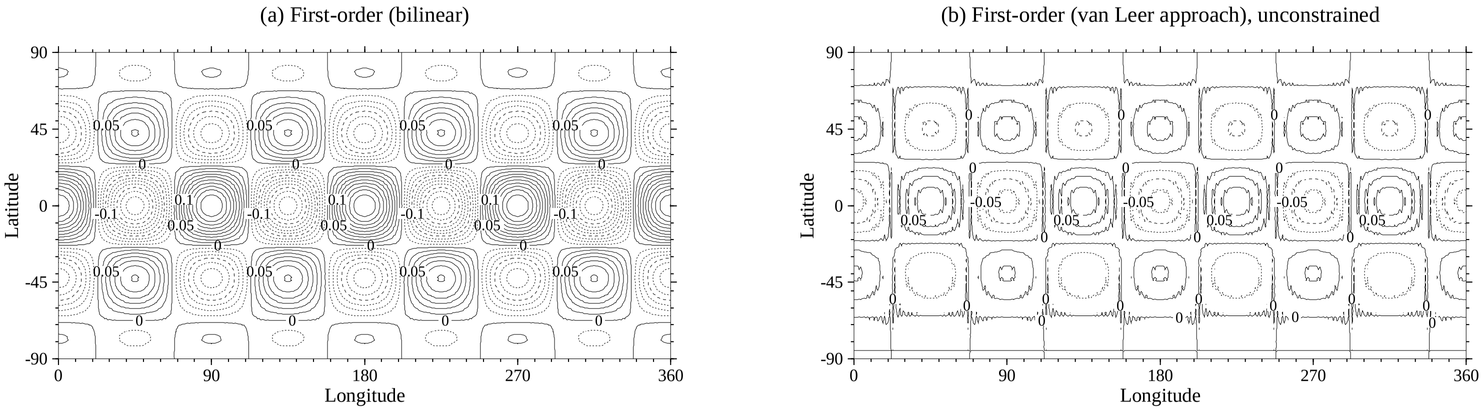

(a) First-order (bilinear)

(b) First-order (van Leer approach), unconstrained

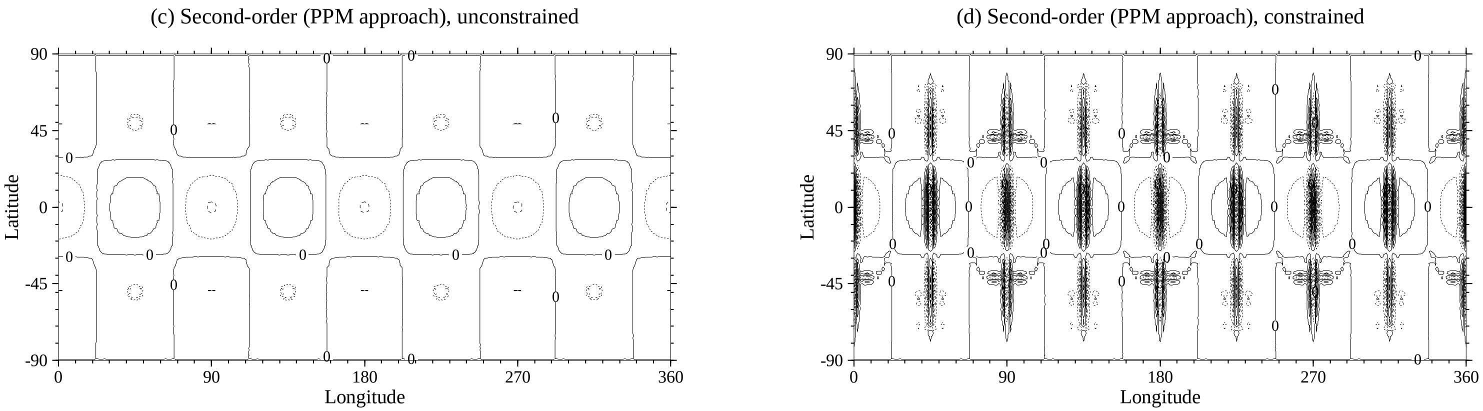

(c) Second-order (PPM approach), unconstrained

(d) Second-order (PPM approach), constrained

Figure 3.15: Differences of the zonal wind u with the analytic solution after refining the whole domain from a 2.5° × 2.5° to a 1.25° × 1.25° resolution. The data are initialized with (a) 1st order bilinear interpolations, (b) 1st order unconstrained van Leer-type scheme, (c) 2nd order unconstrained PPM interpolation approach and (d) same as (c) but with monotonicity constraint. Contour intervals are 0.025 ms^{-1} (test case 6).

Error streaks are also present in the conservative monotonic PPM interpolations shown in figure 3.16. The plot shows the differences of the interpolated geopotential height field with its analytic solution after refinements occurred. Despite the distinct error bands, the use of the monotonicity constraint is imperative for the mass variable and other conserved scalars. It prevents the model from developing over- and undershoots and therefore suppresses the introduction of spurious noise.

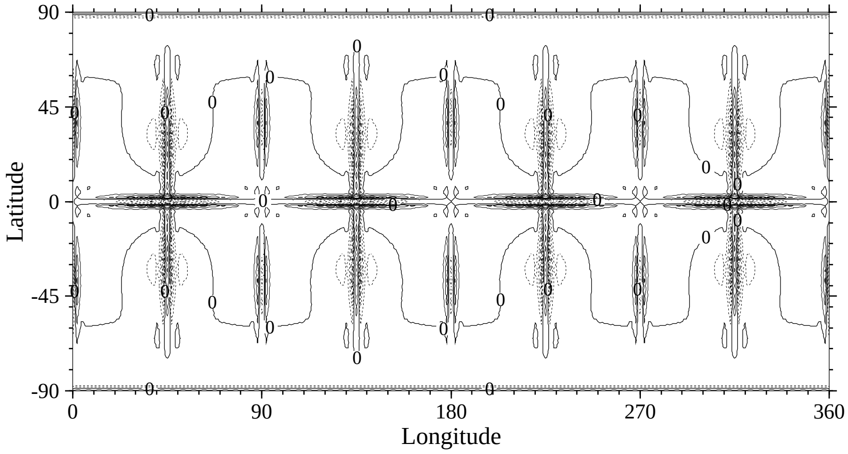

Figure 3.16: Differences of the geopotential height with the analytic solution after refining the whole domain as in figure 3.15. The data are initialized with second-order conservative interpolations (PPM method with monotonicity constraint). Contour interval is 1 m (test case 6).

The overall performance of the three interpolation mechanisms is summarized in table 3.4. Here, the normalized height and wind error norms (see also Section 4.1 on page 114) are used as quantitative measures of the interpolation error. The table lists the errors for unconstrained and constrained non-conservative wind interpolations (middle column) as well as for the conservative monotonicity-preserving interpolations of the scalar height field (right column). As above, the error norms are reported for shallow water test case 6. The table confirms the significant decrease in the interpolation error in case of unconstrained interpolations. This decrease in error

Interpolation order	Wind error norms			Height error norms		
	l_1	l_2	l_∞	l_1	l_2	l_∞
Monotonicity:	constrained			constrained		
1 van Leer approach	1.160E-3	1.281E-3	2.791E-3	7.794E-5	1.123E-4	6.043E-4
2 PPM approach	6.655E-4	8.633E-4	2.249E-3	6.758E-5	1.063E-4	6.043E-4
Monotonicity:	unconstrained					
1 bilinear	2.997E-3	3.003E-3	2.802E-3			
1 van Leer approach	1.011E-3	1.015E-3	9.683E-4			
2 PPM approach	4.178E-4	4.135E-4	5.080E-4			

Table 3.4: Height and wind error norms for different interpolation schemes after refining the whole domain from a 2.5° × 2.5° to a 1.25° × 1.25° resolution. Results are for test case 6 (see also figures 3.15 and 3.16).

is less obvious but still present in the case of monotonicity-preserving conservative or non-conservative interpolations. The error is then mostly dominated by the clipping of the extreme values in both monotonic van Leer and PPM approaches. Further assessments of the interpolation error and its interaction with the overall solution error in a shallow water run are presented in figure 4.8 on page 131 in Chapter IV. This figure illustrates the time evolution of the error measures in statically adapted (reduced grid) and non-adapted model simulations with different interpolation schemes.

In practice, third-order interpolation techniques are sometimes used in adaptive grid simulations (e.g. *Almgren et al.* [1998]) although lower order methods are also often discussed in the AMR literature (*Berger and Colella* [1989]). Low-order methods are attractive due their simplicity and reduced computational overhead. Though the choice of the ideal interpolation scheme also depends on the flow characteristics. For example, the reduced grid shallow water tests in Section 4.3 (figure 4.7 on page 129) show that a first-order bilinear method can be sufficient in case of a very smooth flow pattern. But a higher order method is preferable in the presence of strong gradients in high wind speed regimes (figure 4.9 on page 132). This aspect is discussed later. In the finite-volume dynamical core, the default quasi-biparabolic PPM interpolation method almost matches the underlying numerical PPM transport scheme which is also second-order accurate in two dimensions. This has been one of the design aspects and furthermore was recommended by *Clark and Farley* [1984] and *Chesshire and Henshaw* [1990]. In addition, *Chesshire and Henshaw* [1990] pointed out that the boundary value interpolations for elliptic equations on overlapping grids should be at least as accurate as the model's numerical scheme. This principle also applies to hyperbolic systems. Ideally, an even higher order interpolation method should be applied in the finite-volume model which, on the other hand, is impracticle due to the computational costs.

High-order interpolations were also suggested by *Skamarock* [1988] who initialized the new blocks with a third-order scheme. In this study it was found that bilinear initializations excited spurious gravity waves which took several hours to decay. The higher order interpolations significantly reduced the noise on the fine mesh. For interfaces though, *Skamarock* [1988] used bilinear interpolations for the inflow and outflow boundary conditions which worked satisfactorily in a short 3-day barotropic cyclone simulation. Later, when switching to a non-hydrostatic regime, *Skamarock and Klemp* [1993] proposed quadratic interpolations for interface updates.

In the adaptive Lin-Rood model, the aforementioned quasi-biparabolic interpolation techniques are applied to the prognostic variable u,v,δp and to the conserved scalar $\delta p\,\Theta$. Θ is then retrieved by dividing the interpolated value by δp on the new mesh. As *Skamarock* [1988] indicated, care must be taken not to violate the hydrostatic approximation when interpolating variables independently. This is not a concern here since the geopotential is not a prognostic variable. Instead, it is diagnostically computed during each time step based on the updated δp and Θ values (see eqn. 2.6 and *Lin* [1997]). This automatically guarantees the consistency.

3.3.2 Model interfaces

There are three basic types of fine-coarse grid interfaces in the finite-volume dynamical core which require interpolation and averaging procedures during a ghost cell update. Two of these three interfaces are solely associated with the reduced grid arrangement (see also Chapter 4.2). The third interface depicts the regular fine-coarse grid boundary and is shown in figure 3.17. Here, the blue color indicates the positions of the prognostic variables on the coarse mesh whereas the variables in black denote the fine grid locations. In the figure two refined regions surround the coarse cell to the south and east which clearly shows the staggering of the variables in the two domains. The positions of the variables are shifted by various fractions of the coarse grid lengths in the two dimensions.

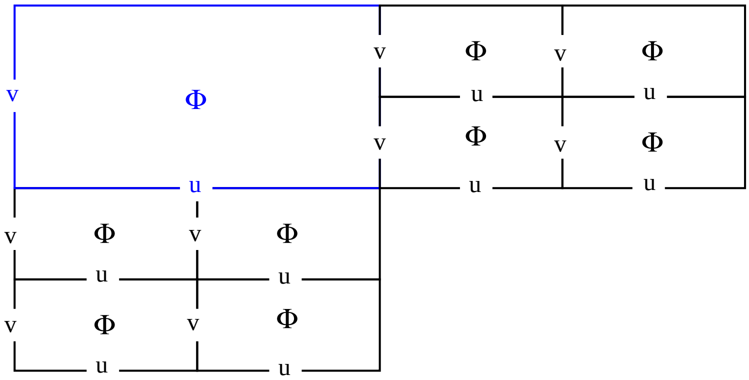

Figure 3.17: Fine-coarse grid interface.

On the other hand the reduced grid interfaces only occur in the north-south direction at the specific latitudes where reduction levels are defined. For example, in case of 1 reduction level this position lies at 75° N/S in the current setup (Chapter IV). A second reduction level can then be placed at 60° N/S. Figure 3.18 displays such an interface in the Northern Hemisphere which can be viewed as a static coarsening step in the longitudinal direction. The variables in blue denote the reduced grid arrangement, while the variables in black indicate the regular grid positions. The u and Φ positions are shifted by a quarter of the coarse grid length in the zonal direction. In contrast, the v positions coincide so that the the ghost cell data can be directly injected during the ghost cell update.

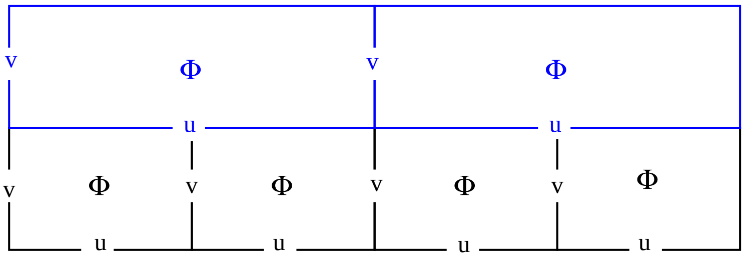

Figure 3.18: Reduced grid interface without adaptations.

In case refinements are applied in the reduced grid domain this interface changes as illustrated in figure 3.19 As before, the blue color denotes the variables in the now refined reduced grid domain. The regular grid to the south (in black) remains unchanged. Here all variable locations are only shifted in meridional direction. Interpolation and averaging routines need to be fully applied to v and Φ whereas u can be partly copied (also called injection) during the ghost cell exchange.

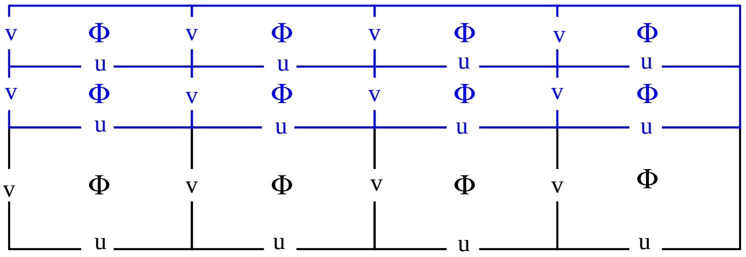

Figure 3.19: Reduced grid interface with adaptations.

The API interface of the spherical adaptive grid library requires that the user provides the interpolation and averaging routines for all possible scenarios. These program modules have been implemented in this research project which, in addition, allow the choice of the three different interpolation schemes via an input parameter (as discussed in Section 3.3.1).

3.3.3 Flux corrections

In an adaptive grid setup flux corrections at fine-coarse grid interfaces are imperative in order to ensure mass conservation properties. Several flux correction strategies have been discussed in the literature. For example, *Berger and Colella* [1989] and *Almgren et al.* [1998] present flux correction mechanisms at the fine-coarse grid boundary when different time steps are used in the two domains. Then fluxes need to be accumulated until a synchronization point is reached. In contrast, the in-situ fluxes can be directly assessed in case of a constant time step in both regions. This simplifies the interface condition as shown in figure 3.20. In general, it is assumed that the fluxes in the fine grid domain are more accurate than the corresponding flux on the coarse grid. Therefore, the goal is to average the fine grid fluxes appropriately

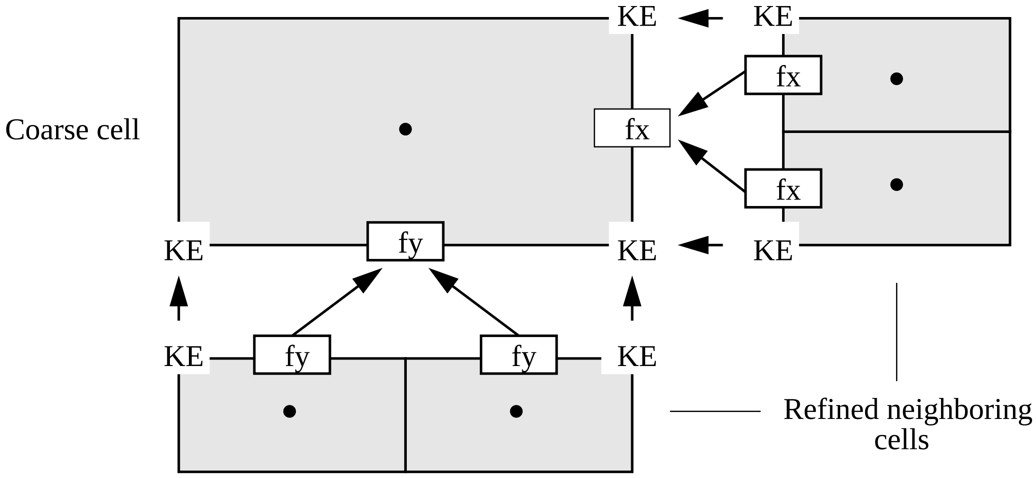

Figure 3.20: Flux and kinetic energy (KE) updates at fine-coarse grid interfaces, fx and fy symbolize the fluxes in longitudinal and meridional direction. Fine grid fluxes are averaged and override the coarse grid flux at the interface.

in order to override the coarse grid information.

In the finite-volume dynamical core, three types of interface corrections are considered. These are the updates of the mass and heat fluxes across boundaries as well as the synchronization of kinetic energy (KE) values at cell corner positions. The mass and heat fluxes are defined at identical locations and are denoted by their generic names fx and fy in figure 3.20. Here fx represents the flux in the zonal direction whereas fy stands for the flux in the meridional direction.

The correct average of the fine grid fluxes in the spherical coordinate system must take weighting functions into account that correspond to the areas of the surface patches. In particular, each position of a flux needs to be considered a cell center of a representative grid box around it. Then the boundary condition becomes

$$\begin{aligned} f^c\,A^c &= \sum_{i=1}^{n} f_i^r\,A_i^r \\ \Leftrightarrow f^c &= \frac{1}{A^c}\left[f_1^r\,A_1^r + f_2^r\,A_2^r\right] \end{aligned} \tag{3.18}$$

where the superscripts c and r stand for the coarse and refined grid, A represents the surface area and the sum adds all fluxes f along the interface. Here $n = 2$ fluxes need to be considered in the 2D setup. This flux update algorithm ensures mass conservation up to the last digit which is further documented in figure 4.11 on page 134 (Section 4.2). On the other hand, such an averaging procedure is not necessary for the scalar KE component. The coarse grid KE values can simply be replaced with the matching KE components on the fine grid.

CHAPTER IV

Reduced grid and static adaptations

Adaptive blocks are flexible tools that can be used for static and dynamic grid adaptations. Static adaptations are placed in user-defined regions of interest at the beginning of a forecast and are held fixed during the model run. Typical applications include static refinements in mountainous terrain or static refinements over selected geographical areas e.g. for weather prediction applications. Such an approach could replace today's nested grid configurations that employ regional high-resolution models with coarse grid forcing along the boundaries. Adaptive blocks can also be used to define a special type of grid, the so-called reduced grid. In a reduced grid, grid points are coarsened in longitudinal direction as the poles are approached. This effectively relaxes the strict time step restrictions in a regular latitude-longitude grid with $|CFL| < 1$ and, in addition, reduces the overall workload of the model by up to 20%. From a high level viewpoint, such a grid can be considered a statically adapted grid with 1D coarsenings.

In this chapter, the adaptive finite-volume shallow water model is used in two basic configurations, the reduced grid setup and the statically adapted setup with an underlying full grid. The discussion of the results starts with an introduction of suitable error measures and global invariants in Section 4.1. These measures are used throughout Chapter IV-V and provide important information on the accuracy and performance of the adaptive simulations. Section 4.2 is concentrated on the reduced grid design. In particular, two reduced grid configurations with one and two reduction levels are compared. Furthermore, Section 4.3 surveys more general static adaptation setups and raises new questions concerning adapted model simulations with external forcing functions.

4.1 Error measures and global diagnostics

Global error norms and global invariants, like the mass, energy or enstrophy, provide quantitative and objective measures for the performance of a model run. They are used extensively in the following chapters that describe the adaptive simulations with the finite-volume dynamical core. Here, an overview of the global measures is given, together with their continuous and discrete definitions (see also *Williamson et al.* [1992]).

4.1.1 Normalized error norms

The normalized l_1, l_2 and l_∞ error norms assess the horizontally integrated relative error of the model results. The error assessment requires the computation of the 2D global integral I of a variable $h(\lambda, \varphi)$ in spherical space

$$I(h) = \frac{1}{4\pi} \int_0^{2\pi} \int_{-\pi/2}^{\pi/2} h(\lambda, \varphi)\, \cos\varphi \, d\varphi \, d\lambda \,. \tag{4.1}$$

The discrete approximation to this integral in an adaptive model setup is then given by

$$I(h) = \frac{1}{A_{sphere}} \sum_{k=1}^{\#all\ cells} h_k \, A_k \tag{4.2}$$

where the sum adds up the weighted h values at all grid points covering the sphere. The weights, or more precisely the spherical surface patches, A_k of a rectangular cell centered at $k \rightarrow (i,j)$ are defined by

$$A_k = \int_{\lambda_{i-i/2}}^{\lambda_{i+1/2}} \int_{\varphi_{j-1/2}}^{\varphi_{j+1/2}} h\, a^2 \cos\varphi \, d\varphi \, d\lambda \tag{4.3}$$

$$\approx h_{i,j}\, a^2 \ \Delta\lambda_i \left(\sin(\varphi_{j+1/2}) - \sin(\varphi_{j-1/2})\right) \tag{4.4}$$

with a = Earth's radius and $\Delta\lambda_i = (\lambda_{i+1/2} - \lambda_{i-1/2})$. The half indices describe the coordinate positions of the cell edges and each k represents a unique pair (i,j). In addition, $A_{sphere} = 4\,\pi\, a^2$ is the surface area of the whole sphere. In the block-structured dynamical core, the sum over all cells (eqn. 4.2) is computed as three nested sums that cover all blocks

$$I(h) = \frac{1}{A_{sphere}} \sum_{n=1}^{\#blocks} \sum_{j=1}^{N_y} \sum_{i=1}^{N_x} h_{i,j,n}\, A_{i,j,n} \tag{4.5}$$

with N_x, N_y = number of longitudinal and meridional cells per block and n = block index. In a parallel computing setup, each processor then loops over its assigned blocks and computes a partial sum, which is collectively communicated over the network in order to determine the global value.

Using the discrete representation of I, the normalized (a) mean absolute error norm l_1, (b) root mean square error norm l_2 and (c) maximum absolute error norm l_∞ for a scalar quantity h are defined by

$$l_1(h) = \frac{I\left[|h(\lambda,\varphi) - h_T(\lambda,\varphi)|\right]}{I\left[|h_T(\lambda,\varphi)|\right]} \tag{4.6}$$

$$l_2(h) = \frac{\left(I\left[\left(h(\lambda,\varphi) - h_T(\lambda,\varphi)\right)^2\right]\right)^{\frac{1}{2}}}{\left(I\left[h_T(\lambda,\varphi)^2\right]\right)^{\frac{1}{2}}} \tag{4.7}$$

$$l_\infty(h) = \frac{\max_{all\ \lambda,\varphi} |h(\lambda,\varphi) - h_T(\lambda,\varphi)|}{\max_{all\ \lambda,\varphi} |h_T(\lambda,\varphi)|} \tag{4.8}$$

where h_T represents the true solution.

The corresponding error norms for a vector quantity $\vec{v} = (u, v)$ are given by

$$l_1(\vec{v}) = \frac{I\left[\left((u(\lambda,\varphi) - u_T(\lambda,\varphi))^2 + (v(\lambda,\varphi) - v_T(\lambda,\varphi))^2\right)^{\frac{1}{2}}\right]}{I\left[\left(u_T(\lambda,\varphi)^2 + v_T(\lambda,\varphi)^2\right)^{\frac{1}{2}}\right]} \tag{4.9}$$

$$l_2(\vec{v}) = \frac{\left(I\left[(u(\lambda,\varphi) - u_T(\lambda,\varphi))^2 + (v(\lambda,\varphi) - v_T(\lambda,\varphi))^2\right]\right)^{\frac{1}{2}}}{\left(I\left[u_T(\lambda,\varphi)^2 + v_T(\lambda,\varphi)^2\right]\right)^{\frac{1}{2}}} \tag{4.10}$$

$$l_\infty(\vec{v}) = \frac{\max_{all\ \lambda,\varphi}\left[\left((u(\lambda,\varphi) - u_T(\lambda,\varphi))^2 + (v(\lambda,\varphi) - v_T(\lambda,\varphi))^2\right)^{\frac{1}{2}}\right]}{\max_{all\ \lambda,\varphi}\left[\left(u_T(\lambda,\varphi)^2 + v_T(\lambda,\varphi)^2\right)^{\frac{1}{2}}\right]} \tag{4.11}$$

with the true wind speeds u_T and v_T. Here, a difficulty arises due to the grid staggering of the wind components in the finite-volume dynamical core. The error norms require that the u and v data are defined at the same grid point position. Therefore, the D-grid wind is linearly interpolated to the A-grid (cell center) position before the error norms are computed. This introduces an interpolation error, but tests with shallow water test 2 showed that this error is at least one order of magnitude smaller than the model errors.

In addition, the definitions of the normalized maximum and minimum of a scalar h are

$$h_{max} = \frac{\max_{all\ \lambda,\varphi} h(\lambda,\varphi) - \max_{all\ \lambda,\varphi} h_T(\lambda,\varphi)}{\Delta h} \tag{4.12}$$

$$h_{min} = \frac{\min_{all\ \lambda,\varphi} h(\lambda,\varphi) - \min_{all\ \lambda,\varphi} h_T(\lambda,\varphi)}{\Delta h} \tag{4.13}$$

where Δh is the difference between the maximum and minimum values of the true solution at the beginning of the forecast. These error measures are used for 2D advection experiments in the shallow water setup. For example h_{max} assesses the decrease in the peak amplitude of the transported feature.

4.1.2 Global invariants

Additional model assessments are based on normalized global invariants. The normalized integral $I_i(\xi(t))$ (notation as in *Williamson et al.* [1992]) is defined by

$$I_i(\xi(t)) = \frac{I[\xi(\lambda,\varphi,t)] - I[\xi(\lambda,\varphi,0)]}{I[\xi(\lambda,\varphi,0)]} \tag{4.14}$$

where the discrete integral is given as in equation 4.2. Here, the time-dependent variable ξ stands for e.g. the mass ($i = 1$) which is defined by the geopotential height $\xi = h$ in the shallow water system or the surface pressure $\xi = p_s$ in the 3D case. Alternatively, the total energy ($i = 2$) in the shallow water system can be assessed via

$$\xi = \frac{1}{2}\, h\, \vec{v}\cdot\vec{v} + \frac{1}{2}\, g\left((h+h_s)^2 - h_s^2\right) \tag{4.15}$$

and the potential enstrophy ($i = 3$) is given by

$$\xi = \frac{1}{2}\left(\zeta + f\right)^2 / \, h \tag{4.16}$$

where g is the gravitational acceleration, h_s denotes the height of the surface orography, ζ represents for the relative vorticity and f symbolizes the Coriolis parameter.

These global invariants are normalized with the integral at time step $t = 0$. As in Section 4.1.1 the wind data need to be interpolated to the cell center before the total energy can be evaluated. This interpolation error will be visible as an initial error in figure 4.10 on page 133.

4.1.3 Reference solutions

For the error measures, the model results need to be compared to a reference or "true" solution h_T, u_T and v_T. In case of the shallow water runs this solution is either an analytic solution (shallow water tests 1-4) or a high-resolution reference solution (test 5 and 6) computed with an NCAR spectral model at resolution T213. This resolution corresponds to approximately $50km$ in grid point space near the equator. The NCAR reference solution (see details in *Jakob et al.* [1993] and *Jakob-Chien et al.* [1995]) is provided in the form of spectral expansion coefficients using the portable NetCDF data format. The solution can then be evaluated in grid point space at arbitrary locations.

The analytic solutions for the test cases 1-4 can be directly calculated in any grid configuration, although test case 3 and 4 require the computation of integrals. These are approximated with a numerical method, in particular the trapezoidal rule. In addition, the reference solution for test case 1, the advection of a cosine bell, relies on an accurate estimate of the location of the cosine bell at any time. Since the advection can be specified with a rotation angle α this position (λ, φ) of the center is not obvious. It can either be assessed via coordinate transformations or with an iterative trajectory calculation. Here, the second option is chosen. The trajectory or path s of a parcel in the Cartesian system (see also *Holton* [1992])

$$\frac{D\,s}{D\,t} = V(x, y, t) \tag{4.17}$$

is then replaced with

$$\begin{aligned} \frac{D\,\varphi}{D\,t} &= \frac{v}{a} && (4.18) \\ \frac{D\,\lambda}{D\,t} &= \frac{u}{a\,\cos\varphi} && (4.19) \end{aligned}$$

in the spherical representation. This system is solved iteratively

$$\begin{aligned} \varphi^{n+1} &= \varphi^n + \frac{v(\lambda^n, \varphi^n)}{a}\,\Delta t && (4.20) \\ \lambda^{n+1} &= \lambda^n + \frac{u(\lambda^n, \varphi^n)}{a\,\cos\varphi^n}\,\Delta t && (4.21) \end{aligned}$$

with small time steps Δt starting at the initial location $(\lambda^0, \varphi^0) = (\lambda_c, \varphi_c)$. The velocities u and v are specified analytically (see *Williamson et al.* [1992])..

4.2 Reduced grid

“Reduced” or “skipped” grid setups have long been used in atmospheric general circulation modeling. The first reduced grid configurations for finite difference models were proposed by *Gates and Riegel* [1962], *Kurihara* [1965] and *Kurihara and Holloway* [1967]. The latter designed the so-called Kurihara grid with only four grid points next to the poles which offered a more homogeneous grid distribution from a physical standpoint. But when serious deficiencies of the Kurihara grid were discovered, which e.g. included an excessive pressure build-up in polar regions, more grid points in longitudinal direction needed to be added again to significantly improve the accuracy (see *Rao and Umscheid* [1969] and *Dey* [1969]). It was soon realized by *Shuman* [1970] and *Williamson and Browning* [1973] that reduced grid setups need to be carefully constructed for grid point models with finite difference approximations.

The difficulties arise due to the polar singularities in curvilinear coordinates that result in an extreme curvature of the inner circle of data. As a consequence, large truncation errors are present when longitudinal differences are taken over large longitudinal grid intervals. As shown in *Williamson and Browning* [1973] this is in particular true for terms containing the spherical vector components u and v whereas the approximation of terms with only scalar quantities, like the pressure or geopotential gradient, are not necessarily affected. It was concluded that very coarse longitudinal resolutions near the poles are not able to properly handle even the large-scale, small wavenumber features. *Shuman* [1970] in fact recommended that grid points should be added in high latitudes rather than dropped. As an alternative, derivatives could be calculated in Cartesian coordinates on cones locally tangent to each grid point. Similar findings were also reported by *Lanser et al.* [2000] and *Layton* [2002] for finite-volume approaches and cubic spline collocation methods, respectively.

In order to improve the accuracy of the zonal gradients in the immediate vicinity of the poles special treatments can be introduced as suggested by *Purser* [1988b]. *Purser* [1988b] pointed out that zonal derivatives can still be calculated with sufficient precision when high frequency information is interpolated through an assumption of smoothness from nearest neighbors in the polar region. The difficulties of the reduced grid setup can further be avoided when switching to a spectral model that does not need to calculate difference operators in grid point space. Instead, derivatives are evaluated in a spherical representation after applying Fourier and Legendre transforms. These so-called reduced Gaussian grids have been successfully used in spectral models for many years. Examples include *Hortal and Simmons* [1991], *Courtier and Naughton* [1994] and *Williamson and Rosinski* [2000] who developed reduced grids for weather and climate applications that are partly in operational use today. No significant loss of accuracy has been observed in comparison to full grid simulations.

4.2.1 Design of the reduced grid in the finite-volume dynamical core

Decreasing the number of grid points near the poles is attractive due to computational performance considerations. This is in particular true if the CFL condition in the polar regions limits the time step for the global domain.

In the finite-volume dynamical core, two new reduced grid designs have been tested that are based on the block-structured data layout. They are shown in figure 4.1 on the facing page which illustrates the reduced grid setups with one and two reduction levels projected onto the sphere. Here, the initial grid parameter set with 16x12 blocks and 9x6 cells per block is chosen as in table 3.2 on page 76 which

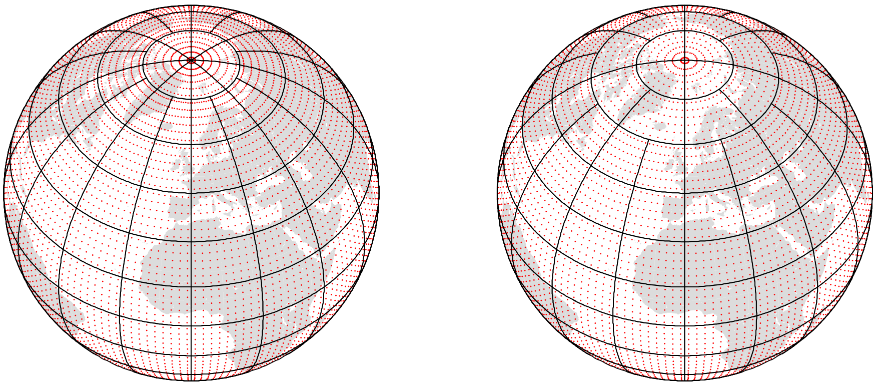

Figure 4.1: Distribution of blocks and grid points over the sphere (orthographic projection centered at 0E,45N). Reduced grid with 1 reduction (left) and 2 reductions (right) in the polar regions. Base resolution is 2.5° × 2.5°.

consequently places the reduction levels at 75° N/S and 60° N/S, respectively. At each transition point, the physical grid spacing in longitudinal direction then changes abruptly by a factor of 2 as depicted in figure 4.2. The figure also displays the underlying design principle that the physical distances at any latitude should not greatly exceed the maximum grid spacing at the equator. This condition is well-met by both designs, although a small overshoot at 75° N/S is present in case of 2 reductions.

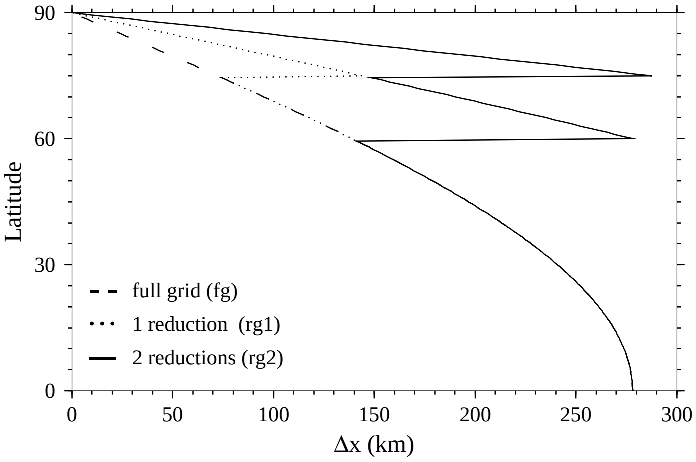

Figure 4.2: Physical grid distance (km) in longitudinal direction for the full grid and reduced grid setups.

The reduced grid setups can be convieniently chosen via input parameters at run time. The resulting number of blocks for the two designs is documented in table 4.1.

4.2.2 Advection tests

The reduced grid designs are tested with shallow water test case 1 (see also Appendix A.1) that describes the passive advection of a cosine bell once around the sphere. This test does not deal with the complete nonlinear shallow water equations but evaluates the advection algorithm in isolation. Here, the rotation angle $\alpha = 90°$ is chosen so that the feature is transported over the poles.

Three model runs with the base resolution $2.5° \times 2.5°$ have been performed. These include the full grid (fg) control run as well as the reduced grid (rg) simulations with 1 and 2 reduction levels. The numerical transport scheme used in the whole domain is the monotonicity-preserving PPM method. No filtering techniques need to be applied due to the absence of gravity wave motions in the advection experiment.

The error measures for the geopotential height field after one revolution of the cosine bell (day 12) are shown in table 4.1. In addition, the table contains information on timing data and the total number of time steps that are necessary for the completion of one revolution. The timing results represent the total CPU time for the simulations on a SUN Ultrix workstation. The time steps are severely limited by the CFL condition in the longitudinal direction at the circle next to the poles.

Base resol.	Refin. level	Reduced grid	Height error norms			Final h (m)	# Blocks	# Time steps	CPU time (s)
			l_1	l_2	l_∞				
$\alpha = 90°$									
2.5°	0	0	0.0965	0.0952	0.1285	853.5	192	7200	1202
2.5°	0	1	0.0927	0.0911	0.1264	855.5	176	3744	415
2.5°	0	2	0.0881	0.0889	0.1333	848.8	152	2016	205

Table 4.1: Error statistics for the cosine bell advection test over the poles (test case 1, $\alpha = 90°$) with two reduced grid configurations.

Here, CFL=0.95 is chosen for all model runs which results in time steps $\Delta t \approx 149\,s$ (fg), $\Delta \approx 297.5\,s$ (rg1) and $\Delta \approx 597\,s$ (rg2), respectively. Due to the increase in the length of the time step, a sharp decrease in the total number of integration steps is observed for the two reduced grid simulations. It is interesting to note that the reduction in integration steps leads to improved l_1 and l_2 error measures despite the use of the reduced grid. Though, this is not true for the l_∞ norm and the final amplitude that slightly degrades in case of 2 reduction levels. Here, the initial peak amplitude is $979.0\,m$. The error measures in table 4.1 compare favorably to similar advection experiments documented in the literature. In particular, *Rasch* [1994] performed the cosine bell advection test with a reduced grid design and comparable base resolution (2.8°). The error measures for Rasch's RG2.8 configuration with a monotonic upstream-biased transport scheme exceed the errors in table 4.1 by a factor of 1.5-2.

In comparison to the control run, both reduced grid simulations perform well which is further depicted in figure 4.3 on the next page. The figure shows 5 snapshots of the solution at day 1 through 5 mapped onto a North polar stereographic projection. Here, the cosine bell is transported over the North Pole (from the bottom to the top) in the reduced grid setups with one and two reduction levels. It can clearly be seen that the cosine bell crosses the pole without spatial distortions in both cases, although a very minor loss in peak amplitude is visible in the rg2 run. The full grid control run is almost indistinguishable from the rg1 case (not shown). This confirms the conclusion by *Williamson and Browning* [1973] that the reduced grid can be successfully employed for the transport of scalar quantities.

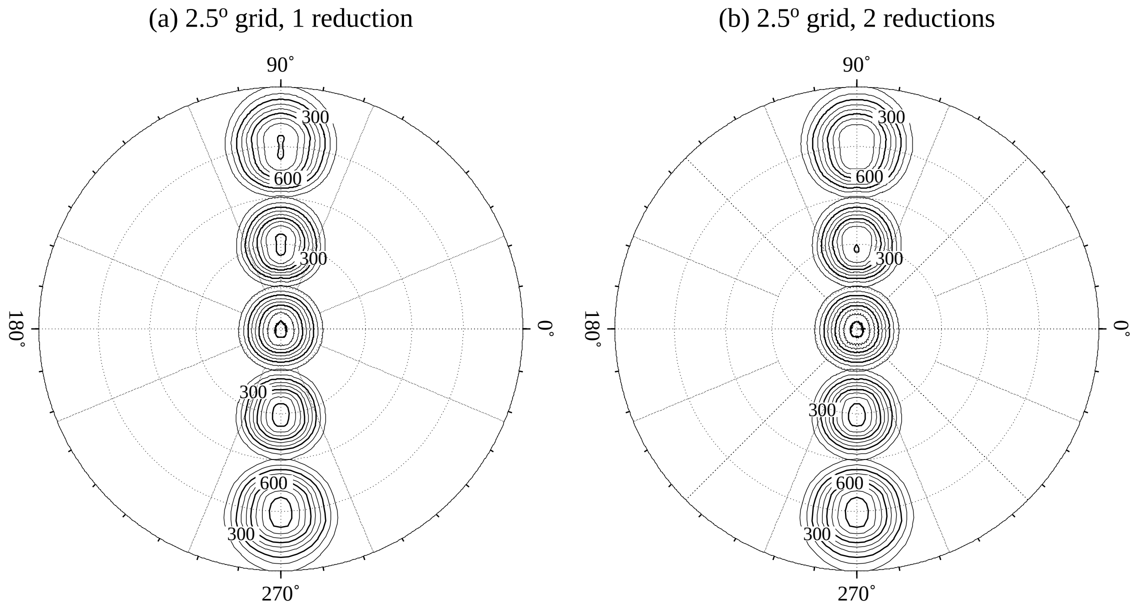

Figure 4.3: Polar stereographic projection of the cosine bell (test case 1, $\alpha = 90°$) transported over the North Pole (from the bottom to the top of the figure, the outer cricle is located at 15N). Snapshots are taken after 1, 2, 3, 4 and 5 days, respectively. Base resolution is $2.5° \times 2.5°$. Reduced grid runs with (a) 1 reduction, (b) 2 reductions. The block distribution is indicated by dotted lines. Contour intervals of the geopotential height field are 100 m.

4.2.3 Non-linear shallow water tests

In order to assess the performance of the reduced grid setups in the nonlinear shallow water system, three test scenarios are examined. These include the *McDonalds and Bates* [1989] test case as well as shallow water test 2 and 6 (see Appendix A).

First, the results of the control run and reduced grid simulations are evaluated qualitatively using the *McDonalds and Bates* [1989] test. This sometimes called dancing high-low wave test case comprises a flow straight over the poles, which is a particularly suitable test for the reduced grid assessments. The wind speeds at the poles are on the order of 10-15 m/s.

The results of the simulations in the Northern Hemisphere at day 10 are illustrated in figure 4.4 which displays the flow pattern of the fg control run (upper row), the rg1 simulation (middle row) and the rg2 setup (bottom row). Here, the geopotential height field and the wind components u and v (from left to right) are shown. The reduced grid simulations in this moderate wind speed regime are almost indistinguishable from the control run. There are no distortions in any of the large-scale flow patterns which are still well-resolved even in the rg2 case with only 36 grid points next to the poles.

Such a conclusion can only partly be drawn in the subsequent examples. The second test scenario is based on shallow water test 2 with chosen rotation angle $\alpha = 45°$. This steady state flow field (see also initial data in figures A.3 and A.4) is expected to remain unchanged during the course of the integration. It describes a strong flow over the poles with wind speeds on the order of $28\,m/s$ that accentuate possible errors in polar regions resulting from the reduced grid coarsenings. Both reduced grid setups have been tested in a 14-day simulation as documented by the

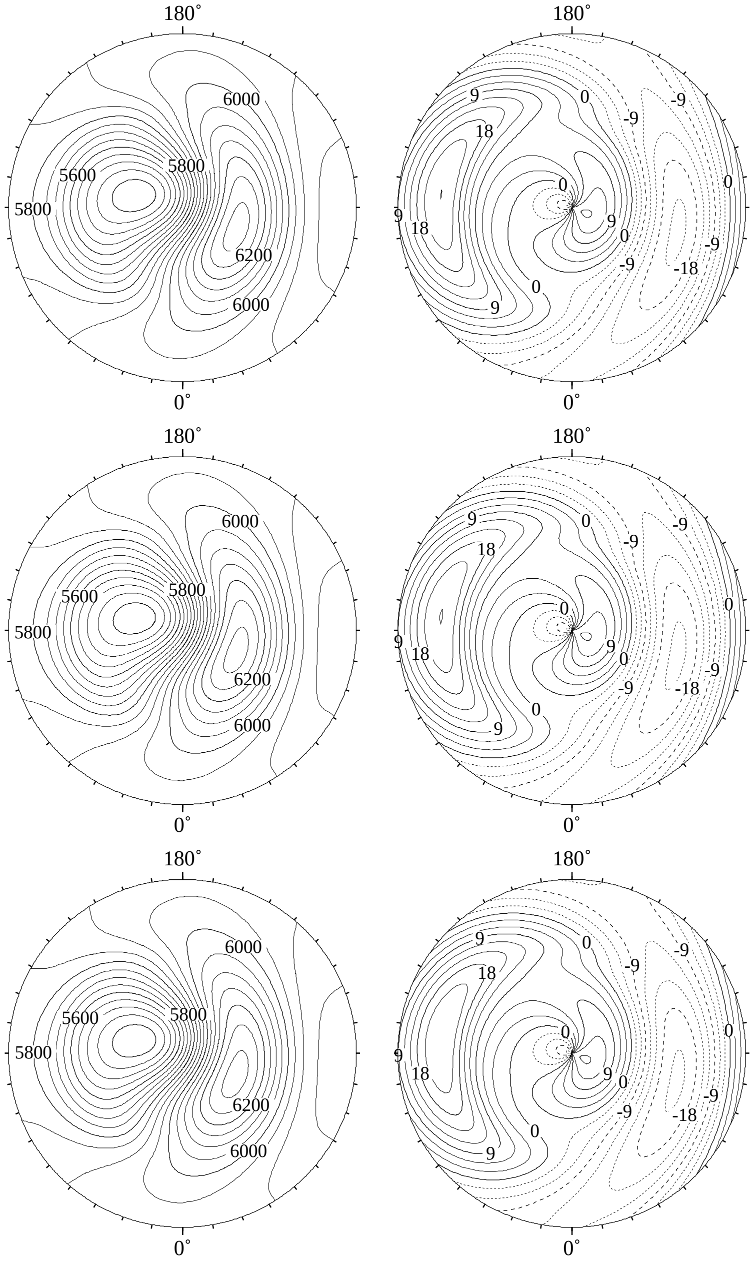

Figure 4.4: North polar stereographic projections of the geopotential height h, the zonal wind u and meridional wind v (from left to right) at day 10 (*McDonalds and Bates* [1989] test case). Contour intervals are 50 m, 3 ms^{-1} and 1.5 ms^{-1}, respectively. The base resolution is 2.5°. Top row: simulation with the full grid. Middle row: grid with 1 reduction at the poles. Bottom row: grid with 2 reductions in the polar regions.

zonal wind field at day 14 in figure 4.5. Although the flow patterns are very similar, a

(a) Reduced grid with 1 reduction (rg1)

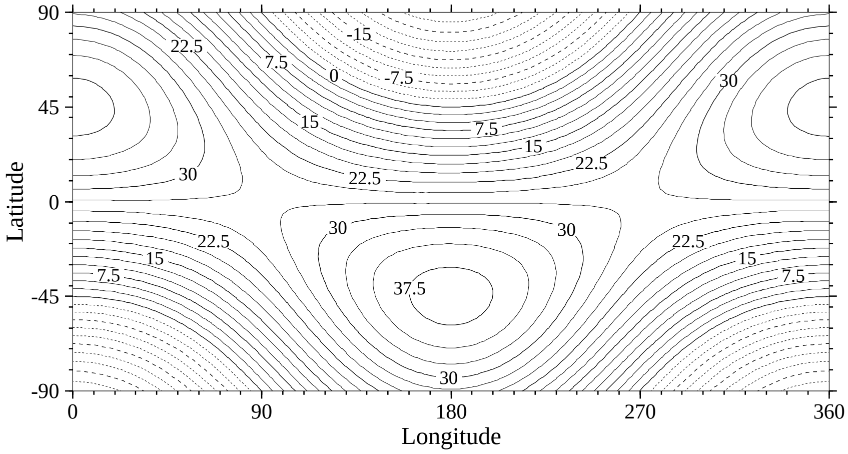

(b) Reduced grid with 2 reductions (rg2)

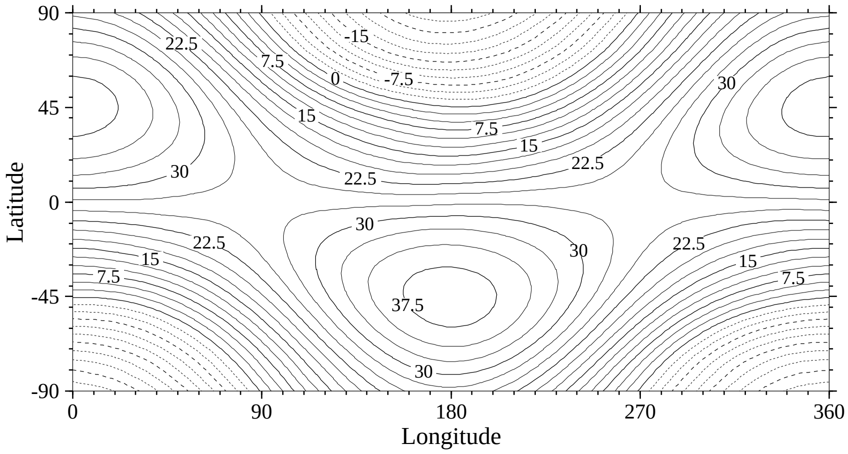

Figure 4.5: Zonal wind u at day 14 (test case 2, $\alpha = 45°$), (a) reduced grid simulation with 1 reduction, (b) with 2 reductions. Contour interval is 2.5 ms^{-1}.

close examination of the rg2 case reveals a slightly slanted distortion of the zonal wind field. This is confirmed in figure 4.6 which displays the differences of the zonal wind fields with the reference solution for both reduced grid setups. In case of 1 reduction level, a moderate error pattern in the zonal wind field can be observed, but errors increase considerably when adding a second reduction level. Here it is interesting to see that the errors of the reduced grid are concentrated but not confined to the polar

a) Reduced grid with 1 reduction (rg1)

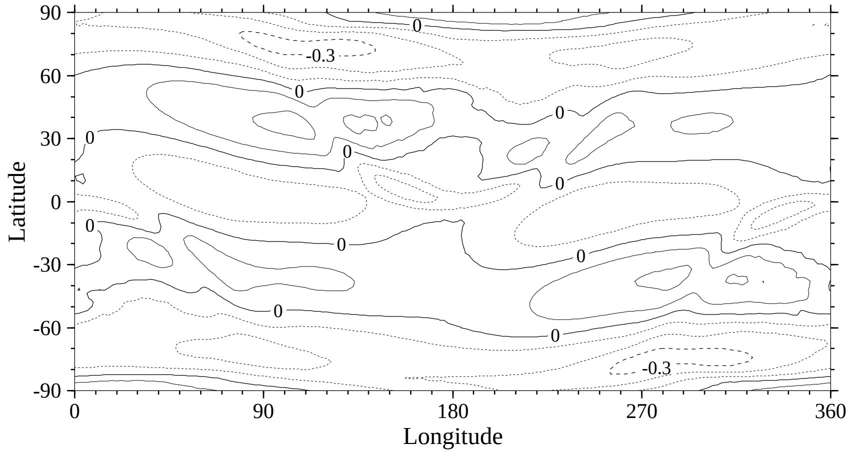

b) Reduced grid with 2 reductions (rg2)

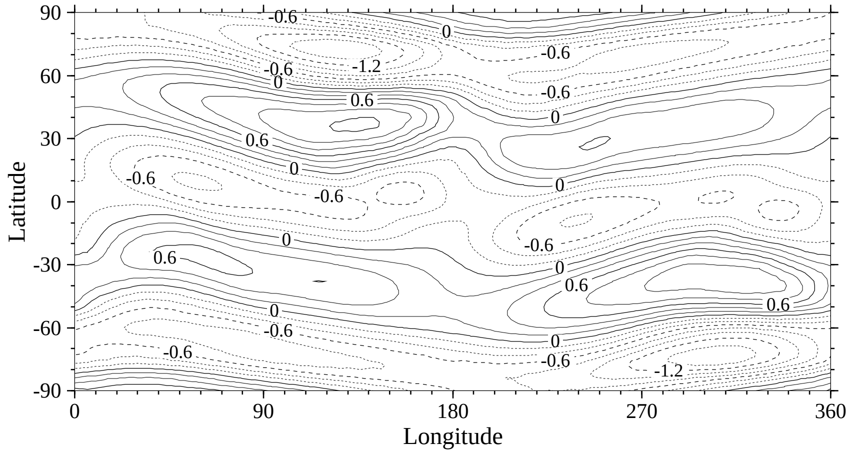

Figure 4.6: Zonal wind differences with reference solution at day 14 (test case 2, $\alpha = 45°$), (a) reduced grid simulation with 1 reduction, (b) with 2 reductions. Contour intervals are (a) 0.1 ms^{-1} and (b) 0.2 ms^{-1}.

regions. Instead, the errors propagate and interact with other model errors over time so that the whole domain is affected.

This qualitative assessment is further quantified in figure 4.7 which illustrates the corresponding l_2 height and wind error norms of the fg, rg1 and rg2 model runs. In addition, the plots assess the impact of the first- and second-order interpolation methods on the overall accuracy of the rg1 simulation. The temporal evolution of the normalized l_2 error norms confirms the significant increase in the solution error in case of the rg2 setup, whereas error levels remain low for one reduction step. For comparison, *Tolstykh* [2002] also reports comparable error measures with $l_2(h) = 4.3 \times 10^{-4}$ after 120 hours. In general, the error curves depict a linear increase in the solution error which is overlaid by inertio-gravity wave oscillations. The latter are damped out over time. In practice, the sharp rise in the error level for rg2 is no longer considered acceptable and therefore, the rg2 design can not be recommended for future nonlinear adaptive grid applications. As an aside, it is interesting to note that the order of the interpolation scheme at the reduced grid boundaries hardly

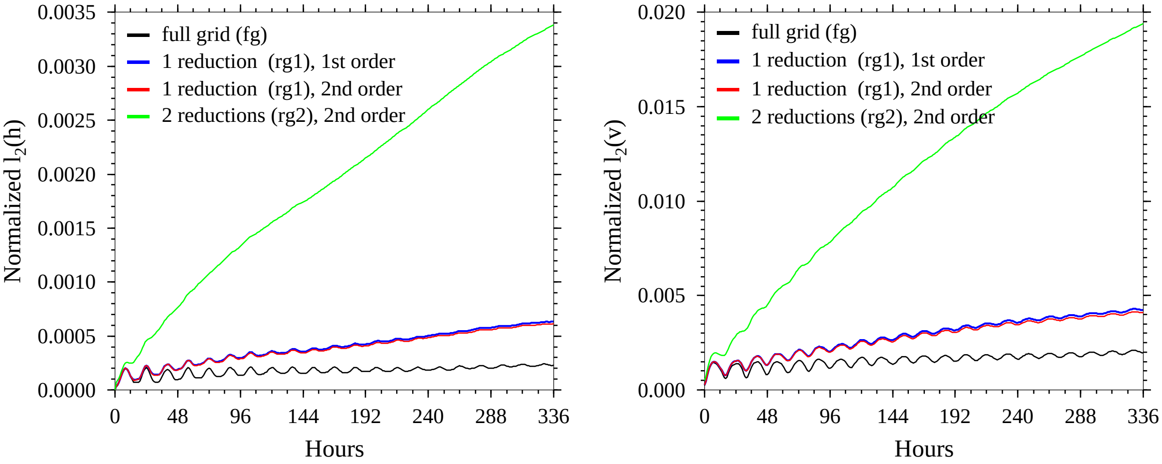

Figure 4.7: Normalized l_2 height errors (left) and l_2 wind errors (right) for the full grid (fg) and the reduced grids with 1 reduction (rg1) and 2 reductions (rg2). The order indicates the interpolation order at the reduced grid interfaces (test case 2, $\alpha = 45°$).

affects the error norms in the rg1 case. This is true for the idealized very smooth flow field selected here. But as shown in the next paragraph, such a conclusion does not generally hold when more complex flow patterns with strong gradients are simulated.

The third assessment of the reduced grid design is based on shallow water test 6 which comprises a Rossby-Haurwitz wave with wavenumber 4. The test translates the symmetric wave pattern without change of shape from west to east. Here, special attention is paid to the order of the interpolation scheme in a reduced grid setup that needs to be applied at the polar interfaces. This aspect is assessed in figure 4.8 on the next page that presents the geopotential height field at day 14 on a reduced grid with 1 reduction level. Two interpolation strategies are employed. In subfigure (a), the wind data are interpolated via bilinear interpolations whereas the first-order conservative van Leer approach is applied to the geopotential height field h. In subfigure (b), the second-order PPM interpolation method is used for all variables. The impact of the interpolation error in this high-wind speed regime is clearly visible. The low-order methods (subfigure (a)) introduce a slightly asymmetric flow pattern over time (see also discussion in Section 3.1.3 on page 76) whereas the more accurate second-order method can maintain the symmetry.

This effect is quantified in figure 4.9 on page 132 that reviews the performance of the reduced grid setups in comparison to the NCAR reference solution. Here it is interesting to see that the l_2 and l_∞ height errors in the rg1 design almost overlay the full grid control run until the errors split after day 11. The overall solution error is therefore hardly affected by one reduction step which is a considered a viable option for nonlinear runs. In contrast, the rg2 model simulation again shows unacceptable large errors and can not be recommended for future use. The superior performance

(a) rg1 with 1st order wind (bilinear) and height (van Leer) interpolation

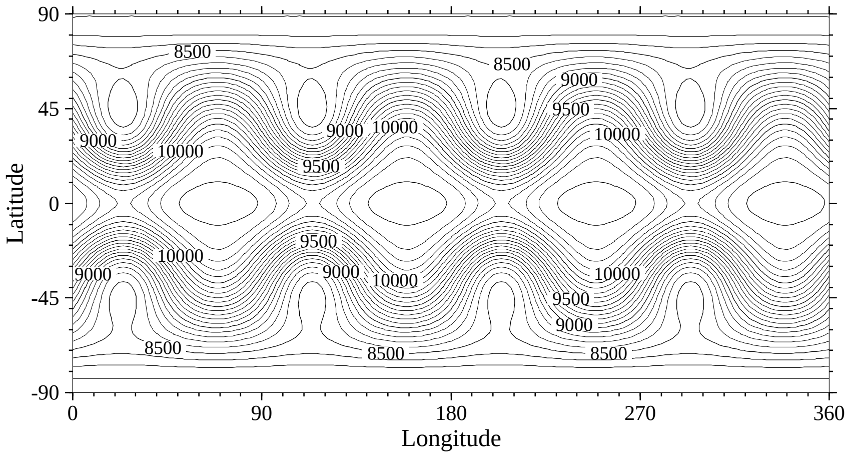

(b) rg1 with 2nd order wind and height (PPM) interpolation

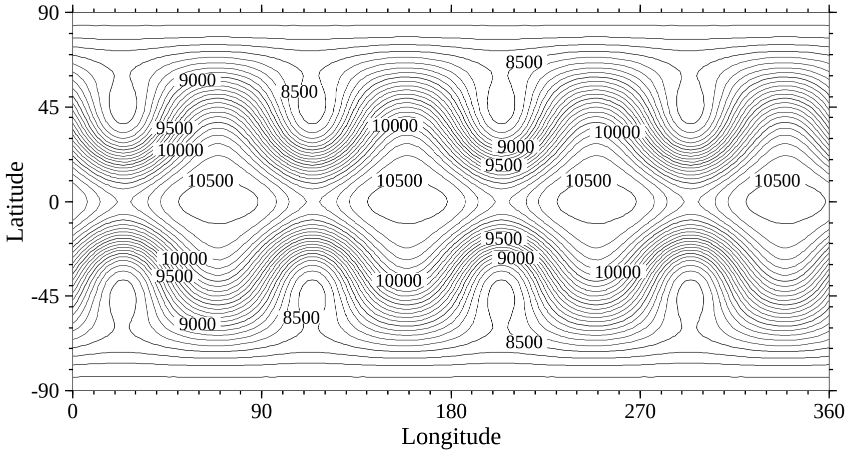

Figure 4.8: Geopotential height at day 14 (test case 6), reduced grid simulations with 1 reduction. (a) 1st order wind interpolation (bilinear) and 1st order height interpolation (conservative van Leer scheme), (b) 2nd order wind and conservative height interpolations (PPM method). Contour intervals are 100 m.

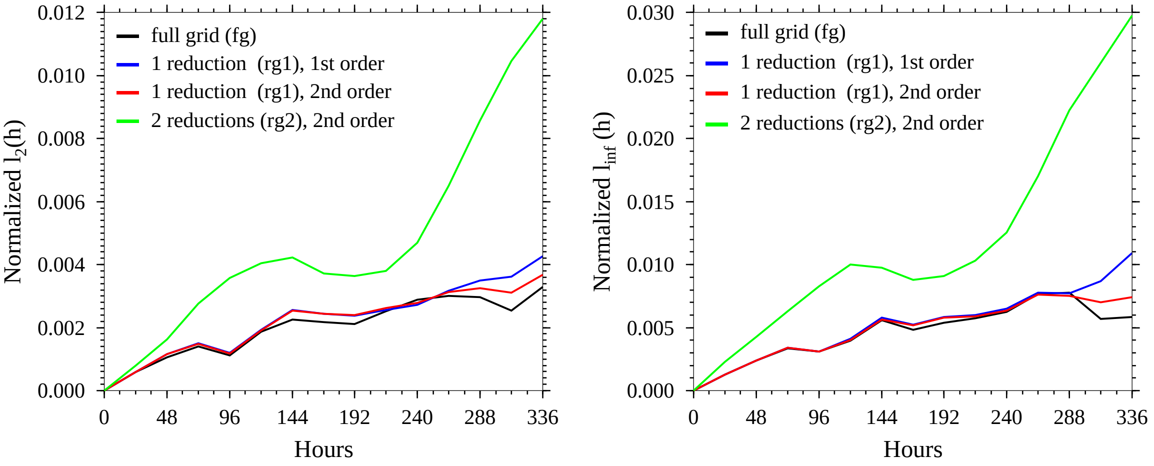

Figure 4.9: Normalized l_2 (left) and l_∞ (right) height errors for the full grid (fg) and the reduced grids with 1 reduction (rg1) and 2 reductions (rg2). The order indicates the interpolation order at the reduced grid interfaces (test case 6).

of the second-order interpolation scheme is clearly demonstrated at the end of the 14-day forecast when the l_2 and l_∞ norm still closely resemble the full grid control run. The l_2 height error in both the fg model run with $l_2(h) = 0.0033$ and the rg1 simulation with $l_2(h) = 0.0036$ at day 14 compare favorably to values published in the literature. These are listed for comparable resolutions in table 4.2. All model

Author	Model	Resolution	$l_2(h)$ at day 14
Jakob-Chien et al. [1995]	spectral	T42	0.0054
Taylor et al. [1997]	spectral elements	≈ 2.5°	0.0079
Spotz et al. [1998]	spectral	T42	0.0044
Spotz et al. [1998]	double Fourier method	T42	0.011
Cheong [2000]	double Fourier method	T42	0.0042
Tolstykh [2002]	finite differences	2.5°	0.0052
Layton and Spotz [2003]	double Fourier method	T42	≈ 0.02

Table 4.2: Error statistics for the Rossby Haurwitz test (test case 6) based on literature search.

runs are compared to the NCAR high-resolution reference solution. Here, it must be kept in mind that this reference solution is also not free of numerical errors as assessed in *Taylor et al.* [1997] and *Jakob-Chien et al.* [1995]. The uncertainty of the normalized l_2 norm is estimated to be 0.0008.

Besides error norms, it is also interesting to examine the impact of the grid reductions on global invariants. This is depicted in figure 4.10 which shows the time evolution of the normalized total energy and potential enstrophy for the fg, rg1 and rg2 model runs. Both quantities are not formally conserved in the finite-volume model. But the decrease in total energy (TE) and potential enstrophy in the fg and rg1 case is moderate in comparison to the rg2 simulation. The initial decrease in the normalized total energy at t=0 is an artifact of the staggered D-grid arrangement. It requires the interpolation of the wind data for the kinetic energy (KE) calculation which decreases the KE value on the order of 10^{-4}. This is the starting point of the TE curves.

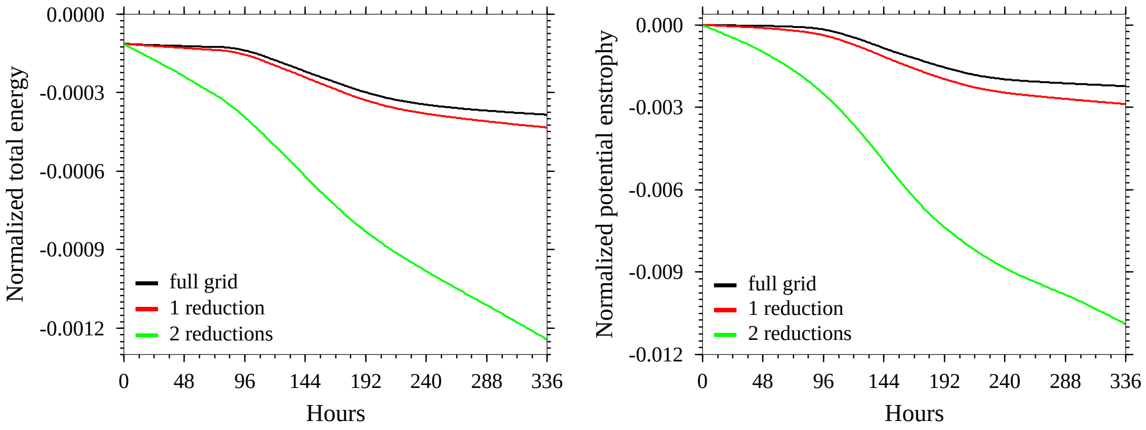

Figure 4.10: Normalized global integrals of total energy (left) and potential enstrophy (right) for the full grid and the reduced grids with 1 reduction and 2 reductions using second-order interpolations at the interfaces (test case 6).

In addition, tests have been performed that assess the conservation of mass in the reduced grid setup with 1 reduction level. This comparison is shown in figure 4.11 on the next page which compares the impact of the flux corrections at the reduced grid boundaries (see Section 3.3.3 on page 110) as well as filtering effects. As discussed in Section 2.2.2, filtering leads to a violation of conservation laws if no a-posterioi restoration mechanisms are applied. For example the filtering of the mass variable Φ violates the conservation of mass principle. It is important to observe that only the flux-corrected, unfiltered[1] simulation conserves the mass up to machine precision. The filter effect on the other hand leads to an increase in mass, whereas the omission of the flux correction at the interfaces tends to decrease the mass. Both effects overlay each other.

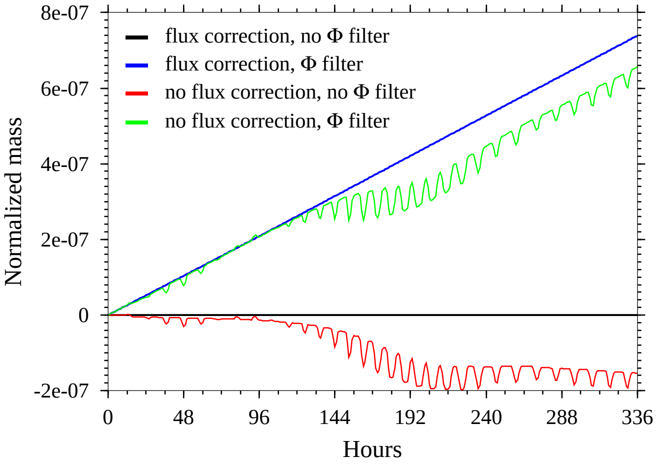

Figure 4.11: Normalized global integrals of the mass for reduced grid simulations with 1 reduction (test case 6). The different model setups include simulations with or without a flux corrected transport at the reduced grid interfaces and polar filtering of the geopotential polewards of 60° N/S, see figure for combinations.

Another aspect must be noted concerning the reduced grid setup in the finite-volume shallow water model. In test case 6 presented above, the time step $\Delta t = 360s$ can not be reduced in the two reduced grid simulations as seen before in the advection experiment. This is due to the fact that the time step in case 6 is not restricted by the

---

[1] Unfiltered with respect to the geopotential Φ, the wind components need to be filtered to maintain stability.

advection speed in polar regions, but by the gravity wave activity in midlatitudes. Coarsening the polar regions has therefore no impact on the stability criterion and identical time step must be used for all three simulations. This has far-reaching implications with respect to the performance of the model runs. The clear speedup of a reduced grid run in the advection experiment can no longer be achieved. On the contrary, choosing the rg1 reduced grid setup adds extra work at the reduced grid interfaces despite the 9% reduction in the number of blocks. When using 16x12 blocks with 9x6 cells per block, the full grid control run needs 1522 CPU seconds on a SUN Ultrix workstation for the 14-day simulation, whereas the rg1 run finishes after 1915 CPU seconds. As a result, the overhead estimate again yields (compare Section 3.2.3) $\frac{1522\,s}{192\,blocks}\Big/\frac{1915\,s}{176\,blocks} \approx 27\%$, which clearly outweighs the advantages of the reduced number of blocks in the rg1 case. Therefore, it is not recommended to use a reduced grid if the global time step is not limited by the CFL restrictions in polar regions. However, it may be possible that future optimizations of the AMR library and the user-provided interpolation routines will reduce the overhead significantly. In the present example, where no dynamic or static adaptations are requested, the most efficient simulation is indeed a uniform model run with big block sizes (see also performance discussion in Section 3.2.3). E.g. the setup with 2x2 blocks and 72x36 cells per block requires only 568 CPU seconds for the 14-day model run. As observed earlier, the large block sizes in the 2D framework lead to a speedup by a factor of approximately 2.5.

4.3 Static adaptations

Adaptive blocks can not only be used for reduced grid configurations but also for user-defined, pre-determined regions of interest that need to be resolved at fine resolutions. Typical examples include high resolution regions in mountainous terrain or grid adaptations for locally refined weather forecasts.

Static adaptations are chosen at the beginning of a model run and remain fixed during the simulation. They can be viewed as a two-way interactive nesting approach that provides consistent inflow and outflow conditions along the interfaces. The following section examines the impact of these high-resolution regions on the global domain. Three test scenarios are assessed in the shallow water framework.

First, steady state shallow water test case 2 with $\alpha = 45°$ is selected. Here, a high resolution refinement area at refinement level 2 is placed in the Northern Hemisphere as illustrated in figure 4.12. The figure shows the geopotential height field with overlaid blocks (in red) at model day 14. The base resolution in this example is a $2.5° \times 2.5°$ grid so that the finest resolution represents a $0.625°$ grid spacing. It

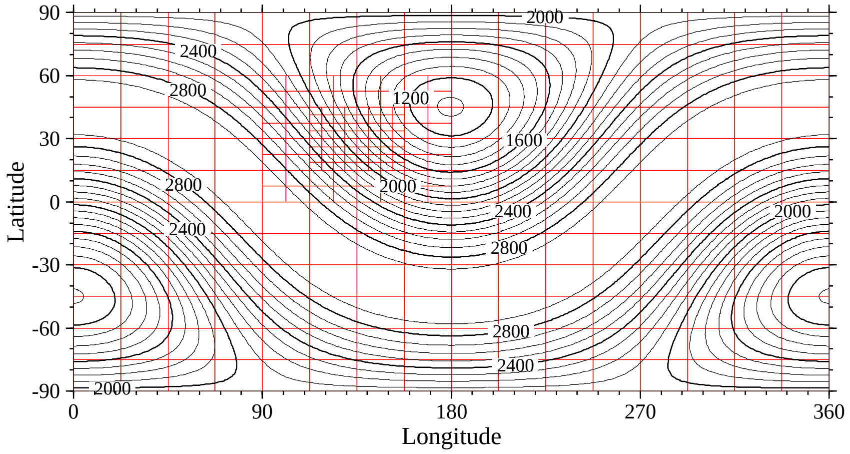

Figure 4.12: Geopotential height at day 14 (test case 2, $\alpha = 45°$) with static refinements (refinement level 2) centered at 135E,30N. The distribution of the blocks is drawn in red. Base resolution is 2.5°, contour interval is 100 m.

can be seen that the flow passes through the refined area without noise and almost no distortions, despite the fact that the refinements are purposely placed in a region with strong geopotential gradients. As discussed later this has measurable impact on the simulation results in comparison to low gradient regimes. A closer examination of the wind components u and v at day 14 in figure 4.13 reveals that only very minor errors are induced at the coarse-fine grid interfaces. The errors are mostly visible in the v field at the outflow boundary east of the refined area.

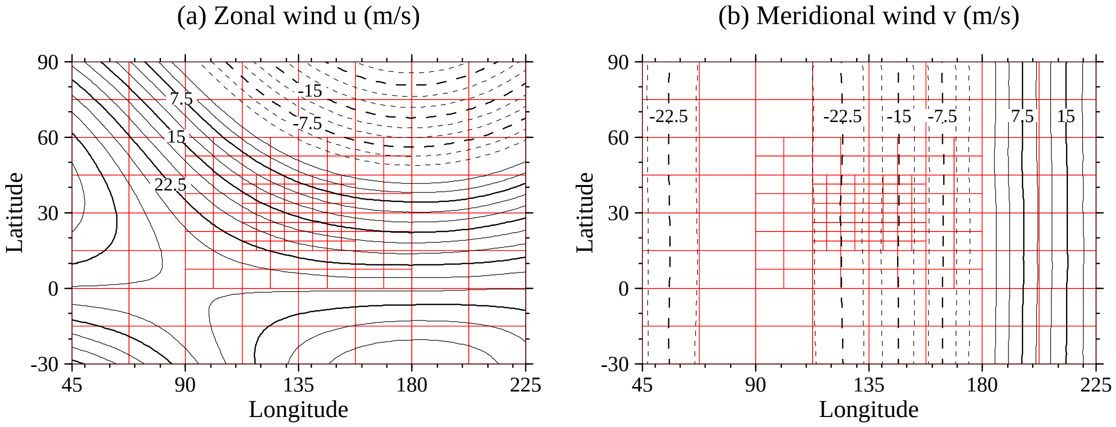
(a) Zonal wind u (m/s)

(b) Meridional wind v (m/s)

Figure 4.13: (a) Zonal and (b) meridional wind at day 14 (test case 2, $\alpha = 45°$) with static refinements (refinement level 2). The distribution of the blocks is drawn in red. Base resolution is 2.5°, contour intervals are 2.5 ms^{-1}.

In order to quantify the performance of such a refined model run, the corresponding height error norms are displayed in figure 4.14 on the next page. The plot shows the time evolution of the normalized l_2 norm in three model runs, the full grid control run at the base resolution and two statically adapted runs, where the center of the refined patch is placed at two different locations. The first location $135°E, 30°N$ coincides with the previous example, whereas the second position at $180°E, 45°N$ symmetrically refines the low pressure center in the Northern Hemisphere (not shown). This region is characterized by lower geopotential gradients which lead to improved l_2 error norm statistics. The error in the first anti-symmetric

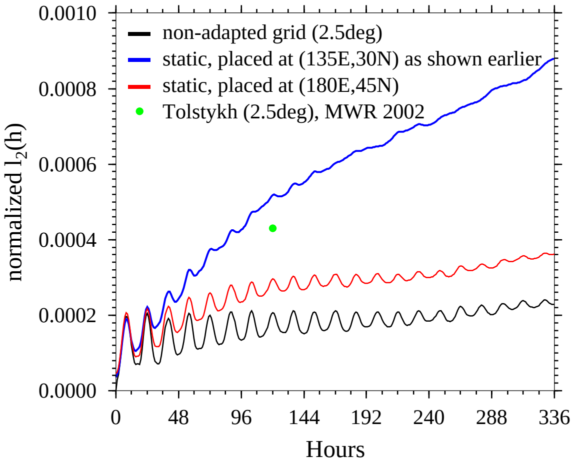

Figure 4.14: Normalized l_2 height errors (test case 2, $\alpha = 45°$) for a non-adapted run (2.5° resolution) and 2 statically adapted runs with 2 refinement levels.

case is slightly enhanced but still well within the expected error margins for this test case. This is shown by a comparison with Tolstykh's results.

There are two possible sources for the increased errors in the statically adapted runs. First, it must be noted that the initial data in the adapted patches are interpolated via quadratic interpolations at the beginning of the forecast. This introduces an interpolation error in comparison to an analytically reinitialized field that obeys the underlying geostrophic balance more accurately. Especially at refinement level 2, the initial conditions are then interpolated based on the already interpolated data at refinement level 1. Second, the interpolations of the ghost cells at fine-coarse grid interfaces take place multiple times per time step during the course of the integration. Since the accuracy of the fluxes across interfaces relies on ghost cell information, an interpolation error in the ghost cell update becomes transparent in the flux calculation.

In order to asses the relative importance of the two error sources, tests with analytically reinitialized initial conditions have been performed. The results of this run (not shown) are almost indistinguishable from the run with interpolated initial data. For this idealized smooth scenario, it can therefore be concluded that the errors in the initial data are not responsible for the resulting higher error norms. The error is clearly dominated by the inaccuracies of the ghost cells and fluxes at the interfaces. In general, these errors do not accumulate along the edges of the blocks but rather interact with the truncation error of the numerical scheme. It has also been observed that errors are higher in regions where the monotonicity constraint is applied, especially in the neighborhood of maxima and minima of the geopotential.

Furthermore, it is also interesting to note that the l_2 error trends are again overlaid by typical inertio-gravity wave oscillations (compare also to figure 4.7). These are due to the geostrophic adjustment process that describes the mutual adaptation of mass and momentum toward a steady geostrophic state. Here the period is on the order of 16 hours which is very close to the period of pure inertial oscillations in midlatitudes. For example, at 45° N/S inertial oscillation are characterized by a period of $\frac{2\pi}{|f|} = \frac{12h}{|\sin 45°|} = 16.97h$ (*Holton* [1992]). Inertio-gravity waves are generated by small deviations from the geostrophic balance in the discrete system. The final state is achieved by the decaying inertial oscillations that dissipate the energy. The wave motion is clearly emphasized in this idealized test setup. In the real atmosphere though, the motions are predominantly generated and maintained by the pressure gradient force. Therefore the conditions for purely inertial oscillations only rarely exist.

High wind speed regimes

The second assessment of the static adaptations is based on shallow water test 6, the Rossby-Haurwitz wave with extremely strong gradients in both the geopotential and wind fields. This test is very hard for adaptive grid simulations due not only to the gradients but also to the preferred 45° transport angle in midlatitudes. This is the worst case scenario for the selected numerical scheme with an underlying operator splitting approach (as discussed later in Section 5.2.1 on page 157). Any minor error will be accentuated. Static refinements at refinement level 1 are placed at eight pre-determined regions of interest. These are indicated in red in figure 4.15 that shows the geopotential height field at day 7. Although the flow is well-simulated in comparison to the reference solution (figure A.13 on page 235), it can clearly be seen that a slightly asymmetric flow pattern evolves in the two hemispheres. This effect can be related to the refined patches (compare also to asymmetric flux discussion in Section 3.1.3). As time progresses, the flow pattern diverges further from the reference solution which is indicated by the error norms in figure 4.16. This plot also includes the final error levels observed in the reduced grid simulations. The errors are acceptable for a 7-10 day time period which represents the typical duration of a weather prediction forecast. For long term climate simulations though, the interface

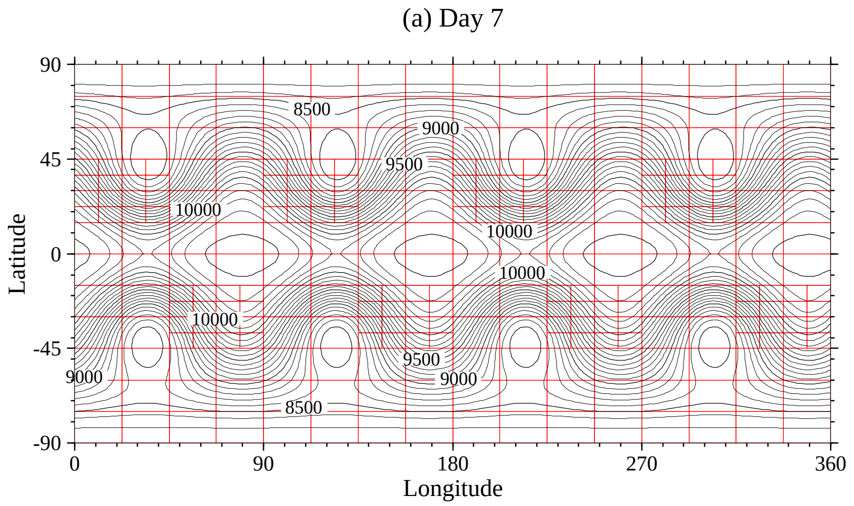

Figure 4.15: Geopotential height at day 7 with statically refined blocks. (refinement level 1) and second-order interpolations at the interfaces (test case 6). The block distribution is indicated in red. The base resolution is 2.5°, in refined regions 1.25°. Contour intervals are 100 m/s.

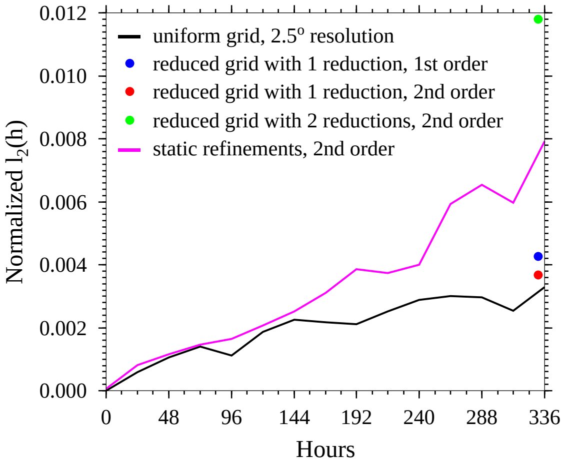

Figure 4.16: Normalized l_2 height errors for the non-adapted run (2.5° resolution) and statically adapted run with 1 refinement level (test case 6). The additional data points show the error norms of reduced grid simulations and are taken from figure 4.9.

treatment must be very carefully examined. True overlap regions as in *Brown et al.* [2003] can possibly be introduced to enhance the accuracy.

Forced nonlinear system with translating low

The third assessment of the statically adapted shallow water model increases the complexity of the test scenario even further. It is based on shallow water test 4 that describes a forced nonlinear system with an embedded translating low pressure center. For this test the shallow water equations need to be modified. In particular, time and grid resolution dependent forcing functions are added to the right hand side of the equations (details in *Williamson et al.* [1992]). This forcing then leads to a translation of the system from west to east without change of shape. From a higher level viewpoint, such a forcing can also be considered a forcing mechanism provided by physics routines in a complete GCM. The test therefore assesses an important aspect concerning future adaptive climate or weather prediction models.

Static adaptations are used to refine the pre-determined cyclone path. A similar approach has also been used by *Fournier et al.* [2004] who used the a-priori knowledge for a statically adapted spectral element model with rather smoothly varying resolution changes. The initial setup in the finite-volume model is displayed in figure 4.17 which shows the geopotential height field with overlaid adapted blocks (in red) at refinement level 1. In contrast to the other simulations discussed so far, a different initial block parameter set is chosen. Here, 10x5 blocks with 18x18 cells per block are selected that define a 2° × 2° base resolution. In addition, a coarser 4° × 4° base resolution with 9x9 cells per block has also been assessed. All resolutions are listed in table 4.3 on page 146.

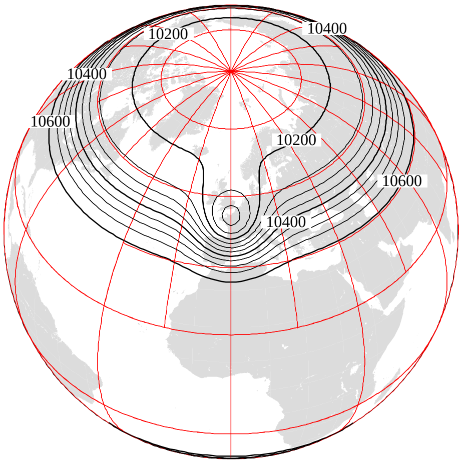

Figure 4.17: Initial geopotential height and static adaptations with 1 refinement level (test case 4) plotted on an orthographic projection centered at (0E,45N). The blocks are drawn in red. Base resolution is 2°, in refined areas 1°. Contour interval is 50 m.

It is important to note that the addition of the grid size dependent forcing functions can cause numerical instabilities in an adapted run, especially at the interface boundaries. This has been discussed by *Berger and LeVeque* [1998] who observed that source terms can generate excessive noise at the interfaces which ultimately contaminate the whole solution. Therefore, the source terms need to be handled with care. For example, *Berger and LeVeque* [1998] applied a fractional step method or the so-called splitting approach. In this approach, the solution is first computed without source terms which are then reintroduced during a second sweep. Such an approach has also been applied here.

Nevertheless, some noise still develops at the interfaces. This poses new research questions for future adaptive GCMs that also need to compute local forcings with grid size dependent data. The difficulties can primarily be detected at grid boundaries as shown later. Here, the following strategy is employed. In order to minimize the noise at the interfaces and in the refined regions the data are reinitialized analytically. In particular, this smoothes the initial height field, whereas the wind data can also be determined via interpolations without detrimental effects.

During each time step, the forcing then needs to be calculated twice. First, the forcing is evaluated for half a time step in order to compute the time-centered wind speeds at the staggered C-grid positions. Second, the forcing is recalculated for the full time step to represent the time-averaged cell-averaged data for the prognostic D-grid variables. This 2-step algorithmic Lin-Rood approach causes slight inconsistencies with respect to the latter forcing functions. The analytically and numerically evaluated forcing expressions are based on grid point data at discrete time steps that only approximate the true volume-mean time-mean representation. Here the best estimate of the time-mean forcing on the D-grid involves calculating the spatial derivatives of the forcing functions at the time-centered step $t^{n+\frac{1}{2}}$. On the other hand the forcing of the C grid winds uses spatial derivatives at t^n. This mixed technique has led to the most accurate and stable simulations. However, the still existing inconsistencies of the forcing in the finite-volume sense clearly lead to increased error measures in comparison to literature values (e.g. *Taylor et al.* [1997]). Alternatively, the forcing could also be computed in a purely analytic way, e.g. with the help of

Mathematica as suggested by *Heikes and Randall* [1995]. This approach enhances the accuracy of the spatial representation but does not offer a better time-averaged estimate. Therefore, this option is not considered here. The present formulation already gives sufficient insight into the performance of the adaptive simulation with forcing constraints.

The comparison of a fine grid 1° control run with a statically adapted 2° run at refinement level 1 is shown in figure 4.18 on the next page. The subfigures (a,c) depict the geopotential height field at day 5 in an orthographic projection centered at the position of the low. Additionally, subfigures (b,d) display the differences with the analytic solution. Both runs develop model errors that are partly attributable to the phase error between the numerical and analytical solutions. In particular, the low pressure system is not moved fast enough in the control run as also seen by *Heikes and Randall* [1995]. In addition, the introduction of the static adaptation leads to a different error pattern that is spread out over a large domain. A closer examination reveals that most of the errors are generated at the static grid boundaries. These interface errors then interact with the solution error of the transported feature.

The model errors are quantified in figure 4.19 on page 146 which compares a collection of adapted and non-adapted model runs (see also summary in table 4.3). Here, the time evolution of the l_2 and l_∞ height errors for the 5-day simulations are displayed. As suggested by *Williamson et al.* [1992], the mean zonal background flow is subtracted from the fields which emphasizes the errors associated with the low pressure system. It is interesting to observe that the l_∞ errors decrease continuously with increasing resolution. The adapted runs closely resemble the uniform runs with respect to this error measure. Here, the l_∞ norm represents the maximum error of the transported feature which can be found close to the center of the low pressure

(a) 1^{o} uniform resolution (b) Difference with analytic solution

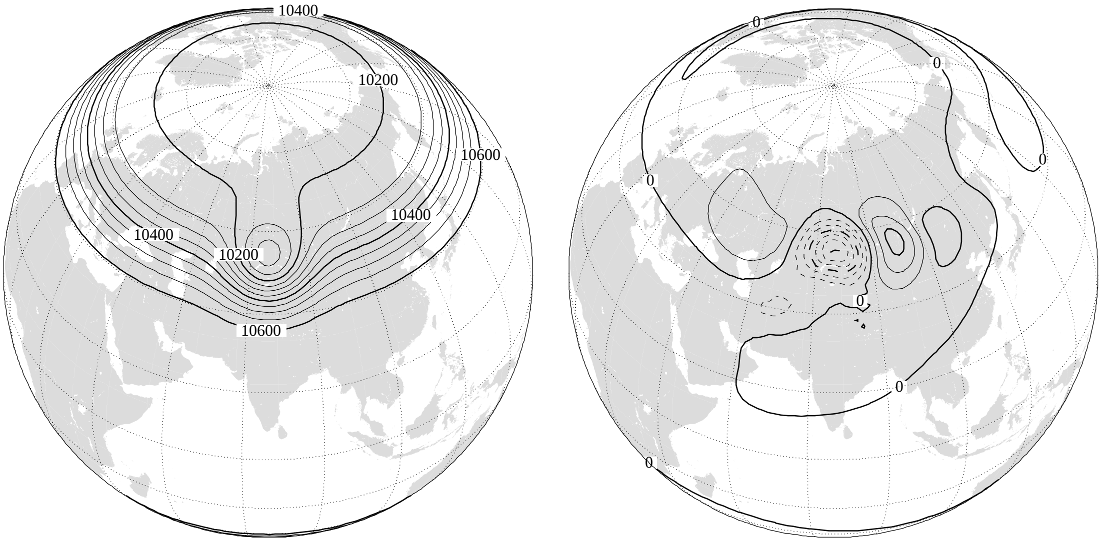

(c) 2^{o} resolution with static refinements (1^{o}) (d) Difference with analytic solution

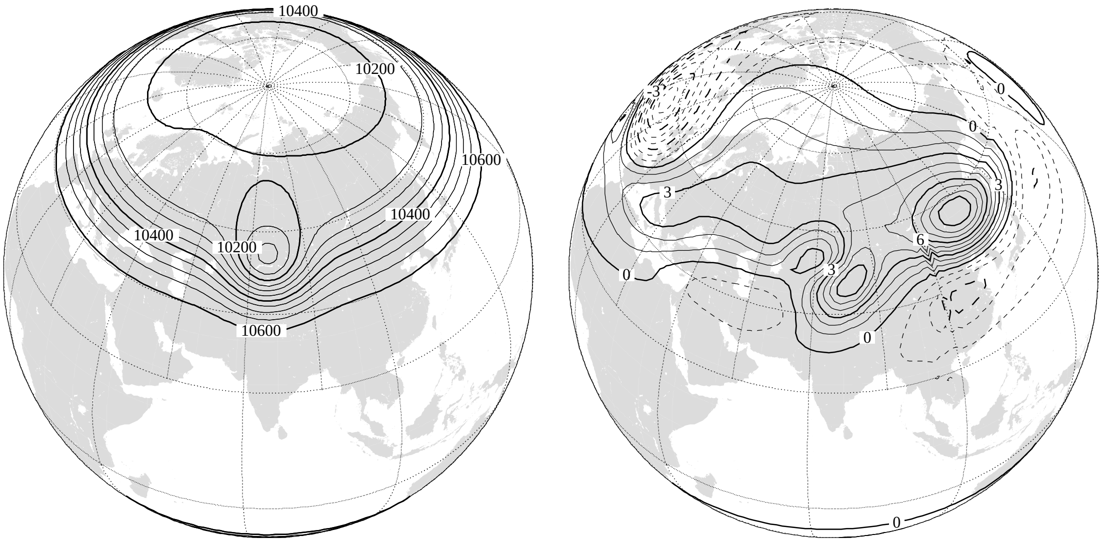

Figure 4.18: Geopotential height (a,c) and height errors (b,d) at day 5 (test case 4) plotted on an orthographic projection centered at 45N and the longitude of the trough 77.7E. The top row (a,b) shows the non-adapted run with a uniform 1° resolution, the bottom row (c,d) shows a statically adapted run (base resolution 2°) with 1 refinement level. The block distribution is indicated by the dotted lines. Contour intervals are 50 m (a,c) and 1 m (b,d).

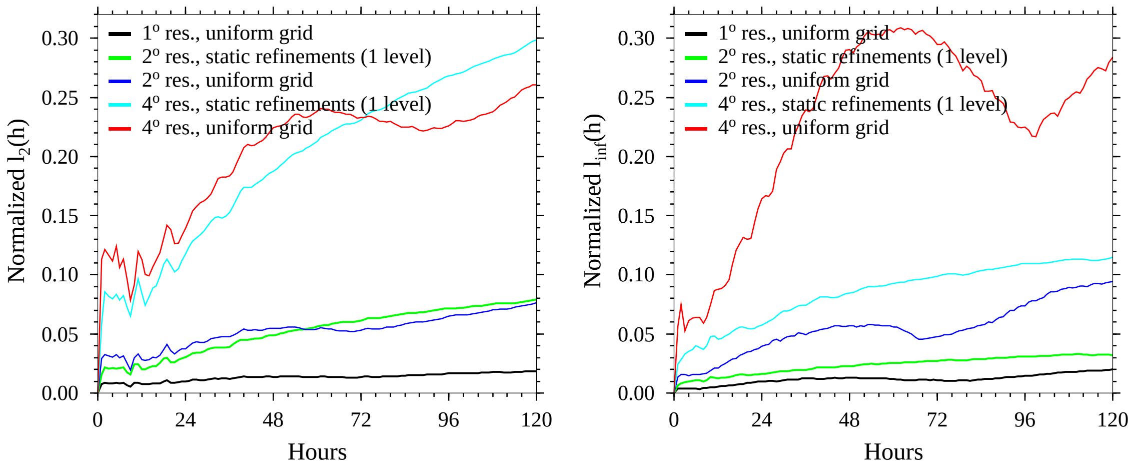

Figure 4.19: Normalized l_2 (left) and l_∞ (right) height error norms for the adapted and non-adapted model runs at different resolutions (test case 4).

trough. This can not be concluded for the l_2 error norms. The l_2 error assesses the error in the whole model domain and clearly identifies the additional noise at the interfaces. This prevents the characteristic converging trend in the adaptive grid simulation. All error statistics, including the corresponding wind errors, at day 5 are summarized in table 4.3. Despite the noise at the interfaces, the transport of the low pressure system improves significantly in the statically adapted runs without the need of a fine resolution in the global domain.

Base resolution	Refin. level	Equivalent resolution	Time step (s)	Normalized error norms after 5 days			
				$l_2(h)$	$l_2(v)$	$l_\infty(h)$	$l_\infty(v)$
4°	0	4°	600	0.2609	0.2397	0.2838	0.3869
4°	1	2°	300	0.2988	0.2114	0.1146	0.1806
2°	0	2°	300	0.0763	0.0771	0.0941	0.1159
2°	1	1°	150	0.0789	0.0605	0.0322	0.0388
1°	0	1°	150	0.0186	0.0203	0.0202	0.0268

Table 4.3: Error measures and statistics for test case 4 after five model days.

CHAPTER V

Adaptation criteria and 2D dynamic adaptations

Adaptive blocks have long been used for dynamic grid adaptations that can track features of interest during a model run. Examples include the pioneering work of *Berger and Oliger* [1984] which was applied to atmospheric science questions by *Skamarock et al.* [1989] and other investigators (see Section 1.3). Adaptive blocks offer the advantages of regular data structures that allow the use of a single solution technique in all adapted patches. Then the flow can be independently solved on a block-by-block basis, which is in particular true for the self-similar block approach used here.

In this chapter, the dynamically adaptive finite-volume model is assessed in the 2D shallow water framework. The discussion starts with an introduction to suitable adaptation criteria which are reviewed in Section 5.1. Here a variety of adaptation indicators are suggested that are based on flow characteristics. The results of the dynamically adapted shallow water runs are then examined in Section 5.2. These simulations are presented in an increasing order of complexity. First, the adaptive passive advection test is shown with and without an additional reduced grid setup (Sections 5.2.1 and 5.2.2). Second, the adaptive nonlinear shallow water system is assessed using an idealized flow over a single mountain (Section 5.2.3). This test combines statically and dynamically adaptive grid approaches and serves as a testbed for different refinement criteria.

5.1 Adaptation criteria

Setting the right criteria for grid refinements and coarsenings is very important due to the significant cost associated with adaptations. The ideal criteria are those that require minimum computational efforts to evaluate and still indicate the refinement and coarsening regions reliably. Two basic adaptation principles need to be distinguished, namely, the "physical" flow based adaptation indicators and the local truncation error estimators. The latter are built upon a purely numerical idea since they limit the global solution or local discretization error of the numerical scheme. This technique was for example used by *Berger and Oliger* [1984] and further assessed by *Skamarock* [1989] and *Skamarock and Klemp* [1993]. Here Richardson-type truncation error estimators were applied that are based on the difference of the numerical solution on fine and coarse overlapping meshes. Regions with high truncation errors get then refined by comparison to user-defined tolerances. In general, numerical error estimation techniques can be further classified as "a-priori" or "a-posteriori" methods. The a-priori schemes predict the numerical errors prior to the actual time step, whereas the a-posteriori estimates are based on results obtained during the prior run. Such an a-posteriori approach is most commonly selected if adaptations are to be guided by the numerical errors (see also *Verfürt* [1993] for an overview of error estimators).

In practice though, flow-based adaptation criteria are predominantly used in adaptive CFD applications. They typically rely on measures of a solution gradient or curvature that are compared to user-defined and problem-dependent thresholds.

In addition, assessments of the vorticity, potential vorticity, divergence or instability indicators like the Richardson number are feasible options for atmospheric AMR applications. Today, gradient-based adaptation criteria are most commonly applied to atmospheric transport problems, e.g. by *Behrens* [1996] who developed an adaptive passive semi-Lagrangian advection algorithm. Here the adaptations are based on a simple two-dimensional assessment of the local gradient of a tracer component. Such an indicator works well for pure passive advection scenarios as also shown by *Hubbard and Nikiforakis* [2003]. The grid is refined in regions with sharp gradients and coarsenings are applied in areas where the gradient lies under a specified threshold. In general, a gradient-based indicator is scale-dependent.

Similar gradient-based criteria are also popular in CFD applications where shock waves and discontinuities dominate the flow (*Hansen et al.* [2002]). But atmospheric flows, and here in particular hydrostatically approximated climate and weather prediction models, are mainly characterized by smoothly varying large-scale motions. In the absence of real discontinuities, the features of interest are less well-defined. This is especially true for long-term climate studies that typically assess time-mean spatially averaged climatic states. Nevertheless, scale contradictions with sharp gradients do frequently occur in geophysical flows as the result of stretching and shearing deformation by the velocity field. Therefore, the features of interest could be associated with the atmospheric wave patterns and their resulting vorticity distributions and temperature fronts. Such flow-based adaptation criteria are in particular suitable for short-term weather predictions runs. In general, adaptations are problem-dependent and specifically tailored indicators need to be examined for different flow scenarios. An 'optimal' criterion then captures the evolving features early in the developing stages and tracks their evolution and decay reliably. Such an ideal adaptation indicator might possibly combine numerical truncation error information and the physical flow characteristics. Both refinement strategies were compared by *Kessler* [1999] when developing a two-dimensional, adaptive finite element advection scheme for tracer transports. It was found that the gradient indicator tended to track sharp, single concentration peaks more closely, whereas the numerical residual estimator recognized multiple smooth concentration peaks and their transition regions effectively. Overall, both error indicators captured the emergence of a plume in an idealized test problem satisfactorily, but the gradient indicator maintained a more accurate tracer mass distribution.

5.1.1 Flow-based criteria

What are the flow features of interest in a weather prediction or climate run? This is the basic question that determines the subsequent adaptive refinement and coarsening strategy based on purely flow-based characteristics. In general, the criterion must be well-suited to the research problem and numerous decisions need to be made. For example, the aspects to be considered include the choice of the vertical level at which a refinement criterion is evaluated as well as the selection of one or more primary model variables. Alternatively, post-processing quantities, like the mean sea level pressure or potential vorticity gradients on isentropes (as in *Hubbard and Nikiforakis* [2003]), could be assessed that then require extra computations during the adaptation cycle. As indicated in Section 3.2.1 the length of an ideal adaptation cycle is also problem-dependent. It relies on the time scales of the observed phenomenon, e.g. a quickly changing phenomenon, like 'the emergence of cumulus clouds', requires very short assessment periods on the order of minutes. On the other hand, the evolution of a low pressure center can be sufficiently captured on a time scale of hours. In any case, it must be guaranteed that the tracked feature can not be transported out of the refined area during the selected time interval. This creates a fine balance between accuracy and computational overhead.

There are many answers to the above-mentioned research question that have been proposed in the literature. Here a snapshot of the discussion is presented that is primarily focused on feature tracking approaches. These are mainly developed in the context of uniform resolution model runs and serve as a guideline for adaptive grid applications. For example, a variety of feature tracking techniques were reviewed for long-term AMIP-II assessments (Atmospheric Model Intercomparison Project, see *Boyle et al.* [1998]). The study included the tracking of the 850hPa relative vorticity pattern as well as the tracing of potential vorticity features on upper level Θ-surfaces. Here the tracking algorithms by *Murray and Simmonds* [1991], *Jones and Simmonds* [1993], *Hodges* [1994] and *Hodges* [1995] were used. They were also applied to alternative levels and variables, such as the 250hPa and 500hPa geopotential and the 850hPa temperature. It was concluded that the tracking of the relative vorticity field allows a precise diagnosis of the initial stages of cyclogenesis in the extratropics. Furthermore, the vorticity assessment also enables studies in tropical regions that are not characterized by low and high pressure regimes with closed contours.

In an alternative study by *Sinclair* [1994] the geostrophic relative vorticity at 1000hPa was used as an objective measure of cyclonic disturbances. It was found that the relative vorticity criterion detected the cyclone centers more reliably than the more traditional use of local pressure minima. As also pointed out by *Sinclair* [1997] the use of pressure minima favors the detection of more intense slow-moving systems and misses many mobile centers where a local minimum can not instantly be found. Most often the local pressure minimum does not appear until after considerable cyclogenesis has already occurred. Therefore, the pressure-based criterion might not capture the very early stages of a developing system.

These pressure-based criteria for cyclone tracking applications were further evaluated by *Jones and Simmonds* [1993] who suggested a combined assessment of the mean sea level pressure value, its gradient and curvature. Additionally, *König et al.* [1993] identified cyclones via a combination of three synoptic criteria: the local geopotential height minimum at 1000hPa, a pronounced intensity of the system and a lifetime longer than one day. A comparison of this scheme to the *Murray and Simmonds* [1991] approach (also *Jones and Simmonds* [1993]) is provided in *Leonard et al.* [1999]. A simpler algorithm was used by *Lambert* [1988] who just focused on local minima of the geopotential height at 1000hPa that were surrounded by four grid points at higher height levels. Such an approach is clearly grid size dependent.

In general, it must be kept in mind that all evaluated quantities, like the mean sea level pressure or variables on pressure or potential temperature surfaces, are not readily available in a model with orography following model levels. Rather they are diagnostically derived quantities that require additional calculations and vertical interpolations. The overhead and trade-off also need to be considered if more elaborate vortex tracking algorithms are to be used as suggested by *Jeong and Hussain* [1995].

5.1.2 Adaptation criteria for the finite-volume dynamical core

How can the life cycles of the “features of interest” reliably be captured with an adapted grid? This is the key question for the adaptive finite-volume simulations presented in the subsequent sections. The adaptations are assessed not only in the 2D shallow water system but also in the 3D hydrostatic framework. The selected test cases cover a variety of flow scenarios that require individual adaptation strategies. Among them are assessments of the vorticity, the geopotential gradient or simple threshold values in mountainous areas or for advection tests. Here the shallow water equations serve as an idealized test bed for the 3D adaptive design.

Table 5.1 lists the adaptation strategies applied to the different test cases. The tests are represented in an increasing order of complexity. The dynamically adaptive approach for the pure advection tests is based on a simple assessment of the geopotential. Such a concept works well for the passive transport problem in a nondivergent flow field. Alternatively, a gradient-based indicator can also be recommended (not shown). As pointed out earlier, the gradient of a tracer field was successfully used by e.g. *Hubbard and Nikiforakis* [2003] and other investigators for passive advection tests.

Dim.	Test scenario	AMR setup	Adaptation criteria
2D	Advection (test 1)	dynamic	Φ threshold
	Advection using a reduced grid	dynamic + static	Φ threshold
	Flow over a mountain (test 5)	dynamic + static	vorticity threshold + mountain
		dynamic + static	Φ gradient threshold + mount.
		dynamic	vorticity threshold
3D	Baroclinic wave with orography	static	adapted storm track
	Baroclinic wave without orography	dynamic	vorticity threshold (surface)

Table 5.1: Strategies for dynamically and statically adapted model runs.

Solution gradients are also the refinement criterion of choice for many nonlinear CFD applications. In this study, the performance of the geopotential gradient indicator is tested using an idealized flow over a single mountain (test case 5). Alternatively, a vorticity-based criterion is tested that allows the direct comparison of the two approaches. Both simulations combine the dynamic adaptations with static refinements of the mountain. In addition, tests are also performed without the adapted orography.

In three dimensions two adaptation strategies are examined for the hydrostatic dynamical core. First, the storm track of a developing idealized baroclinic wave (*Jablonowski and Williamson* [2004]) is statically adapted. Second, the baroclinic wave test without orography (*Polvani et al.* [2004]) is evaluated with purely dynamic adaptations based on vorticity thresholds. Here the model level closest to the surface is selected for the assessment. Tests with combined criteria, like the combination of surface pressure extrema and vorticity thresholds, have also been performed and led to similar results (not shown). As discussed earlier, vorticity-based refinements are appealing since they detect the developing wave trains early. In addition they have been successfully used in idealized adaptive hurricane track predictions as shown by *Fulton* [1997].

As a first glimpse, three choices of possible adaptation criteria are presented in figure 5.1. The figure displays an analysis of the initial state of shallow water test

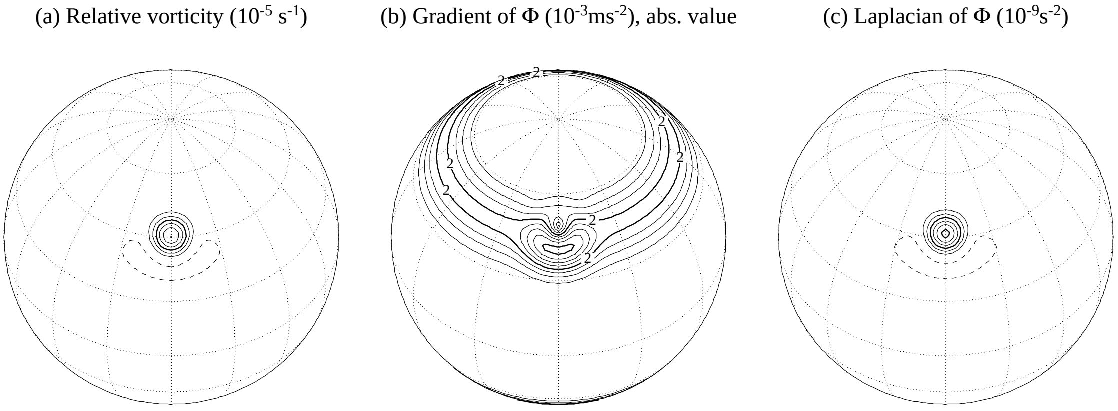

Figure 5.1: Possible choices for refinement criteria illustrated with the initial state of test case 4 (orthographic projections centered at 0E,45N). (a) Relative vorticity, (b) absolute value of the gepotential gradient and (c) the Laplacian of the geopotential. Contour intervals are $10^{-5}s^{-1}$, $10^{-3}ms^{-2}$ and $10^{-9}s^{-2}$, respectively.

case 4. This test is comprised of a forced nonlinear system with translating low (see also figure A.7). Here the relative vorticity as well as the gradient and the curvature (Laplace) of the geopotential height field are illustrated. It can clearly be seen that all three indicators pick out the center of the low pressure system that is surrounded by a rotating wind field. In practice though, tests have suggested that the Laplacian of the geopotential height field is not a suitable indicator for curvature-based refinement regions. Instead, the vorticity pattern is recommended as a measure of the curvilinearity of the geopotential or pressure field. This is due to the observation that the second-order derivative of the geopotential height field tends to develop small scale noise over time that misleads the refinement strategy. On the other hand, the vorticity and the gradient indicator performed reliably in all studies. Overall, the main difficulty arises when setting the user-defined threshold values. These are highly problem-dependent, but crucially important when considering that features of interest need to be detected early on the coarse mesh. The sensitivity of the empirical threshold values again determines a fine balance between accuracy and efficiency. The threshold values for the adaptive finite-volume dynamical core are documented in the corresponding sections.

There are lots of choices for possible adaptation criteria. For example, single indicators can be combined to form a more elaborate system. Additionally, weighted refinement criteria are feasible that are based on varying threshold values at different refinement levels. In practice though, the latter strategy will be impossible to meet exactly in the adaptive block setup. This is due to the requirement that neighboring blocks can only differ by one refinement level, which triggers cascading refinement requests. Therefore, such an option has not been implemented in the dynamical core. If the adaptation criterion is fulfilled, the blocks are flagged by the user and adapted by calling the AMR library functions. Currently, refinements are triggered consecutively up to the highest user-defined refinement level as soon as at least one grid point within a block exceeds the threshold value. Coarsenings occur if all grid points of four neighboring blocks (children) no longer meet the refinement criterion. Furthermore, the neighboring block constraint needs to allow a coarsening step.

Here it is important to keep in mind that there are two factors that limit the refinement levels. Besides the user-defined thresholds and maximum number of refinement levels, the hydrostatic approximation also restricts the adaptations from a physical viewpoint to horizontal scales larger than 10km (see Section 3.1.2).

Refinement indicators are implemented as plug-and-play components. Therefore, they can be easily exchanged and adjusted for future assessments.

5.2 Dynamic adaptations: Shallow water tests

The dynamically adaptive finite-volume model is tested in the 2D shallow water configuration. Two basic test scenarios are assessed using the standard test suite for the shallow water equations. First, the tests are concentrated on the assessment of the adaptive advection algorithm. Second, the full nonlinear system is examined with a flow field over a single mountain.

5.2.1 Advection tests with the full grid

The advection algorithm is one of the fundamental building blocks of atmospheric flow simulations. It is therefore imperative to evaluate its performance not only in the adaptive shallow water setup but also in a non-adapted case. Therefore, the adapted model results are both compared with the analytical reference solution and the solution from uniform-grid model runs.

There are a variety of standard test cases for advection schemes. For example *Zalesak* [1979] introduced the two dimensional solid body rotation problem with a slotted cylinder. Furthermore, *Doswell* [1984] developed an idealized cyclogenesis test that defines a strong deformational flow field. This test was later reformulated for spherical coordinates by *Nair et al.* [1999] and *Nair and Machenhauer* [2002] and consequently tested with an adaptive advection model by *Hubbard and Nikiforakis* [2003].

Here the adaptive finite-volume advection scheme is tested with an alternative standard approach that has been most commonly used in the atmospheric science literature. It is the cosine bell advection test (shallow water test case 1, see Appendix A) that was already applied to the reduced grid in Section 4.2.2. The advection of the cosine bell is tested with different rotation angles α. In particular, $\alpha = 0°$,

$\alpha = 45°$ and $\alpha = 90°$ are selected that describe the transport of the cosine bell along the equator, at a 45° angle in the tropics and midlatitudes as well as the transport straight over the poles.

The refinement criterion for the adaptive transport of the cosine bell is a simple threshold criterion that assesses the value of the geopotential at each grid point. In case the geopotential exceeds the empirical limit $\Phi \geq 520 m^2 s^{-2}$ the block is flagged for refinement. This value corresponds to $h \approx 53m$, which is approximately 5% of the initial peak with $h \approx 1000m$. If on the other hand the grid points no longer meet the adaptation criterion the coarsening flag in the corresponding block is set. The refinement criterion is examined during each time step that is held variable in order to match the $|CFL| = 0.95$ limit. All adaptations occur consecutively until either the maximum refinement level or the coarse $5° \times 5°$ initial resolution is reached. This resolution is the base resolution for all adaptive shallow water runs. The grid can not be coarsened further than the initial setup. The passive advection is driven by pre-determined analytical wind speeds. These are reinitialized analytically whenever adaptations occur. This applies also to the initial state of the geopotential at the various refinement levels. During the model run though, the geopotential in newly adapted blocks is initialized via second-order conservative PPM-like interpolations. The chosen advection algorithm is also based on the PPM scheme and no filtering of any variable is applied. For the adaptive model simulations the maximum refinement level is user-defined and varies between 0 and 4. These model setups correspond to the grid spacings 5°, 2.5°, 1.25°, 0.625° and 0.3125° at the finest level, respectively. The resolutions and initial block parameter sets are further explained in table 3.1 on page 74.

The basic adaptation principle is illustrated in figure 5.2 with $\alpha = 90°$ that shows

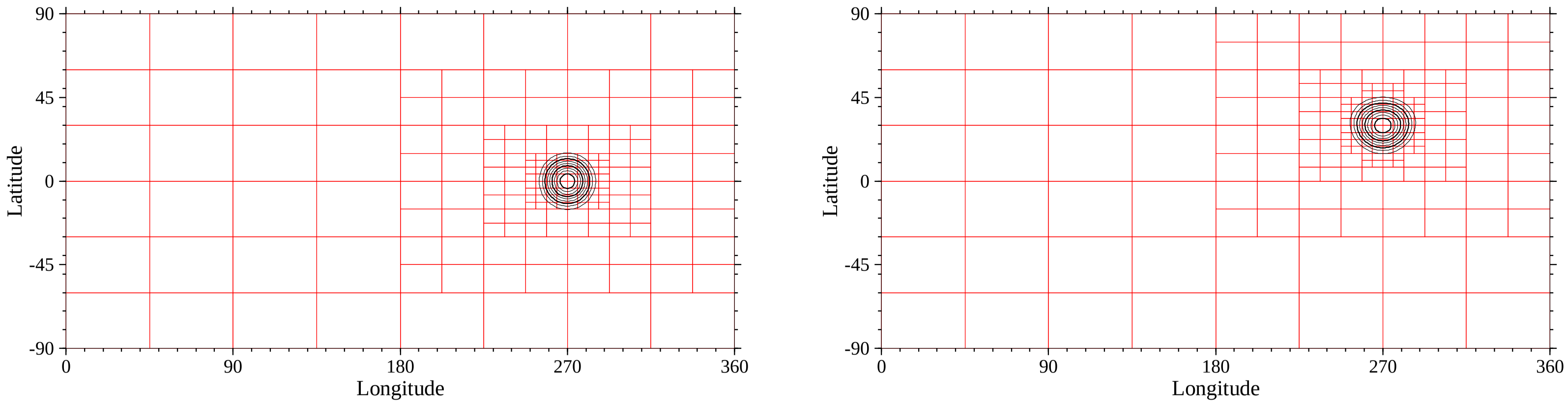
(a) Initial state

(b) 24 hours

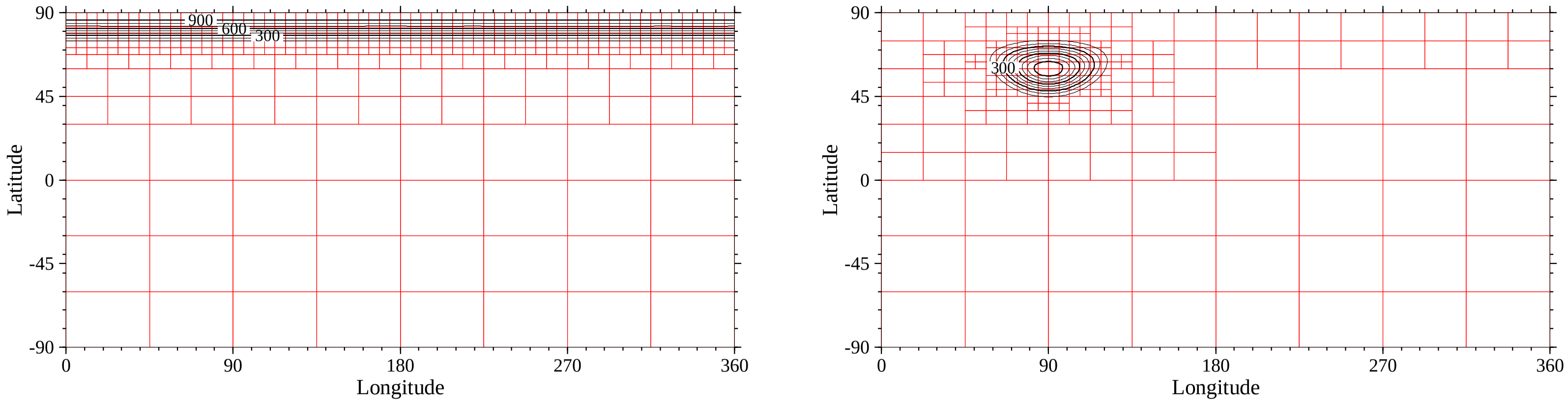
(c) 72 hours

(d) 96 hours

Figure 5.2: Geopotential height of the cosine bell (test case 1, $\alpha = 90°$) with 3 refinement levels ($0.625°$) at different points in time. (a) Initial state, (b) after 24 hours, (c) 72 hours and (d) 96 hours. The adapted blocks are indicated in red. Contour intervals are 100 m, the zero contour is omitted.

four snapshots of the adaptive simulation at refinement level 3. The figure depicts the cosine bell at day 0, 1, 3 and 4 with overlaid adapted blocks (in red) that track the "feature of interest". As it can clearly be seen, the cosine bell passes over the North Pole without distortions or noise. The pole point itself with its converging grid lines is spread out in the chosen equidistant cylindrical map projection. This emphasizes the numerous grid boxes in polar regions that need to be refined for transport processes at high latitudes. They severely restrict the maximum allowable time step that obeys the $|CFL| = 0.95$ condition in polar regions. For example, in this simulation with three refinement levels and a maximum zonal wind speed of $u \approx 38.6 ms^{-1}$ at the poles the adaptive time step varies between $\Delta t \approx 597.3\,s$ in equatorial regions and $\Delta t \approx 9.3\,s$ at very high latitudes. In this passive advection test, the grid boxes adjacent to the poles do not need to be kept at the same refinement level since there is neither a need to filter gravity wave motions nor to calculate vorticity and wind data at the pole points (see also Section 2.2.1 and 2.2.2).

The cosine bell is advected once around the sphere and reaches its initial position after 12 days. Then the solution can be compared to the initial conditions that serve as the true reference field. A closer examination of the final states at refinement level 1 and different rotation angles α is illustrated in figure 5.3 on the next page that also presents the overlaid true solution with dotted lines. The figure shows that the cosine bell undergoes a stretching in the flow direction which is a typically observed for monotonicity-constrained finite-volume advection algorithms (see also *Lin and Rood* [1996], *Nair and Machenhauer* [2002] and *Hubbard and Nikiforakis* [2003]). The effect is clearly visible at this relatively coarse resolution and diminishes significantly with decreasing grid sizes (figure 5.4). As pointed out by *Nair and Machenhauer* [2002] the degradation of the shape caused by the monotonocity constraint trans-

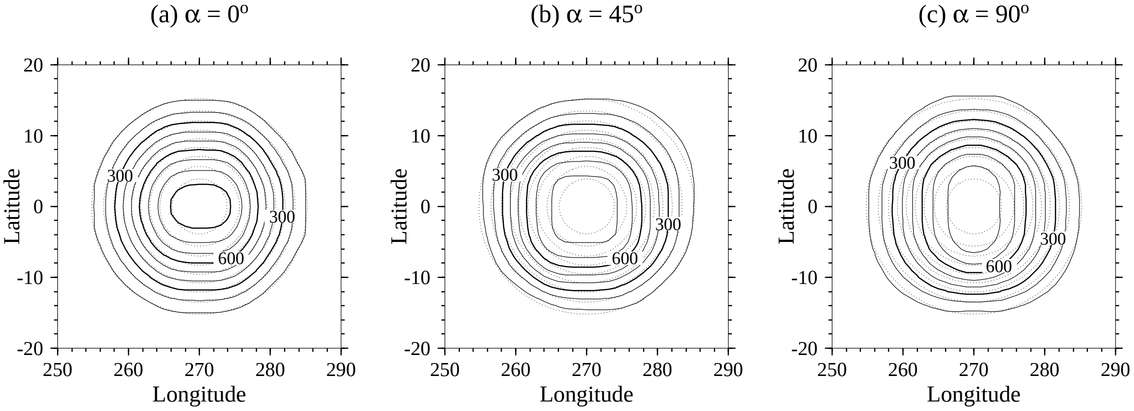

Figure 5.3: Geopotential height of the cosine bell (test case 1) after 1 revolution (12 days) with one refinement level (2.5°) and different rotation angles α. (a) $\alpha = 0°$: advection along the equator, (b) $\alpha = 45°$: advection at a 45 degree angle, (c) $\alpha = 90°$: advection over the poles. The analytic solution is overlaid (indicated by the dotted lines). Contour intervals are 100 m, the zero contour is omitted.

lates into slightly less accurate error norms in comparison to e.g. positive definite methods. A similar result was also found in Section 3.3.1 with respect to constrained and unconstrained interpolation strategies (table 3.4). Nevertheless, the advantages of the monotonicity preserving advection algorithm outweigh the slight decrease in accuracy (see also comparisons in *van Leer* [1977]).

Figure 5.4 confirms that the shape of the cosine bell after one rotation is well-preserved at high resolutions. The figure depicts a sequence of model runs with increasing number of refinement levels at rotation angle 45°. This transport direction represents the "worst case" scenario for the advection algorithm with underlying operator splitting approach. The results at the highest refinement levels 3 and 4 are almost indistinguishable from each other. It is also interesting to note that the cosine bell in (c)-(e) no longer shows the small phase error, which is visible in the subfigures (a) and (b). The solutions then resemble the true solution very closely which is demonstrated in subfigure (f). This subfigure displays the difference of the

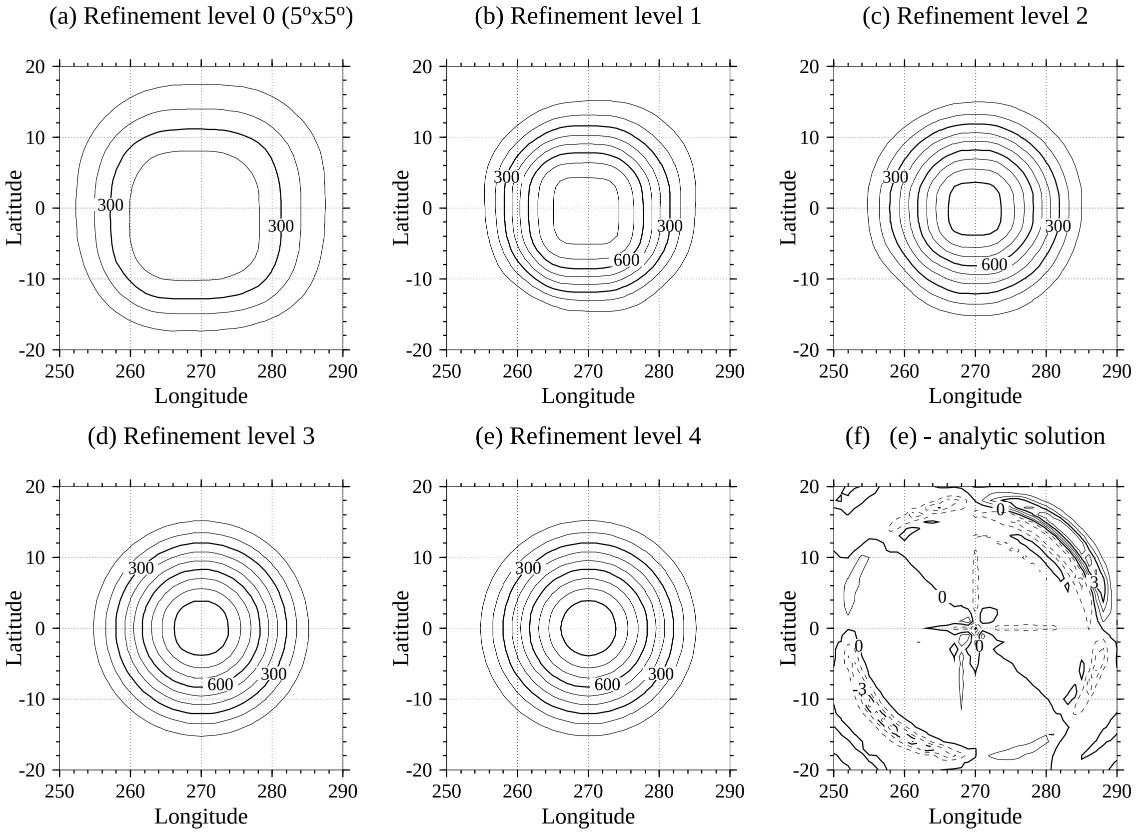
(a) Refinement level 0 (5ºx5º)

(b) Refinement level 1

(c) Refinement level 2

(d) Refinement level 3

(e) Refinement level 4

(f) (e) - analytic solution

Figure 5.4: (a-e) Geopotential height of the cosine bell (test case 1) and (f) height errors after 1 revolution (day 12) with rotation angle $\alpha = 45°$. (a) No refinements (5° resolution), (b) 1 refinement level (2.5°), (c) 2 refinement levels (1.25°), (d) 3 refinement levels (0.625°), (e) 4 refinement levels (0.3125°) and (f) difference of the solution on the finest mesh (case (e)) with the analytic solution. Contour intervals are 100 m (a-e) and 1 m (f). The zero contour is omitted (a-e).

cosine bell at refinement level 4 with the reference state. The differences mainly develop along the edges in the 45° flow direction. In particular, the leading edge shows slightly enhanced geopotential height values, whereas the tail drops below the reference state. These errors are small in comparison to the peak amplitude of the cosine bell. In general, the same type of error patterns can also be found in non-adapted model runs.

Further, it is interesting to assess the adaptive model performance with a cross polar flow field at $\alpha = 90°$. Dynamic adaptations in polar regions are demanding since they involve many more adapted blocks close to the poles (see also figure 5.2). Nevertheless, the adapted advection scheme performs very well at all refinement levels as displayed in figure 5.5. Each subfigure shows three snapshots of the cosine bell at day 2, 3 and 4 in a north polar stereographic projection. There are no visible distortions of the height field at any resolution as the cosine bell approaches, passes over and leaves the North Pole. The increased resolution clearly helps preserve the

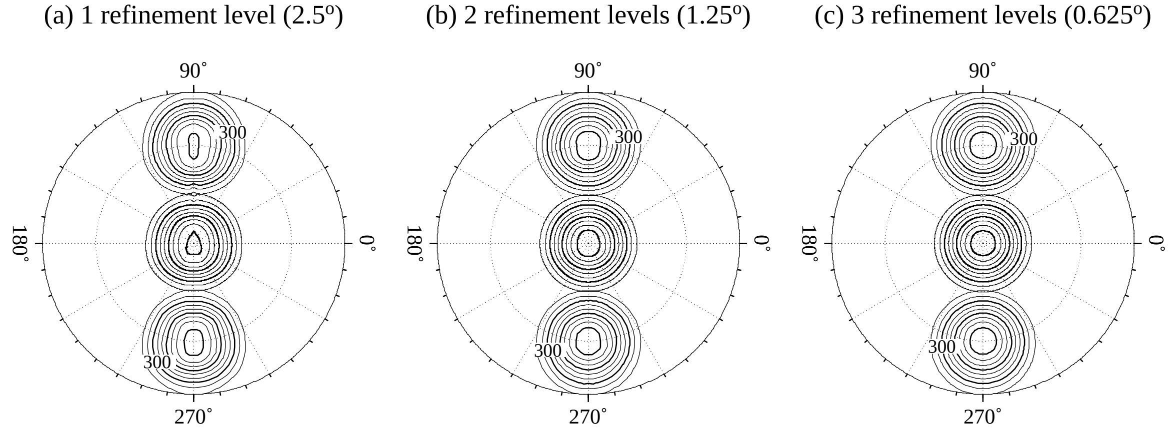

Figure 5.5: Polar stereographic projections of the cosine bell (test case 1, $\alpha = 90°$) transported over the North Pole (from the bottom to the top of the figure, the outer circle is located at 45N). Snapshots are taken after 48, 72 and 96 hours, respectively, with refinement levels (a) 1, (b) 2 and (c) 3. Contour intervals of the geopotential height fields are 100 m, zero contour is omitted.

shape and peak amplitude.

Here it is important to point out that the multidimensional transport of the cosine bell is not strictly monotonic. Tiny under- and overshoots are possible in the current formulation that have been especially observed at a 45° transport angle. This is documented in table 5.2 that lists the minimum geopotential height values after one rotation for uniform and adapted runs at refinement level 2. The latter are tested with and without flux corrections at the interface boundaries (see also Section 3.3.3). Even in the non-adapted runs (second column), vanishingly small negative height values develop in case of non-zero rotation angles. Then the cosine bell is truly transported in both dimensions. Such an effect has also been observed by *Lin and Rood* [1996] for the equivalent 2D advection tests in Cartesian coordinates. The violation of the monotonicity constraint in two dimensions is a consequence of applying a sequence of solely 1D limiters during the transport calculations. Such an approach does not guarantee that the resulting multidimensional advection scheme keeps the monotonic attribute. In practice, the negative values are small, but may be significant when transporting positive definite quantities, like atmospheric tracer components or water vapor. Then these undershoots may cause difficulties in other

Test case 1 with angle α	Non-adapted runs with uniform 1.25° resolution	Adapted 5° × 5° runs and 2 refinements	
		flux corrections	no flux corrections
$\alpha = 0°$	0.	0.	0.
$\alpha = 45°$	$-0.5605 * 10^{-44}$	-0.1761	$-0.6557 * 10^{-3}$
$\alpha = 90°$	$-0.8178 * 10^{-54}$	$-0.5999 * 10^{-5}$	$-0.1383 * 10^{-10}$

Table 5.2: Minimum amplitude of the cosine bell in m (test case 1) after one revolution for adapted and non-adapted runs at the equivalent resolution 1.25° × 1.25°. Adapted runs are tested with and without flux corrections at coarse-fine grid interfaces.

code modules. If negative values need to be avoided, three strategies can be employed. First, the subgrid distributions could be further manipulated in order to guarantee a positive definite constraint. Second, an a-posteriori filling algorithm can be applied that borrows the missing tracer mass from neighboring grid cells. Such an algorithm is in fact implemented in today's NASA/NCAR dynamical core. Third, a strictly monotonic Zalesak-type multidimensional transport algorithm could be used (*Zalesak* [1979]).

Here these three options are not considered in the adaptive finite-volume model. Instead, special attention needs to be paid to an even more dominant effect in the adaptive simulations. This is indicated in column 3 of table 5.2 which shows the minimum height values in the adapted runs with flux corrections at interface boundaries. These flux corrections are necessary to ensure the mass conservation principle in the adapted model. It can clearly be seen that the flux corrections lead to an additional violation of the monotonicity principle. The undershoots, although still small, are orders of magnitude bigger then the negative values in the non-flux corrected runs. The latter also show enhanced undershoots in comparison to the uniform grid simulations. They are caused by the conservative PPM-type interpolations that are used for the adaptive split-join operations as well as for the ghost cell updates at interfaces. When looking at the spatial pattern, the undershoots can be pre-dominantly found around the feature's non-smooth circular base, which has a discontinuous first derivative. This minor undershoot effect of the interpolation scheme can be avoided when applying additional monotonicity constraints to the 2D PPM-type subgrid distribution. Especially corner values of the subgrid distribution need to be checked. However, it is an open question whether a truly monotonic multi-dimensional conservative transport scheme with flux corrections can be developed for adaptive grid simulations.

The overall performance of the adapted advection tests with different rotation angles and increasing refinement levels is summarized in table 5.3. The table shows not only the l_1, l_2, l_∞ and h_{max} errors after one revolution (see also Section 4.1) but also contains information on the final peak amplitude, the number of blocks and

Base resol.	Refin. level	Height error norms			h_{max}	Final h (m)	# Blocks		# Time steps	CPU time (s)
		l_1	l_2	l_∞			min	max		
$\alpha = 0°$										
1.25°	0	0.0073	0.0078	0.0107	-0.0106	984.2	768		312	230
5°	0	0.1157	0.1001	0.0949	-0.0869	838.0	48		84	4
5°	1	0.0341	0.0301	0.0317	-0.0305	949.1	54	60	156	12
5°	2	0.0097	0.0103	0.0150	-0.0106	984.2	72	84	312	32
5°	3	0.0016	0.0021	0.0044	-0.0036	995.0	174	204	612	159
5°	4	0.0003	0.0005	0.0014	-0.0012	998.4	348	384	1224	642
$\alpha = 45°$										
1.25°	0	0.0264	0.0259	0.0557	-0.0555	939.5	768		19872	13873
5°	0	0.5077	0.4194	0.4835	-0.4762	480.8	48		1440	64
5°	1	0.0927	0.0911	0.1525	-0.1514	830.7	54	60	1440	97
5°	2	0.0278	0.0251	0.0507	-0.0505	944.4	72	106	3333	418
5°	3	0.0088	0.0080	0.0159	-0.0159	982.8	171	210	3871	994
5°	4	0.0031	0.0030	0.0053	-0.0039	995.8	348	462	4120	2407
$\alpha = 90°$										
1.25°	0	0.0250	0.0256	0.0421	-0.0420	953.0	768		27936	19551
5°	0	0.4683	0.3860	0.3923	-0.3902	559.7	48		2016	97
5°	1	0.0924	0.0898	0.1253	-0.1250	856.6	60	72	4085	305
5°	2	0.0244	0.0240	0.0405	-0.0405	954.5	72	200	11152	1885
5°	3	0.0048	0.0052	0.0125	-0.0125	986.2	192	480	33288	15465
5°	4	0.0010	0.0011	0.0038	-0.0038	995.9	348	1440	107199	159708

Table 5.3: Error measures and statistics for the solid body rotation of the cosine bell (test case 1) after one revolution (12 model days) for different refinement levels and rotation angles α. The CFL number is 0.95. The CPU time is the user time on a single processor of a SUN workstation.

time steps as well as the total CPU time measured on a SUN Ultrix workstation. In addition, the error statistics of selected uniform model runs are listed for comparison. It can clearly be observed that the cosine bell is successfully tracked in the adapted model simulations. This is not only true for the l_1 and l_2 error norms that assess the overall shape, but also for the peak amplitudes evaluated by the l_∞ errors. The peak amplitudes improve considerably with increasing refinement levels. In addition, the table shows that the CPU time in the adapted runs is significantly reduced in comparison to the uniform resolution runs. For example, when comparing the uniform 1.25° runs with the corresponding adapted runs at refinement level 2 the speed-up factors are approximately 7, 33 and 10 for the rotation angle $\alpha = 0°$, $\alpha = 45°$ and $\alpha = 90°$, respectively. The speed-up is determined by two main factors. First, the number of blocks and therefore the overall work load is decreased in the adapted simulations. Second, the total number of time steps necessary for the 12-day integration is drastically reduced. The latter is due to the fact that the adaptive time step can be greatly increased if the fine grid does not cover the polar regions. In particular, this effect can be seen in the $\alpha = 45°$ case where the time step in the uniform run solely depends on the CFL restriction at the poles. This consequently leads to a rather short time step and large number of iterations. In the corresponding adapted run, the grid around the poles is mostly kept at the coarse resolution so that the time step is mainly determined by the traveling cosine bell. The latter is especially true for the $\alpha = 0°$ test case, where the time step exclusively relies on the true advective wind speeds and grid distances at the equator. Therefore, an identical number of time steps is required for both the uniform and adapted runs at the 1.25° resolution and the computational savings are only due to the reduced work load.

The error norms for the adapted simulations in table 5.3 compare well to values presented in the literature. For example, the errors of the $\alpha = 90°$ run with 1 refinement level (2.5°) closely resemble the corresponding error measures for the monotonic FFSL-3 scheme in *Lin and Rood* [1996] and the CISL-M method in *Nair and Machenhauer* [2002] at comparable resolutions. This is important to note since the above-mentioned algorithms are semi-Lagrangian type schemes that only require very few time steps for one revolution of the cosine bell. Both schemes finish after 256 integration steps, whereas the adaptive finite-volume model needs 4085 time steps due to the CFL restriction. Therefore, it must be emphasized that the error norms match despite the large difference in the number of time steps. The sheer number of integrations has significant implications on the model results. This has been already documented in table 5.3, which shows that the error norms of the adapted runs at refinement level 2 for non-zero rotation angles are in fact slightly lower than the errors of the uniform grid runs. The effect can be linked to the reduced number of integration steps. An even clearer example is given in table 5.4 that assesses the performance of the $\alpha = 0°$ advection test with different maximum CFL numbers. As the CFL numbers decrease, the resulting number of time steps for one revolution increases, which leads to considerably less accurate results. This conclusion might

Base resol.	Refin. level	CFL number	Height error norms			Final h (m)	Base time step (s)	# Time steps	CPU time (s)
			l_1	l_2	l_∞				
$\alpha = 0°$									
5°	2	0.95	0.0097	0.0103	0.0150	984.2	3420	312	32
5°	2	0.5	0.0170	0.0184	0.0279	967.0	1800	576	58
5°	2	0.1	0.0295	0.0275	0.0354	959.6	360	2880	275

Table 5.4: Error measures and statistics for the solid body rotation of the cosine bell (test case 1, $\alpha = 0°$) after one revolution with refinement level 2 (1.25°). Results are shown for different CFL numbers. The CPU time is the user time on a single processor of a SUN workstation.

be surprising at first since a small CFL number is expected to decrease the temporal errors of the time stepping scheme. Here, it shows that the overall error is in fact dominated by the spatial errors. A similar time stepping effect was also observed by *Stevens and Bretherton* [1996], but was not generally found (except once) in the adaptive advection tests by *Hubbard and Nikiforakis* [2003].

To sum up, time traces of the normalized l_2 and l_∞ error norms with $\alpha = 45°$ and $\alpha = 90°$ are illustrated in figure 5.6. The figure displays the evolution of the errors at three different refinement levels that show the expected decline of the solution error. The norms are slightly sensitive to the rotation angle, especially in comparison to the $\alpha = 0°$ values listed in table 5.3.

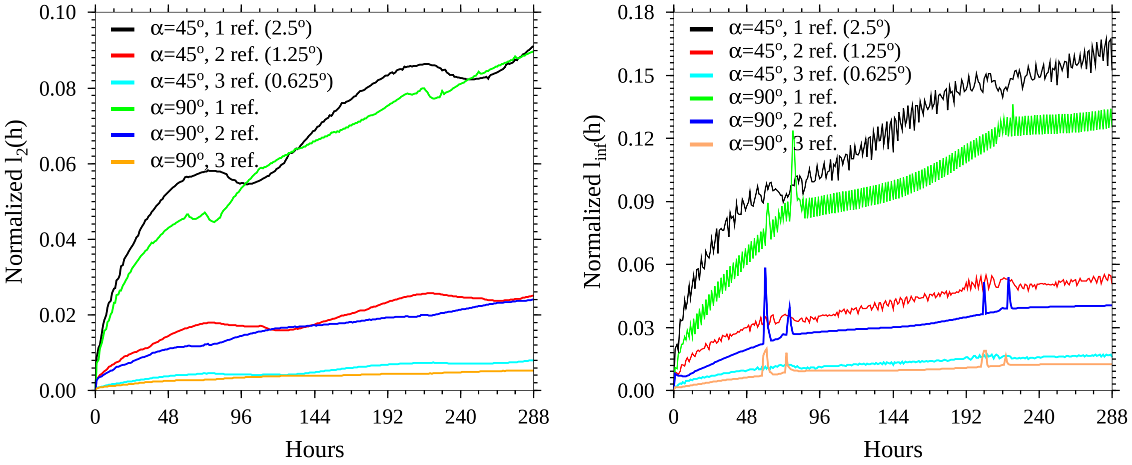

Figure 5.6: Normalized l_2 (left) and l_∞ (right) height errors for different refinement levels and rotation angles α (test case 1).

The trace of the l_∞ norm is rather noisy at low resolutions and additionally, shows distinct spikes when the cosine bell is transported over the poles. This was also observed by *Rasch* [1994], *Taylor et al.* [1997] and *Nair and Machenhauer* [2002]. These spikes are not a consequence of the dynamically adaptive grid implementation, but occur in the full grid model runs as well as in the reduced grid simulations shown later. As pointed out by *Jakob et al.* [1993] the source of the noise is the discrete sampling of the numerical and reference solution. Here the reference solution is computed analytically during the course of the integration using the trajectory approach as outlined in Section 4.1.3. This leads to an occasional small increase in the peak amplitude of the reference field depending on the distance of the center to the closest grid point. This effect diminishes with increasing resolution.

5.2.2 Advection tests with the reduced grid

The cross polar advection test with $\alpha = 90°$ is also applied to the reduced grid setups discussed in Section 4.2.1. This approach combines the statically coarsened reduced grids with the additional flexibility of dynamic grid adaptations. The interface treatment of the adaptive reduced grids is quite elaborate since all three fine-coarse grid interfaces (discussed in Section 3.3.2) play a crucial role at different stages during the integration. This requires a variety of different interpolation modules for the ghost cell exchange.

As argued in Section 4.2.1, the base resolution for the reduced grid simulations needs to be finer than the typical 5° grid. This allows the introduction of up to two reduction levels north or south of 60° N/S. Therefore, the following examples are computed on a $2.5° \times 2.5°$ base grid with one or two reduction levels. A single refinement level is then used to track the path of the cosine bell. All other initial parameter settings are identical to the advection tests presented in Section 5.2.1. In particular, the maximum CFL number is also set to $|CFL| = 0.95$ and the refinement criterion assesses the geopotential threshold value $\Phi \geq 520 m^2 s^{-2}$.

Figure 5.7 on the facing page shows snapshots of the adapted reduced grid simulations with one and two reduction levels. The cosine bell is displayed at day 1 through 5 as it passes over the North Pole. Here the layout of the reduced blocks

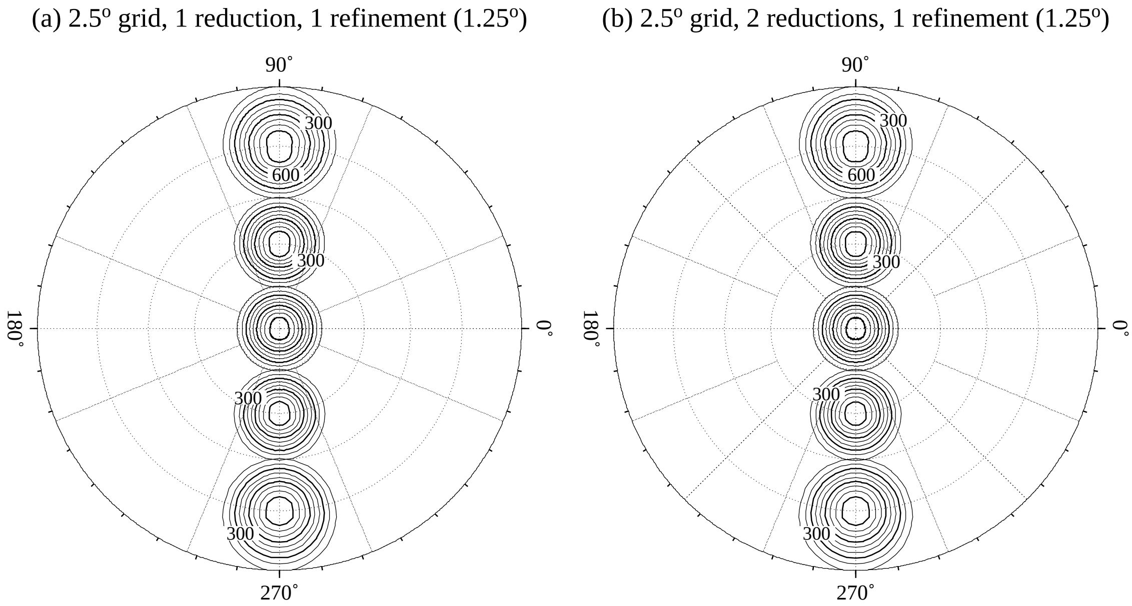

Figure 5.7: Polar stereographic projections of the cosine bell (test case 1, $\alpha = 90°$) transported over the North Pole (from the bottom to the top of the figure, the outer circle is located at 15N). Snapshots are taken after 24, 48, 72, 96 and 120 hours, respectively. Base resolution is 2.5° with 1 refinement level. (a) Reduced grid with 1 reduction, (b) reduced grid with 2 reductions. Contour intervals of the geopotential height fields are 100 m, zero contour is omitted.

is indicated by the dotted grid lines. For clarity, no attempt is made to overlay the adaptations. Both model runs are almost indistinguishable from each other and furthermore, compare very well to the full grid adaptive advection tests depicted in figure 5.5 on page 163. As seen before, the cosine bell crosses the pole point without visible distortions or noise. In addition, a comparison with figure 4.3 on page 124 reveals that the refinement area not only improves the shape but also the peak amplitude of the advected feature.

This is quantified in table 5.5 which lists the error norms for the adapted reduced grid runs and the full grid 1.25° control simulation after one revolution. All error norms are very similar in the adapted model setups. Here it is interesting to note, that the adapted reduced grid simulations show slightly improved l_1 and l_2 error measures despite the coarser longitudinal resolution at high latitudes. This effect is mainly attributable to the decrease in the total number of integration steps. The enhanced zonal grid spacing now allows a longer time step, which helps preserve the peak amplitude in case of one reduction level. In case of two reduction levels this time stepping effect is overshadowed by the slight smoothing effect of the second

Base resol.	Refin. level	Reduced grid	Height error norms			Final h (m)	# Blocks		# Time steps	CPU time (s)
			l_1	l_2	l_∞		min	max		
$\alpha = 90°$										
1.25°	0	0	0.0250	0.0256	0.0421	953.0	768		27936	19551
2.5°	1	0	0.0269	0.0262	0.0419	953.1	204	276	13218	3529
2.5°	1	1	0.0254	0.0249	0.0409	954.1	188	236	8696	2175
2.5°	1	2	0.0239	0.0237	0.0427	952.3	164	194	5484	1228

Table 5.5: Error measures and statistics for the solid body rotation of the cosine bell (test case 1, $\alpha = 90°$) after one revolution for different reduced grids and refinement levels. Base resolution is 2.5°. The CPU time is the user time on a single processor of a SUN workstation.

grid reduction. As a result, a very minor degradation of the peak amplitude can be observed.

Figure 5.8 shows the time trace of the l_2 and l_∞ error norms over the 12-day forecast period. The error growth is very similar in the depicted adapted and reduced grid cases. The characteristic spikes in the l_∞ norm can again be found in case of one reduction level (see also figure 5.6). They are absent though in the simulation with two reduction steps.

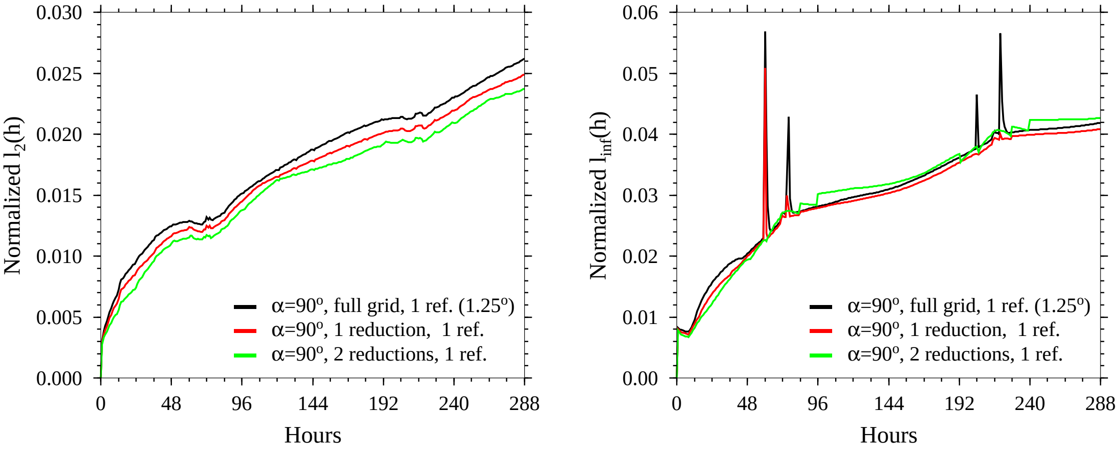

Figure 5.8: Normalized l_2 (left) and l_∞ (right) height errors for the full grid and different reduced grid configurations with 1 refinement level. The base resolution is 2.5° (test case 1, $\alpha = 90°$).

5.2.3 Flow over a mountain

The second assessment of the dynamically adaptive grid approach is concentrated on the full nonlinear shallow water equations. Two test scenarios are closely examined using an idealized flow field over a single mountain (test case 5, see also Appendix A.1.5). First, the dynamic adaptations are combined with statically adapted areas that cover the mountain region. Second, a purely dynamic adaptive grid approach is tested that also dynamically refines the orography.

The model simulations start with zonally symmetric geostrophic initial conditions that do not balance the orography field. As a result, a complex flow pattern evolves over time that is characterized by a lee-side wave train. Due to the complexity of the flow, this test case represents an idealized test bed for 3D hydrostatic regimes. Here, the test is primarily used to assess different refinement criteria and strategies.

Statically adapted orography

A combination of static and dynamic refinement strategies is evaluated over a 15-day forecast period. The initial setup of the grid is displayed in figure 5.9 which shows the initial geopotential height field with overlaid orography contours and corresponding statically adapted blocks. Here the static adaptations refine the single mountain in the Northern Hemisphere. This grid arrangement has also been shown earlier in an orthographic map projection in figure 3.3 on page 70. The underlying base resolution is the standard 5° × 5° grid that is comprised of 8x6 initial blocks with 9x6 cells per block.

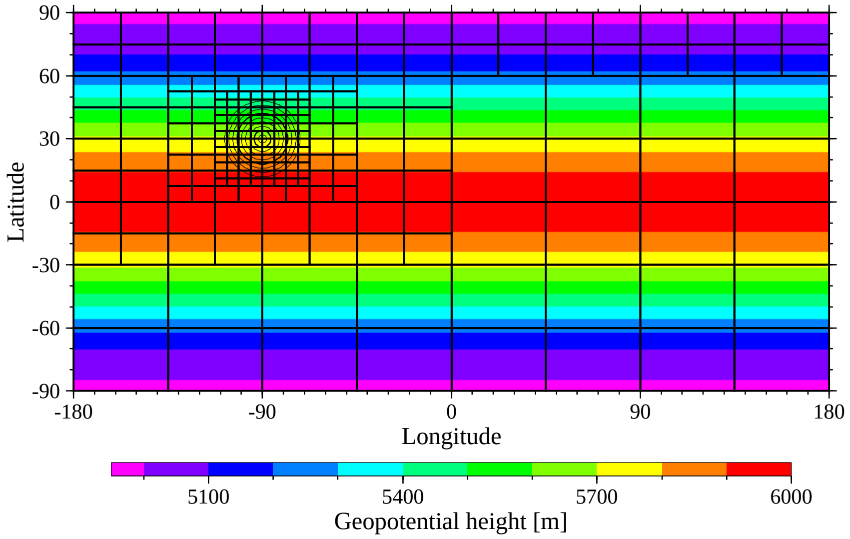

Figure 5.9: Initial geopotential height (m) and orography with the overlaid statically refined blocks at refinement level 3. The mountain is 2000 m high.

After the initial adaptations are applied, the geopotential height and orography fields are reinitialized analytically, whereas the wind components in the newly adapted blocks are computed via second-order non-conservative interpolations. This provides a slightly more consistent flow representation at the block interfaces and suppresses spurious noise at the beginning of the forecast. However, since the initial wind field is very smooth such an approach is almost indistinguishable from analytically reinitialized wind patterns in this scenario.

The test is concentrated on the assessment of two dynamic adaptation criteria. First, a vorticity-based criterion is selected that is based on the evaluation of the relative vorticity ζ at each grid point. Grid points are then flagged for refinement if the absolute value of the relative vorticity exceeds the empirical threshold $|\zeta| \geq 2 \times 10^{-5} s^{-1}$. Alternatively, a threshold value of $|\zeta| \geq 2.5 \times 10^{-5} s^{-1}$ is also reviewed. Second, a gradient-based refinement criterion is examined that assesses the absolute value of the geopotential gradient. Here, a threshold value of $|\nabla\Phi| \geq 2 \times 10^{-3} m s^{-2}$ is chosen. Both thresholds lie above the relative vorticity and Φ gradient values of the initial setup which are illustrated in figure 5.10. These profiles clearly depict the idealized nature of the test since its initial vorticity and gradient values are very small and furthermore zonally symmetric. The test therefore provides an excellent

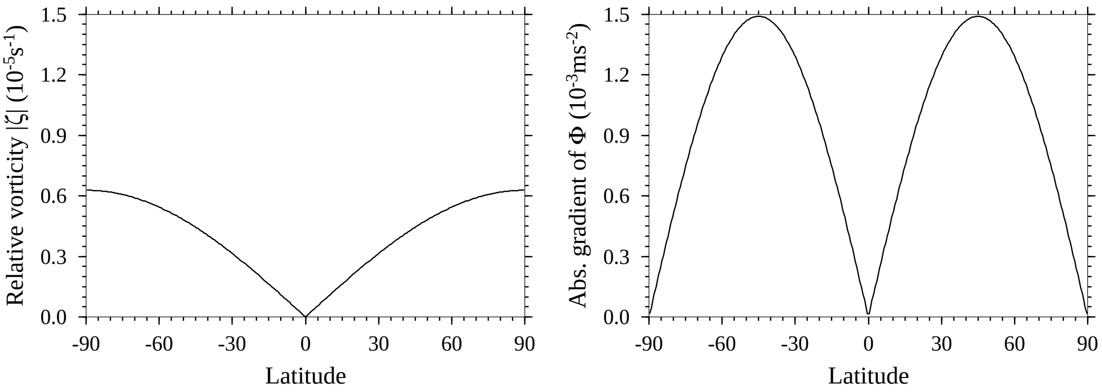

Figure 5.10: Initial absolute values of the relative vorticity (left) and the geopotential gradient (right) at the model level closest to the surface (test case 5).

example of a smoothly developing system based on a homogeneous basic state.

The test scenarios are listed in more detail in table 5.6. The table gives not only information on the selected constant time steps and corresponding integration steps for the 15-day forecast, but also shows some block statistics. In particular, the number of blocks at different stages of the simulation is presented. As expected the user-defined threshold values play an important role with respect to the sensitivity of the block adaptations. This can be seen in the direct comparison of the two runs with vorticity thresholds. A minor increase in the vorticity limit from $2.0 * 10^{-5}s^{-1}$ to $2.5 * 10^{-5}s^{-1}$ leads to a 30% reduction in the number of total blocks after 15 days.

Refinement criterion	Threshold	Number of blocks at day				Time step (s)	# Model steps
		0	5	10	15		
$\lvert\zeta\rvert$	$\geq 2.5 * 10^{-5}s^{-1}$	228	312	444	582	120	10800
$\lvert\zeta\rvert$	$\geq 2.0 * 10^{-5}s^{-1}$	228	366	573	831	$133\frac{1}{3}$	9720
$\lvert\nabla\Phi\rvert$	$\geq 2.0 * 10^{-3}ms^{-2}$	228	291	513	816	150	8640

Table 5.6: Characteristics of the dynamically adapted runs with vorticity and geopotential gradient criteria (test case 5).

For a thorough comparison of the adapted model runs, the vorticity and gradient-based refinement criteria with threshold values $2.0 * 10^{-5}s^{-1}$ and $2.0 * 10^{-3}ms^{-2}$ are selected. These generate a comparable number of adapted blocks so that the differences in the positions of the adaptations can clearly be assessed. The following adaptation strategy is employed. Both grids are statically adapted at the beginning of the model runs. Here the maximum refinement level is set to 3, which corresponds to a 0.625° resolution on the finest grid. The static adaptations (with criterion $\Phi_s > 0 m^2 s^{-2}$) are confined to the mountainous area and stay fixed during the model simulations. The dynamic adaptations are assessed every two hours, which is a suitable adaptation cycle for the selected slowly evolving features of interest. In principal, an even longer time interval can also be used, for example a nine hour adaptation cycle as in *Skamarock* [1988]. These intervals allow the flow to evolve smoothly before new adaptations are applied (see also discussion in Section 3.2.1). Furthermore, two additional adaptation constraints are selected that restrict the number of the refinement levels at high latitudes. In particular, the blocks adjacent to the poles are only allowed to refine once and the subsequent neighboring blocks are limited to two refinement levels. The latter is necessary in order to prevent a passive second refinement request for the pole blocks due to cascading refinements at the lower latitudes. In practice when starting with a 5° initial grid, these constraints result in the setup shown in table 5.7. The restriction on the total number of refinement levels in polar regions is recommended for efficiency reasons since the global time step should not be further limited by extremely small longitudinal grid distances at the poles. In the current setup the global time steps are already short since the $|CFL| < 1$ condition for gravity waves in midlatitudes needs to be obeyed for grid distances at the finest refinement level. In addition, the restriction limits computational noise at high latitudes.

Maximum refinement level	Geographical region
1	75° – 90° N/S
2	67.5° – 75° N/S
3	67.5° S - 67.5° N

Table 5.7: Maximum refinement levels in different geographical regions for the dynamically adapted runs with vorticity and geopotential gradient criteria.

First, the performance of the adapted simulation with the vorticity refinement criterion is evaluated. Figure 5.11 on page 179 shows two snapshots of the geopotential height field (including orography) at day 10 and day 15 with overlaid adapted blocks (subfigures c,d). Additionally, subfigures (a,b) depict the relative vorticity field that guides the refinement and coarsening requests. It can clearly be seen that the vorticity criterion picks out the lee-side wave train effectively and refines the regions with strong curvature in the geopotential height field. These regions are associated with high vorticity values. The criterion detects both troughs and ridges in the flow field since its absolute value is used for the assessments. The overall number of adapted blocks increases steadily during the course of the simulation despite the coarsenings in some regions. This is due to the selection of the rather sensitive threshold value that favors early refinements in the developing system. It can also be observed that there is some minor noise in the vorticity field at 60° N (day 10) and 75° N/S (day 15). These latitudes mark the positions of the digital Shapiro and FFT filtering mechanisms that are applied poleward of 60° N/S and 75° N/S, respectively (see also Section 2.2.2). Such small scale noise can possibly mislead the adaptation requests, which is suggested by the adapted patch in the smooth region at $170E, 60N$. This effect must therefore closely be observed in the AMR simulations. For example, the noise pattern could be reduced by additional or alternative filtering strategies at high latitudes.

For comparison, the same simulation with the gradient-based refinement indicator is presented in figure 5.12 on page 180. Here subfigures (a,b) show the absolute value of the geopotential gradient, which determines the refined regions in the geopotential height field with incorporated orography (subfigures c,d). The resulting flow fields closely resemble the vorticity-guided solutions although minor differences can be detected at day 15. In general though, both simulations match the NCAR high resolution reference solution (figure A.9) very well. The gradient indicator clearly

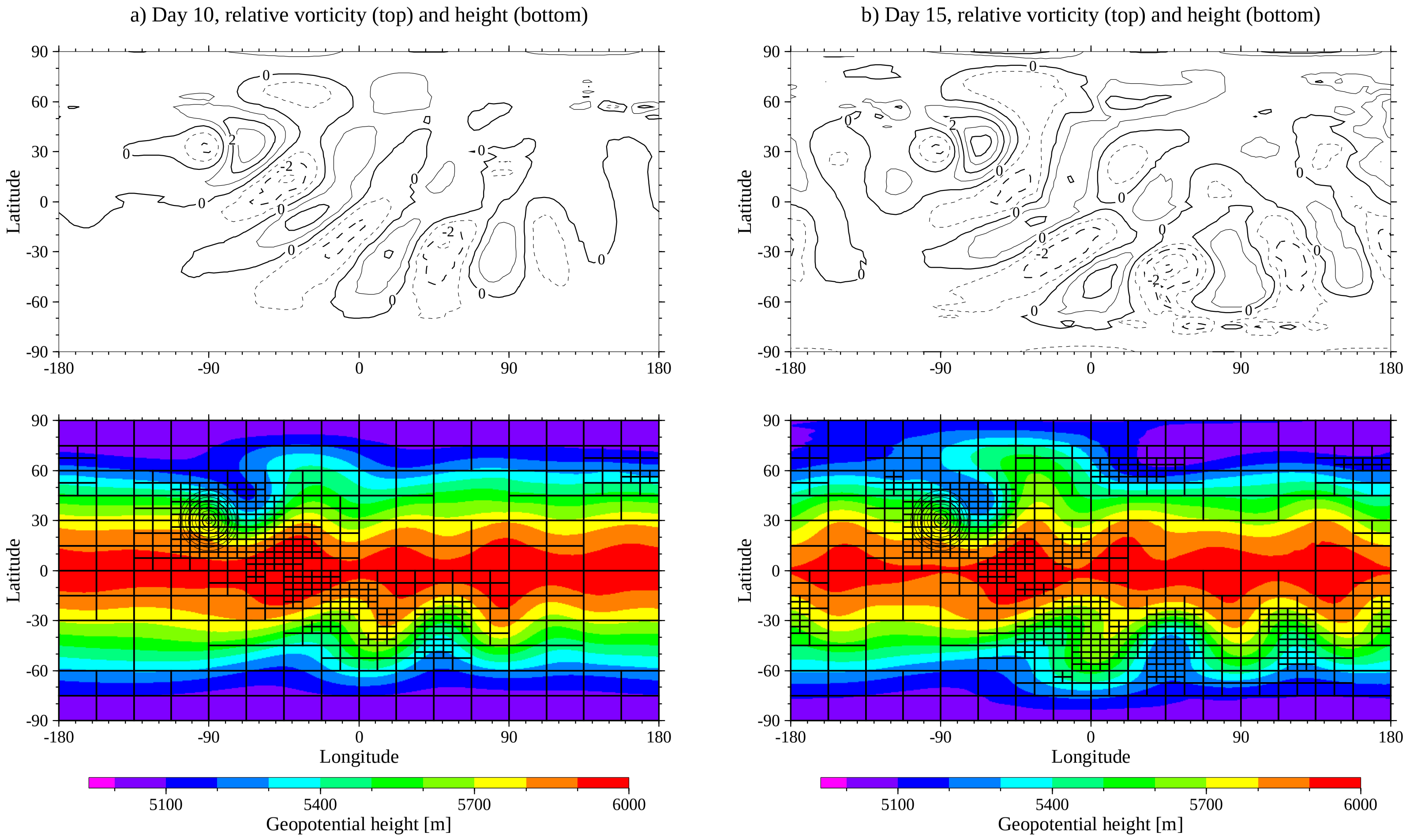

a) Day 10, relative vorticity (top) and height (bottom)

b) Day 15, relative vorticity (top) and height (bottom)

Figure 5.11: Relative vorticity (top row) and the geopotential height field & statically adapted orography (bottom row) at (a) day 10 and (b) day 15 with refinement criterion $|\zeta| \geq 2 * 10^{-5} s^{-1}$. The adapted blocks with refinement level 3 overlay the height field.

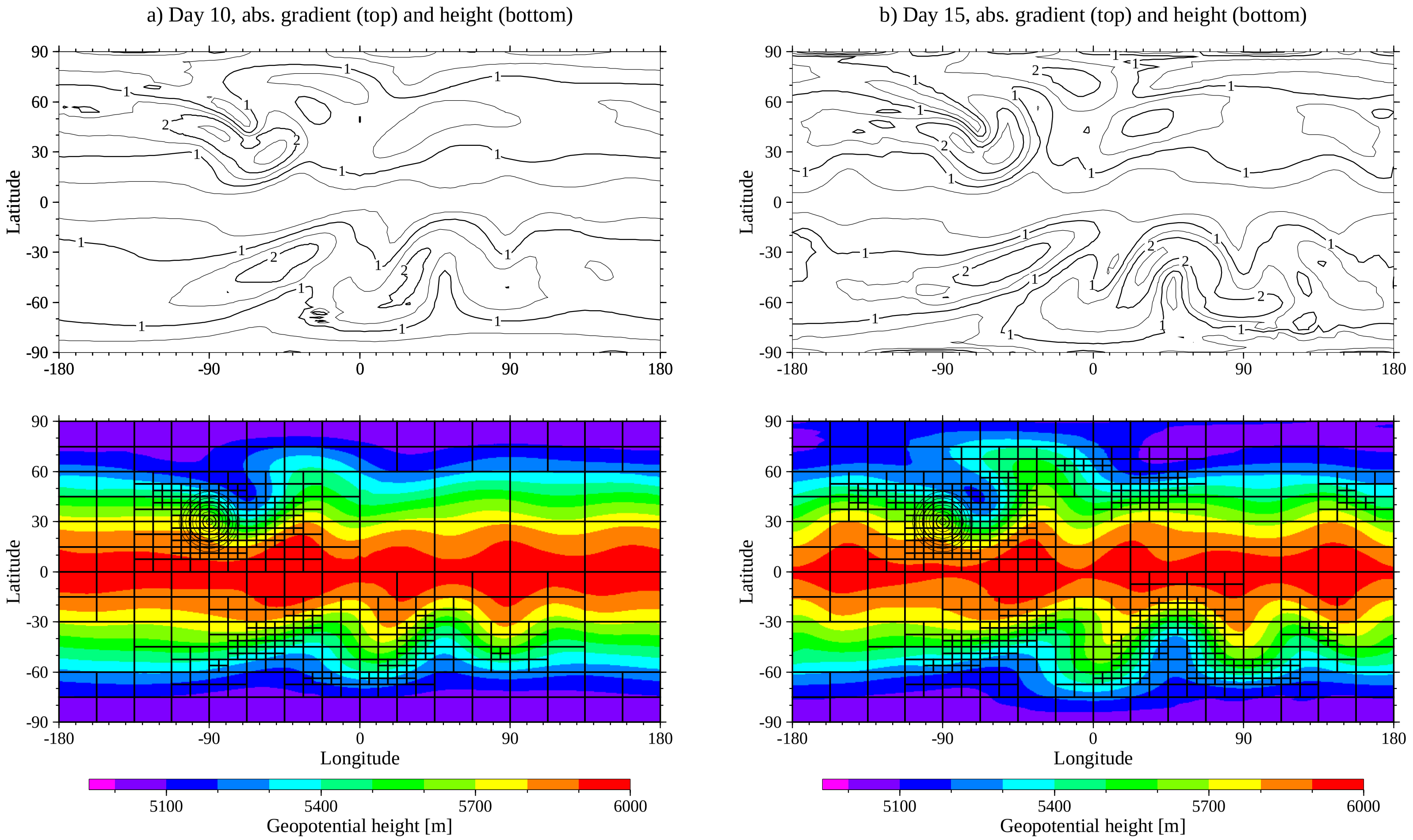

Figure 5.12: Absolute value of the geopotential gradient (top row) and the geopotential height field & orography (bottom row) at (a) day 10 and (b) day 15 with refinement criterion $|\nabla\Phi| \geq 2e^{-3} ms^{-2}$. The adapted blocks with refinement level 3 overlay the height field.

marks the frontal zones that particularly develop in the Southern Hemisphere. It reliably detects the strong gradient regimes that are again associated with the lee-side wave train in the evolving flow field. The gradient criterion consequently tends to select confined geographical areas that are clearly aligned. In comparison, the refinements based on the vorticity criterion seem to cover slightly broader areas. The number of refined blocks in the gradient-guided adaptive simulation also increases continuously due to the choice of the sensitive threshold value. In addition, there is some minor evidence of noise at high latitudes.

A second comparison of the vorticity- and gradient-based adapted simulations is provided in figure 5.13. Here the meridional velocity fields of the two adapted runs at day 15 are shown. Both fields closely resemble the NCAR reference solution, which is depicted in figure A.11 on page 232. Though this qualitative comparison suggests that the gradient-based adaptive simulation shows slightly more deviations from the reference field than the vorticity-based run. Here it must be kept in mind that the adapted runs are not expected to completely match the uniform high resolution reference state. Instead, they resolve only selected features or regions of interest at comparable high resolutions. The adaptive simulations therefore represent a true mix of the four resolutions that vary by a total factor of 8. Nevertheless, the adapted runs should be a good representation of the solution since the evolving flow field is still characterized by rather large-scale wave patterns that can be adequately captured at resolutions around $1.25^\circ - 2^\circ$.

In addition to the qualitative assessments, a quantitative comparison of the vorticity-guided simulation with a variety of uniform grid control runs is presented in figure 5.14. The figure illustrates the evolution of the l_2 and l_∞ height errors over the 15-day forecast period. Here the uniform resolution runs serve as an indi-

a) with relative vorticity criterion

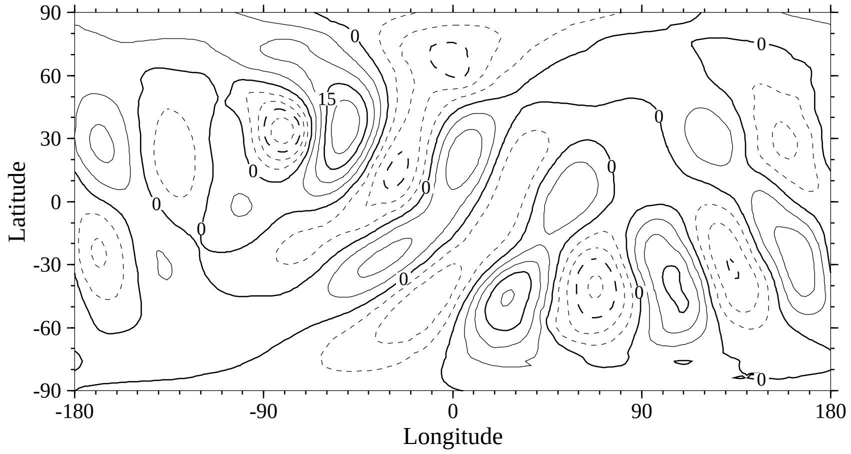

b) with geopotential gradient criterion

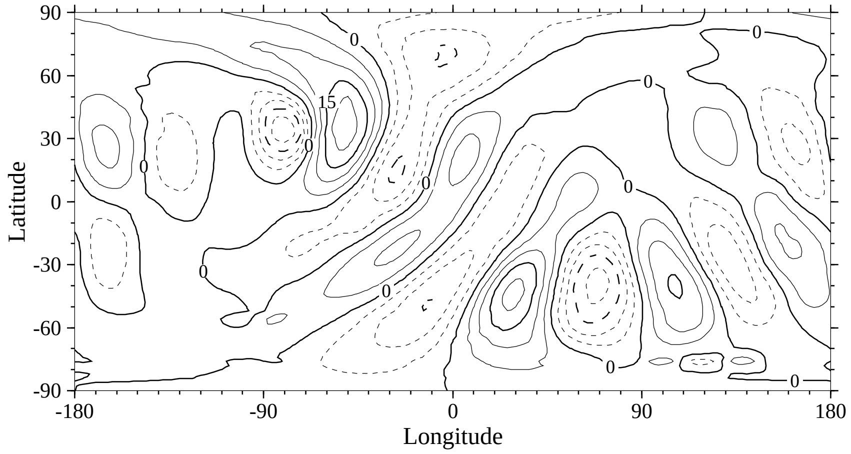

Figure 5.13: Meridional wind v at day 15. (a) Adapted run with vorticity criterion, (b) adapted run with the geopotential gradient criterion. Contour intervals are 5 ms^{-1}.

cator for the expected error margins in the adapted case. They cover the horizontal mesh resolution 5° - 0.625° that also occur in the adapted run. All model runs are

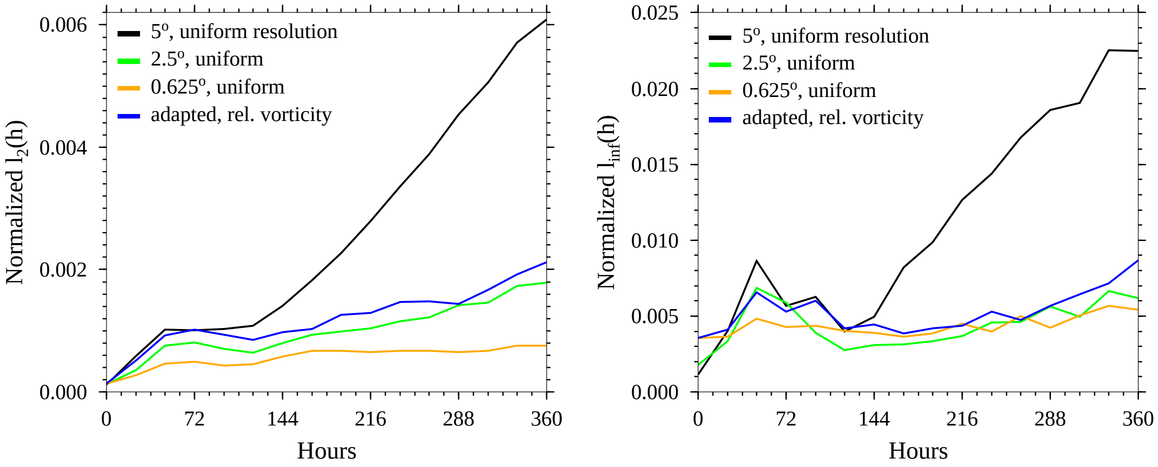

Figure 5.14: Normalized l_2 (left) and l_∞ (right) height errors for different uniform grids (at varying resolutions) and the adapted run with vorticity criterion (test case 5).

compared to the NCAR high resolution reference state. This solution has an uncertainty of 0.00072 as estimated by *Taylor et al.* [1997]. As an aside, the l_2 errors for the finite-volume model compare well to values presented in the literature e.g. by *Jakob-Chien et al.* [1995], *Taylor et al.* [1997]) and *Spotz et al.* [1998]. In figure 5.14 the errors for the uniform grid simulations show the expected convergence with increasing resolution and can be considered the upper and lower error margin for the adapted simulation. It can clearly be seen that the adapted run falls within this range. Both l_2 and l_∞ errors closely resemble the 2.5° uniform model run with respect to these global solution errors.

In practice though, this conclusion is slightly misleading since the primary goal of the adapted run presented here is not to improve the global solution error, but the local representation of features of interest. The global solution error might then decrease as a consequence of the improved local representation of the selected features, but it can not be guaranteed in a strict sense. This must clearly be distinguished. More precisely, if the global solution error is the target of an adaptive grid simulation as e.g. in *Berger and Colella* [1989] then the adaptation criterion needs to be modified. It requires the replacement of the current flow-based indicator with a numerical criterion like the truncation error estimator as in *Skamarock and Klemp* [1993]. Then the refinements can be placed in regions with the highest truncation errors that are often associated with second and third-order derivatives of the horizontal velocities. *Skamarock and Klemp* [1993] pointed out that

> Truncation errors can only be associated with flow physics in so far as interesting flow phenomena are likely to contain regions in which there are large higher order derivatives; thus, interesting flow phenomena may possibly, but not necessarily, indicate locations of large truncation error. Large truncation errors are not necessarily linked to regions of large gradients.

If a flow-based refinement criterion is selected, then the questions to be asked are

- whether the AMR results closely resemble the full grid high-resolution simulation with respect to the features of interest.

- whether the overall errors, including the newly introduced interpolation errors, are acceptable.

In addition to the error norms, global invariants also provide more general information on the model runs (see Section 4.1.2). Figure 5.15 depicts a comparison of the total energy and potential enstrophy. Here, the uniform resolution simulations are compared to the two adapted approaches with the vorticity and gradient-based

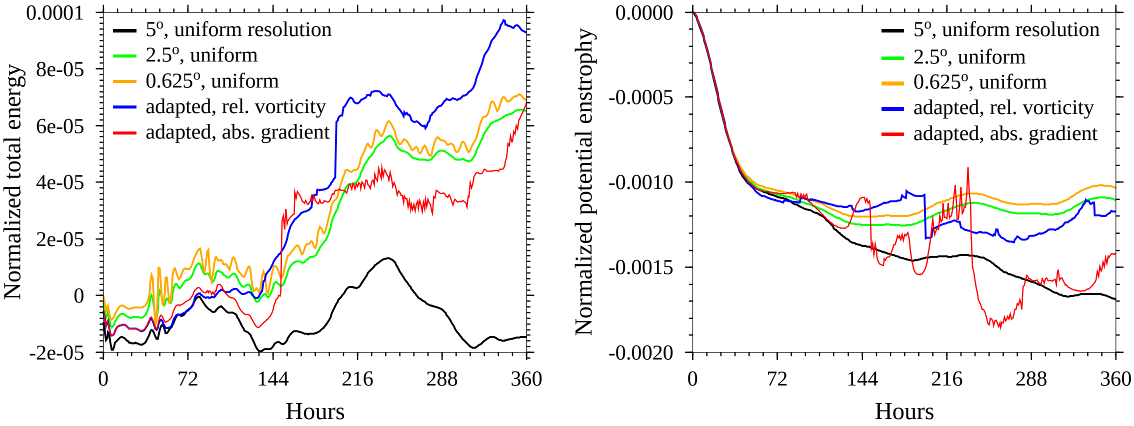

Figure 5.15: Normalized global total energy (left) and potential enstrophy (right) for different uniform grids (at varying resolutions) and the adapted runs with vorticity and geopotential gradient criteria (test case 5).

adaptation indicators. In general, it can be observed that the total energy tends to increase over time, whereas the potential enstrophy decreases moderately. As seen before, the uniform resolution simulations span a range in which the adapted runs are likely to fall. This is true in the potential enstrophy case where both adapted runs lie almost entirely in the given envelope. Further, it is approximately true for the adapted total energy curves that closely follow the trend of the high resolution uniform runs. In both cases though the adapted simulations are rather noisy.

In conclusion, both adaptation indicators perform well with respect to detecting the features of interest. They both reliably refine flow patterns that are associated with the lee-side wave train. In general, the relative vorticity criterion is recommended as the criterion of choice. It has the potential to detect the vortices in the flow early and tracks them reliably during their life time.

Dynamically adapted orography

In the preceding discussion all model runs started with a statically adapted mountain region with analytically reinitialized orography and geopotential data. This ensured that the representation of the topographic forcing was optimal with respect to the finest resolution in the adapted simulation.

In order to assess whether an adapted run can also be successfully integrated with a dynamically adapted orography field, tests are performed that only take the aforementioned vorticity adaptation criterion with threshold $|\zeta| \geq 2 \times 10^{-5} s^{-1}$ into account. The initial data are then entirely represented at the coarse $5^\circ \times 5^\circ$ resolution. As a consequence, the initial height of the mountain peak is reduced by approximately 19% on the coarse resolution mesh as the mountain top is not well-captured by the sparse grid (1955.81 m versus 1646.45 m).

In the event of dynamic adaptations in mountainous terrain, the mountain height is analytically reinitialized in order to match the refined grid. As a result, the mountain height increases if adaptations near the peak are requested by the refinement criterion. Figure 5.16 shows the resulting fully adaptive flow patterns. Here, snapshots of the geopotential height field (including orography) at day 1, 5, 10 and 15 with overlaid orography contours and block adaptations are presented. The flow field is successfully refined and undisturbed despite the adaptively varying mountain top and refined shape. It is interesting to observe, that the resulting flow patterns closely resemble the model simulations with the statically adapted mountain region (figure 5.11 on page 179). Since major parts of the mountainous terrain are refined early during the course of the integration (after 13 hours), the initial coarse representation does not strongly influence the final flow fields. In addition, no evidence of noise near the adapted mountainous terrain is noticeable.

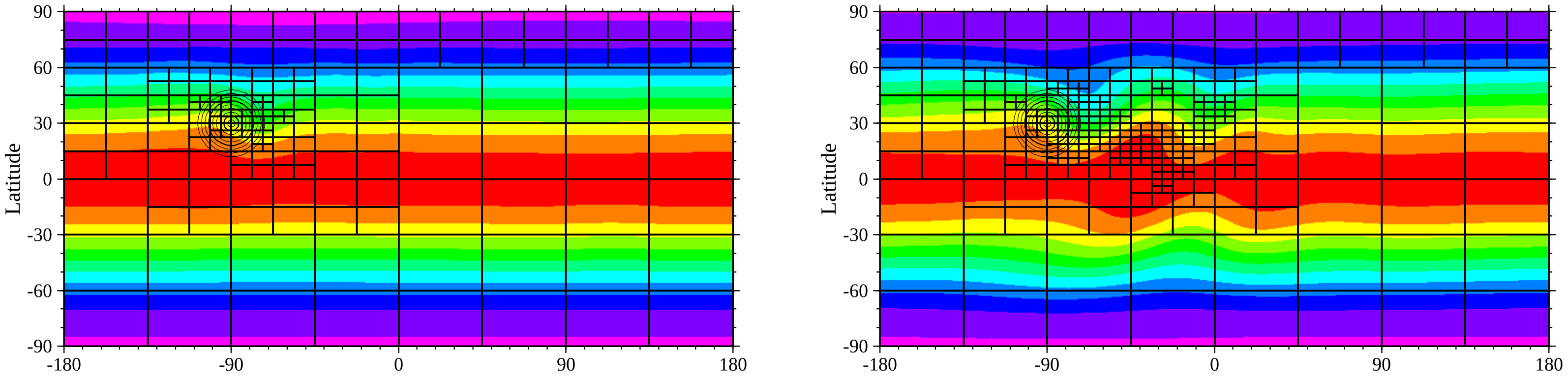

(a) Day 1

(b) Day 5

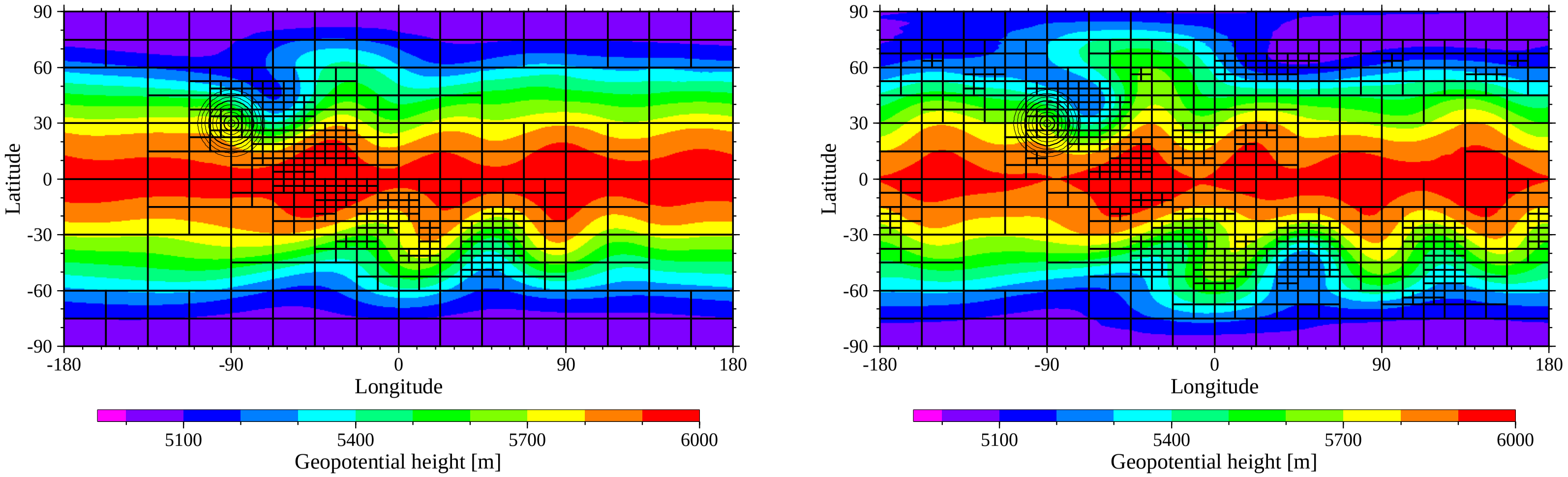

(c) Day 10

(d) Day 15

Figure 5.16: Geopotential height field & orography (dynamically adapted) at (a) day 1, (b) day 5, (c) day 10 and (d) day 15 with refinement criterion $|\zeta| \geq 2 * 10^{-5} s^{-1}$. The adapted blocks with refinement level 3 overlay the height field.

CHAPTER VI

Test of the adaptive 3D dynamical core

Dynamically adaptive general circulation models on the sphere are not standard in the atmospheric science community. So far, an adaptive dynamical core for global atmospheric general circulation models with regular data-structures has never been built before. This chapter provides insight into the newly developed adaptive finite-volume model in the 3D configuration. As in the 2D shallow water framework, the adaptations are based on the block structured data layout. They are confined to the horizontal directions so that the whole vertical column is always contained in a block. From a higher level viewpoint, the 3D model can be considered a staggered shallow water system with a floating Lagrangian vertical coordinate. All 2D adaptation principles apply.

This chapter discusses the first experiences with the adaptive 3D dynamical core. It is divided into three sections. First, a new deterministic test case for 3D dynamical cores is introduced in Section 6.1. This Jablonowski-Williamson test case describes the evolution of an idealized baroclinic wave that develops from a perturbed balanced initial state over a short 10-day forecast period. It is an ideal test example for the 3D adaptive grid simulations since the evolving wave train is confined to a small geographical area. The adaptive dynamical core is tested both in a statically and dynamically adaptive setup. In Section 6.2 statically adapted model simulations with up to three refinement levels along the storm track are assessed using the baroclinic wave test. Here new questions arise with respect to adapted orography fields in the 3D framework. In Section 6.3 the dynamically adapted simulations with one refinement level are presented. These results are based on an alternative idealized baroclinic wave test case without orography (*Polvani et al.* [2004]).

6.1 New idealized test cases for dynamical cores: The Jablonowski-Williamson test

Tests of general circulation models and, in particular, dynamical core tests are an important step towards future model improvements. They reveal the influence of an individual model design on climate and weather simulations and indicate whether the circulation is described representatively by the numerical approach.

Testing a 3D dynamical core is not straightforward even in a non-adapted case. This research topic has received increased attention in recent years. In the absence of non-trivial analytical solutions the model assessments most commonly rely on intuition, experience or model intercomparisons. Furthermore, full GCMs with physics modules are typically compared to observations. These are not available for pure dynamical core assessments that isolate the dynamics package from the physical parameterizations.

Very few standard test cases for 3D dynamical cores have been developed so far. Among them are the long-term assessments of idealized climatic states suggested by *Held and Suarez* [1994] and *Boer and Denis* [1997]. They require a 1000-day model integration with analytically specified forcing functions that replace the physics components. Typically time-mean zonal-mean flow fields are evaluated for both test scenarios that assess the model's climate and its variability. But as a consequence, the averaging of the flow patterns essentially eliminates all small-scale flow features in the analysis although they are the main contributors to the mean state. Improvements in the statistical mean state are therefore directly related to improved local representations of the flow pattern. Nevertheless, such a long-term simulation is rather impractical for the adaptive grid simulations considered here. The real strengths of the adaptive grid approach would then be masked by the averaging procedure. Therefore, short-term tests are recommended for the AMR simulations that are mainly targeted at resolving and tracking features of interest at high resolutions.

Standard techniques for short-term dynamical core assessments can only rarely be found in the literature. This is in contrast to the long history of test cases available for shallow water models. Only recently, *Polvani and Saravanan* [2000] suggested a short-term assessment technique that simulates the breakdown of the polar vortex in a 3D dynamical core. The definition of this test case was inspired by earlier 1D and 2D studies of the vortex erosion problem. These were conducted by *Juckes and McIntyre* [1987] and *Bates and Li* [1997], respectively, who applied the 1D principles to the 2D shallow water framework. In addition, *Giraldo and Rosmond* [2004] used a 3D version of the classical Rossby-Haurwitz test (*Phillips* [1959]) for dynamical core assessments. This 3D extension of the 2D shallow water Rossby-Haurwitz test was derived by *Monaco and Williams* [1975].

The lack of standard short-term dynamical core tests was one of the main motivations for the development of a new test technique that is in particular suitable for the assessment of an adaptive grid simulation. The test assesses the evolution of an idealized baroclinic wave in the Northern Hemisphere over a short 10-day period. The design principles as well as the derivation and discussion of the initial data set are presented in the following sections 6.1.1 and 6.1.2 as well as in Appendix A.3.1. A more detailed description of suitable diagnostics and a comparison of high resolution reference states are given in *Jablonowski and Williamson* [2004]. This is joint work with David L. Williamson (NCAR) who helped decide on the optimal test strategy and developed diagnostics tools. At the same time, a similar baroclinic wave test was independently developed by *Polvani et al.* [2004] (later also referenced as the Polvani test). The two tests complement each other and have created renewed interest in building a standard test suite for 3D dynamical cores in the future. Both tests, the Jablonowski-Williamson test and the Polvani test have the potential to become part of such a test suite. The Jablonowski-Williamson test has already been used for dynamical core assessment by *Giraldo and Rosmond* [2004].

6.1.1 Design of the test case

The new baroclinic wave test case has been developed for dynamical cores with pressure-based vertical coordinates. The underlying concept of this initial value test was inspired by ideas in *Hoskins and Simmons* [1975] and *Simmons and Hoskins* [1975]. In contrast to these authors though, the new idealized test is entirely described by analytic initial conditions. These allow an easy use regardless of the grid point arrangement of the selected computational grid.

The deterministic test is comprised of two parts. First, the dynamical core is initialized with steady state, balanced initial conditions that are an analytic solution to the hydrostatic primitive equations. Second, this flow is perturbed which triggers the development of a baroclinic wave train after several days. The initial flow consists of a zonally symmetric basic state with two jets in midlatitudes and a realistic temperature distribution, which are displayed in figure 6.1. Here, the atmospheric

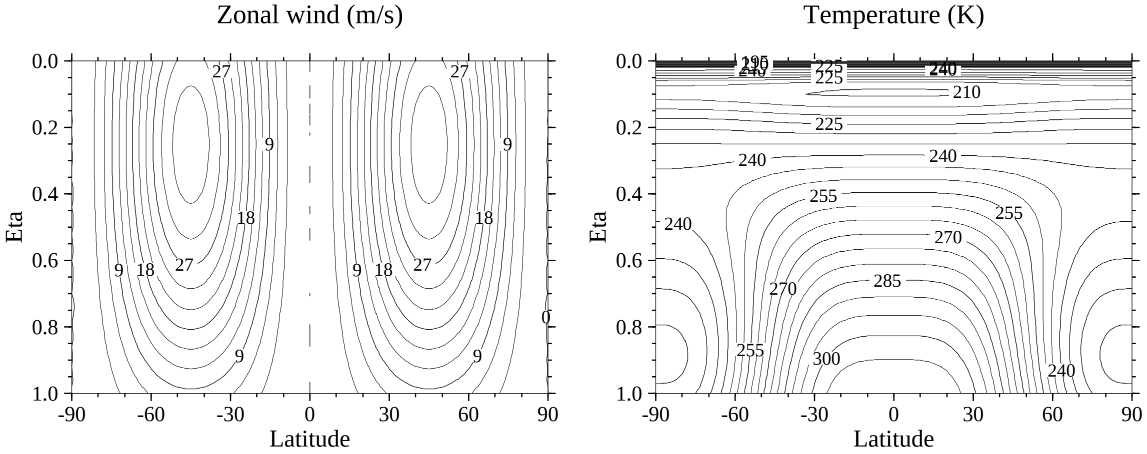

Figure 6.1: Initial zonal wind (left) and temperature field (right). Contour intervals are 3 ms^{-1} and 3 K, respectively.

conditions closely resemble the climatic state of a winter hemisphere. The centers of the midlatitudinal jets at 45° N/S are placed at the pressure level $p = 252\,hPa$, which purposely lies just below the tropopause level at $p = 200\,hPa$. Furthermore, the globally averaged temperature of this distribution is approximately $255\,K$, which matches that of the observed value in the atmosphere. The horizontally averaged temperature at the surface is selected to be $<T>= 288\,K$ which corresponds exactly to the temperature in the so-called U.S. standard atmosphere. The vertical temperature profiles are shown in more detail in figure 6.2. The figure also illustrates the geopotential of the surface orography field that is necessary to balance the initial state with non-zero wind speeds at the surface. As an aside, this is one of the differences to the *Polvani et al.* [2004] test case. It can clearly be seen that the initial temperature profiles at the equator, in midlatitudes and at the poles show the characteristic behaviors found in the atmosphere with e.g. a low level inversion at high latitudes. In addition, the stratospheric and mesospheric temperature profiles are approximated at upper levels.

The careful test design guarantees static, inertial and symmetric stability proper-

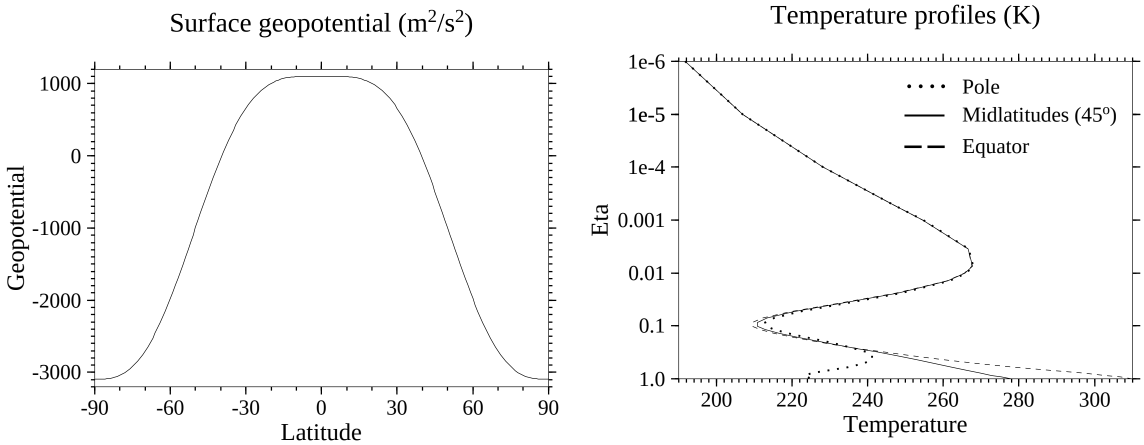

Figure 6.2: Surface geopotential (left) and temperature profiles at 0N, 45N and 90N (right).

ties, but is unstable with respect to baroclinic or barotropic instability mechanisms. These two forms of instabilities result from the vertical and horizontal wind shear characteristics. The inertial and symmetric stability criteria are analyzed in figure 6.3. The figure shows the absolute and potential vorticity fields. The flow is stable

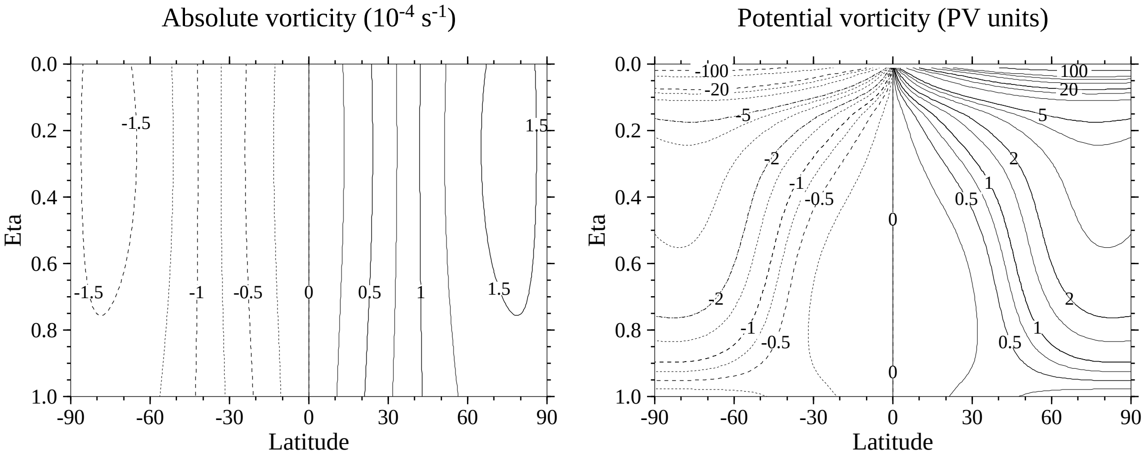

Figure 6.3: Absolute vorticity (left) and potential vorticity (right) of the initialized fields. Contour intervals are $2.5{*}10^{-5}s^{-1}$ and 0.25 PV units ($1\, PV unit = 10^{-6}\, K\, kg^{-1}\, m^2\, s^{-1}$).

with respect to inertial motions since the absolute vorticity field of the basic flow is positive in the Northern Hemisphere and negative in the Southern Hemisphere (see

Holton [1992]). The same argument holds for the potential vorticity that indicates the symmetric stability of the flow. The potential vorticity PV is assessed in form of the Ertel potential vorticity. It is defined by

$$PV_\Theta = (\zeta_\Theta + f)\left(-g\,\frac{\partial\Theta}{\partial p}\right) \qquad (6.1)$$

on constant potential temperature (Θ) surfaces. All symbols are standard (see also Appendix C). Though in figure 6.3 the potential vorticity is displayed on constant η model surfaces. This requires the application of a vertical coordinate transformation from the Θ into the η system (calculation not shown). As an aside, the η-surfaces coincide with constant pressure surfaces at $t = 0$ since there are no surface pressure variations in the initial state. Similar distributions of the Ertel potential vorticity have also been found by *Simmons and Hoskins* [1976].

The initial data set is also stable with respect to static stability. This is displayed in figure 6.4 which shows the potential temperature distribution Θ and the Brunt Väisällä (or buoyancy) frequency N. Both indicator are interchangeable. The flow is stable with respect to the static stability if the vertical potential temperature

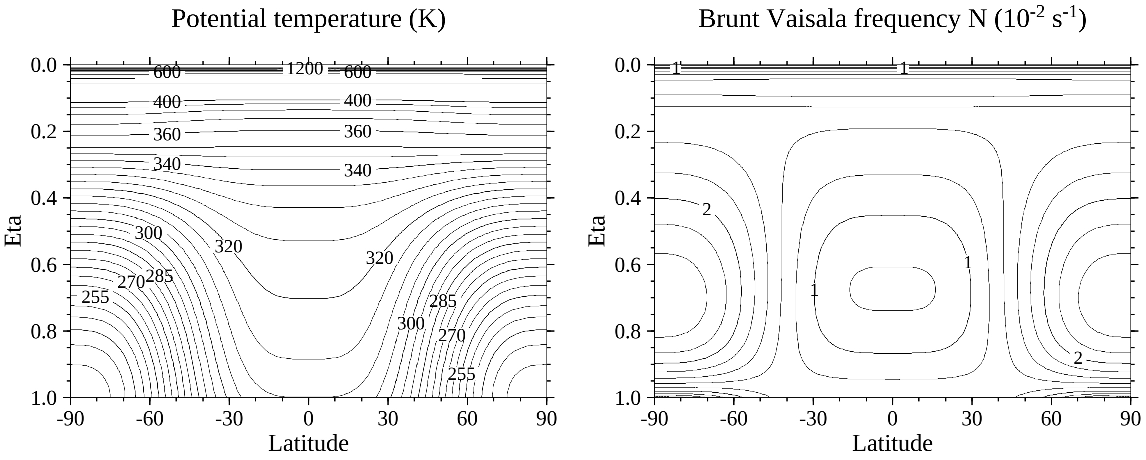

Figure 6.4: Potential temperature (left) and Brunt-Vaisala frequency N (right) of the initialized state. Contour interval for the potential temperature is 5 K in the troposphere, the contour interval for N is $2.5 * 10^{-3}s^{-1}$.

gradient $d\Theta/dz$ is positive or equivalently, if the frequency N is positive everywhere (as shown).

The initial conditions can be used for two model setups. First, the model can be initialized with the steady-state conditions and run without an overlaid perturbation. Then model integrations over e.g. thirty days reveal how well a dynamical core can keep its initial state (which is the analytical solution for this scenario). This is a stringent test of the stability of the numerical scheme. Second, a well-resolved small amplitude Gaussian hill perturbation can be superimposed on the initial state. This triggers baroclinic wave activities after several days which are characterized by explosive cyclogenesis at model day 8. In the current setup, the Gaussian perturbation as shown in figure 6.5 with a maximum amplitude of $1m/s$ is superimposed on the zonal wind field in midlatitudes at (20E,40N).

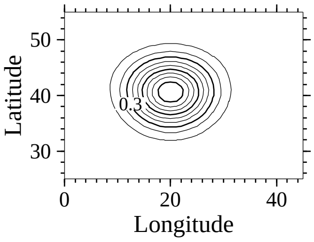

Figure 6.5: u perturbation (m/s).

6.1.2 Formal test definition and test strategy

The initial state is defined via analytic expressions. All parameters and physical constants are also listed in Appendix C and are not necessarily repeated in the following description. For a hydrostatic dynamical core with a pressure based vertical coordinate η the auxiliary variable η_v is defined by

$$\eta_v = (\eta - \eta_0)\,\frac{\pi}{2} \tag{6.2}$$

with $\eta_0 = 0.252$. In case of a vertical σ coordinate the η level in equation 6.2 can be simply replaced with the σ value. This is true for all following equations. Both representations are equivalent since there are no initial pressure variations at the surface. Expression 6.2 can also easily be modified for models with a pure pressure coordinate p. The surface pressure p_s is constant and given by

$$p_s(\lambda, \varphi) = 100000 \; Pa \tag{6.3}$$

The flow field is comprised of two symmetric zonal jets in midlatitudes. The zonal wind u and meridional wind v in m/s are defined as

$$\begin{aligned} u(\lambda, \varphi, \eta) &= u_0 \cos^{\frac{3}{2}} \eta_v \; \sin^2(2\,\varphi) && (6.4) \\ v(\lambda, \varphi, \eta) &= 0\,. && (6.5) \end{aligned}$$

Here the maximum amplitude u_0 is set to $35\,m/s$ which is close to the wind speed of the zonal-mean time-mean jet stream in the atmosphere. Furthermore, the horizontally averaged temperature $\langle\, T(\eta)\rangle$ in degree K is split into two representations for the lower (eqn. 6.6) and upper (eqn. 6.7) atmosphere. This introduces the characteristic stratospheric and mesospheric temperature profiles. Both background profiles are given by

$$\begin{aligned} \langle\, T(\eta)\rangle &= T_0\, \eta^{\frac{R_d \Gamma}{g}} && (for\ \eta_s \geq \eta \geq \eta_t) && (6.6) \\ \langle\, T(\eta)\rangle &= T_0\, \eta^{\frac{R_d \Gamma}{g}} + \Delta T\, (\eta_t - \eta)^5 && (for\ \eta_t > \eta) && (6.7) \end{aligned}$$

with the tropopause level $\eta_t = 0.2$ and the horizontal-mean temperature at the surface $T_0 = 288K$. The temperature lapse rate Γ is set to $0.005\,K/m$ which is similar to the observed diabatic lapse rate. Additionally, the empirical temperature difference $\Delta T = 48 * 10^4 K$ is chosen. The resulting temperature distribution is comprised of the horizontal-mean temperature and a horizontal variation at each level. It is given by

$$\begin{aligned} T(\lambda, \varphi, \eta) = {} & \langle\, T(\eta)\rangle + \frac{3}{4}\,\frac{\eta\,\pi\,u_0}{R_d}\; \sin\eta_v\; \cos^{\frac{1}{2}}\eta_v\; * \\ & \Bigg[\Big(-2\sin^6\varphi\,(\cos^2\varphi + \frac{1}{3}) + \frac{10}{63} \Big)\, 2\,u_0 \cos^{\frac{3}{2}}\eta_v\; + \\ & \Big(\frac{8}{5}\cos^3\varphi\,(\sin^2\varphi + \frac{2}{3}) - \frac{\pi}{4} \Big)\, a\,\Omega \Bigg]. \end{aligned} \tag{6.8}$$

The surface geopotential Φ_s in m^2/s^2 completes the description of the steady state initial conditions. The orography field balances the zonal wind field at the surface and is determined by

$$\begin{aligned}\Phi_s(\lambda,\varphi) \;\; = \;\; & u_0 \; \cos^{\frac{3}{2}}\Big((\eta_s-\eta_0)\,\frac{\pi}{2}\Big) \; * \\ & \Big[\Big(-2\sin^6\varphi\;(\cos^2\varphi+\frac{1}{3})+\frac{10}{63}\Big)\,u_0\;\cos^{\frac{3}{2}}\Big((\eta_s-\eta_0)\,\frac{\pi}{2}\Big)\; + \\ & \Big(\frac{8}{5}\cos^3\varphi\;(\sin^2\varphi+\frac{2}{3})-\frac{\pi}{4}\Big)\;a\,\Omega\;\Big]. \qquad (6.9)\end{aligned}$$

When initializing the finite-volume dynamical core with this data set the simulations have been observed to stay stable for typical time periods on the order of weeks. During this time period the basic flow remains almost unchanged despite the initial generation of gravity wave motions. They adjust the geostrophic balance in the discrete system since the analytic balanced state is not entirely balanced in a discrete representation. This is the typical geostrophic adjustment process that is characterized by decaying gravity waves.

For an irregular computational grid such as an icosahedral grid, simulations with the German weather model GME have shown that the truncation error of the numerical scheme has a wave number 5 structure. This is due to the built-in wave number 5 of the grid. It introduces small-scale wave number 5 perturbations during the steady state integration that are unstable and considerably grow over time. Such a model maintains the initial state for shorter time periods on the order of only days. The balance improves with increasing resolution. This is an artifact of the computational grid and not necessarily a model problem for a real atmospheric flow that represents the whole wave number spectrum. The effect is clearly enhanced by the idealized zonally symmetric setup. The same conclusion applies to models that utilize a cubed sphere computational grid with a built-in wave number 4, especially when using low-order numerical schemes. High-order methods postpone the breakdown of the steady-state pattern.

If possible, the unperturbed model simulations should be run without horizontal diffusion or Rayleigh friction near the model top (if implemented). Otherwise, the diffusion mechanism damps the initial data over time.

Besides the assessment of the steady state solution, the test is primarily designed to simulate a baroclinic wave. It can be triggered if the initial conditions are overlaid with an unbalanced perturbation. Here a perturbation with a Gaussian profile is selected and centered at

$$(\lambda_c, \varphi_c) = \Big(\frac{\pi}{9}, \frac{2\,\pi}{9}\Big) \tag{6.10}$$

which points to the location (20E,40N). The perturbation u'

$$u'(\lambda, \varphi) = exp\Big(- \Big(\frac{r}{R}\Big)^2 \Big) \tag{6.11}$$

with $R = \frac{a}{10}$ is superimposed on the zonal wind field at each vertical level by adding u' to u at each grid point. The great circle distance r is defined by

$$r = a \ \arccos\Big(\sin\varphi_c \ \sin\varphi + \cos\varphi_c \ \cos\varphi \ \cos(\lambda - \lambda_c) \Big) \tag{6.12}$$

where a is the Earth's radius. Typically the simulation should cover a 10-12 day time period, but simulations over longer time intervals (e.g. 30 days) have also been successfully performed. The baroclinic wave in the Northern Hemisphere starts growing noticeably around day 4 and evolves rapidly thereafter. The wave train breaks around day 9 and generates a full circulation in both hemispheres around day 20. Until day 20 the Southern Hemisphere does not show baroclinic wave activities. This makes the test ideal for adaptive grid simulations since the features of interest are well-defined and confined to the Northern Hemisphere. The adaptive grid is capable of tracking the localized wave train at high horizontal resolutions. The baroclinic wave, although idealized, represents very realistic flow features. For example, strong temperature fronts develop that are associated with the low and high pressure systems. In addition, the wave number of maximum growth rate lies between 5-9 which agrees well with observations and assessments in the literature (e.g. *Simmons and Hoskins* [1977]).

The baroclinic wave test sequence with unperturbed and perturbed initial conditions has been applied to NCAR's dynamical cores that are part of the CAM2 climate model framework. In particular, these are the NASA/NCAR finite-volume dynamical core and NCAR's semi-Lagrangian and Eulerian spectral dynamics packages. In addition, model results based on cubed meshes (Aimé Fournier, Steve Thomas, NCAR, personal communication) and icosahedral grids are available. The icosahedral dynamical core is part of the operational German weather forecast model GME. The code was kindly provided for the baroclinic wave studies by Detlev Majewski (German Weather Service, DWD). This model intercomparison and convergence studies reveal interesting flow characteristics that have already led to model improvements with respect to NCAR's semi-Lagrangian dynamical core. Typical diagnostics applied to the test results include error norm statistics, grid point data comparisons, phase shift assessments and wave number analyses that has been done in close collaboration with David L. Williamson (NCAR). Furthermore, potential vorticity analyses have been performed.

The baroclinic wave test case does not have an analytic solution, but high resolution reference solutions can be derived. This has been done during the baroclinic wave studies with NCAR's dynamical cores and GME. The comparison of all high resolution reference fields reveals that the dynamical cores converge despite their individual design and that a reference state can be recommended with a specific uncertainty estimate (see details in *Jablonowski and Williamson* [2004]). With respect to the adaptive grid simulations, the results can therefore be compared not only to the equivalent uniform resolution runs, but also to a high resolution reference simulation. Plots of uniform resolution runs generated with the NCAR/NASA finite-volume dynamical core are shown in the Appendix A.3.1.

6.2 Dynamical core tests with static adaptations

In this section, the 3D adaptive finite-volume dynamical core is assessed with a statically adaptive setup that utilizes prior knowledge of the developing flow field. The model is evaluated with the Jablonowski-Williamson baroclinic wave test case. The flow field is characterized by a baroclinic wave train in the Northern Hemisphere that is triggered by a small perturbation superimposed upon the smooth initial zonal wind field.

The adapted blocks are used to refine the pre-determined storm track in the midlatitudes (Northern Hemisphere) with increasing horizontal resolutions. The refinements are confined to the horizontal directions so that the whole vertical column is refined in the event of refinement requests. Refinements are selected at the beginning of the forecast, which is followed by an analytical reinitialization step. The convergence tests with uniform resolutions have shown that the representation of the baroclinic wave improves considerably with increasing horizontal resolution until the pattern converges at resolutions around $0.5^\circ - 1^\circ$ (see figures A.16 and A.17). It has also been observed that the flow is rather insensitive to the number of vertical levels which justifies a purely horizontal refinement strategy. The same convergence behavior is expected for the locally adapted finite-volume dynamical core.

Four scenarios are assessed that all start with the basic 8x6 block setup and 9x6 cells per block. This parameter set represents an initial $5^\circ \times 5^\circ$ grid. In addition, 26 vertical levels are selected (see Appendix B). The four simulations comprise a coarse uniform 5° run as well as adapted grid simulations with 1, 2 and 3 refinement levels. The refinements at each level then cover the whole latitudinal band structure. Snapshots of the simulations at day 8 and day 10 are shown in figures 6.6 and 6.7

Here the analysis of the baroclinic wave train is concentrated on the surface pressure field. The figures show the surface pressure patterns for all four grid setups (a-d) at day 8 and 10. In addition, the adapted blocks are overlaid that clearly illustrate the band structure of the refinement approach. The Southern Hemisphere is passive in all simulations and therefore kept at the coarsest resolution at any time. The corresponding time steps for the four model runs are determined by the gravity wave activity at the finest refinement level in the midlatitudes. In particular the chosen global time steps are $720\,s$, $360\,s$, $180\,s$ and $90\,s$, respectively. In addition, a mild filtering mechanism is applied to the wind components in tropical regions in case of subfigures (d), which show the model simulation at the highest adapted resolution. The filtering suppresses small-scale noise in the tropics and has negligible effects on the evolution of the baroclinic wave in midlatitudes. Filtering other than the regular FFT filtering in blocks adjacent to the poles and the digital Shapiro filtering poleward of 60° N/S is not applied in the coarser model runs (a) through (c). The latter two filtering strategies are identical to the mechanisms in the 2D shallow water framework.

It can clearly be seen at both model day 8 and 10 that the representation of the baroclinic wave improves significantly with an increasing number of refinement levels. The baroclinic wave intensifies as expected in the fine grid adaptive runs and

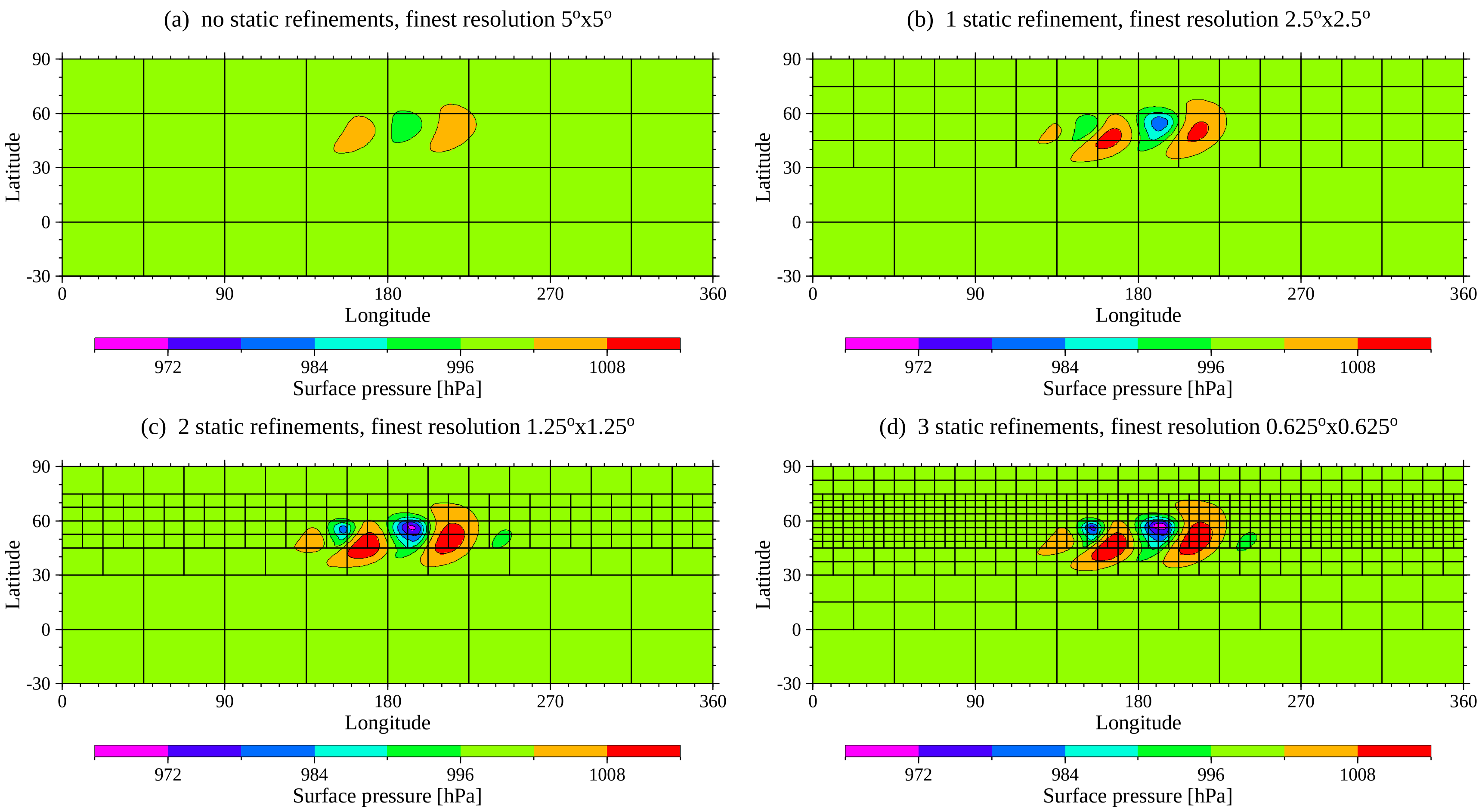

Figure 6.6: Surface pressure at day 8 for dynamical core runs with (a) no, (b) 1, (c) 2 and (d) 3 static refinements. The adapted blocks are overlaid, the finest resolution is indicated in the titles. Contour intervals are 6hPa.

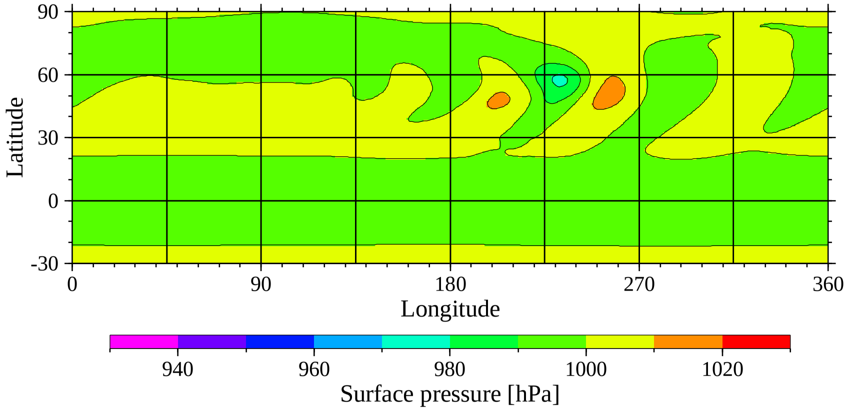

(a) no static refinements, finest resolution 5°x5°

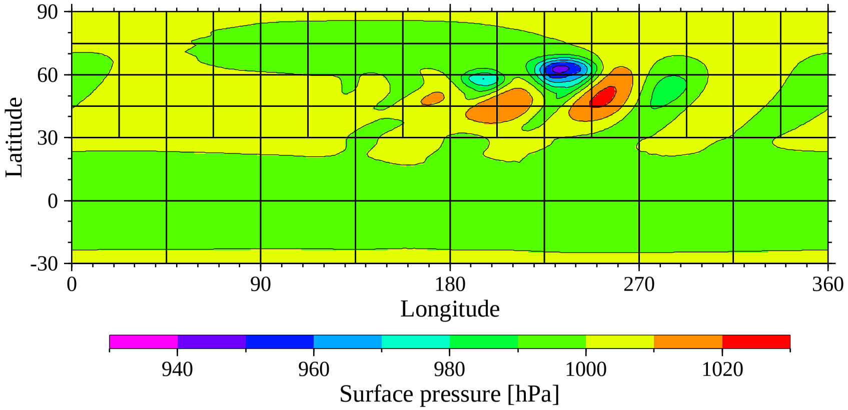

(b) 1 static refinement, finest resolution 2.5°x2.5°

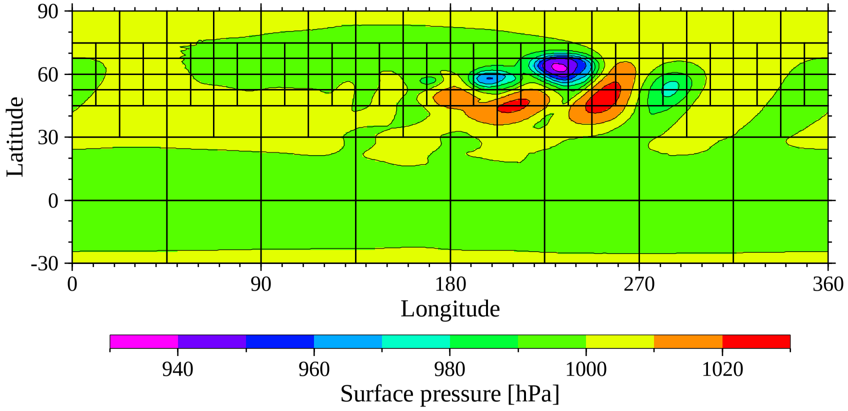

(c) 2 static refinements, finest resolution 1.25°x1.25°

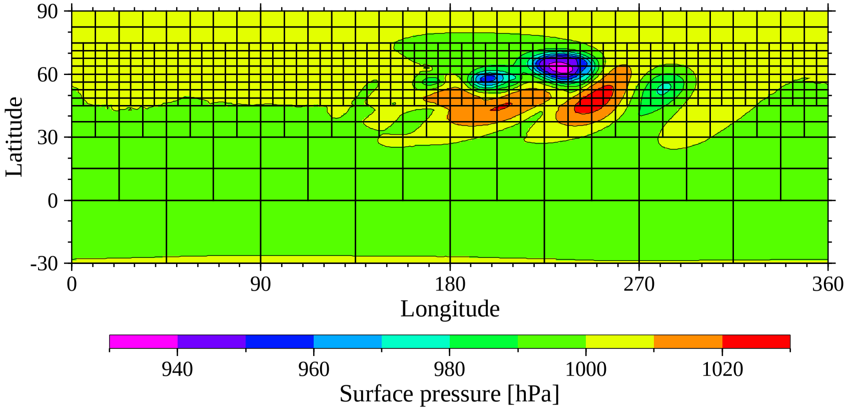

(d) 3 static refinements, finest resolution 0.625°x0.625°

Figure 6.7: Surface pressure at day 10 for dynamical core runs with (a) no, (b) 1, (c) 2 and (d) 3 static refinements. The adapted blocks are overlaid, the finest resolution is indicated in the titles. Contour intervals are 10hPa.

is rather damped on the coarse uniform 5° grid. Here the two model days represent different growth stages of the system. Model day 8 in figure 6.6 shows the wave in an explosive cyclogenesis state, whereas model day 10 in figure 6.7 depicts the wave after wave breaking events set in. After day 10 all forecasts, even on non-adapted grids, slowly start diverging from each other when predictability issues come into play.

The model results at all refinement levels compare very well to the corresponding uniform grid reference solutions. Especially the reference surface pressure fields at day 8 (figure A.16 on page 243) are almost indistinguishable from the adapted simulations (figure 6.6). Minor differences can be seen in the maximum amplitudes of the low and high pressure systems. But it must be kept in mind that the reference solutions are computed with a slightly finer grid in meridional direction that could also cause minor deviations. The same conclusions apply to the surface pressure fields at model day 10. The two highest resolutions in figure 6.7 closely resemble the reference fields in figure A.17 on page 244. Slight deviations are again detectable in the maximum amplitudes of the baroclinic wave train, especially around the position (210E,45N). No noise or distortions of the flow fields are visible in the adapted runs. The flow varies smoothly at fine-coarse grid interfaces.

An additional comparison of the surface pressure fields for both the adapted and uniform model runs is displayed in figure 6.8. The figure illustrates the time evolution of the minimum and maximum surface pressure in the global domain. Such an analysis clearly shows the convergence with increasing resolutions, but on the other hand does not indicate the spatial positions of the global extrema. Consequently, phase shifts of the baroclinic wave are possible which can be assessed in grid point space (see also *Jablonowski and Williamson* [2004]). For brevity, they are not dis-

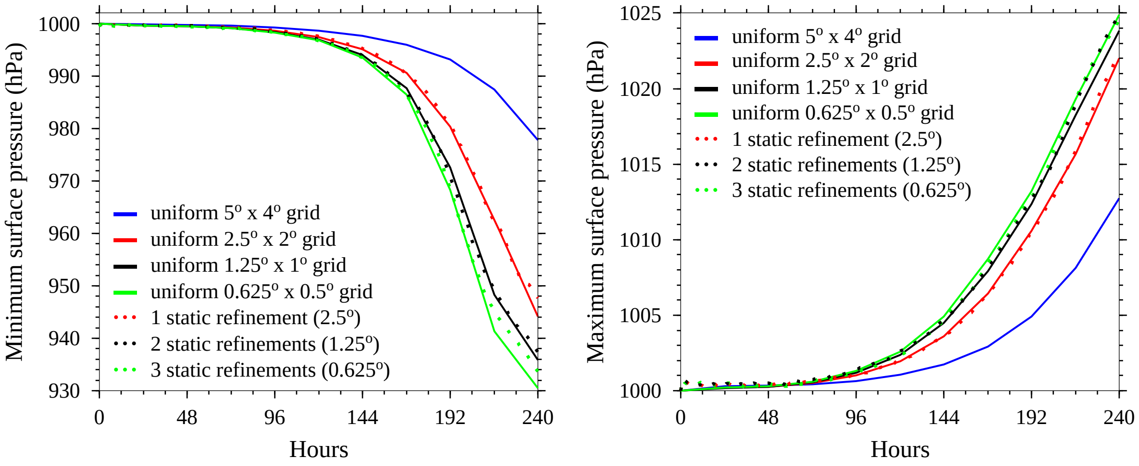

Figure 6.8: Global minimum and maximum surface pressure evolution (hPa) for runs with uniform grids and static adaptations with three different refinement levels.

cussed here. The time evolution of the extreme surface pressure values confirms that the adapted runs closely match the uniform grid reference solutions. This is in particular true for all simulations until day 8. After day 8, the minimum surface pressure in the adapted run at the highest resolution slightly diverges which could be related to the wave breaking processes in both simulations. It must be kept in mind that an exact match can not necessarily be expected since the truncation errors in the remaining coarse grid domain and the interpolation errors at the interfaces will ultimately interact with the flow field.

The static adaptation are successfully used for the 3D adaptive model assessment with band-structured refinement regions. However, attempts to relax the band structure in order to avoid the overhead in regions without significant baroclinic wave activity raised new questions concerning the underlying topography field. This problem is depicted in figure 6.9. Two refinement strategies are employed. The figures show a very early stage of the surface pressure field after eight model hours with one refinement level. In the left figure one adapted block (in red) only refines

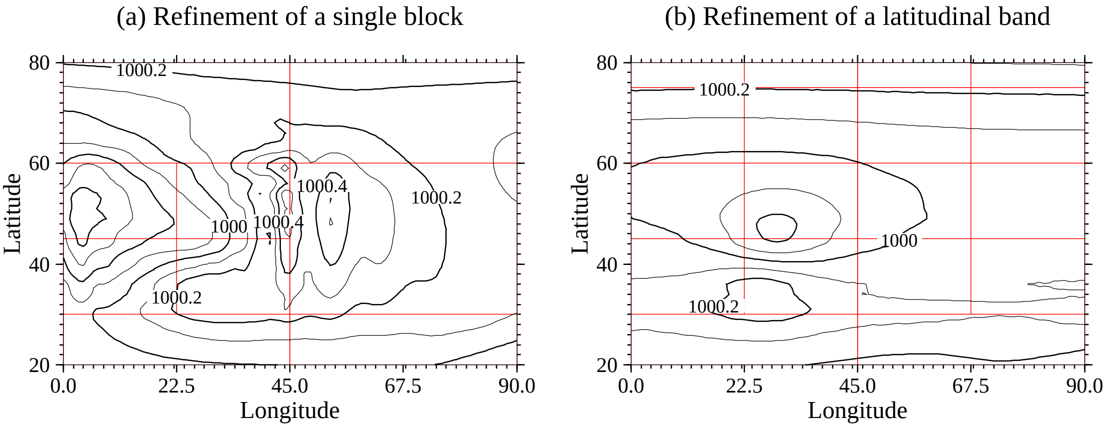

Figure 6.9: Surface pressure field after 8 hours with refinements of (a) a single block and (b) the whole latitudinal band (as in figure 6.7b).

the immediate vicinity of the initial perturbation, whereas in the right figure the whole latitudinal band is refined as discussed earlier. Both underlying orography fields are reinitialized analytically after adaptations occurred. It is important to note that there are no variations in the orography in the east-west direction, but that the orography varies smoothly in north-south direction (see figure 6.2). This north-south variation causes difficulty at the block interface in the adapted simulation with a jump in resolution in longitudinal direction. The flow accumulates mass at the eastern outflow boundary which leads to an instability after short time intervals. This effect can not be observed if the jump in the resolution only affects the north-south boundaries where there is no change in orography along the interface.

However, it is interesting to observe that dynamically adapted orography fields did not cause a problem in the 2D shallow water model as shown earlier in figure 5.16 on page 187. This observation is possibly related to the treatment of the geopotential gradient in both the 2D and 3D configurations, which represents the main difference of the two setups. It is an open research problem how to handle the orography field in the adapted regions in a 3D model simulation. So far, this aspect has not been well-documented in the literature. Only *Bacon et al.* [2000] reported on adaptive orography data and lower boundary conditions for adaptive limited-area simulations. Future research activities will address this topic further.

6.3 Dynamical core tests with dynamic adaptations

In addition to static adaptations in the 3D framework, it is of particular interest to assess the dynamically adaptive approach without prior knowledge of the flow field. This is the classical application of adaptive mesh refinements. The dynamically adapted model is tested using an alternative idealized baroclinic wave test. This test was developed by *Polvani et al.* [2004]. The underlying test strategy of the Polvani test is very similar to the Jablonowski-Williamson test case. The simulation starts with smooth balanced initial conditions that are perturbed to trigger a baroclinic wave over a 10-day forecast period. The initial data are displayed in Appendix A.3.2 on page 245. One of the main differences is that the wind speed at the surface is identically zero in the Polvani test case. Therefore the orography field is zero since there is no active flow field to be balanced. In addition, all initial data only show patterns in the Northern Hemisphere where the baroclinic wave is observed. This leads to a less realistic global initial data set, which on the other hand is irrelevant with respect to the developing wave train. Furthermore, the specification of the initial data is only partly analytic and partly based on numerical integrals.

As argued before, the evolution of a baroclinic wave train with strong gradients is an ideal test example for adaptive grid simulations. Here the baroclinic wave is triggered by perturbing the initial temperature field at each level. It must be noted that the base resolution for this test is increased in order to allow a more accurate representation of the initial data at the coarsest level. It is recommended for this test case since the initial conditions contain rather strong gradients. As a consequence, the adaptive grid simulation does not suffer from a severe underrepresentation of the initial data. The base resolution is $2.5° \times 2.5°$ with 16x12 blocks and 9x6 cells per block.

The adaptations are guided by a user-defined refinement criterion. Based on the experiences in Chapter V a vorticity-based refinement indicator at the model level closest to the surface (at approximately 992hPa) is selected. In particular, the refinement criterion for the runs depicted in figure 6.10 is set to $|\zeta| \geq 0.75 * 10^{-5} s^{-1}$ As an aside, the initial relative vorticity at the surface is zero. The rather sensitive threshold for the absolute value of the relative vorticity is chosen in order to capture the evolution of the wave early in its developing stages. Here the first adaptations occur at day 3. An alternative increased threshold such as $|\zeta| \geq 2 * 10^{-5} s^{-1}$ triggers the first refinements at model day 4. Day 4 is the point in time when the baroclinic wave enters its rapid development phase. Therefore, the increased refinement threshold does not capture the initial organization of the wave disturbance by a refined area. In practice though, a compromise must be found in order to balance the accuracy and efficiency of an adapted run.

For the dynamically adaptive 3D tests, the maximum number of refinement levels is set to 1. The integrations cover a 10-day time period and snapshots of the adaptive simulation at day 3, 4, 8 and 10 are shown in figure 6.10. The refinement region clearly captures and tracks the developing wave. As in the statically adapted case the additional resolution leads to a more accurate representation of the wave train. This can be seen in comparison to figure A.19 on page 247 that displays the comparable uniform grid solutions at day 8 and 10. The surface pressure distributions are very similar at the refined resolution 1.25°. The adapted run successfully predicts the

(a) Day 3 (b) Day 4

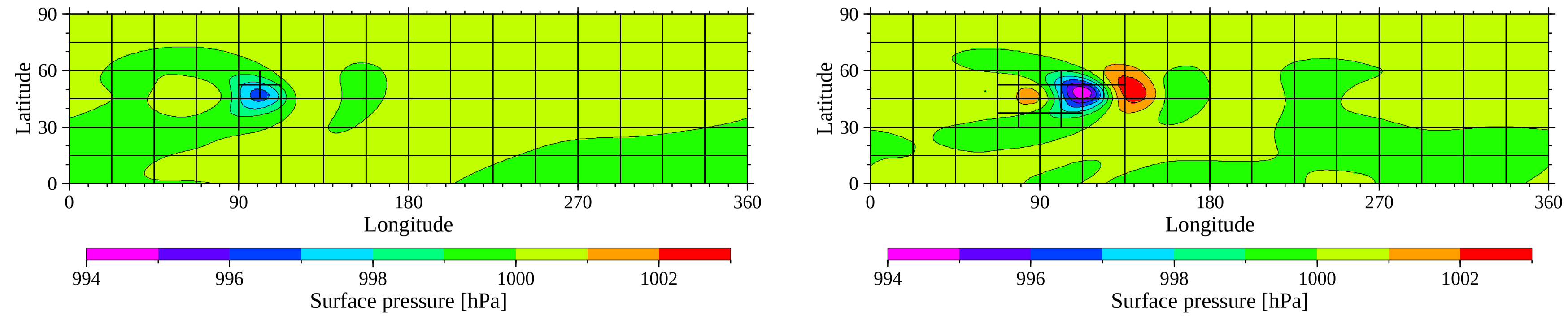

(c) Day 8 (d) Day 10

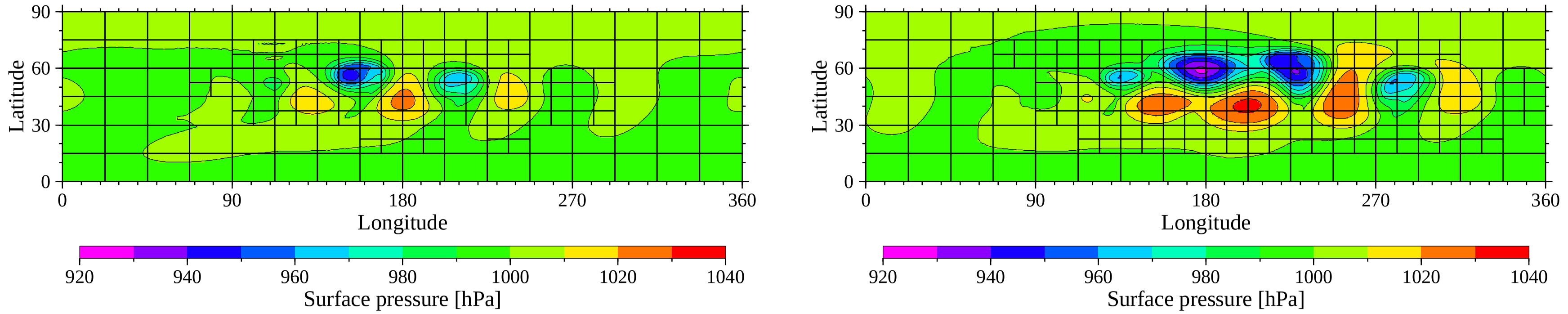

Figure 6.10: Surface pressure in the Northern Hemisphere at (a) day 3, (b) day 4, (c) day 8 and (d) day 10 for a dynamically adapted 3d model run with 1 refinement level. Refinement criterion is $|\zeta_{sfc}| \geq 0.75 * 10^{-5}s^{-1}$. Contour intervals are (a,b) 1hPa and (c,d) 10hPa.

intensification of the wave train with increased resolution. Minor differences can again be found with respect the amplitudes of the extreme values. In this test case the wave breaking event sets in after day 8 which can contribute to slowly diverging flow patterns thereafter.

Here no static pre-determined refinement regions are defined. In the event that the developing wave needs to be detected even earlier than day 3, a combination of several refinement criteria is feasible. For example, a combination of a surface pressure indicator and a vorticity-based assessment could replace the pure vorticity criterion. Initial tests with a surface pressure indicator that locates the positions of the maximum and minimum pressure centers have been successfully performed.

CHAPTER VII

Summary and future research directions

Climate and weather systems are true multi-scale phenomena that are characterized by widely varying spatial and temporal scales. Solving such a problem more efficiently and accurately requires variable resolution that tracks small-scale features embedded in a large-scale flow. This approach provides new insight into small-scale large-scale flow interactions that are unresolved by uniform grid applications. A dynamically adaptive model for global climate and weather research with regular data-structures has never been built before. So far, only irregular triangulated data have been discussed for adaptive atmospheric modeling systems (*Bacon et al.* [2002], *Gopalakrishnan et al.* [2002]) on the sphere. This dissertation is a step towards developing new adaptive methods for future weather and climate studies. It documents the design principles and successful implementation of a statically and dynamically adaptive dynamical core for general circulation models on the sphere.

The adaptive grid techniques have been applied to a revised version of NCAR/NASA's next generation dynamical core for climate and weather research. The adaptive model design is based on two fundamental building blocks, a block structured data layout and a spherical adaptive grid library. This AMR communication library for parallel processors has been newly developed at the Computer Science Department at the University of Michigan.

The adaptive dynamical core has been run in two model configurations: the full 3D hydrostatic dynamical core on the sphere and the corresponding 2D shallow water configuration that is extracted out of the 3D version. This shallow water setup serves as an ideal testbed for the horizontal discretizations and the 2D adaptive mesh strategies.

The static and dynamic adaptations have been tested using the standard shallow water suite and a newly-developed idealized 3d baroclinic wave test case. Static adaptations are used to vary the resolution in pre-defined regions of interest. This includes static refinements near mountain ranges or static coarsenings in longitudinal direction for the implementation of a so-called reduced grid in polar regions. Dynamic adaptations are based on flow characteristics and guided by refinement criteria that detect user-defined features of interest during a simulation. In particular, flow-based refinement criteria, like vorticity or gradient indicators, have been suggested. Refinements and coarsenings occur according to pre-defined threshold values.

Summary

Static and dynamic adaptations have been assessed both in the 2D and 3D model framework. The statically adaptive runs in the 2D shallow water setup show that the reduced grid with two reduction levels can be successfully used for passive advection problems. The model results are almost indistinguishable from the full grid control run. In case of nonlinear model simulations, the reduced grid performs well in case of one reduction level close to the poles, whereas the addition of the second reduction can not be recommended. The second reduction level increases the solution error in the spherical grid system to unacceptable levels. Overall, the reduced grid with one reduction is in particular a viable choice if the global time step is constrained by the advective wind speeds in polar regions. Then it allows an increase in the time step which saves computational costs despite the overhead associated with adaptations.

In addition, 2D shallow water tests with static refinements in user-determined regions of interest have revealed that refinement regions can be successfully placed at arbitrary positions within the model domain. The flow passes through the interface boundaries without noise or significant distortions for at least a 7-14 day time period. Such a time period represents the typical duration of a weather prediction forecast. After this time span grid interface effects might play a role in flow fields with strong gradients and high wind speeds. Statically adapted runs with external forcing though, present a challenge for the adaptive grid approach. Although the transport of a low pressure system has been well-simulated in the adapted runs, the noise along the boundaries prevents the overall solution error from decreasing accordingly. In future studies, the interface treatment in a forced system needs to be revisited.

Static adaptations have also been tested in the 3D dynamical core setup. For these studies, a new idealized baroclinic wave test case for short-term dynamical core assessments has been developed. The design principles and test strategies are documented in the dissertation. The test has the potential to become part of a future standard test suite for dynamical cores. The 3D evaluations of the static adaptations along the storm track have shown that the evolution of the baroclinic wave can be successfully predicted without noise or distortions at fine-coarse grid boundaries. The refinements capture the correct intensification of the wave train with increased resolution without the need of a fine resolution in the global domain.

Besides static adaptations, dynamically adaptive simulations have been successfully performed in both the 2D and 3D framework with up to four refinement levels.

The dynamically adaptive grid is able to track selected features of interest according to user-defined adaptation criteria. A variety of flow based adaptation indicators has been investigated that reliably detect features such as a lee-side wave train behind a mountain or a cosine bell in a pure advection experiment. Special attention has been paid to a relative vorticity based refinement criterion that is compared to a gradient based indicator. Both perform well in the 2D shallow water setup. For future studies, a vorticity criterion is recommended that captures the waves in an evolving flow field early. The vorticity criterion at the lowermost model level has also been used for 3D assessments of the dynamically adaptive approach. Tests with an alternative baroclinic wave test case show that the flow is well-captured with increased accuracy in the refined region. Overall, the selection of the optimal adaptation criterion and threshold is highly problem dependent and balances the efficiency and accuracy of the run. In general, significant computational savings can be made in comparison to fine-grid fixed resolution runs as shown by the timing results for the dynamically adapted advection tests.

The development of the dynamically adaptive dynamical core also raised questions concerning numerical and computational stability issues. Among them has been the so-called pole problem in a regular latitude-longitude grid that leads to the convergence of the grid lines in polar regions. The resulting extremely small grid boxes then require efficient filtering strategies. Several filtering and divergence damping techniques for the adaptive grid framework have been assessed that successfully smooth the gravity wave motions without distorting the relevant atmospheric wave patterns. Filtering has been found to be imperative for stable simulations. Furthermore, numerical questions have been addressed with respect to suitable interpolation techniques for adaptive simulations. Interpolations are necessary for split and join operations as well as for ghost cells updates along the interfaces. A variety of conservative and non-conservative techniques with increased accuracy have been investigated. A second-order scheme based on a quasi-biparabolic PPM approach is recommended for accuracy reasons. The applied interpolation scheme has been slightly modified in comparison to published techniques.

Accomplishments and highlights of the research project

Significance: Adaptive methods offer an attractive framework for future climate and weather models. For the first time, it has been shown that the adaptive grid approach can be successfully applied to a dynamical core of a GCM with regular data structures in spherical geometry. In the future, AMR has the potential to become a key technique for improved atmospheric flow simulations that resolve features of interest, like regions with strong gradients or curvature, more adequately. The keys to the success of adaptive grid methods in the atmospheric sciences lie in their parallel performance on high- speed supercomputers and high accuracy with respect to the underlying numerical scheme.

Relevance and future potential: NCAR's future climate model is likely to be based on the NASA finite-volume dynamical core and NCAR's physics package. This finite-volume dynamical core has been one of the building blocks of the adaptive grid research project. It therefore represents an essential step towards an adaptive full GCM with dynamics and physics package. Future research will address the incorporation of physics components into the model. Furthermore, a new idealized test case for dynamical cores has been developed that is targeted at short-term deterministic 3D model assessments. This test case might become a standard tool for model developers.

Collaboration: The research project has established a collaboration between the University of Michigan, the NASA Goddard Space Flight Center (GSFC) and the National Center for Atmospheric Research. In particular, the science team supporting the research consisted of Joyce E. Penner and Michael Herzog[1], Robert Oehmke and Quentin F. Stout[2], Bram van Leer and Ken Powell[3], Shian-Jiann Lin and Kevin Yeh[4], and David L. Williamson[5].

Interdisciplinary research: This project involves interdisciplinary ideas and requires knowledge of atmospheric science, computer science and numerical techniques. It ideally combines global climate modeling aspects, the newest parallel and high performance computing techniques and advanced numerical methods pioneered for CFD applications in other disciplines. The adaptive model is based on the physical-motivated finite-volume approach and is designed for distributed-memory parallel computer architectures.

Future research direction

Dynamic grid adaptations for climate and weather applications are a current research topic for the atmospheric science community. New studies are under way at NCAR, the University of Cambridge, UK and the Center for Atmospheric Physics (Science Applications International Corporation, Virginia, USA). The promising results of this dissertation and the efforts of the community will help answer the open

---

[1] Atmospheric Science, University of Michigan, Ann Arbor

[2] Computer Science, University of Michigan, Ann Arbor

[3] Aerospace Engineering, University of Michigan, Ann Arbor

[4] NASA/GSFC, Data Assimilation Office, Greenbelt, Maryland

[5] NCAR, Climate and Global Dynamics Division, Boulder, Colorado

question whether AMR can be successfully used in full GCMs with dynamics and physics components. Incorporating physics into an adaptive model represents a challenging research problem. So far, only *Bacon et al.* [2000] and *Gopalakrishnan et al.* [2002] have included a complete physics package in their adaptive modeling system OMEGA. As observed by *Skamarock and Klemp* [1993], the truncation error estimates in adaptive grid simulations with parameterized mixing do not exhibit the expected rate of decrease when refining the mesh. Even error increases were apparent that can not be found in dynamical core simulations without parameterized physics. As a consequence. a fundamental concern in adaptive mesh applications is the validity and consistency of grid-scale dependent physical parameterizations that are used over a wide range of refinement levels. Two aspects need to be considered. On the one hand, grid-dependent model parameters like the horizontal diffusion coefficient are no longer optimal or even valid when changing the mesh resolution. On the other hand, it is unclear at what grid scale the parameterizations like convection or turbulence packages become unnecessary or even detrimental.

In addition, the influence of the lower boundary conditions in adaptive mesh applications is of equal importance. Atmospheric models rely on worldwide data sets for the surface elevation, land/water coverage, soil types, land use, deep soil temperatures, deep soil moisture and sea surface temperatures at varying grid resolutions. These are used to derive important secondary parameters such as the surface roughness and albedo. Therefore, in adaptive mesh applications the treatment of the refined lower boundary conditions needs to be carefully addressed in order to improve the overall accuracy. A starting point for future research efforts could be the assessment of adaptive orography based on experiences with nested grid models (*Zhang et al.* [1986] and *Fox and Maskell* [1995]) and the adaptive modeling system OMEGA

(*Bacon et al.* [2000]). The latter provides routines and data bases for dynamically adaptive lower boundary conditions.

From a computational standpoint, future developments could include a new load-balancing strategy for the AMR communication library that is based on the space-filling curve approach. Furthermore, library support for adaptive time steps is desirable that allows different time steps for each refinement level. This reduces the overhead of the adaptive simulation. In addition, refinements in the vertical direction might become imperative for very high horizontal resolutions, especially if the underlying equations are switched from a hydrostatic to a non-hydrostatic regime.

In conclusion, in the future dynamically and statically adaptive mesh refinements are feasible for short-term weather predictions. A statically refined model could possibly replace today's nested grid approaches for improved local weather forecasts. It furthermore guarantees consistent boundary conditions that do not violate the conservation principles across interfaces. Dynamically adaptive techniques could add extra flexibility to a weather prediction system that allows, for example, the tracking of low pressure centers in the global domain. Static adaptations in predetermined regions of interest, especially near mountain ranges, are also a viable option for long-term climate predictions with a regional focus.

On the other hand whether dynamic adaptations can be successfully applied to climate simulations remains an open research question that needs to identify the features of interest for long-term climate assessments.

APPENDICES

APPENDIX A

Overview of the 2D shallow water and 3D dynamical core test set

A.1 The standard test suite for the 2D shallow water equations

The standard test suite for the shallow water equations in spherical coordinates has been proposed by *Williamson et al.* [1992]. It comprises a collection of 7 test cases with increasing complexity which have been designed by various authors. Here, six of the seven test scenarios have been used in order to assess the performance of the adaptive finite-volume dynamical core. In addition, a shallow water test case suggested by *McDonalds and Bates* [1989] has been applied. All test cases start with analytic initial data sets that are briefly described in the following section. A general overview of the shallow water test results is provided by *Jakob et al.* [1993].

A.1.1 Test case 1: Advection of a cosine bell

Test case 1 assesses the advection scheme in isolation and does not deal with the complete nonlinear shallow water equations. In this two-dimensional solid body rotation test case a cosine bell is passively advected around the sphere at various rotation angles α to the equator. The nondivergent velocity is defined by

$$u = u_0 (\cos\alpha \, \cos\varphi \, + \, \sin\alpha \, \cos\lambda \, \sin\varphi) \tag{A.1}$$

$$v = -u_0 \, \sin\alpha \, \sin\lambda \tag{A.2}$$

where $u_0 \approx 38.61ms^{-1}$ (details in *Williamson et al.* [1992]). The initial distribution of the geopotential height field h is given by

$$h(\lambda, \varphi) = \begin{cases} \left(\frac{h_0}{2}\right)\left(1 + \cos(\pi r/R)\right) & if \;\; r < R \\ \\ 0 & if \;\; r \geq R \end{cases} \tag{A.3}$$

with the peak amplitude $h_0 = 1000m$. r is the great circle distance between a position (λ, φ) and the center of the cosine bell, initially set to $(\lambda_c, \varphi_c) = (3\pi/2, 0)$. The orography h_s is set to zero. The numerical scheme is expected to translate the cosine bell without any change in shape. The true solution can be analytically computed when updating the position of the cell center (see also the trajectory calculation in Section 4.1.3).

The initial cosine bell and the zonal wind field for $\alpha = 0°$ are displayed in figures A.1 and A.2. The meridional wind v is zero for $\alpha = 0°$.

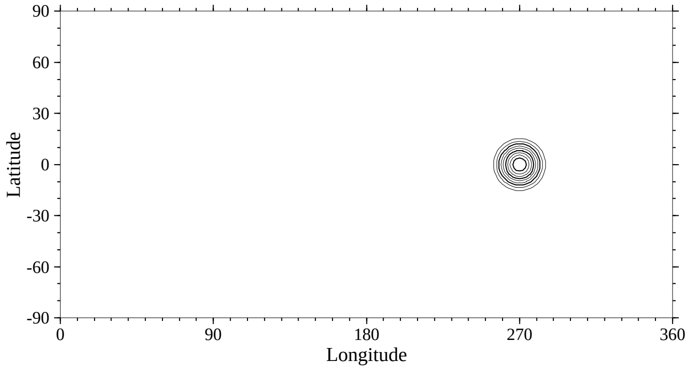

Figure A.1: Initial geopotential height (and reference solution after 12 days) of the cosine bell. Contour interval is 100 m, the zero contour is omitted.

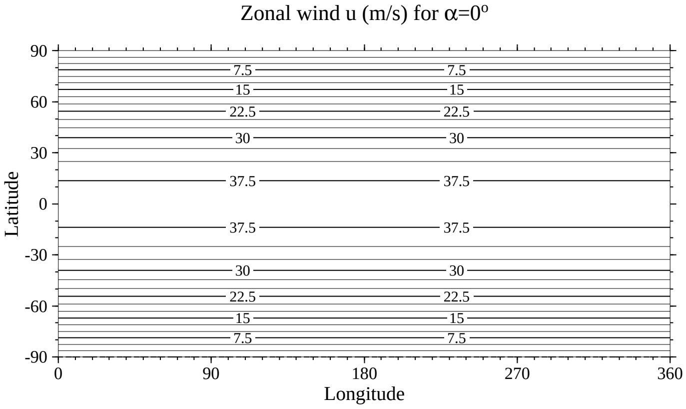

Figure A.2: Zonal wind u for $\alpha = 0°$. Contour interval is 2.5 ms^{-1}.

Figure A.3 on the next page displays the advective wind components for the rotation angles $\alpha = 45°$ and $\alpha = 90°$. Then the wind field advects the feature slantwise ($\alpha = 45°$) or across the poles ($\alpha = 90°$) around the sphere.

A.1.2 Test case 2: Steady state geostrophic flow

Test case 2 is a steady state solution to the nonlinear shallow water equations. It is comprised of a solid body rotation with a balanced geostrophic height field. As in test 1, several rotation angles α can be specified which then require the recalculation of the Coriolis parameter f. The wind field is identical to the wind definitions in test case 1 (eqn. A.1 and A.2). The analytic geopotential $\Phi = g\,h$ is defined by

$$gh = g\,h_0 - \left(a\,\Omega\,u_0 + \frac{u_0^2}{2}\right) * \left(-\cos\lambda\,\cos\varphi\sin\alpha + \sin\varphi\,\cos\alpha\right)^2 \tag{A.4}$$

with $g\,h_0 = 2.94 \times 10^4 m^2/s^2$ and u_0 as in test case 1. The reference solution or true solution at any time is the initial data set. The initial geopotential height fields for the rotation angles $\alpha = 45°$ and $\alpha = 90°$ are shown in figures A.4 and A.5 on page 227. The corresponding initial wind fields are displayed in figure A.3 (test cases 1 & 2).

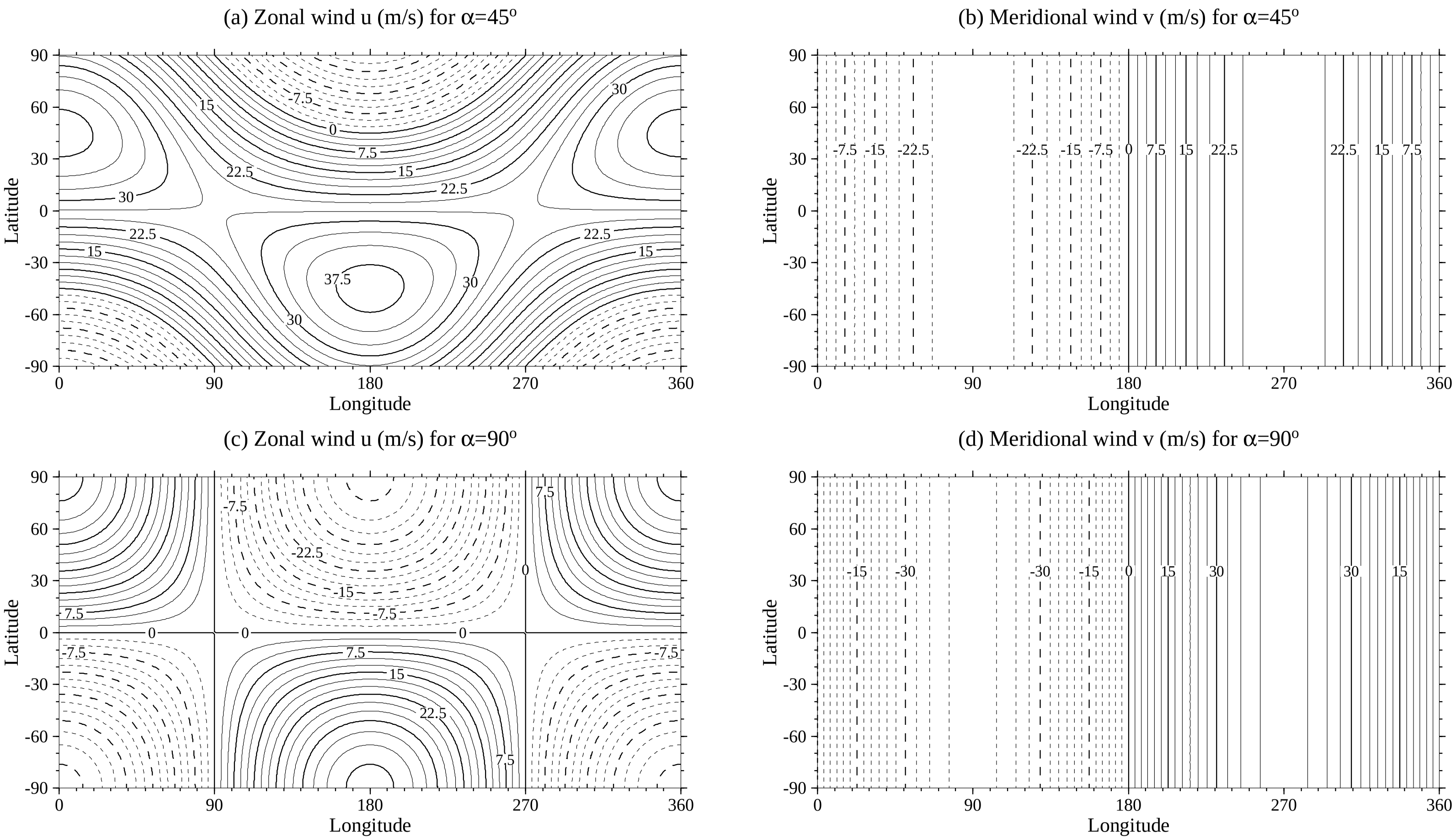

Figure A.3: (a,c) Zonal wind u and (b,d) meridional wind v for different rotation angles α. Top row (a,b): $\alpha = 45°$, bottom row (c,d): $\alpha = 90°$. Contour intervals are 2.5 ms^{-1} (test cases 1 & 2).

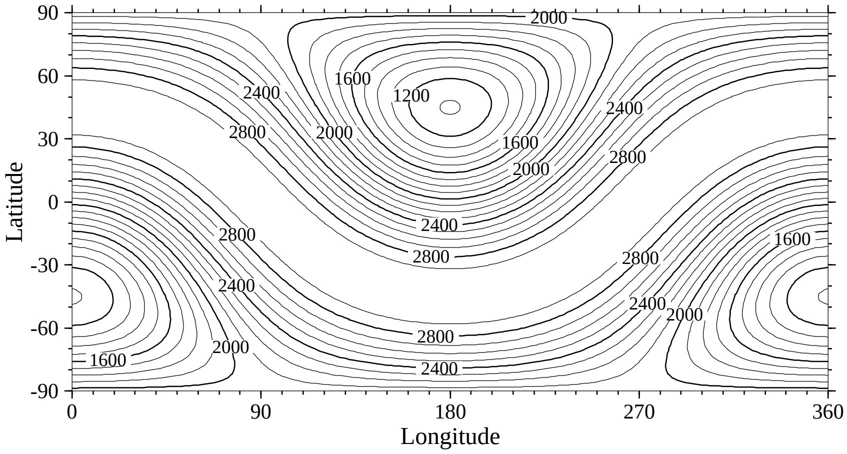

Figure A.4: Initial geopotential height and reference solution of test case 2 with $\alpha = 45°$. Contour interval is 100 m.

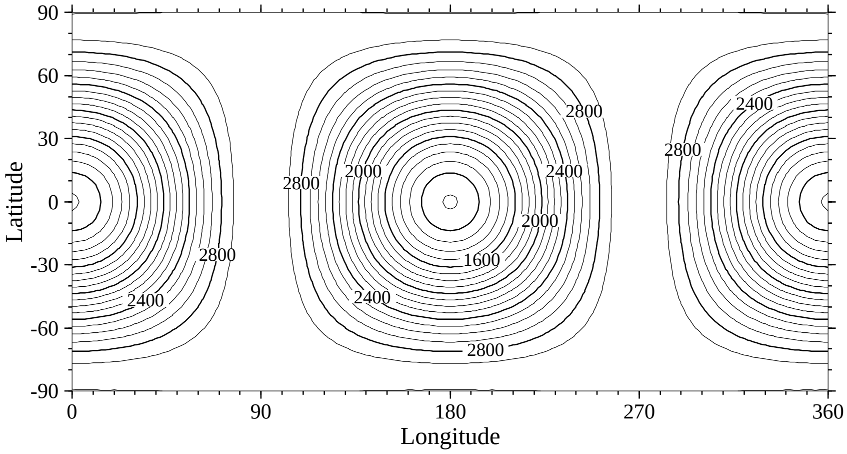

Figure A.5: Initial geopotential height and reference solution of test case 2 with $\alpha = 90°$. Contour interval is 100 m.

A.1.3 Test case 3: Steady state geostrophic flow with compact support

Test case 3 is similar to test case 2 as it defines a steady state flow field that should remain constant during the course of the integration. Here, the wind field is nonzero only in a limited region. The rotation angle has been set to $\alpha = 0°$. Then the initial conditions describe a zonal flow whose u and h profiles are illustrated in figure A.6. The meridional wind is zero. In this test case, the geopotential height can no longer be evaluated analytically but with a numerical integration method (e.g. trapezoidal rule). The initial conditions are also the reference solution (see details in *Williamson et al.* [1992]. The height of the mountain h_s is zero.

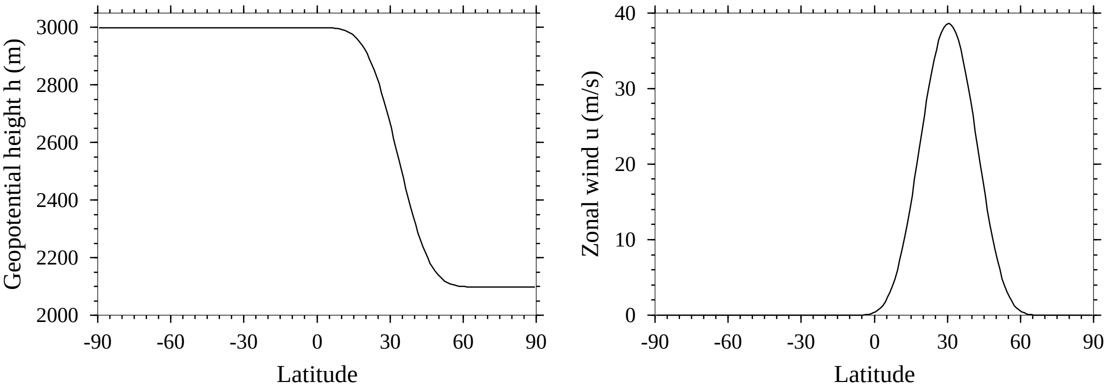

Figure A.6: Initial latitudinal profiles and reference solutions of the geopotential height (left) and the zonal wind u (right).

A.1.4 Test case 4: Forced nonlinear system with a translating low

The flow field of test case 4 is the solution to a forced shallow water system where the right hand sides of the equations 2.1 and 2.2 are replaced with the time-dependent forcing functions F_h, F_u and F_v (see *Williamson et al.* [1992]). The flow is a translating low pressure center in the Northern Hemisphere which is superimposed on a symmetric jet stream about the equator. The maximum translating wind speed is $u_0 = 20m/s$. The initial and analytic solution at day 5 of the geopotential height field are displayed in figure A.7. The reference position (λ, φ) of the low pressure center at day 5 is $77.7^\circ\, E, 45^\circ\, N$. The orography field is set to zero.

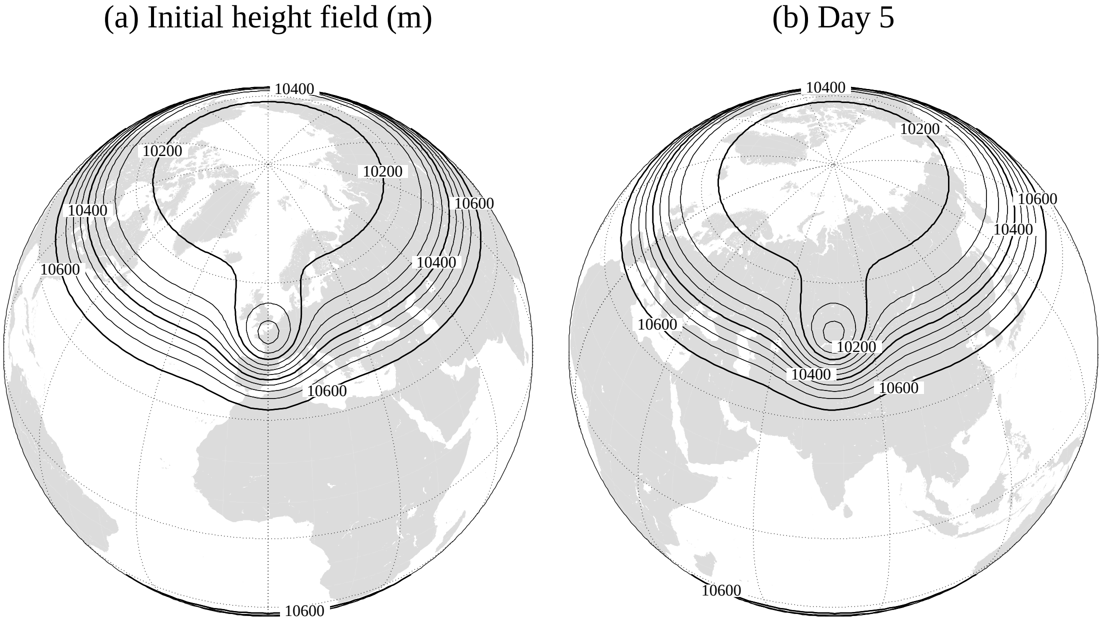

Figure A.7: (a) Initial geopotential height and (b) analytic reference solution after 5 days plotted on an orthographic projection centered at 45N and the longitude of the through ((a) 0E and (b) 77.7E). The contour intervals are 100 m.

A.1.5 Test case 5: Flow over a mountain

Test case 5 consists of a zonal flow over an isolated mountain on the Northern Hemisphere. The wind components and geostrophic initial height field are defined as in test case 2 with $\alpha = 0^\circ$, but $h_0 = 5960m$ and $u_0 = 20m/s$. The height of the mountain is given by

$$h_s = h_{s0}\,(1 - r/R) \tag{A.5}$$

where $h_{s0} = 2000m$, $R = \pi/9$ and $r^2 = \min[R^2, (\lambda - \lambda_c)^2 + (\varphi - \varphi_c)^2]$. The center of the mountain is placed at $(\lambda_c, \varphi_c) = (3\pi/2, \pi/6)$. The initial geopotential height and orography fields are depicted in Chapter V in figure 5.9 on page 174. The initial meridional wind v is zero and the initial zonal wind profile u is shown in figure A.8.

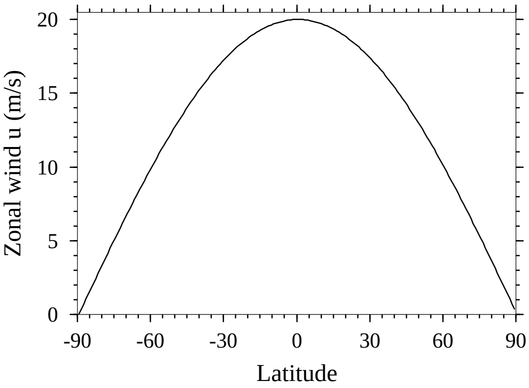

Figure A.8: Initial latitude-height profile of the zonal wind u.

The initial flow is not in geostrophic equilibrium with the topography, resulting in gravity waves of significant amplitude. Over time a complex flow pattern develops that illustrates the evolution of a lee-side trough with subsequent wave trains. This flow field does not have an analytic solution. Therefore, a high resolution reference solution in form of spectral expansion coefficients has been provided by NCAR (see also explanations in Section 4.1.3 on page 117 and *Jakob et al.* [1993]). The NCAR reference solutions for the geopotential height plus orography field at day 10 and 15 are presented in figure A.9 on the next page. The mountain is overlaid for illustration purposes. In addition, figures A.10 and A.11 on page 232 show the NCAR reference solution for the wind components u and v at day 15.

These reference flow fields are used for the computation of the normalized error norms in Chapter V.

a) Day 10

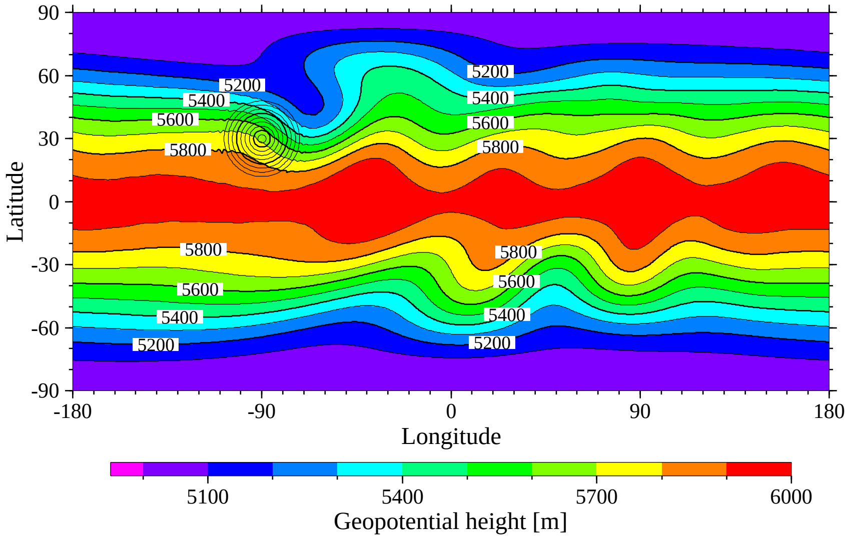

b) Day 15

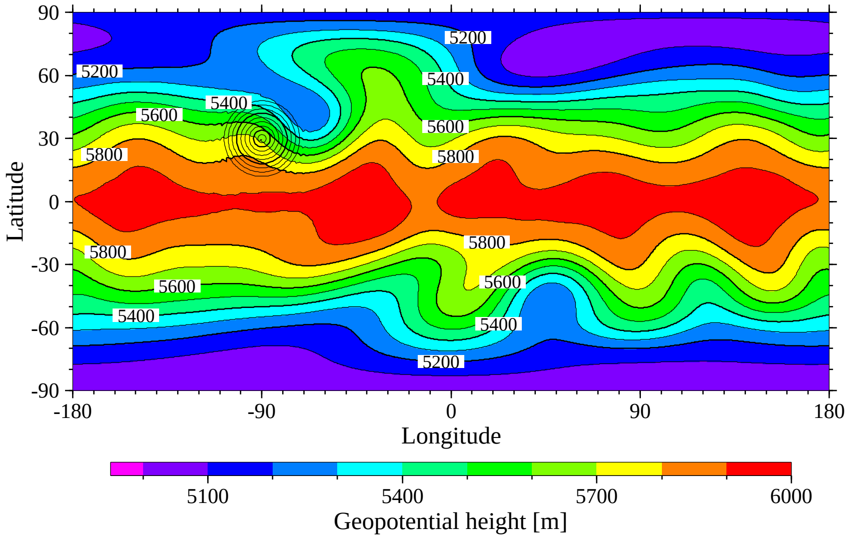

Figure A.9: NCAR reference solution of $h = h^* + h_s$ (geopotential height plus orography) at (a) day 10 and (b) day 15. The mountain is overlaid for illustration purposes.

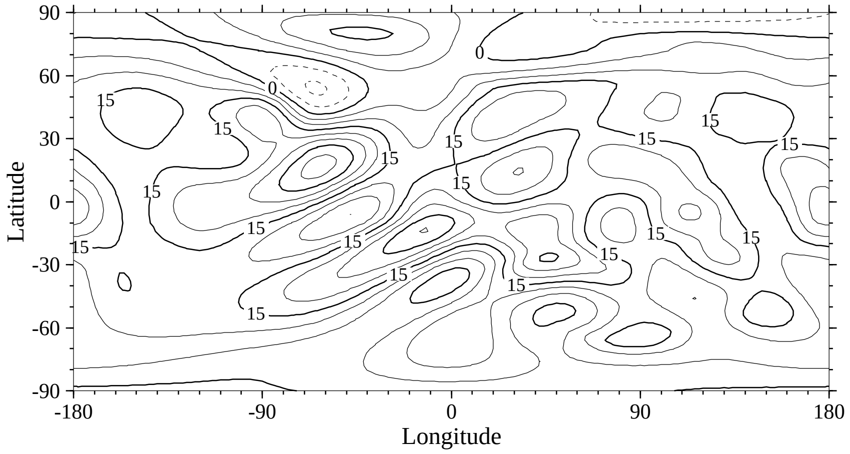

Figure A.10: NCAR reference solution of the zonal wind u at day 15. Contour interval is 5 ms^{-1}.

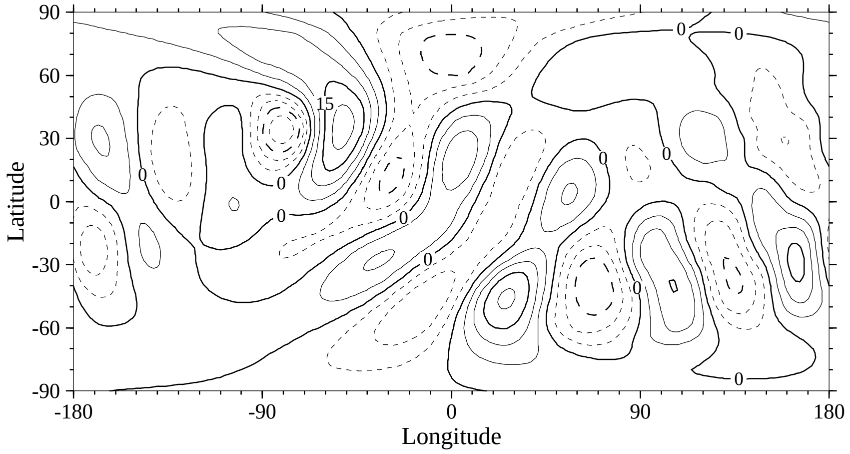

Figure A.11: NCAR reference solution of the meridional wind v at day 15. Contour interval is 5 ms^{-1}.

A.1.6 Test case 6: Rossby-Haurwitz wave

Shallow water test case 6 comprises a Rossby-Haurwitz wave with wavenumber 4 which is an analytic solution to the nonlinear barotropic vorticity equation on the sphere. However, the flow field is not an analytic solution of the shallow water equations but has been used many times for shallow water model assessments.

The initial h and nondivergent u and v fields are defined by analytic expressions (see *Phillips* [1959] or *Williamson et al.* [1992]) which describe a global wavenumber 4 pattern. This flow field is depicted in figure A.12 on the next page. During the course of the integration the pattern moves from west to east without change of shape. The orography field is set to zero.

As in test case 5, the reference solutions to test case 6 are provided by high resolution spectral model integrations (NCAR). The corresponding flow fields of the geopotential height h at day 7 and 14 as well as the wind components u and v at day 14 are shown in figure A.13 on page 235.

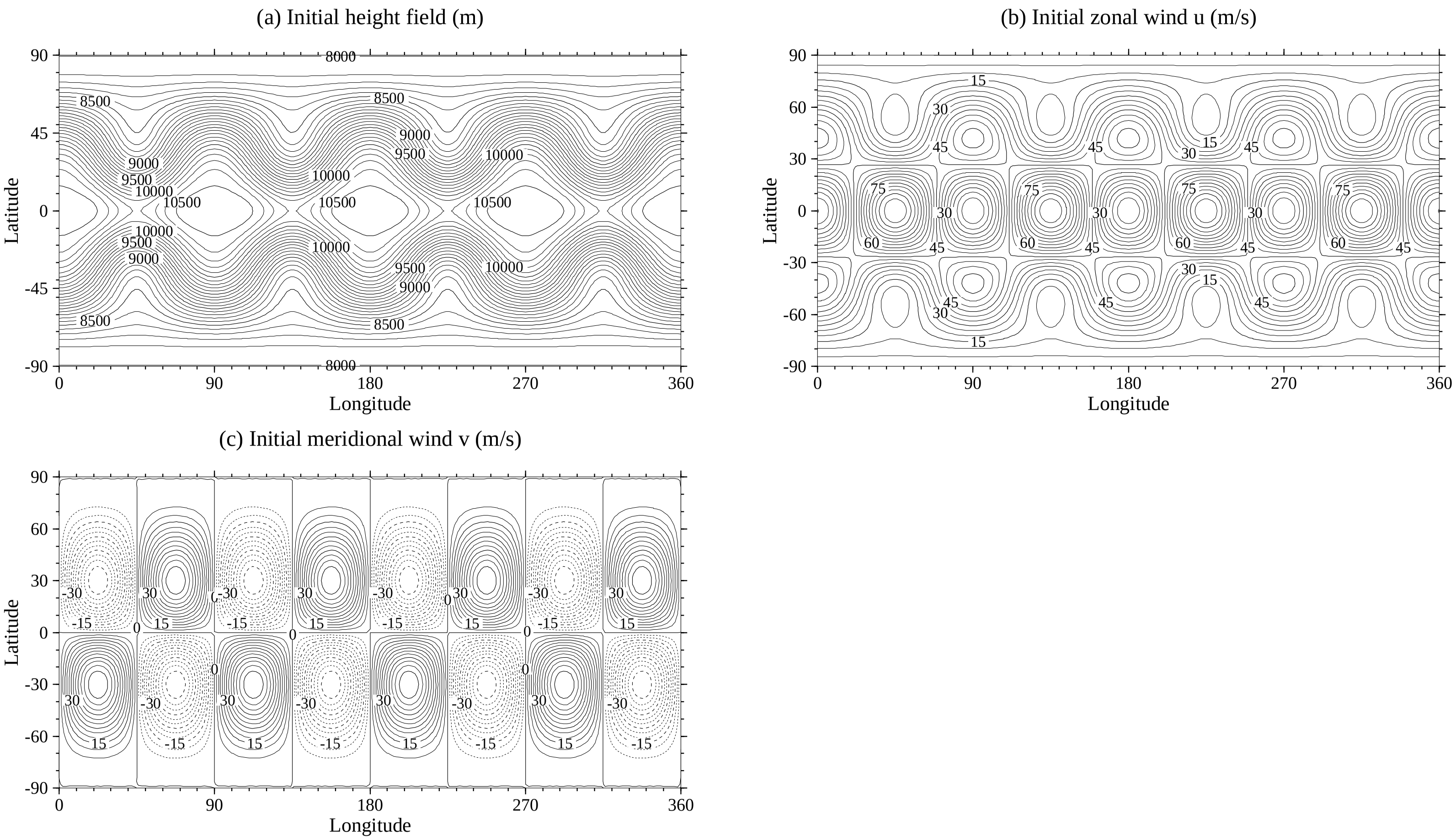

Figure A.12: Initial (a) geopotential height, (b) zonal wind u and (c) meridional wind v for test case 6. Contour intervals are (a) 100 m and (b,c) 5 ms^{-1}.

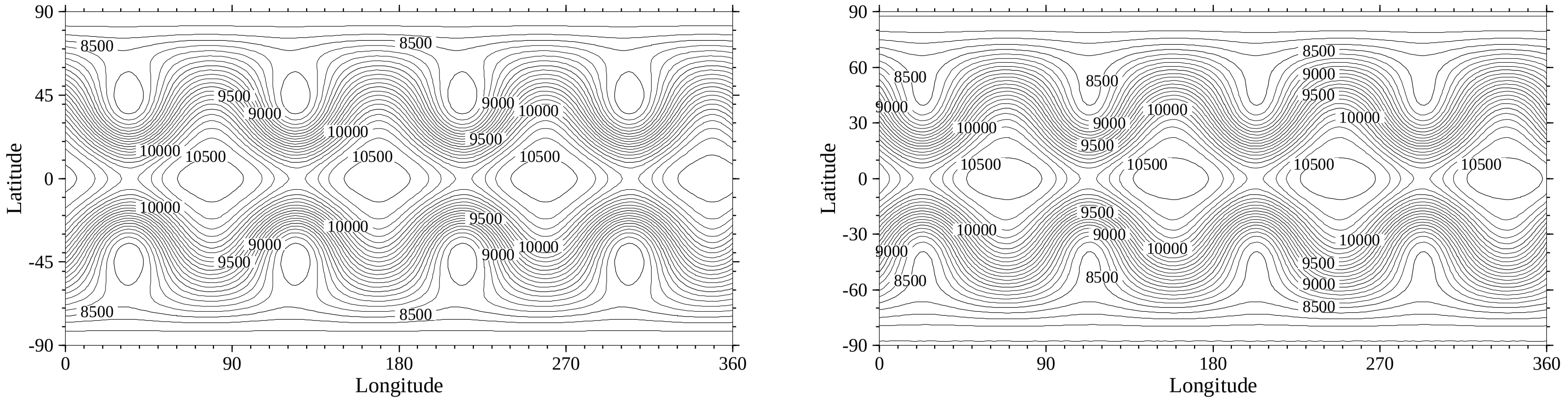
(a) Day 7, geopotential height (m)

(b) Day 14, geopotential height (m)

(c) Day 14, zonal wind u (m/s)

(d) Day 14, meridional wind v (m/s)

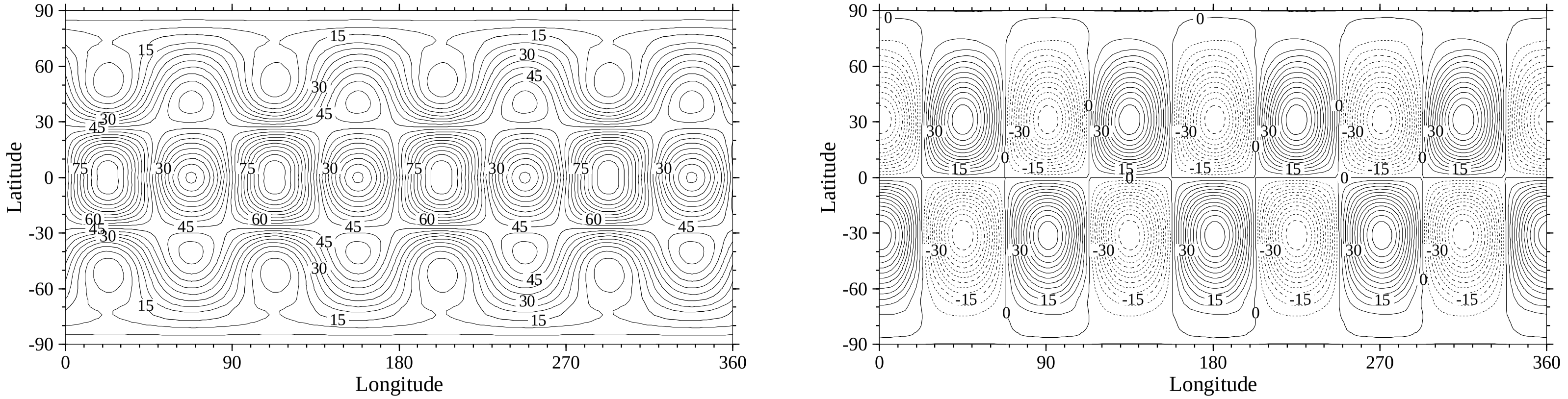

Figure A.13: NCAR reference solution of (a,b) the geopotential height at (a) day 7 and (b) day 14, (c) the zonal wind and (d) meridional wind at day 14. Contour intervals are (a,b) 100 m and (c,d) 5 ms^{-1}.

A.2 McDonald-Bates shallow water test

The *McDonalds and Bates* [1989] shallow water test case is not part of the standard shallow test suite but could be considered an extension of the standard testing framework. The test has been e.g. used by *Bates et al.* [1990], *Giraldo* [2000b] and *Giraldo et al.* [2002] who also coined the name “Dancing High-Low Waves”. The initial condition consists of a geostrophically balanced flow pattern where the geopotential is given by

$$\Phi(\lambda,\varphi) = \bar{\Phi} + 2\,\Omega\,a\,v_0\,\sin^3\varphi\,\cos\varphi\,\sin\lambda \tag{A.6}$$

with $\bar{\Phi} = 5.768 \times 10^4\,m^2s^{-2}$ and $v_0 = 20ms^{-1}$. The corresponding geopotential height field is displayed in figure A.14. The wind components u and v can then be derived from expression A.6 using the geostrophic relationship. The resulting wind field is shown in figure A.15 on the facing page.

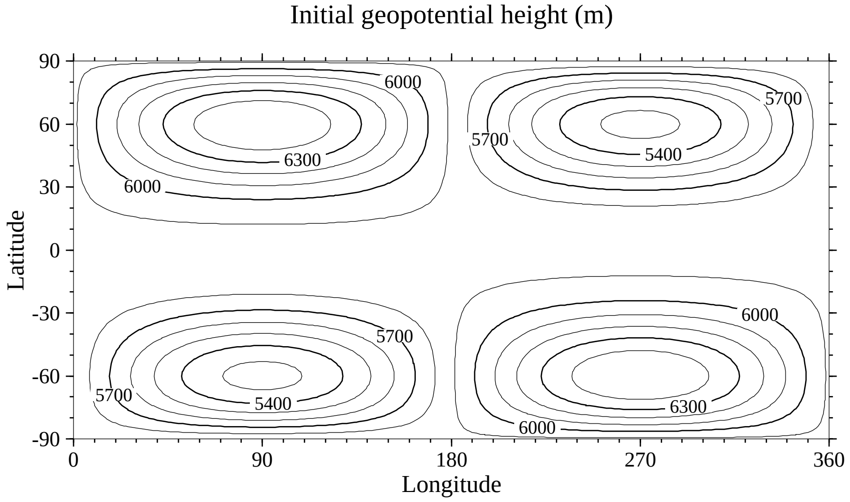

Figure A.14: Initial geopotential height for the McDonald test. Contour interval is 100 m.

This test does not have an analytic solution. It consists of two large waves with the high wave in the west and the low wave in the east (in the Northern Hemisphere). The positions in the Southern Hemisphere are reversed. The wave rotates clockwise

(a) Initial zonal wind u (m/s)

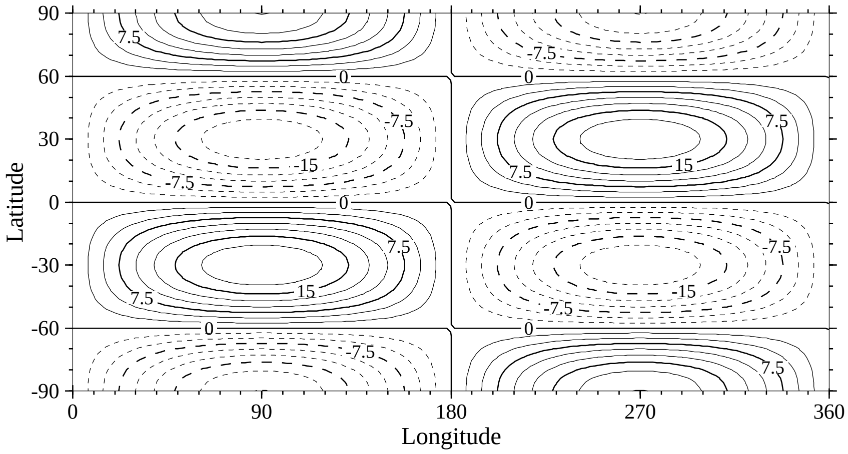

(b) Initial meridional wind v (m/s)

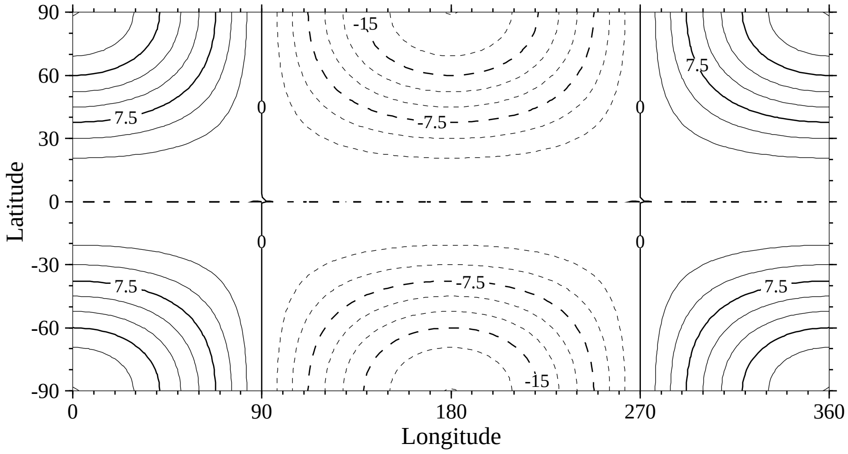

Figure A.15: Initial (a) zonal wind and (b) meridional wind for the McDonald test. Contour intervals are 2.5 m^{-1}.

in a dance like fashion. After 5 days, the low and high wave exchange their positions and arrive again at their original locations at day 10.

A.3 Idealized tests for 3D dynamical cores

A.3.1 Jablonowski-Williamson baroclinic wave test

The Jablonowski-Williamson baroclinic wave test case for 3D dynamical cores has been developed as part of the adaptive grid research project. As outlined in Section 6.1 on page 190, the initial conditions are defined analytically. A brief overview of the derivation is given below.

Derivation of the Jablonowski-Williamson baroclinic wave test case

The starting point is the 3D primitive equation system in spherical coordinates (λ, φ) with a pressure-based hybrid vertical coordinate η. The PE equations are given by

Horizontal momentum equations:

$$\begin{aligned} \frac{du}{dt} - \frac{u\,v\,\tan\varphi}{a} &= \frac{-1}{a\,\cos\varphi}\left(\frac{\partial\Phi}{\partial\lambda} + R_d\,T\,\frac{\partial\ln p}{\partial\lambda}\right) + f\,v + \mathcal{F}_{r,\lambda} \\ \frac{dv}{dt} + \frac{u^2\,\tan\varphi}{a} &= \frac{-1}{a}\left(\frac{\partial\Phi}{\partial\varphi} + R_d\,T\,\frac{\partial\ln p}{\partial\varphi}\right) - f\,u + \mathcal{F}_{r,\varphi} \end{aligned}$$

Hydrostatic equation:

$$\begin{aligned} \frac{\partial\Phi}{\partial\eta} &= -\frac{R_d\,T}{p}\,\frac{\partial p}{\partial\eta} \\ if\;\; p_s = p_0 \;\;\Rightarrow\;\; \eta\,\frac{\partial\Phi'}{\partial\eta} &= -R_d\,T' \end{aligned}$$

Thermodynamic equation:

$$\frac{d\Theta}{dt} = \frac{\Theta}{T}\,\frac{\mathcal{Q}}{c_p}$$

Continuity equation:

$$\frac{\partial}{\partial t}\left(\frac{\partial p}{\partial \eta}\right)+\frac{1}{a\,\cos\varphi}\,\frac{\partial}{\partial \lambda}\,\left(\frac{\partial p}{\partial \eta}\,u\right)+\frac{1}{a\,\cos\varphi}\,\frac{\partial}{\partial \varphi}\,\left(\frac{\partial p}{\partial \eta}\,(v\,\cos\varphi)\right)+\frac{\partial}{\partial \eta}\left(\frac{\partial p}{\partial \eta}\,\dot{\eta}\right)=0$$

Equation of state for dry air:

$$p=\rho\,R_d\,T$$

with:

$$\begin{aligned}
\dot{\eta} &= \frac{d\eta}{dt} \\
\frac{d}{dt}() &= \frac{\partial}{\partial t}() + (\vec{v}\nabla)() \\
&= \frac{\partial}{\partial t}() + \frac{u}{a\,\cos\varphi}\frac{\partial}{\partial \lambda}() + \frac{v}{a}\frac{\partial}{\partial \varphi}() + \dot{\eta}\,\frac{\partial}{\partial \eta}()
\end{aligned}$$

Based on this formulation the goal is to derive a steady state, balanced initial data set for the model variables u, v, p_s, T, Φ_s where u and v stand for the horizontal wind components, p_s symbolizes the surface pressure, T denotes the temperature field and Φ_s is the geopotential of the surface orography. The derivation of such an initial data set contains several degrees of freedom, e.g. the chosen wind profiles and constant parameters. Here, the selected profiles and parameters guarantee that the resulting initial data closely resemble a realistic climatic state and fulfill the symmetric and static stability criterion. On the other hand, the flow is designed to be baroclinically and barotropically unstable. The design principles and derivation steps are

1. Assume adiabatic and frictionless atmosphere, set $\mathcal{Q}$ and $\vec{\mathcal{F}}$ to zero.

2. Choose nondivergent wind field u and v (e.g. as in Section 6.1).

3. Choose constant surface pressure p_s, e.g. $p_s = p_0 = 1000\,hPa$.

4. Choose the horizontally averaged temperature profile $\langle\, T(\eta)\,\rangle$. This can easily be done in z coordinates, e.g. $\langle T\rangle = T_0 - \Gamma\, z$ where Γ is the vertical temperature gradient. This equation can then be transformed into the p system (or equivalently into the $\eta-$ or σ-systems) via integration of the hydrostatic relationship $\frac{\partial\, p}{p} = -\,\frac{g}{R_d\,\langle T\rangle}\,\partial z$. It follows $z = \frac{T_0}{\Gamma}\left(1 - \left(\frac{p}{p_0}\right)^{\frac{R_d\,\Gamma}{g}}\right)$.

5. Derive the geopotential Φ and compute the surface geopotential Φ_s:

    - start with v momentum equation
    - assume steady state solution: set $\frac{d\,v}{d\,t}$ to zero
    - take chosen equation for u, plug it into the momentum equation for v and integrate (note that $\frac{\partial\,\ln p_s}{\partial\,\varphi} = 0$ on η-surfaces)

      $$\frac{1}{a}\,\frac{\partial\Phi'}{\partial\varphi} = -\,u\,(2\,\Omega\,\sin\varphi\,+\,\frac{u}{a}\,\tan\varphi)$$

      Φ' is the deviation of the geopotential from a horizontal mean value $\langle\,\Phi\,\rangle$
    - integrate analytically in order to arrive at the expression $\Phi' = (\ldots) + \Phi_0$
    - find integration constant Φ_0 using the condition that the deviations vanish when averaged horizontally

      $$\frac{1}{4\pi}\int_0^{2\pi}\int_{-\frac{\pi}{2}}^{\frac{\pi}{2}}\Phi'\,\cos\varphi\,d\varphi\,d\lambda = 0$$
    - calculate: $\Phi(\varphi,\lambda,\eta) = \langle\,\Phi(\eta)\,\rangle + \Phi'(\varphi,\lambda,\eta)$ where $\langle\,\Phi(\eta)\,\rangle$ is the horizontally averaged geopotential. In hydrostatic GCMs, it is only necessary to calculate the surface geopotential Φ_s which represents the orography. Therefore, the horizontally averaged geopotential at the surface $\langle\,\Phi(\eta)\,\rangle = \langle\,\Phi(\eta_s)\,\rangle$ is set to zero. In general, $\langle\,\Phi\,\rangle$ can be computed via $\langle\,\Phi\,\rangle = gz(p)$.

6. Derive the temperature T:

   - Determine the horizntal temperature deviation T' using the hydrostatic equation (differentiate Φ')

     $$T'(\lambda, \varphi, \eta) = \frac{-\eta}{R_d} \frac{\partial \Phi'(\lambda, \varphi, \eta)}{\partial \eta}$$

   - calculate: $T(\varphi, \lambda, \eta) = \langle T(\eta) \rangle + T'(\varphi, \lambda, \eta)$ where $\langle T(\eta) \rangle$ is the horizontally averaged temperature discussed in step 4.

In this setup, the initial vertical velocity is zero and the thermodynamic equation is automatically fulfilled. A baroclinic wave can then be triggered when disturbing the steady state initial conditions as explained in Section 6.1. All constants are listed in Appendix C.

High resolution reference solution

The baroclinic wave test case can be used in two configurations. First, model runs without a perturbation can be performed. They assess how well the model keeps its initial state which ultimately could break down over time due to the possible accumulation of truncation errors. In this configuration, error norms can be computed using the initial state as the true solution. Second, when adding the perturbation to the zonal wind field a complex flow field evolves over time that no longer has an analytic solution. Therefore, high-resolution runs can serve as the best estimate of the true reference field. High resolution simulations with the baroclinic wave test case have been performed with 4 different dynamical cores, namely with the dynamics package of the weather prediction code GME (German Weather Service DWD) and the three dynamical cores in the NCAR CCSM/CAM2.0 model framework. Among theses three NCAR dynamics modules is the NASA/NCAR finite-volume dynamical core.

The results of this comparison are presented in *Jablonowski and Williamson* [2004]. In summary, the high resolution reference simulations converge (see also figure A.16) and produce very similar 10-day forecasts.

As an example of the reference flow pattern, the results of the NASA/NCAR finite-volume dynamical core (CAM2 model framework) at the resolution $0.625° \times 0.5°$ are selected. It is important to note, that this dynamical core is very similar to the adaptive finite-volume dynamical core. The numerical concepts are identical but the computational grid in the CAM2 framework is shifted by half a grid length in longitudinal and meridional direction. This adds one more grid point in the meridional direction that now includes the two grid boxes centered at the pole points. The selected horizontal resolutions, e.g. the $0.625° \times 0.5°$ grid, represent a standard NCAR setting with a slightly finer resolution in the meridional direction. Though, this resolution is comparable to the finest adapted grid run with a $0.625° \times 0.625°$ grid (Section 6.2 on page 201). 26 vertical levels are chosen (see also Appendix B).

In figure A.16 on the next page snapshots of the surface pressure field in the Northern Hemisphere at day 8 are presented that have been computed with the CAM2.0 finite-volume dynamical core at three different horizontal resolutions. This plot provides a reference for the statically adapted 3D runs in Section 6.2. The flow has evolved rapidly up to this point and wave breaking processes set in shortly thereafter.

In addition, figure A.17 on page 244 shows the surface pressure and surface[1] temperature field at day 10 for two different horizontal resolutions. The flow fields have almost converged at these resolutions and only a minor intensification of the low

---

[1] Temperature at the lowermost η model level.

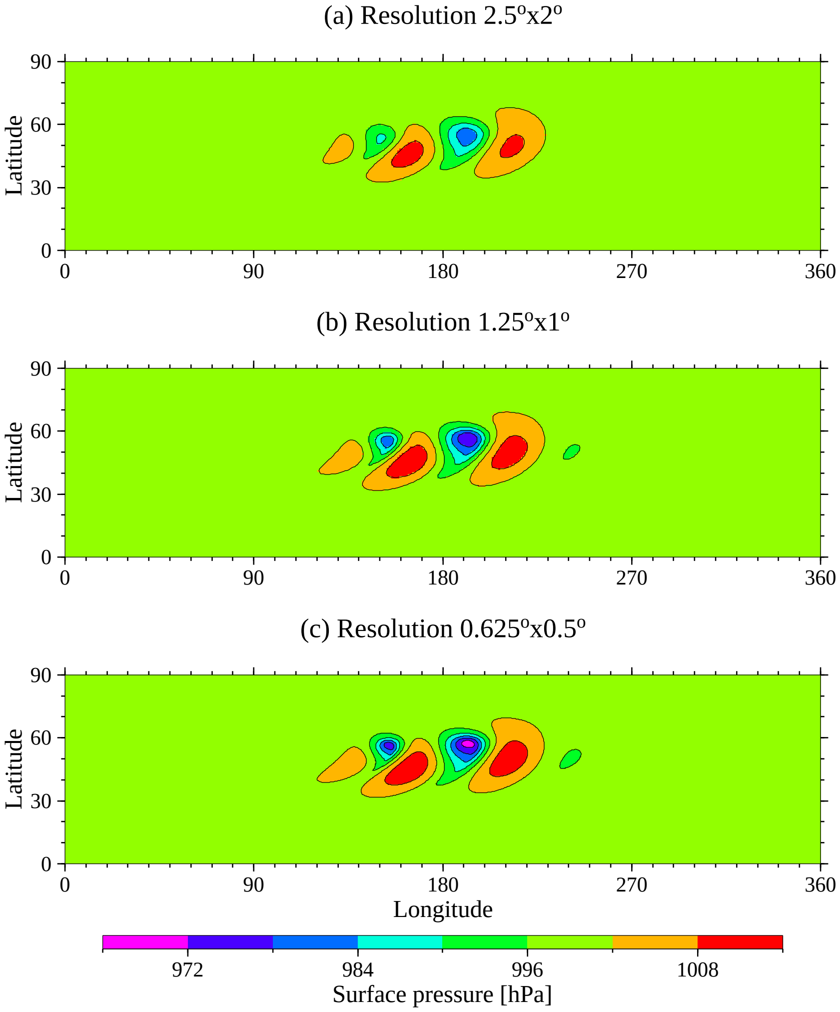

Figure A.16: Surface pressure in the Northern Hemisphere at day 8 for the horizontal resolutions (lon x lat) (a) 2.5° × 2°, (b) 1.25° × 1° and (c) 0.625° × 0.5°. The contour intervals are 6 hPa.

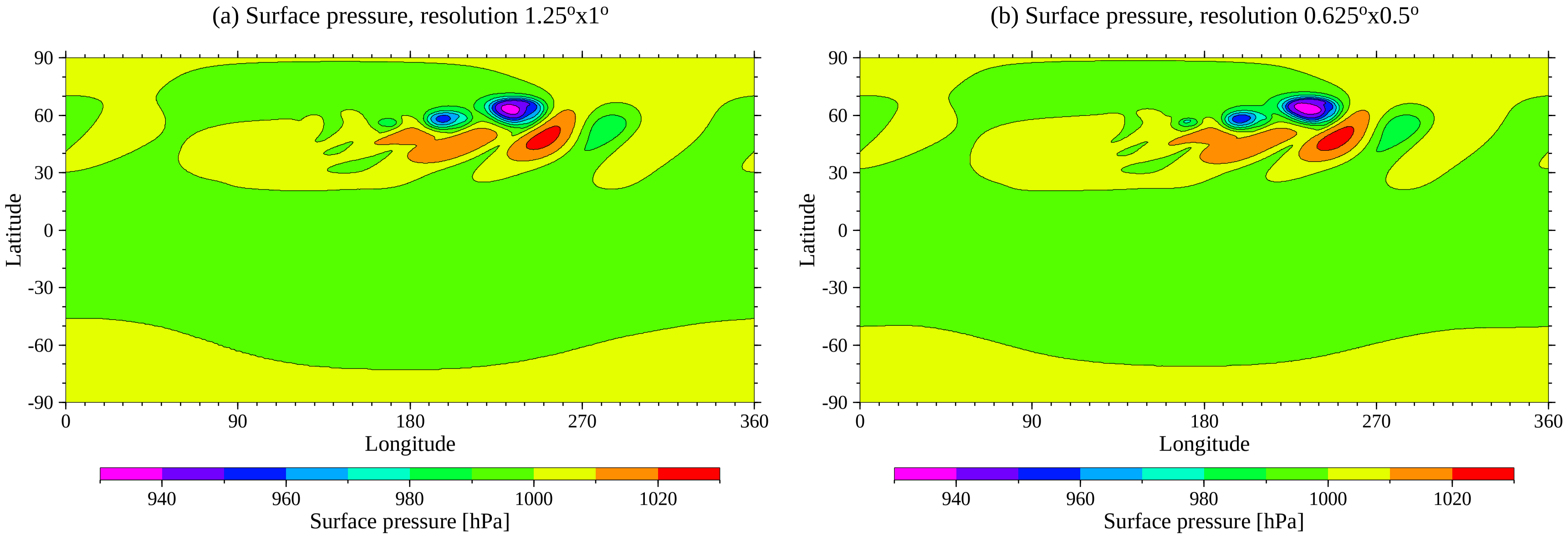

(a) Surface pressure, resolution 1.25ºx1º

(b) Surface pressure, resolution 0.625ºx0.5º

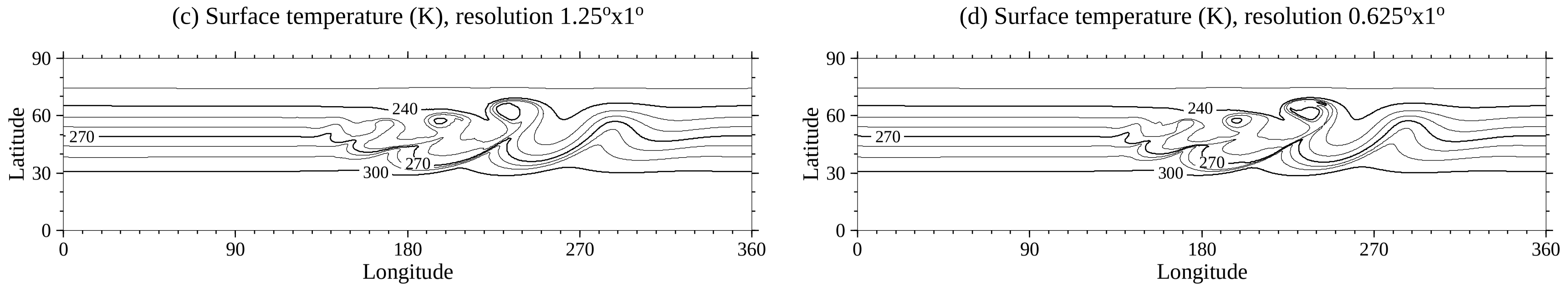

(c) Surface temperature (K), resolution 1.25ºx1º

(d) Surface temperature (K), resolution 0.625ºx1º

Figure A.17: (a,b) Surface pressure and (c,d) surface temperature in the Northern Hemisphere at day 10 for the horizontal resolutions (a,c) 1.25° × 1° and (b,d) 0.625° × 0.5°. The contour intervals are 10 hPa and 10 K, respectively.

pressure system is apparent in the $0.625^\circ \times 0.5^\circ$ plot. In the Southern Hemisphere, no wave activities develop during the first 10 days, which makes the test ideal for adaptive mesh simulations.

A.3.2 Polvani baroclinic wave test

An alternative test case for idealized baroclinic wave assessments in 3D dynamical cores has recently been suggested by *Polvani et al.* [2004]. The test strategy is similar to the aforementioned Jablonowski-Williamson test. The Polvani test case also starts with a steady state initial data set. Baroclinic waves are then triggered by an unbalanced temperature perturbation that overlays the temperature field. The forecast period also covers 10-12 model days. In the Polvani test, the initial conditions are not entirely based on analytic expressions. Here, numerically approximated integrals need to be computed for the initial temperature field. The resulting flow pattern resembles the realistic climatic state only in the Northern Hemisphere whereas the Southern Hemisphere is held passive.

Figure A.18 on the next page shows the initial conditions for the zonal wind u and temperature T (see details in *Polvani et al.* [2004]). In addition, the potential temperature field and initial temperature perturbation are presented. It must be noted that the temperature perturbation is placed at $(\lambda_c, \varphi_c) = (67.5^\circ E, 45^\circ N)$ which is different from the position mentioned in the publication. Furthermore, the initial meridional wind v as well as the surface geopotential Φ_s are zero and the surface pressure field is set to $p_s = 1000\,hPa$.

As before, reference solutions have been computed with the NASA/NCAR CAM2.0 finite-volume dynamical core with 26 vertical levels. Examples of the surface pressure field in the Northern Hemisphere at day 8 and day 10 are shown in figure A.19. These

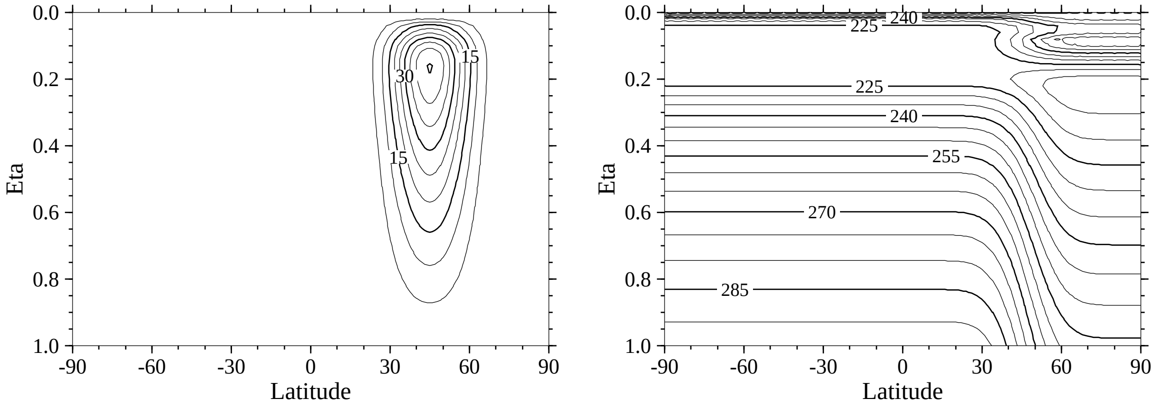

(a) Zonal wind (m/s)

(b) Temperature (K)

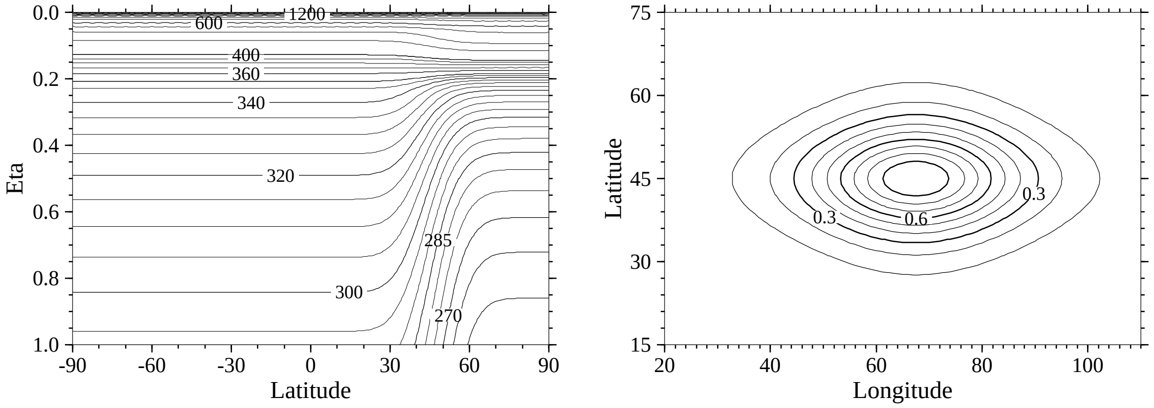

(c) Potential temperature (K)

(d) Temperature perturbation (K)

Figure A.18: Initial (a) zonal wind, (b) temperature, (c) potential temperature and (d) temperature perturbation that is added to the temperature field at each level. Contour intervals are (a) 5 ms^{-1}, (b) 5 K, (c) 5 K (except at upper levels) and (d) 0.1 K. The zero contour is omitted.

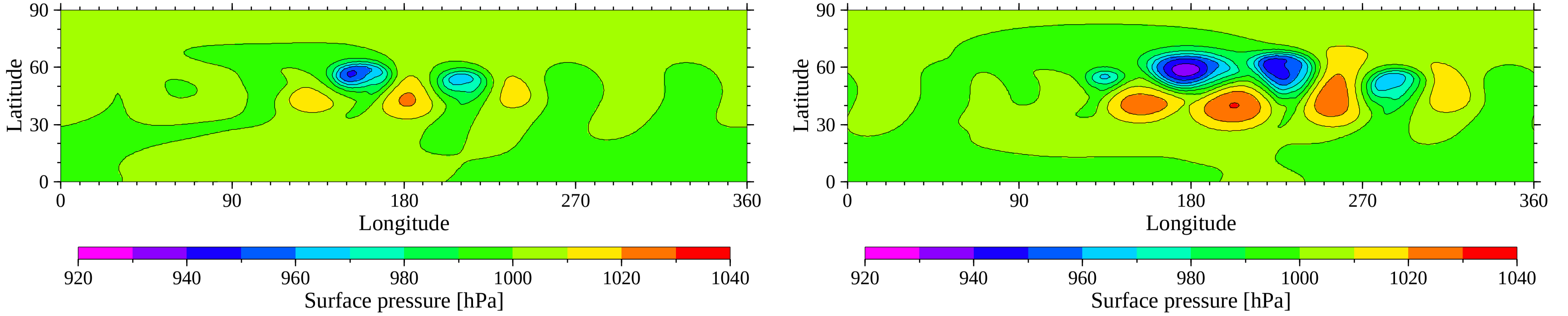

(a) Day 8, uniform resolution 2.5ºx2º

(b) Day 10, uniform resolution 2.5ºx2º

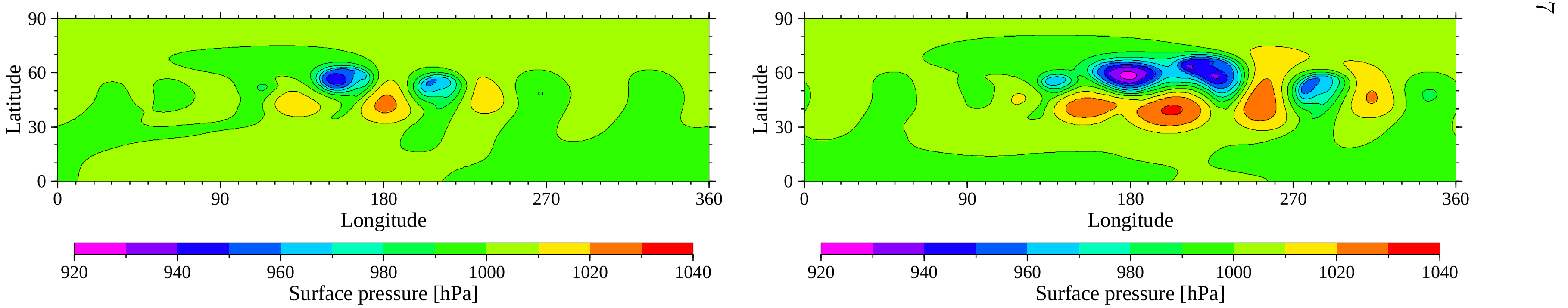

(c) Day 8, uniform resolution 1.25ºx1º

(d) Day 10, uniform resolution 1.25ºx1º

Figure A.19: Surface pressure fields in the Northern Hemisphere for two different model days at the resolutions 2.5° × 2° (top row, a & b) and 1.25° × 1° (bottom row, c & d). (a,c) show model day 8, (b,d) day 10. Contour intervals are 10 hPa.

two days illustrate the baroclinic wave shortly before and after the wave breaking event. Subfigures A.19 (c,d) represent an almost converged solution (see also convergence discussion for this test case in *Polvani et al.* [2004]. Here they are considered the reference solution for the adaptive run in Section 6.3. Higher resolution runs with a uniform $0.625^\circ \times 0.5^\circ$ grid have also been performed with the CAM2.0 finite-volume dynamical core (not shown). The figures are almost indistinguishable from subfigures (c,d) although a slight intensification of the main low pressure system can be observed.

APPENDIX B

Vertical coordinate

The Eulerian reference frame of the NASA/NCAR dynamical core is based on the hybrid, orography following η-coordinate in the vertical direction (see also *Simmons and Burridge* [1981]. It is comprised of a pure pressure and the so-called σ-component with $\sigma = \frac{p}{p_s}$. Here, p and p_s symbolize the pressure and surface pressure, respectively.

The pressure at any model level η is given by

$$p(\lambda, \varphi, \eta, t) = a(\eta) + b(\eta)\, p_s(\lambda, \varphi, t)$$

where the coefficients $a(\eta)$ and $b(\eta)$ are solely height-dependent and provided in tabular form (see table B.1).

In the discrete system, the vertical direction is subdivided into N_{lev} model levels which are bounded by $N_{lev}+1$ interfaces, here also viewed as Lagrangian surfaces. This leads to the following discrete representation

$$p_{k+\frac{1}{2}} = a_{k+\frac{1}{2}} + b_{k+\frac{1}{2}}\, p_s \quad ,$$

with $k = 0, 1, 2, \cdots N_{lev}$. The index $\frac{1}{2}$ denotes the positions of the level interfaces, the index $N_{lev}+1$ symbolizes the model level at the ground. In order to ensure, that this lowermost Lagrangian surface follows the actual topography in the system the following boundary conditions are imposed

$$a_{N_{lev}+\frac{1}{2}} = 0 \qquad \text{and} \qquad b_{N_{lev}+\frac{1}{2}} = 1 \quad .$$

This guarantees that the pressure at the lowermost interface is the actual surface pressure at any given location.

If the pressure needs to be evaluated at the center of a model layer, then the pressure values can be linearly interpolated based on the surrounding surfaces

$$p_k = \frac{1}{2}\left(p_{k+\frac{1}{2}} + p_{k-\frac{1}{2}}\right) \quad .$$

Furthermore, the pressure thickness Δp_k in the Eulerian reference frame is defined by

$$\Delta p_k = p_{k+\frac{1}{2}} - p_{k-\frac{1}{2}} \quad .$$

and the thickness in terms of the time-invariant η levels is given by

$$\eta_{k+\frac{1}{2}} = \frac{a_{k+\frac{1}{2}}}{p_0} + b_{k+\frac{1}{2}}$$

where the parameter p_0 symbolizes a constant reference surface pressure, usually set to $1000hPa$ or $1013.25hPa$. Here the lower boundary condition is $\eta_{N_{lev}+\frac{1}{2}} = 1$.

If η values are required that lie in between two model interfaces, then they can be computed via linear interpolations

$$\eta = \eta_{k+\frac{1}{2}} + \frac{(p - p_{k+\frac{1}{2}})(\eta_{k+\frac{1}{2}} - \eta_{k-\frac{1}{2}})}{(p_{k+\frac{1}{2}} - p_{k-\frac{1}{2}})} \qquad \text{for} \qquad p_{k-\frac{1}{2}} \le p \le p_{k+\frac{1}{2}} \quad .$$

Table B.1 on the facing page shows the vertical coefficients $a_{k+\frac{1}{2}}$ and $b_{k+\frac{1}{2}}$ that have been used for the 3D dynamical core model runs. The table contains the $N_{lev}+1 = 27$ coefficients for the Lagrangian model surfaces that enclose the $N_{lev} = 26$ model layers. These model levels have been derived for NCAR's atmosphere model CAM and represent the current 26 standard layers for climate simulations with CAM.

Level k	26 model layers	
	$a_{k+\frac{1}{2}}$ (Pa)	$b_{k+\frac{1}{2}}$
0	219.4067	0.00000000
1	489.5209	0.00000000
2	988.2418	0.00000000
3	1805.201	0.00000000
4	2983.724	0.00000000
5	4462.334	0.00000000
6	6160.587	0.00000000
7	7851.243	0.00000000
8	7731.271	0.01505309
9	7590.131	0.03276228
10	7424.086	0.05359622
11	7228.744	0.07810627
12	6998.933	0.10694110
13	6728.574	0.14086370
14	6410.509	0.18077200
15	6036.322	0.22772200
16	5596.111	0.28295620
17	5078.225	0.34793640
18	4468.96	0.42438220
19	3752.191	0.51431680
20	2908.949	0.62012020
21	2084.739	0.72353550
22	1334.443	0.81767680
23	708.499	0.89621530
24	252.136	0.95347610
25	0.	0.98511220
26	0.	1.00000000

Table B.1: Vertical coefficients for the 26 model levels. The parameter $a_{k+\frac{1}{2}}$ denotes the pure pressure component (in Pa), $b_{k+\frac{1}{2}}$ defines the σ part of the hybrid η-system

.

APPENDIX C

Symbols and Acronyms

Model variables

σ	vertical coordinate ($\sigma = \frac{p}{p_s}$)
η	vertical coordinate (hybrid σ-p system)
φ	geographical latitude in spherical coordinates ($\frac{-\pi}{2} \leq \varphi \leq \frac{\pi}{2}$)
λ	geographical longitude in spherical coordinates ($0 \leq \lambda \leq 2\pi$)
u	zonal wind (m/s)
v	meridional wind (m/s)
h	geopotential height in m (shallow water system)
h_s	height of the orography in m (shallow water system)
T	temperature (K)
Θ	potential temperature (K), $\Theta = T\left(\frac{p_0}{p}\right)^{\kappa}$
p_s	surface pressure (Pa)
p	pressure (Pa)
δp	pressure thickness of a Lagrangian layer (Pa)
ρ	density (kgm^{-3}), $\rho = \frac{p}{R_d T}$
Φ	geopotential (m^2/s^2)
Φ_s	surface geopotential (m^2/s^2)

ζ	relative vorticity (s^{-1}), $\zeta = \vec{k} \cdot (\nabla \times \vec{v})$
D	divergence (s^{-1}), $D = \nabla \cdot \vec{v}$
$\langle\,\rangle$	horizontal average
$(\,)'$	deviation from the horizontal average

Model parameters for the idealized test case

u_0	maximum wind speed of the zonal jet	$u_0 = 35\ m/s$
η_0	center of the jet stream	$\eta_0 = 0.252$
η_t	tropopause level	$\eta_t = 0.2$
η_s	surface level	$\eta_s = 1.0$
Γ	lapse rate of the horizontally averaged temperature	$\Gamma = 0.005\ K/m$
p_0	reference pressure at the ground	$p_0 = 100000\ Pa$
T_0	reference temperature	$T_0 = 288\ K$
ΔT	parameter to adjust the temperature at upper levels	$\Delta T = 480000\ K$
(λ_c, φ_c)	center of the Gaussian perturbation	$(\lambda_c, \varphi_c) = (\frac{\pi}{9}, \frac{2\pi}{9})$
R	radius of the Gaussian perturbation	$R = \frac{a}{10}$

Physical constants and parameters

a	radius of the earth	$a = 6371229\ m$
Ω	angular velocity	$\Omega = 7.29211 * 10^{-5}\ s^{-1}$
f	Coriolis parameter	$f = 2\Omega \sin\varphi$
R_d	gas constant for dry air	$R_d = 287.0\ J/kgK$
c_p	specific heat at constant pressure	$c_p = 1004\ J/kgK$
κ		$\kappa = \frac{R_d}{c_p} = \frac{2}{7}$

g	gravitational acceleration	$g = 9.80616\ m/s^2$

Acronyms

AMIP	Atmospheric Model Intercomparison Project conducted by LLNL
AMR	Adaptive Mesh Refinement
AMR++	AMR class library in the software package Overture
AMRCLAW	Software package: Berger-Oliger AMR library and CLAWPACK
API	Application Programmable Interface
ARPEGE	Numerical Weather Prediction model at Meteo France
BATS-R-US	Block Adaptive Tree Solar-wind Roe Upwind Scheme, UM
C, C++	Programming languages
CAM	Community Atmosphere Model, dynamics package for CCSM
CCSM	Community Climate System Model, developed at NCAR
CFD	Computational Fluid Dynamics
CFL	Courant-Friedrichs-Lewy condition for numerical stability
CHOMBO	AMR software infrastructure
CLAWPACK	Numerical toolbox 'Conservation LAW PACKage'
DAGH	AMR software library (Distributed Adaptive Grid Hierarchy)
DWD	German Weather Service, Offenbach, Germany
ECMWF	European Centre for Medium-Range Weather Forecasts, England
FFT	Fast Fourier Transformation
Fortran	Programming language, Fortran77 or Fortran90
GCM	General Circulation Model
GME	Global weather prediction model at DWD

GSFC	Goddard Space Flight Center, Greenbelt, Maryland, USA
HDF5	Hierachical Data Format: self-describing data convention
IFS	Integrated Forecasting System: ECMWF weather prediction code
KE	Kinetic Energy
LBNL	Lawrence Berkeley National Laboratory, Berkeley, CA, USA
LLNL	Lawrence Livermore National Laboratory, Livermore, CA, USA
MC	Monotonized central-difference limiter for finite-volume methods
MHD	Magnetohydrodynamics
MPI	Message Passing Interface, parallel communication library
NASA	National Aeronautics and Space Administration, USA
NCAR	National Center for Atmospheric Research, Boulder, CO, USA
NetCDF	Portable data format, developed by NCAR
OpenMP	Communication constructs for shared memory architectures
Overture	Object-oriented library for overlapping grids for PDEs
PE	Primitive Equations
PDE	Partial Differential Equation
PARAMESH	AMR software library for block-structured data
PPM	Piecewise Parabolic Method
PV	Potential vorticity
PYRAMID	AMR software library for unstructured data
SAMRAI	Structured AMR Application Infrastructure
SHMEM	Parallel communication library (designed by CRAY)
SL	semi-Lagrangian approach
T42	spectral resolution of a GCM, $\approx 2.8^\circ \times 2.8^\circ$ grid
TE	Total Energy

BIBLIOGRAPHY

BIBLIOGRAPHY

Alapaty, K., R. Mathur, and T. Odman, Intercomparison of spatial interpolation schemes for use in nested grid models, *Monthly Weather Review*, *126*, 243–249, 1998.

Allen, D. J., A. R. Douglass, R. B. Rood, and P. D. Guthrie, Application of a monotonic upstream-biased transport scheme to three-dimensional constituent transport calculations, *Monthly Weather Review*, *119*, 2456–2464, 1991.

Almgren, A. S., J. B. Bell, P. Colella, L. H. Howell, and M. L. Welcome, A conservative adaptive projection method for the variable density incompressible Navier-Stokes equations, *Journal of Computational Physics*, *142*, 1–46, 1998.

Arakawa, A., and V. R. Lamb, Computational design of the basic dynamical process of the UCLA general circulation model, in *Methods in Computational Physics*, edited by J. Chang, pp. 173–265, Academic Press, 1977.

Bacon, D. P., et al., A dynamically adapting weather and dispersion model: The Operational Multiscale Environment Model with Grid Adaptivity (OMEGA), *Monthly Weather Review*, *128*, 2044–2076, 2000.

Bacon, D. P., et al., Dynamically adapting unstructured triangular grids: A new paradigm for geophysical fluid dynamics modeling, *Proceedings of the Indian Academy of Science*, 2002, Accepted for publication. Pre-print available at URL: `http://vortex.atgteam.com/papers/`.

Barros, S. R. M., and C. I. Garcia, A global semi-implicit semi-Lagrangian shallow-water model on locally refined grids, *Monthly Weather Review*, *132*, 53–65, 2004.

Bates, J., and Y. Li, Simulation of stratospheric vortex erosion using three global shallow water numerical models, in *Numerical Methods in Atmospheric and Oceanic Modelling: The André J. Robert Memorial Volume of Atmos.-Ocean*, edited by J. Coté, pp. 55–73, 1997.

Bates, J. R., F. H. M. Semazzi, and R. W. Higgins, Integration of the shallow water equations on the sphere using a vector semi-Lagrangian scheme with a multigrid solver, *Monthly Weather Review*, *118*, 1615–1627, 1990.

Behrens, J., Adaptive Semi-Lagrange-Finite-Elemente-Methode zur Lösung der Flachwassergleichungen. Implementierung und Parallelisierung, Ph.D. thesis, Universität Bremen, Germany, 1995, Fachbereich Mathematik und Informatik.

Behrens, J., An adaptive semi-Lagrangian advection scheme and its parallelization, *Monthly Weather Review*, *124*, 2386–2395, 1996.

Behrens, J., Atmospheric and ocean modelling with an adaptive finite element solver for the shallow-water equations, *Applied Numerical Mathematics*, *26*, 217–226, 1998.

Behrens, J., and J. Zimmermann, Parallelizing an unstructured grid generator with a space-filling curce approach, in *Euro-Par 2000, Lecture Notes in Computer Science*, edited by A. Bode, vol. 1900, pp. 815–823, Springer-Verlag Berlin Heidelberg, 2000.

Behrens, J., K. Dethloff, W. Hiller, and A. Rinke, Evolution of small-scale filaments in an adaptive advection model for idealized tracer transport, *Monthly Weather Review*, *128*, 2976–2982, 2000.

Berger, M., Adaptive mesh refinement software for hyperbolic conservation laws, 2003, Courant Institute, New York, N.Y. URL: `http://cs.nyu.edu/cs/faculty/berger/amrsoftware.html`.

Berger, M., and R. J. LeVeque, Adaptive mesh refinement using wave-propagation algorithms for hyperbolic systems, *Siam J. Num. Anal.*, *35*(6), 2298–2316, 1998.

Berger, M., and J. Oliger, Adaptive mesh refinement for hyperbolic partial differential equations, *Journal of Computational Physics*, *53*, 484–512, 1984.

Berger, M. J., and P. Colella, Local adaptive mesh refinement for shock hydrodynamics, *Journal of Computational Physics*, *82*(1), 64–84, 1989.

Blayo, E., and L. Debreu, Adaptive mesh refinement for finite-difference ocean models: First experiments, *Journal of Physical Oceanography*, *29*, 1239–1250, 1999.

Blayo, E., L. Debreu, G. Mounie, and D. Trystram, Dynamic load balancing for ocean circulation model with adaptive meshing, in *Euro-Par 1999, Lecture Notes in Computer Science*, edited by P. Amestoy, vol. 1685, pp. 303–312, Springer-Verlag Berlin Heidelberg, 1999.

Boer, G. J., and B. Denis, Numerical covergence of the dynamics of a GCM, *Climate Dynamics*, *13*, 359–374, 1997.

Boville, B. A., Sensitivity of simulated climate to model resolution, *Journal of Climate*, *4*, 469–485, 1991.

Boybeyi, Z., N. N. Ahmad, D. P. Bacon, T. J. Dunn, M. S. Hall, P. C. S. Lee, and R. A. Sarma, Evaluation of the Operational Multiscale Environment Model with Grid Adaptivity against the European tracer experiment, *Journal of Applied Meteorology*, *40*, 1541–1558, 2001.

Boyle, J., K. Hodges, I. Simmonds, and D. Jones, AMIP II Diagnostic Subproject No. 3: Statistics of transient circulation systems, 1998, URL http://www-pcmdi.llnl.gov/amip/DIAGSUBS/sp3.html.

Boyle, J. S., Sensitivity of dynamical quantities to horizontal resolution for a climate simulation using the ECMWF (Cycle 33) model, *Journal of Climate*, *6*, 796–815, 1993.

Brackbill, J. U., and J. S. Saltzmann, Adaptive zoning and singular problems in two dimensions, *Journal of Computational Physics*, *46*, 342–368, 1982.

Brown, D., W. Henshaw, and D. Quinlan, Overview of Overture, 2003, Lawrence Livermore National Laboratory, Livermore, CA. URL: `http://www.llnl.gov/CASC/Overture`.

Carpenter, R. L., K. K. Droegemeier, P. R. Woodward, and C. E. Hane, Application of the Piecewise Parabolic Method (PPM) to meteorological modeling, *Monthly Weather Review*, *118*, 586–612, 1990.

CCSM, Eighth annual CCSM workshop: Atmosphere Model Working Group Report, 2003, 25 June 2003, Breckenridge, CO. Available at URL: `http://www.ccsm.ucar.edu/working_groups/Atmosphere/reports/062503.html`.

Cheong, H.-B., Application of double Fourier series to the shallow-water equations on the sphere, *Journal of Computational Physics*, *155*, 1–27, 2000.

Chesshire, G., and W. D. Henshaw, Composite overlapping meshes for the solution of partial differential equations, *Journal of Computational Physics*, *90*, 1–64, 1990.

Clark, T. L., and R. D. Farley, Severe downslope windstorm calculations in two and three spatial dimensions using anelastic interactive grid nesting: A possible meachanism for gustiness, *Journal of the Atmospheric Sciences*, *41*(3), 329–350, 1984.

Colella, P., and P. R. Woodward, The Piecewise Parabolic Method (PPM) for gas-dynamical simulations, *Journal of Computational Physics*, *54*, 174–201, 1984.

Coté, J., M. Roch, A. Stanisforth, and L. Fillion, A variable-resolution semi-Lagrangian finite-element global model of the shallow water equations, *Monthly Weather Review*, *121*, 231–243, 1993.

Coté, J., S. Gravel, A. Methot, A. Patoine, M. Roch, and A. Stanisforth, The operational CMC-MRB Global Environmental Multiscale (GEM) model. Part I: Design considerations and formulation, *Monthly Weather Review*, *126*, 1373–1395, 1998.

Courtier, P., and J. F. Geleyn, A global numerical weather prediction model with variable resolution: Application to the shallow water equations, *Quart. J. Royal Meteor. Soc.*, *114*, 1321–1346, 1988.

Courtier, P., and M. Naughton, A pole problem in the reduced Gaussian grid, *Quart. J. Royal Meteor. Soc.*, *120*, 1389–1407, 1994.

Davies, H. C., A lateral boundary formulation for multi-level prediction models, *Quart. J. Royal Meteor. Soc.*, *102*, 405–418, 1976.

Dennis, J. M., Partitioning with space-filling curces on the cubed sphere, in *Proceedings of the International Parallel and Distributed Processing Symposium (IPDPS), Nice, France*, 2003, Workshop on Massively Parallel Processing at IPDPS.

Dey, C. H., A note on global forecasting with the Kurihara grid, *Monthly Weather Review*, *97*, 597–601, 1969.

Dietachmayer, G. S., and K. K. Droegemeier, Applications of continuous dynamic grid adaptation techniques to meteorological modeling. Part I: Basic formulation and accuracy, *Monthly Weather Review*, *120*, 1675–1706, 1992a.

Dietachmayer, G. S., and K. K. Droegemeier, Applications of continuous dynamic grid adaptation techniques to meteorological modeling. Part II: Efficiency, *Monthly Weather Review*, *120*, 1707–1722, 1992b.

Doswell, C. A., A kinematic analysis associated with a nondivergent flow, *Journal of the Atmospheric Sciences*, *41*, 1242–1248, 1984.

Duffy, P. B., B. Govindasamy, J. Milovich, K. Taylor, M. Wehner, A. Lamont, and S. Thompson, High resolution simulations of global climate, Part 1: Present climate, *Climate Dynamics*, *21*(5-6), 2003.

Durran, D. R., *Numerical Methods for Wave Equations in Geophysical Fluid Dynamics*, Springer, 1999, ISBN 0-387-98376-7.

Falkovich, A. I., A. P. Khain, and I. Ginis, The influence of air-sea interaction on the development and motion of a tropical cyclone: Numerical experiments with a triply nested model, *Meteorol. Atmos. Phys.*, *55*, 167–184, 1995.

Fournier, A., M. A. Taylor, and J. J. Tribbia, Spectral element method part I: Numerical algorithms, in *Proc. 8th Annual Conf. CFD Soc. Canada*, pp. 173–180, 2000, Available on-line at ftp://ftp.cgd.ucar.edu/pub/fournier/publications/AlNu.ps.gz.

Fournier, A., M. A. Taylor, and J. J. Tribbia, The spectral element atmospheric model: High-resolution parallel computation and response to regional forcing, *Monthly Weather Review*, *132*, 726–748, 2004.

Fox, A. D., and S. J. Maskell, Two-way interactive nesting of primitive equation ocean models with topography, *Journal of Physical Oceanography*, *25*, 2977–2996, 1995.

Fox-Rabinovitz, M., and R. S. Lindzen, Numerical experiments on consistent horizontal and vertical resolution for atmospheric models and observing systems, *Monthly Weather Review*, *121*, 264–271, 1993.

Fox-Rabinovitz, M. S., G. L. Stenchikov, M. J. Suarez, and L. L. Takacs, A finite-difference GCM dynamical core with a variable-resolution stretched grid, *Monthly Weather Review*, *125*, 2943–2968, 1997.

Fox-Rabinovitz, M. S., L. L. Takacs, R. C. Govindaraju, and M. J. Suarez, A variable-resolution stretched grid general circulation model: Regional climate simulation, *Monthly Weather Review*, *129*, 453–469, 2001.

Fulton, S. R., A comparison of multilevel adaptive methods for hurricane track prediction, *Electronic Transactions on Numerical Analysis*, *6*, 120–132, 1997.

Fulton, S. R., An adaptive multigrid barotropic tropical cyclone track model, *Monthly Weather Review*, *129*, 138–151, 2001.

Gates, W. L., and C. A. Riegel, A study of numerical errors in the integration of barotropic flow on a spherical grid, *Journal of Geophysical Research*, *67*(2), 773–784, 1962.

Ginis, I., R. A. Richardson, and L. M. Rothstein, Design of a multiply nested primitive equation ocean model, *Monthly Weather Review*, *126*, 1054–1079, 1998.

Giraldo, F., The Lagrange-Galerkin method for the two-dimensional shallow water equations on adaptive grids, *International Journal for Numerical Methods in Fluids*, *33*, 789–832, 2000a.

Giraldo, F., Lagrange-Galerkin methods on spherical geodesic grids: the shallow water equations, *Journal of Computational Physics*, *160*, 336–368, 2000b.

Giraldo, F., and T. E. Rosmond, A scalable spectral element eulerian atmospheric model (SEE-AM) for NWP: Dynamical core tests, *Monthly Weather Review*, *132*, 133–153, 2004.

Giraldo, F., J. S. Hesthaven, and T. Wartburton, Nodal high-order discontinous galerkin methods for the shallow water equations, *Journal of Computational Physics*, *181*, 499–525, 2002.

Gopalakrishnan, S. G., et al., An operational multiscale hurricane forecasting system, *Monthly Weather Review*, *130*, 1830–1847, 2002.

Gravel, S., and A. N. Staniforth, Variable resolution and robustness, *Monthly Weather Review*, *120*, 2633–2639, 1992.

Griebel, M., and G. Zumbusch, Parallel multigrid in an adaptive PDE solver based on hashing and space-filling curves, *Parallel Computing*, *25*, 827–843, 1999.

Haltiner, G. J., and R. T. Williams, *Numerical Prediction and Dynamic Meteorology*, John Wiley & Sons, 1980, ISBN 0-471-05971-4.

Hansen, K. C., G. Toth, A. Ridley, and D. DeZeeuw, *BATS-R-US Design, Code Version 7.5.0*, 2002, University of Michigan, Ann Arbor, Department of Atmospheric, Oceanic and Space Sciences, Center for Space Environment Modeling. URL: `http://csem.engin.umich.edu/docs/DESIGN.pdf`.

Hardiker, V., A global numerical weather prediction model with variable resolution, *Monthly Weather Review*, *125*, 59–73, 1997.

Heikes, R., and D. A. Randall, Numerical integration of the shallow water equations on a twisted icosahedral grid. Part I: Basic design and results of tests, *Monthly Weather Review*, *123*, 1862–1880, 1995.

Held, I. M., and M. J. Suarez, A proposal for the intercomparison of the dynamical cores of atmospheric general circulation models, *Bulletin of the American Meteorological Society*, *75*(10), 1825–1830, 1994.

Hess, R., Dynamically adaptive multigrid on parallel computers for a semi-implicit discretization of the shallow-water equations, Tech. Rep. No. 9, GMD – German National Research Center for Information Technology, St. Augustin, Germany, 1999.

Hodges, K. I., A general method for tracking analysis and its application to meteorological data, *Monthly Weather Review*, *122*, 2573–2586, 1994.

Hodges, K. I., Feature tracking on the unit sphere, *Monthly Weather Review*, *123*, 3458–3465, 1995.

Holton, J. R., *An Introduction to Dynamic Meteorology*, Academic Press, Inc., 1992, ISBN 0-12-354355-X.

Hornung, R., A. Wissink, S. Smith, and N. Elliott, SAMRAI - structured adaptive mesh refinement application infrastructure, 2003, Lawrence Livermore National Laboratory, Livermore, CA. URL: `http://www.llnl.gov/CASC/SAMRAI/`.

Hortal, M., and A. J. Simmons, Use of reduced grids in spectral models, *Monthly Weather Review*, *119*, 1057–1074, 1991.

Hoskins, B. J., and A. J. Simmons, A multi-layer spectral model and the semi-implicit method, *Quart. J. R. Met. Soc.*, *101*, 637–655, 1975.

Hubbard, M. E., and N. Nikiforakis, A three-dimensional, adaptive, Godunov-type model for global atmospheric flows, *Monthly Weather Review*, *131*, 1848–1864, 2003.

Iselin, J. P., J. M. Prusa, and W. J. Gutowski, Dynamic grid adaptation using the MPDATA scheme, *Monthly Weather Review*, *130*, 1026–1039, 2002.

Jablonowski, C., and D. L. Williamson, A baroclinic instabilitiy test case for atmospheric model dynamical cores, 2004, In preparation.

Jakob, R., J. J. Hack, and D. L. Williamson, Solutions to the shallow-water test set using the spectral transform method, Tech. Rep. NCAR/TN-388+STR, National Center for Atmospheric Research, Boulder, Colorado, 1993.

Jakob-Chien, R., J. J. Hack, and D. L. Williamson, Spectral transform solutions to the shallow water test set, *Journal of Computational Physics*, *119*, 164–187, 1995.

Janjić, T., Comments on 'A finite volume integration method for computing pressure gradient forces in general vertical coordinates' by Shian-Jiann Lin (July B, 1997, 123, 1749–1762), *Quart. J. Royal Meteor. Soc.*, *124*, 2527–2529, 1998.

Jeong, J., and F. Hussain, On the identification of a vortex, *J. Fluid Mech.*, *285*, 69–94, 1995.

Jones, D. A., and I. Simmonds, A climatology of southern hemisphere extratropical cyclones, *Climate Dynamics*, *9*, 131–145, 1993.

Jones, R. W., A nested grid for a three-dimensional model of a tropical cyclone, *Journal of the Atmospheric Sciences*, *34*, 1528–1553, 1977.

Juckes, M. N., and M. E. McIntyre, A high-resolution one-layer model of breaking planetary waves in the stratosphere, *Nature*, *328*, 590–596, 1987.

Kalnay-Rivas, E., A. Bayliss, and J. Storch, The 4th GISS model of the global atmosphere, *Beiträge zur Physik der Atmosphäre*, *50*, 299–311, 1977.

Kessler, M., Development and analysis of an adaptive transport scheme, *Atmospheric Environment*, *33*(15), 2347–2360, 1999.

König, W., R. Sausen, and F. Sielmann, Objective identification of cyclones in GCM simulations, *Journal of Climate*, *6*, 2217–2231, 1993.

Kurihara, Y., Numerical integration of the primitive equations on a spherical grid, *Monthly Weather Review*, *93*, 399–415, 1965.

Kurihara, Y., and M. A. Bender, Use of a movable nested-mesh model for tracking a small vortex, *Monthly Weather Review*, *108*, 1792–1809, 1980.

Kurihara, Y., and L. Holloway, Numerical integration of a nine-level global primitive equations model formulated by the box method, *Monthly Weather Review*, *95*, 509–530, 1967.

Kurihara, Y., G. J. Tripoli, and M. A. Bender, Design of a movable nested-mesh primitive equation model, *Monthly Weather Review*, *107*, 239–249, 1979.

Lambert, S. J., A cyclone climatology of the Canadian Centre General Circulation Model, *Journal of Climate*, *1*, 109–115, 1988.

Lanser, D., J. G. Blom, and J. G. Verwer, Spatial discretization of the shallow water equations in spherical geometry using Osher's scheme, *Journal of Computational Physics*, *165*, 542–564, 2000.

Layton, A. T., Cubic spline collocation method for the shallow water equations on the sphere, *Journal of Computational Physics*, *179*, 578–592, 2002.

Layton, A. T., and W. F. Spotz, A semi-Lagrangian double Fourier method for the shallow water equations on the sphere, *Journal of Computational Physics*, *189*, 180–196, 2003.

Leonard, S. R., J. Turner, and A. V. D. Wal, An assessment of three automatic depression tracking systems, *Meteorol. Appl.*, *6*, 173–183, 1999.

Leslie, L. M., and R. J. Purser, Three dimensional mass-conserving semi-Lagrangian schemes employing forward trajectories, *Monthly Weather Review*, *123*, 2551–2566, 1995.

LeVeque, R., and M. Berger, AMRCLAW: A synthesis of CLAWPACK with marsha berger's adaptive mesh refinement codes, 2003, University of Washington, Seattle, WA. URL: `http://www.amath.washington.edu/~rjl/amrclaw/`.

LeVeque, R. J., *Finite Volume Methods for Hyperbolic Problems*, Cambridge University Press, 2002, ISBN 0-521-00924-3.

Ley, G. W., and R. L. Elsberry, Forecasts of typhoon Irma using a nested-grid model, *Monthly Weather Review*, *104*, 1154–1161, 1976.

Lin, S.-J., A finite volume integration method for computing pressure gradient forces in general vertical coordinates, *Quart. J. Royal Meteor. Soc.*, *123*, 1749–1762, 1997.

Lin, S.-J., The flux-form semi-Lagrangian transport scheme and its applications in atmospheric models, in *MPI Workshop on Conservative Transport Schemes, Report No. 265*, edited by B. Machenhauer, pp. 54–64, Max-Planck-Institut für Meteorologie, 1998a.

Lin, S.-J., Reply to comments by T. Janjić on ‘A finite volume integration method for computing pressure gradient forces in general vertical coordinates’ (July B, 1997, 123, 1749–1762), *Quart. J. Royal Meteor. Soc.*, *124*, 2531–2533, 1998b.

Lin, S.-J., and R. B. Rood, Multidimensional flux-form semi-Lagrangian transport scheme, *Monthly Weather Review*, *124*, 2046–2070, 1996.

Lin, S.-J., and R. B. Rood, An explicit flux-form semi-Lagrangian shallow water model on the sphere, *Quart. J. Royal Meteor. Soc.*, *123*, 2477–2498, 1997.

Lin, S.-J., W. C. Chao, Y. C. Sud, and G. K. Walker, A class of the van Leer-type transport schemes and its application to the moisture transport in a general circulation model, *Monthly Weather Review*, *122*, 1575–1593, 1994.

Lin, S.-J., R. B. Rood, and K.-S. Yeh, Development of the NASA finite-volume dynamical core for global models, 2001, Internal report, NASA Goddard Space Flight Center, Greenbelt, Maryland.

Lindzen, R. S., and M. Fox-Rabinovitz, Consistent vertical and horizontal resolution, *Monthly Weather Review*, *117*, 2575–2583, 1989.

Lou, J. Z., and C. D. Norton, PYRAMID – unstructured adaptive mesh refinement, 1999, NASA Jet Propulsion Laboratory, Pasadena, CA. URL: `http://www-hpc.jpl.nasa.gov/APPS/AMR/`.

MacNeice, P., K. Olson, C. Mobarry, R. de Fainchtein, and C. Packer, PARAMESH 3.0 – structured adaptive mesh refinement, 2003, NASA Goddard Space Flight Center, Greenbelt, MD. URL: `http://ct.gsfc.nasa.gov/paramesh/Users_manual/amr.html`.

Majewski, D., D. Liermann, P. Prohl, B. Ritter, M. Buchhold, T. Hanisch, G. Paul, W. Wergen, and J. Baumgardner, The operational global icosahedral-hexagonal gridpoint model GME: Description and high-resolution tests, *Monthly Weather Review*, *130*, 319–338, 2002.

McDonalds, A., and J. R. Bates, Semi-Lagrangian integration of a gridpoint shallow-water model on the sphere, *Monthly Weather Review*, *117*, 130–137, 1989.

McGregor, J. L., Semi-Lagrangian advection on conformal-cubic grids, *Monthly Weather Review*, *124*, 1311–1322, 1996.

McGregor, J. L., and J. J. Katzfey, NWP experiments with a variable-resolution conformal-cubic primitive equations model, in *Research Activities in Atmospheric and Oceanic Modelling*, edited by A. Staniforth, pp. 3.20–3.21, CAS/JSC Working Group on Numerical Experimentation, WMO/TD–No. 865, 1998, Report No. 27.

Miyakoda, K., and A. Rosati, One-way nested grid models: The interface conditions and the numerical accuracy, *Monthly Weather Review*, *105*, 1092–1107, 1977.

Monaco, A. V., and R. T. Williams, An atmospheric global prediction model using a modified Arakawa differencing scheme, Tech. rep., Naval Postgraduate School, Monterey, CA, 1975, NPS-51WU75041.

Murray, R. J., and I. Simmonds, A numerical scheme for tracking cyclone centers from digital data. Part I: Dvelopment and operation of the scheme, *Aust. Meteorol. Mag.*, *39*, 155–166, 1991.

Nair, R., J. Coté, and A. Stanisforth, Cascade interpolation for semi-Lagrangian advection over the sphere, *Quart. J. Royal Meteor. Soc.*, *125*, 1445–1468, 1999.

Nair, R. D., and B. Machenhauer, The mass-conservative cell-integrated semi-Lagrangian advection scheme on the sphere, *Monthly Weather Review*, *130*, 649–667, 2002.

Odman, M. T., R. Mathur, K. Alapaty, R. K. Srivastava, D. S. McRae, and R. J. Yamartino, Nested and adaptive grids for multiscale air quality modeling, in *Next generation environmental models and computational methods*, edited by G. Delic, and M. F. Wheeler, pp. 59–68, Society for Industrial and Applied Mathematics (SIAM), 1997.

Oehmke, R., High performance dynamic array structures, Ph.D. thesis, University of Michigan, Ann Arbor, USA, 2004, Department of Electrical Engineering and Computer Science.

Oehmke, R., and Q. F. Stout, Parallel adaptive blocks on a sphere, in *Proc. 11th SIAM Conference on Parallel Processing for Scientific Computing*, 2001, URL: `http://www.eecs.umich.edu/~qstout/pap/SIAMPP01.ps`.

Parashar, M., and J. C. Browne, System engineering for high performance computing software: The HDDA/DAGH infrastructure for implementation of parallel structured adaptive mesh refinements, in *Structured Adaptive Mesh Grid Methods: IMA Volumes in Mathematics and its Applications*, Springer-Verlag, 1999, URL: `http://www.caip.rutgers.edu/~parashar/Personal/pubs.html`.

Phillips, N. A., Numerical integration of the primitive equations on the hemisphere, *Monthly Weather Review*, pp. 333–345, 1959.

Polvani, L. M., and R. Saravanan, The three-dimensional structure of breaking rossby waves in the polar wintertime stratosphere, *Journal of the Atmospheric Sciences*, *57*, 3663–3685, 2000.

Polvani, L. M., R. K. Scott, and S. J. Thomas, Numerically converged solutions of the global primitive equations for testing the dynamical core of atmospheric GCMs, *Monthy Weather Review*, 2004, Accepted for publication.

Prusa, J. M., and P. K. Smolarkiewicz, An all-scale anelastic model for geophysical flows: Dynamic grid deformation, *Journal of Computational Physics*, *190*(2), 601–622, 2003.

Purser, R. J., The filtering of meteorological fields, *Journal of Climate and Applied Meteorology*, *26*, 1764–1769, 1987.

Purser, R. J., Degradation of numerical differencing caused by Fourier filtering at high latitudes, *Monthly Weather Review*, *116*, 1057–1066, 1988a.

Purser, R. J., Accurate numerical differencing near a polar singularity skipped grid, *Monthly Weather Review*, *116*, 1067–1076, 1988b.

Purser, R. J., and L. M. Leslie, An efficient interpolation procedure for high-order three-dimensional semi-Lagrangian models, *Monthly Weather Review*, *119*, 2492–2498, 1991.

Rancic, M., Semi-Lagrangian piecewise biparabolic scheme for two-dimensional horizontal advection of a passive scalar, *Monthly Weather Review*, *120*, 1394–1406, 1992.

Rancic, M., An efficient, conservative, monotonic remapping for semi-Lagrangian transport algorithms, *Monthly Weather Review*, *123*, 1213–1217, 1995.

Rao, M. S., and L. Umscheid, Tests of the effect of grid resolution in a global prediction model, *Monthly Weather Review*, *97*, 659–664, 1969.

Rasch, P., Conservative shape-preserving two-dimensional transport on a spherical reduced grid, *Monthly Weather Review*, *122*, 1337–1350, 1994.

Rasch, P. J., and D. L. Williamson, On shape-preserving interpolation and semi-Lagrangian transport, *SIAM J. Sci. Stat. Comput.*, *11*(4), 656–687, 1990.

Raymond, W. H., High-order low-pass implicit tangent filters for use in finite area calculations, *Monthly Weather Review*, *116*, 2132–2141, 1988.

Raymond, W. H., and A. Garder, A spatial filter for use in finite area calculations, *Monthly Weather Review*, *116*, 209–222, 1988.

Rowley, C., and I. Ginis, Implementation of a mesh movement scheme in a multiply nested ocean model and its application to air-sea interaction studies, *Monthly Weather Review*, *127*, 1879–1896, 1999.

Ruge, J. W., S. F. McCormick, and S. Y. K. Yee, Multilevel adaptive methods for semi-implicit solution of shallow-water equations on the sphere, *Monthly Weather Review*, *123*, 2197–2205, 1995.

Sarma, A., N. Ahmad, D. P. Bacon, Z. Boybeyi, T. J. Dunn, M. S. Hall, and P. C. S. Lee, Application of adaptive grid refinement to plume modeling, in *Air pollution VII, Computational Mechanics Publications*, edited by C. A. Brebbia, M. Jacobson, and H. Powell, pp. 59–68, 1999, Also available from WIT Press, Southampton, UK, Advances in Air Pollution, Volume 7 (2000).

Shapiro, R., Smoothing, filtering, and boundary effects, *Reviews of Geophysics and Space Physics*, *8*(2), 359–387, 1970.

Shapiro, R., The use of linear filtering as a parameterization of atmospheric diffusion, *Journal of the Atmospheric Sciences*, *28*, 523–531, 1971.

Shapiro, R., Linear filtering, *Mathmatics of Computation*, *29*(132), 1094–1097, 1975.

Shuman, F. G., On certain truncation errors associated with spherical coordinates, *Journal of Applied Meteorology*, *9*, 564–570, 1970.

Simmons, A. J., and D. M. Burridge, An energy and angular-momentum conserving vertical finite-difference scheme and hybrid vertical coordinates, *Monthly Weather Review*, *109*, 758–766, 1981.

Simmons, A. J., and A. Hollingsworth, Some aspects of the improvement in skill of numerical weather prediction, *Quart. J. Royal Meteor. Soc.*, *128*(580), 647–677, 2002.

Simmons, A. J., and B. J. Hoskins, A comparison of spectral and finite-difference simulations of a growing baroclinic wave, *Quart. J. R. Met. Soc.*, *101*, 551–565, 1975.

Simmons, A. J., and B. J. Hoskins, Baroclinic instability on the sphere: Normal modes of the primitive and quasi-geostrophic equations, *Journal of the Atmospheric Sciences*, *33*, 1454–1477, 1976.

Simmons, A. J., and B. J. Hoskins, Baroclinic instability on the sphere: Solutions with a more realistic tropopause, *Journal of the Atmospheric Sciences*, *34*, 581–588, 1977.

Sinclair, M. R., An objective cyclone climatology for the southern hemisphere, *Monthly Weather Review*, *122*, 2239–2256, 1994.

Sinclair, M. R., Objective identification of cyclones and their circulation intensity, and climatology, *Weather and Forecasting*, *12*, 595–612, 1997.

Skamarock, W. C., Adaptive grid refinements for numerical weather prediction, Ph.D. thesis, Stanford University, California, 1988.

Skamarock, W. C., Truncation error estimates for refinement criteria in nested and adaptive models, *Monthly Weather Review*, *117*, 872–886, 1989.

Skamarock, W. C., and J. B. Klemp, Adaptive grid refinements for two-dimensional and three-dimensional nonhydrostatic atmospheric flow, *Monthly Weather Review*, *121*, 788–804, 1993.

Skamarock, W. C., J. Oliger, and R. L. Street, Adaptive grid refinements for numerical weather prediction, *Journal of Computational Physics*, *80*, 27–60, 1989.

Smolarkiewicz, P. K., The multi-dimensional Crowley advection scheme, *Monthly Weather Review*, *110*, 1968–1983, 1982.

Spall, M. A., and W. R. Holland, A nested primitive equation model for oceanic applications, *Journal of Physical Oceanography*, *21*, 205–220, 1991.

Spotz, W. F., M. A. Taylor, and P. N. Swarztrauber, Fast shallow-water equation solvers in latitude-longitude coordinates, *Journal of Computational Physics*, *145*, 432–444, 1998.

Srivastava, R. K., D. S. McRae, and M. T. Odman, An adaptive grid algorithm for air-quality modeling, *Journal of Computational Physics*, *165*, 437–472, 2000.

Staniforth, A. N., and H. L. Mitchell, A variable-resolution finite-element technique for regional forecasting with the primitive equations, *Monthly Weather Review*, *106*, 439–447, 1978.

Stevens, D. E., and S. Bretherton, A forward-in-time advection scheme and adaptive multilevel flow solver for nearly incompressible atmospheric flows, *Journal of Computational Physics*, *129*, 284–295, 1996.

Stevens, D. E., A. S. Almgren, and J. B. Bell, Adaptive simulations of trade cumulus convection, Tech. rep., Lawrence Livermore National Laboratory, 1999, UCRL-JC-133201.

Stout, Q. F., D. L. DeZeeuw, T. I. Gombosi, C. P. T. Groth, H. G. Marshall, and K. G. Powell, Adaptive blocks: A high-performance data structure, in *Proceedings SC'97*, 1997, URL: `http://www.eecs.umich.edu/~qstout/pap/SC97.ps`.

Stout, Q. F., D. L. DeZeeuw, T. I. Gombosi, C. P. T. Groth, H. G. Marshall, and K. G. Powell, Adaptive parallel computation of a grand-challenge problem: Prediction of the path of a solar-coronal mass ejection, in *Proceedings SC'98*, 1998, URL: `http://www.eecs.umich.edu/~qstout/pap/SC98.ps`.

Sun, W.-Y., and K.-S. Yeh, A general semi-Lagrangian advection scheme employing forward trajectories, *Quart. J. Royal Meteor. Soc.*, *123*, 2463–2476, 1997.

Takacs, L. L., Effect of using a posteriori methods for the conservation of integral invariants, *Monthly Weather Review*, *116*, 525–545, 1988.

Takacs, L. L., and R. C. Balgovind, High-latitude filtering in global grid-point models, *Monthly Weather Review*, *111*, 2005–2015, 1983.

Taylor, M., J. Tribbia, and M. Iskandarani, The spectral element method for the shallow water equations on the sphere, *Journal of Computational Physics*, *130*, 92–108, 1997.

Tolstykh, M. A., Vorticity-divergence semi-Lagrangian shallow-water model of the sphere based on compacy finite differences, *Journal of Computational Physics*, *179*, 180–200, 2002.

Tomlin, A., M. Berzins, J. Ware, J. Smith, and M. J. Pilling, On the use of adaptive gridding methods for modelling chemical transport from multi-scale sources, *Atmospheric Environment*, *31*(18), 2945–2959, 1997.

van Leer, B., Towards the ultimate conservative difference scheme. II. Monotonicity and conservation combined in a second-order scheme, *Journal of Computational Physics*, *14*, 361–370, 1974.

van Leer, B., Towards the ultimate conservative difference scheme. IV. A new approach to numerical convection, *Journal of Computational Physics*, *23*, 276–299, 1977.

van Leer, B., Towards the ultimate conservative difference scheme. V. A second-order sequel to Godunov's method, *Journal of Computational Physics*, *32*, 101–136, 1979.

van Leer, B., Upwind-difference methods for aerodynamic problems governed by the Euler equations, in *Lectures in Applied Mathematics*, vol. 22, pp. 327–336, American Mathematical Society, 1985.

Veldman, A. E. P., and R. W. C. P. Verstappen, Symmetry-conserving discretization with application to the simulation of turbulent flow, in *Numerical Methods for Fluid Dynamics VI*, edited by M. J. Baines, pp. 539–545, Will Print, Oxford, England, 1998.

Verfürt, R., A posteriori error estimators and adaptive mesh refinement techniques for the Navier-Stokes equations, in *Incompressible Computational Fluid Dynamics Trends and Advances*, edited by M. D. Gunzenburger, and R. A. Nicolaides, pp. 447–475, Cambridge University Press, 1993.

Wang, Y., An explicit simulation of tropical cyclones with a triply nested movable mesh primitive equation model: TCM3. Part I: Model desciption and control experiment, *Monthly Weather Review*, *129*, 1370–1394, 2001.

Williamson, D. L., Linear stability of finite-difference approximations on a uniform latitude-longitude grid with Fourier filtering, *Monthly Weather Review*, *104*, 31–41, 1976.

Williamson, D. L., and G. L. Browning, Comparison of grids and difference approximations for numerical weather prediction over the sphere, *Journal of Applied Meteorology*, *12*, 264–274, 1973.

Williamson, D. L., and P. J. Rasch, Two-dimensional semi-Lagrangian transport with shape-preserving interpolation, *Monthly Weather Review*, *117*, 102–129, 1989.

Williamson, D. L., and J. M. Rosinski, Accuracy of reduced grid calculations, *Quart. J. Royal Meteor. Soc.*, *126*, 1619–1640, 2000.

Williamson, D. L., J. B. Drake, J. J. Hack, R. Jakob, and P. N. Swarztrauber, A standard test set for numerical approximations to the shallow water equations in spherical geometry, *Journal of Computational Physics*, *102*, 211–224, 1992.

Williamson, D. L., J. T. Kiehl, and J. J. Hack, Climate sensitivity of the NCAR community climate model (CCM2) to horizontal resolution, *Climate Dynamics*, *11*, 377–397, 1995.

Woodward, P. R., and P. Colella, The numerical simulation of two-dimensional fluid flow with strong shocks, *Journal of Computational Physics*, *54*, 115–173, 1984.

Zalesak, S. T., Fully multidimensional flux-corrected transport algorithms for fluids, *Journal of Computational Physics*, *31*, 335–362, 1979.

Zhang, D.-L., H.-R. Chang, N. L. Seaman, T. T. Warner, and J. M. Fritsch, A two-way interactive nesting procedure with variable terrain resolution, *Monthly Weather Review*, *114*, 1330–1339, 1986.